Comprehensive characterisation and modelling of the surface integrity by deep rolling on flat surface

Dissertation

zur Erlangung des Grades

des Doktors der Ingenieurwissenschaften

der Naturwissenschaftlich-Technischen Fakultät

der Universität des Saarlandes

By Nataliya Lyubenova

Saarbrücken, 2020

Tag des Kolloquiums:	22.07.2020
Dekan:	Univ.-Prof. Dr. rer. nat. Guido Kickelbick
Berichterstatter:	Univ.-Prof. Dr.-Ing. Dirk Bähre
	Prof. Dr.-Ing. Tilmann Beck
	Prof. Dr.-Ing. Stefan Diebels
Vorsitz:	Prof. Dr. Martin Müser
Akad. Mitarbeiter:	Dr.-Ing. Florian Schäfer

Abstract

The modern mechanical engineering is confronted with growing demands for production of high qualitative and durable products, manufactured at low costs and with short time to market. Those demands can be achieved by optimizing the product properties like lightweight, fatigue strength, corrosion resistance, etc. This thesis focuses on the characterisation of a special mechanical surface treatment called deep rolling, which can enhance the fatigue strength of the treated product by altering the material's surface integrity as inducing favourable compressive residual stresses, a cold worked layer and by minimising the surface roughness. The available numerous deep rolling parameters, combined with the unknown material's state inherited from previous manufacturing stages, complicate the prediction and the controlled generation of the above-mentioned treatment effects. In this work, a numerical-empirical approach for the comprehensive characterisation of surface integrity by deep rolling was defined. A finite element modelling was combined with x-ray diffraction method for the investigation of the residual stress state by variable treatment parameters and material's state. Additionally, the cold worked amount, and the surface topography were analysed utilising finite element analysis, indentation micro-hardness method, x-ray diffraction peak widths investigations and mechanical tactile techniques. This work contributes to a better understanding of the deep rolling treatment and facilitates its integration into new product manufacturing chains.

Kurzzusammenfassung

Der moderne Maschinenbau sieht sich mit wachsenden Anforderungen an die Herstellung qualitativ-hochwertiger und langlebiger Produkte konfrontiert, die kostengünstig und in kurzer Zeit auf den Markt gebracht werden sollen. Diese Anforderungen können durch Optimierung der Produkteigenschaften wie: Leichtgewicht, Dauerfestigkeit, Korrosionsbeständigkeit usw. erreicht werden. Der Schwerpunkt dieser Doktorarbeit ist die Charakterisierung einer speziellen mechanischen Oberflächenbehandlung, auch als „Festwalzen“ bezeichnet. Diese Oberflächenbehandlung kann positiv auf die Dauerfestigkeit des behandelten Produkts wirken, mittels Erzeugung von günstigen Druckeigenspannungen, Kaltverfestigung und Minimierung der Oberflächenrauheit.
Die zahlreichen verfügbaren Festwalzparameter, in Kombination mit dem unbekannten und aus früheren Fertigungsstufen übernommen Materialzustand, erschweren Vorhersage und kontrollierte Erzeugung der oben genannten Behandlungseffekte.
In dieser Arbeit wurde ein numerisch-empirischer Ansatz zur umfassenden Charakterisierung der Oberflächenbeschaffenheit durch Festwalzen definiert. Finite-Elemente-Modellierung wurde mit Röntgenbeugungsmethode kombiniert, um den Eigenspannungszustand bei variablen Behandlungsparameter und Materialzustand zu untersuchen. Zusätzlich wurden die Kaltverfestigung sowie die Oberflächentopographie unter Verwendung von Finite-Elemente-Analyse, Mikrohärteprüfungen, Röntgenbeugungspeakbreiten Untersuchungen und Tastschnittverfahren analysiert. Diese Arbeit trägt zu einem besseren Verständnis des Festwalzprozesses bei und erleichtert deren Integration in neue Produktfertigungsketten.

Acknowledgements

Throughout the preparation of this dissertation, I was supported mentally and professionally by several persons, who I would like to acknowledge hereby.
I am expressing my sincere thanks to my lovely family, especially to my mother Daniela and to my best friend Barni, who patiently encouraged me and who gave me the strength to go on.
I would like to extend my very special thanks to my supervisor Professor Dirk Bähre, who guided and taught me throughout the whole promotion, who gave me the freedom to realize my ideas and from whom I have received great mental support.
I would like to thank my second assessor Professor Tilmann Beck and my academic mentor Professor Stefan Diebels for their time to get acquainted with the topic of my thesis and for being part of the assessing process.
My grateful acknowledgement for the financial support of some of my PhD activities and organizing of interesting scientific key-competences workshops, to which I was able to participate, goes to the team of the scientific centre GradUS at the Saarland University.
My very special thanks also go to Professor Joachim Ernst Hoffmann and his team at the University of applied sciences in Kaiserslautern for lighting up my enthusiasm about the world of residual stresses. Professor Hoffmann encouraged me to pursue a doctoral study, and he supported greatly some very important experimental parts of my dissertation, namely the x-ray diffraction analysis and some of the topography- and the microstructure investigations. I am thankful for his regular feedback, tutoring and the fascinating scientific discussions.
I am expressing my gratitude to the former colleagues of the Institute of Production Engineering for accepting me as part of their open-minded and collegial team. They greatly supported me to get through the daily difficulties, which accompanies probably every foreigner moving away from his home country. They patiently introduced me the daily routines at the Institute, and they were always there when I had any questions: scientific, practical, private, etc.
The introduction into the topic “residual stresses in the manufacturing” I own to my supervisor Professor Dirk Bähre and more particularly to my former colleague Dr Horst Brünnet. I am very thankful to both of them to implementing me in this topic, also as co-author of some exciting publications. Dr Brünnet took his time to guide me through the ongoing projects, thus ensuring a fluent and very interesting start of my activities as a PhD student and as a scientific co-worker at the institute.
I would like to acknowledge my bachelor-, master-, EEIGM- and assisting students, who contributed with their diligent and systematic work to the realization of some ideas comprised in my thesis. It was a pleasure to work together with such friendly and intelligent young engineers, who widen my inter-cultural perceptions.
I am thankful to my university colleagues from the Chair of functional materials, the Chair of non-destructive testing and quality assurance, the Chair of material science and methods as well as to those from the University of Applied Sciences in Saarbrücken for the valuable discussions and the realization of some experimental parts of my thesis.

Curriculum vitae

Personal data

Name	**Nataliya Robert Lyubenova**
Date and place of birth	December 8th, 1984 in Pleven Bulgaria

Professional background

09.2018 – 12.2019	Test- and development engineer at XRD Eigenmann GmbH, Schnaittach-Hormersdorf/Bayern, Germany
07.2013 – 07.2018	Scientific employee at the Institute of Production Engineering, Saarland University, Saarbrücken, Germany
05.2012 – 02.2013	Master Thesis, University of Applied Sciences, Kaiserslautern and Robert-Bosch GmbH, Center of Competence Fatigue of Metallic Components, Stuttgart, Germany
12.2008 – 04.2012	Technical assistant at Bulgermed GmbH, Sofia, Bulgaria

Educational background

10.2011 – 06.2013	Master of Science in Mechanical Engineering, Technical University Sofia, Bulgaria
09.2007 – 09.2011	Bachelor of Science in Mechanical Engineering, Technical University Sofia, Bulgaria
09.2003 – 09.2006	Bachelor of Science (not completed) „Computer Systems and Technologies“, Technical University Gabrovo, Bulgaria
09.1999 – 05.2003	High school graduation - Violin Artist-Instrumentalist, Music Gymnasium Panayot Pipkov, Pleven, Bulgaria

TABLE OF CONTENTS

LIST OF ABBREVIATIONS

BC	Boundary conditions
BF	Bauschinger factor
DIN	Deutsche Institut für Normung
DR	Deep Rolling
FE	Finite element
FEA	Finite element analysis
FEM	Finite element method
HTW	Hochschule für Technik und Wirtschaft
longRS	Residual stresses in longitudinal direction
M	Milled specimen
o.l.	Overlapping
o.t.	Overturn
P	Polished specimen
RS	Residual stress
trsvRS	Residual stresses in transverse direction
XRD	X-ray diffraction

LIST OF SYMBOLS

Symbol	Meaning	Unit
A	Fracture strain	%
A_g	Strain before necking	%
d	Diameter	mm
$D^{\{hkl\}}$	Inter-planar (lattice plane) spacing	Å
E	Young's modulus	GPa
E_{IT}	Indentation modulus	GPa
ε	Strain	-
ε_{tech}	Technical strain	-
ε_{true}	True strain	-
F	Force	N
{hkl}	Miller Indices	-
H_M	Martens hardness	-
HV	Vickers hardness	-
L	Length	mm
L_0	Initial length by tensile test	mm
ΔL	Elongation during tensile test	mm
λ	Wavelength	Å
λ_c	Cut off length	mm
μ	Friction coefficient	-
n	Spindle rotational velocity by cutting process	rpm
v	Poison's ratio	-
p	Pressure	MPa
R	Radius	mm
R_a	Arithmetic mean roughness	µm
R_{EH}	Upper Yield strength	MPa

Symbol	Meaning	Unit
R_{EL}	Lower Yield strength	MPa
R_p	Yield strength, general	MPa
$R_{p0,2\%}$	Yield strength at 0,2% strain under tensile loading	MPa
$R_{p0,2\%'}$	Yield strength at 0,2% strain under compression loading	MPa
R_m	Tensile strength	MPa
R_z	Mean roughness depth	µm
s_1/s_2	Elasticity constants	mm^2/N
σ	Stress	MPa
σ^{AX}	Residual stress in axial direction	MPa
σ^{RS}	Residual stress	MPa
σ_{tech}	Technical Stress	MPa
σ_{true}	True Stress	MPa
$\theta^{\{hkl\}}$	Bragg's angle for the corresponding Miller indices	°
v	Velocity	mm/s
v_f	Feed velocity	mm/min

LIST OF FIGURES

LIST OF TABLES

1 Introduction

The modern mechanical engineering is permanently confronted with continually growing demands for production of high qualitative and durable products, manufactured at low costs and with short time to market. Since the worldwide legislation regulating the pollutant emissions is becoming stricter, this drives the development of efficient products even further. The optimisation of product properties like lightweight, fatigue strength, corrosion resistance, etc. can directly influence the demands mentioned above. To achieve the desired product properties, the proper and interdependent design of shape/geometry, material/material's state and manufacturing chain is crucial, as all these features influence the final product's characteristics.

When the optimisation of the product's geometry and material's choice is already fully utilised, the design of the material's properties can be additionally tailored using special manufacturing processes. These processes do not necessarily generate macroscopic geometry changes, but they can have a significant effect on material's properties like hardness, stiffness, elastic-plastic behaviour, microstructure, surface quality, residual stress state, etc., a group of material's properties known in state of the art as the so-called surface integrity.

The above-mentioned special manufacturing processes for improving the surface integrity are described in the European norm DIN EN DIN 8580 "Manufacturing processes – terms, classification", as sub-class 6 "Material properties' change" and are divided into seven sub-classes, namely: material's strengthening through plastic deformation, heat treatments, thermo-mechanical treatments, sintering, magnetising, irradiation and photochemical processes. A central sub-class of this classification is the group of processes, so the called mechanical surface treatments which enhance the material's strength through plastic deformation. As typical examples can be given the peening processes (shot-, piezo-, hammer peening), the rolling processes (deep-, deep cold rolling, low plasticity burnishing) or the autofrettage processes (hydraulic or swage). The common of these processes is that they can selectively generate surface- and subsurface compressive residual stresses. Some of them can additionally reduce the surface roughness and can increase the surface and sub-surface hardness and thus can enhance the fatigue strength of the treated parts. The residual stress state, as materials characteristic, plays a crucial role for the parts' fatigue strength, as tensile residual stresses (positive by sign) facilitate crack initiations and crack propagations. In contrary, compressive (negative by sign) prevent crack initiations and hinder crack propagations. The low surface roughness is also a fatigue enhancer, as the roughness valleys can be considered as surface micro-cracks, meaning that high roughness has a negative effect on the fatigue strength. The hardness, i.e. the material resistance to plastic deformation, has a decisive impact on fatigue life as if hardness is decreased, fatigue life decreases because of an inherent decrease in the material strength.

Following the above-mentioned mechanical engineering demands, this thesis is focused on the comprehensive characterisation of the surface integrity of deep rolling, which is a special mechanical surface treatment that combines the controlled generation of a relatively thick layer of compressive residual stresses, smooth surface and increased hardness. Deep rolling is already established process due to its apparent

benefits on fatigue life. Though, the controlled generation of compressive residual stresses, the prediction of the achieved hardness and the surface quality is still a challenging task, due to several factors like the numerous of available process parameters, the material state and the residual stress state inherited by previous treatments. Up to date, the exact prediction of the surface integrity after deep rolling is still not achieved, despite the available common knowledge about the impact of the most critical process parameters, gathered by extensive research studies throughout the past decades.
The finite element analysis, being in the most cases already an integral part by many process optimisations, also took its place among the scientific work on the modelling and prediction of the surface integrity by deep rolling. Despite the significant progress of this scientific direction, the ultimate deep rolling model able to predict the process output characteristics is still not available, due to the complexity of the process in the manner of input variables. In continuation to these endeavours, in this thesis was employed the finite element analysis to characterise the deep rolling process, where the focus was put to the residual stress surface- and depth distribution, the induced plastic deformation and the topography of the treated surface. In contrary to the most investigated cases, where the process was employed on an axis-symmetric part, here a flat part was defined in order to transfer the gained knowledge for the treatment of complex three-dimensional parts. In the preliminary studies of this work, the boundary conditions of the finite element model were established, which step corresponds to the simplification of the real process and the influence of the boundary conditions on the model's stability and the results' plausibility was investigated. Using the established model, several of the most significant process parameters were varied, and their impact on the resulted surface integrity was systematically studied.
Following the standard scientific approach, after establishing the finite element model, it needed to be verified either theoretically or empirically. Due to the complexity of the process, a theoretical verification of the model could not be utilized; therefore, an empirical approach was chosen. The residual stress state was characterised employing x-ray diffraction technique, where two different measurement devices were used to investigate the influence of the measurement/evaluation parameters on the determined stress values. The change of the hardness was investigated by means of indentation technique and using the x-ray diffraction peak widths. The surface roughness and topography were depicted by mechanical stylus method and white light interferometry. For all experimental studies, along with the process parameter variations, the pre-machining material state was varied, establishing different process chains, in order to study the influence of the pre-machining and consecutive deep rolling on the surface integrity. The results from the finite element analysis and the experimental studies were compared, drawing conclusions about the process interdependencies and thus contributing to the better understanding and prediction of the deep rolling as a single process or applied as part of a process chain.

2 State of the art

2.1 Surface integrity in the manufacturing

Surface integrity describes the surface properties of parts after their manufacturing, which properties can be a result of mechanical, metallurgical, chemical and other alterations. Here, the term “surface” describes the outermost layer of part, including the interface (transition) layer, which divides in terms of properties the outermost layer from the bulk material (substrate). There are two aspects of the surface integrity: topography, e.g. surface roughness, waviness, defects of the form, and surface layer properties, e.g. plastic deformation, residual stress state, hardness, phase changes, recrystallisation and cracks. It is well known that all these properties strongly influence the lifetime of manufactured parts as fatigue and stress corrosion.
The surface engineering has the main to design the surface integrity in order to improve corrosion/oxidation/wear resistance, to reduce energy loses by generating lower friction, to improve mechanical properties for longer fatigue life, etc. (Astakov, 2010).

2.1.1 Properties of the technical surfaces

Figure 2-1 illustrates an exemplary picture of surface properties influenced by surface modification manufacturing processes. It describes the change of the near-surface hardness state (HV), the residual stress state (σ_l^{rs} and σ_t^{rs} in case of anisotropic residual stress distribution), the cold working determined with x-ray diffraction (FWHM), the surface roughness (R_t and R_a) and the texture (the grains with preferred orientation – on the top left work piece’s corner).

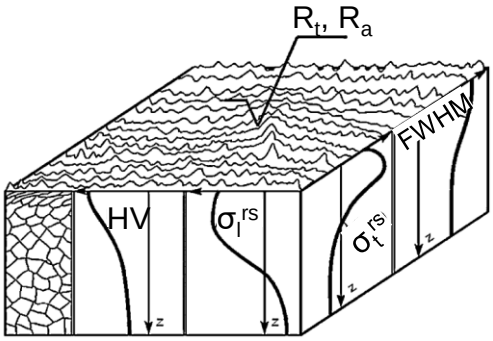

Figure 2-1: Surface properties influenced by surface modification processes (Scholtes, et al., 1986)

The hardness, i.e. the material resistance to plastic deformation, has a decisive effect on fatigue life as if hardness decreases, the material strength decreases, resulting in a reduction of the fatigue life. Thus, the enhanced hardness produced by surface modification processes is preferred.
The residual stress state, as materials characteristic, plays a crucial role for the parts’ fatigue strength, as tensile residual stresses (positive by sign) facilitate crack initiations and crack propagations. In contrary, compressive (negative by sign) prevent crack initiations and hinder crack propagations. The low surface roughness is also a fatigue

enhancer, as the roughness valleys can be considered as surface micro-cracks, meaning that high roughness has a negative effect on the fatigue strength. The hardness, i.e. the material resistance to plastic deformation, has a decisive impact on fatigue life as if hardness is decreased, fatigue life decreases because of an inherent decrease in the material strength.
The surface roughness is also a fatigue enhancer, in case it is low because every roughness valley can be considered as surface micro-crack, meaning that high roughness has a negative effect on the fatigue strength.

2.1.2 Surface topography

The three-dimensional surface topography can be described as the repeatable or randomly deviating topography from the nominal/standard one and includes: roughness (nano- and micro scale), waviness, lay, and flaws. In Figure 2-2 is depicted an exemplary picture of three-dimensional surface topography, where Figure 2-2 a) illustrates a general case; Figure 2-2 b) shows an exemplary topography profile with depicted waviness spacing and height. Figure 2-2 c) takes a closed view in the topography profile, showing the profile peaks and valleys, the roughness spacing and the sampling interval/length.

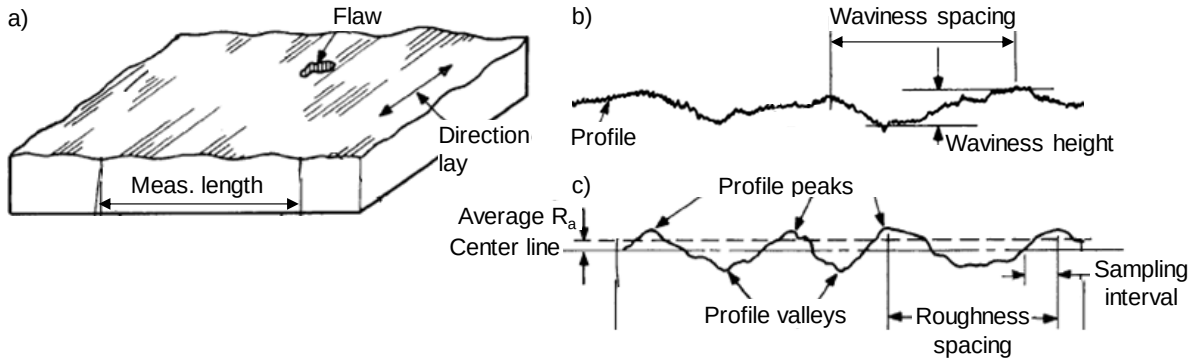

Figure 2-2: Surface topography: a) general view on a macro level, b) topography profile on a macro level and c) topography profile on a micro level

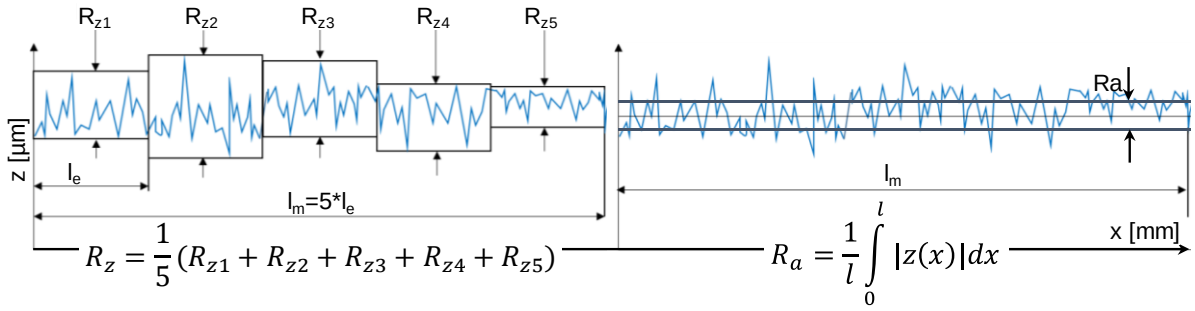

Figure 2-3: Description of the roughness parameters Rz and Ra

When considering the roughness as a two-dimensional variable, there are two parameters, which are mostly used to characterise surface roughness. These are the mean roughness depth **R_z** and the arithmetical mean roughness **R_a**, both parameters are related to the measured two-dimensional roughness profile (see Figure 2-3). The R_z

and R_a parameters are defined in the DIN EN ISO 4287:2010-07 (DIN-EN ISO 4287, 2010) norm as: $\mathbf{R_z}$ - the mean value of the five $\mathbf{R_{zi}}$ values from the five sampling lengths $\mathbf{l_e}$ within the evaluation length $\mathbf{l_m}$; $\mathbf{R_a}$ - the arithmetical mean of the absolute values of the profile deviations (**Zi**) from the mean line of the roughness profile.

2.1.3 Residual stresses

Residual stresses definition

Residual stresses are “locked-in” or internal stresses that exist in materials and structures in the absence of external loading or thermal gradients (Totten, et al., 2002). The residual stresses can be compressive (negative by sign) or tensile (positive by sign), and they always build an equilibrium throughout the whole material or structure. This means if part of the material exhibit compressive residual stresses, another part of the material have to possess tensile residual stresses. The tensile residual stresses have a negative influence on the fatigue life of materials, as they pull the material out, thus promoting new crack initiations and accelerating existing crack propagations. In contrary, compressive residual stresses compress the material, thus preventing new crack initiations and hindering existing crack propagations, and thus positively altering the fatigue strength.
The origin of residual stresses is different, e.g. the inhomogeneous elastoplastic deformation in the material or structure caused by mechanical or thermal loading, which deformation can be in different scale – from micro- to macro level. Residual stresses can be generated by different cooling rates after heating or by microstructure phase transformations accompanied by a change in the volume.
Residual stresses are ubiquitous, as they are present in almost any material. They are attracting particular interest in material science due to their influence on material properties. Hence, by the application of any material, the residual stresses shows its ambivalence:

- Residual stresses are feared due to the unpredictable failure they can trigger.
- They are favoured in cases, where due to lack of accurate knowledge, they are alleged as a possible source of unexpected material behaviour or material failure.
- They are exploited because they can improve the material behaviour when loading under certain conditions is present.
- They need to be considered for the realistic prediction of failure when the target is to design safe structures with optimised material costs.

Regarding the area within the residual stresses are homogeneous, there is a classification dividing them into three types:

- Type 1 – these are macro residual stresses, which are nearly homogeneous in a large material area. The related with them inner forces and/or moments are in equilibrium in the whole specimen. When the force/moment equilibrium is disturbed, this always leads to macroscopic form changes.
- Type 2 – these are micro residual stresses, which are homogeneous within several grains. Here, the disturbance of the force/moment equilibrium may lead to macroscopic form changes.

- Type 3 – are the micro residual stresses, which are not homogeneous within an area of several atoms. The force/moment equilibrium here exists in a very small area (in the region of one grain). The disturbance of the force/moment equilibrium cannot lead to macroscopic form changes.

This classification describes idealised residual stress states. Still, the superposition of residual stresses of any type is also applicable, which is the case for all technical materials. Schematically, this superposition of residual stresses types I – III is shown in Figure 2-4.

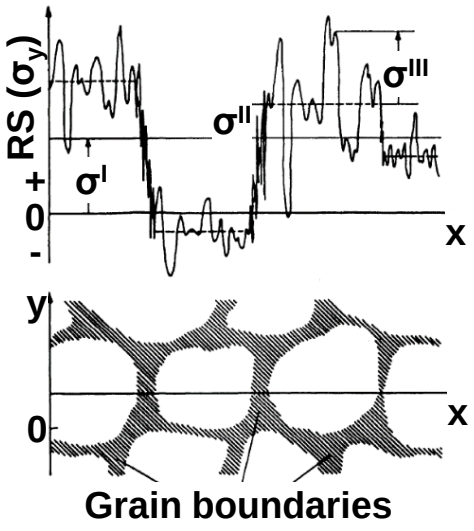

Figure 2-4: Superposition of residual stresses type I - III (Macherauch, et al., 2011)

Generation of residual stresses

Residual stresses are generated by most of the existing manufacturing processes. The stringently necessary condition for their generation is the inhomogeneous elastoplastic deformation of the material, temperature gradients or phase transformations, which lead to macro- or micro deformation incompatibilities. During operation, the residual stress state can change as well, i.e. in case of operational non-uniform plastic deformations, an elastic response of the material develop, thus creating additional residual stresses. Some typical examples of the generation of residual stresses are shown in Figure 2-5, where the macro- or micro stresses in all examples are generated due to the misfits, or the so-called “eigenstrains” between different regions (macro scale) or between different phases (micro scale) within the material.

When considering the classification of the manufacturing processes according to DIN EN 8580 norm (DIN-EN 8580, 2003), i.e. processes serving for, forming, cutting, joining, coating and changing the material properties, it can be stated that all of these process groups can induce residual stresses in the treated materials. A typical example of primary shaping process that produces residual stresses is the casting process, where inhomogeneous cooling temperature/strain gradients in the cast part lead to the generation of residual stresses (Sadrossadat, et al., 2009). The forming processes, typically forging, extrusion, deep drawing, and bending, governing by their common

mechanism of forming through elastoplastic material deformation, can generate complex, three axial residual stress state (Wang, et al., 2002). The group of the cutting processes like milling, turning, grinding, etc., generates mechanically and/or thermally provoked residual stresses. In the case of grinding, the near-surface stresses can be compressive, when using large cutting force or high thermal conductivity of the grinding tool. In contrary, tensile stresses near the surface can be induced, when increasing the cutting velocity, the feeding velocity, or when using great cutting depth (Scholtes, 1990) Another typical example is the milling process. Here, the numerous cutting parameters have a significant impact on the generated residual stress. For example, increasing the cutting speed or the tool diameter leads to the generation of near-surface tensile stresses (Ulutan, et al., 2007), while using coolants instead of dry milling induces compressive stresses (Arunachalam, et al., 2004). In (Denkena, et al., 2007), the several process parameter variations like cutting speed, feeding speed or cutting depth led to tensile stresses on the surface by higher cutting speed; bigger tool radius induced slight tensile near-surface stresses compensated by high compressive stresses at greater depth. In general, it could be said, that by milling processes, tensile residual stresses are formed mainly due to local heating, while compressive stresses are a result of the material's squeezing/compressing (Scholtes, 1987).

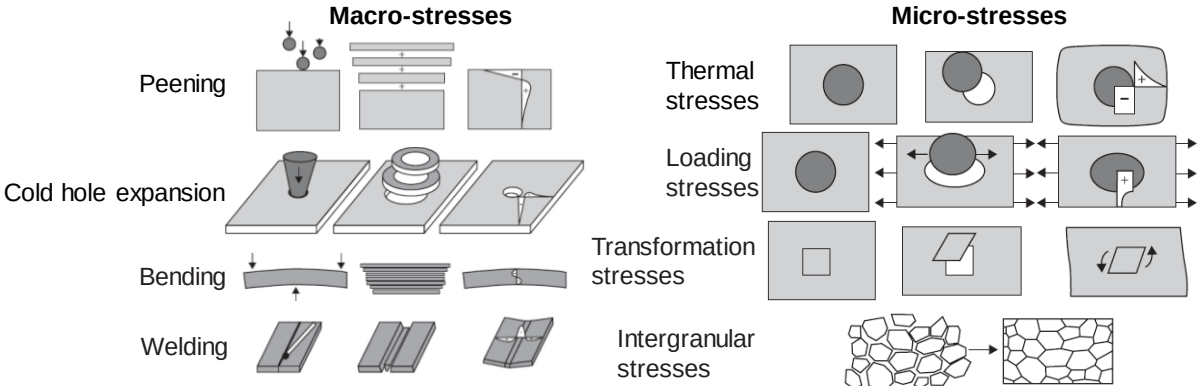

Figure 2-5: Examples for the generation of macro- or micro residual stresses (Withers, et al., 2001)

Figure 2-6 gives a general overview of the residual stresses induced by different types of milling processes. For down-cut milling, the induced stresses are strongly dependent on the cutting direction, where for up-cut milling and face milling, the stresses along (σ^{II}) and transverse ($\sigma^{\perp}$) to the cutting direction are similar. Although, the distribution of the stresses vary from tensile on the surface (down-cut milling and face milling with inclined tool), to compressive on the surface (up-cut milling and face milling with perpendicular tool).

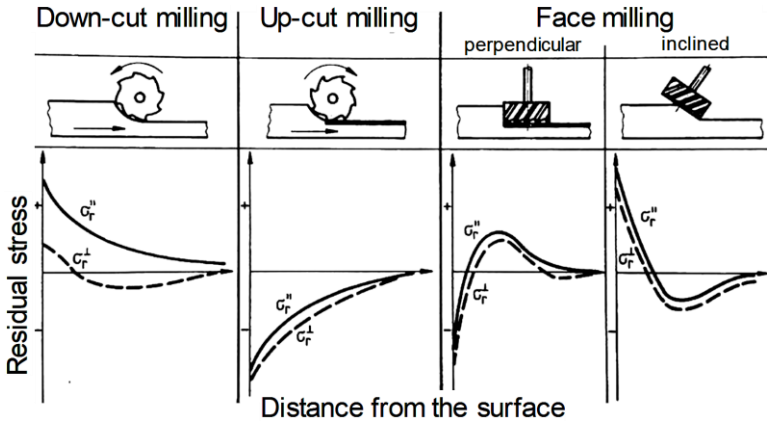

Figure 2-6: Characteristic residual stress depth distributions generated by different milling processes (Scholtes, 1987)

A comprehensive Round Robin collaborative work was performed in (Jawahir, et al., 2011), with the goal to induce defined residual stress state (surface compressive residual stresses in the amount of -200 MPa), employing several machining processes (milling, grinding, fine grinding, turning and electro-discharge machining (EDM)). The process parameters were free selectable. From the chosen 35 process parameter sets, only 10 of them generated surface compressive residual stresses in the range of -300 MPa to -100 MPa. The results spread from -800 MPa (milling and grinding) to +600 MPa (EDM), where the milling induced from high compressive- to low tensile residual stresses (-800 MPa to +100 MPa). The grinding delivered only compressive stresses (-800 MPa to -300 MPa); the turning and the fine grinding induced moderate compressive- to low tensile stresses and EDM generated only tensile stresses (+600 MPa). These results show the complexity of the topic and leave an open floor for further investigations.

The next manufacturing processes group, namely the joining processes, can affect the residual stress state as well. Typical are the welding induced residual stresses, generated due to the non-uniform expansion and compression of the weld and the base material caused by the non-uniform heat distribution during the welding process. The surface residual stress profile of welded structure shows typically tensile residual stresses in the welding seam, compensated with compressive residual stresses in the transition to the base material zone (Zinn, et al., 2002).

The coatings processes induce residual stresses, which are a combination between intrinsic stresses (those developed during the growth of the coating) and thermal stresses, which results from the mismatch in coefficients of thermal expansion between the coating and the base material (Sue, et al., 1994).

The last group of manufacturing processes, classified by the norm DIN EN 8580, namely the processes that change material properties, will be discussed explicitly in subchapter 2.2.1 as they are from a particular interest in this thesis.

2.1.4 Elastoplastic material behaviour

It is essential to describe the elastoplastic behaviour of the treated material, as this is its ability to respond to mechanical loading, resulting from either manufacturing process or during operation.

With means of the classical theory of plasticity, the elastoplastic material behaviour can be described. It refers to materials, which deform initially elastically and then plastically upon reaching yield stress. In metals and other crystalline materials, the occurrence of plastic deformations at the micro-scale level is due to the motion of dislocations and the migration of grain boundaries on the micro-level. Figure 2-7 describes four idealised linear models for one-dimensional elastoplastic material behaviour. Here, the ordinate axis represents the stress/loading **σ** upon which the strain **ε** (abscissa axis) results and with **Y** is noted the elastic limit (yield strength) of the material, i.e. the transition between elastic and plastic material flow. In Figure 2-7 a) is given the linear elastic-plastic model with hardening, typical for the behaviour of metals, where the inclination after the yield strength **Y** describes hardening of the material, as to achieve higher strain values, higher loading is needed. The second material behaviour, elastic perfectly plastic (see Figure 2-7 b)), exhibits materials which are not prone to hardening after yielding. For both models, it is essential to note that a high yield point means high ductility. If materials with high ductility are subjected to overloading, they can bear large deformations before a fracture occurs. Under real conditions, some ductile materials do not exhibit well-defined yield point, therefore by default, a strain offset of 0.02 % is defined at which the yield point is considered and noted as $\mathbf{R_{p0.2}}$. The models shown in Figure 2-7 c) and Figure 2-7 d) describe brittle materials, which do not exhibit yielding before failure; the difference between both models is in the presence or absence of hardening. Commonly, materials do not behave linearly, as shown in Figure 2-7. Although, this idealised representation helps to recognise some typical behaviour cases.

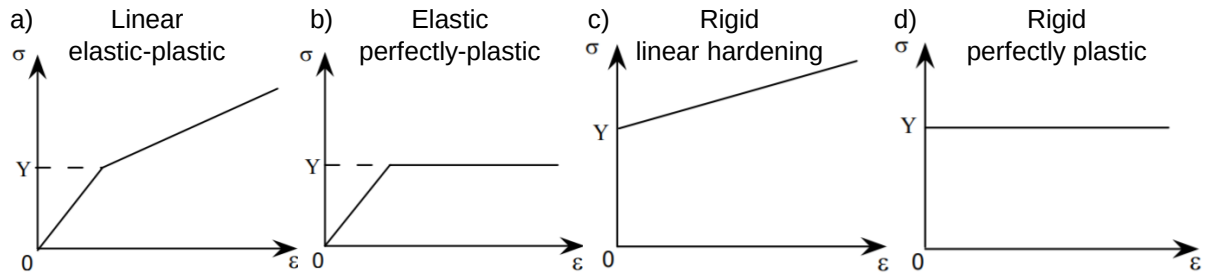

Figure 2-7: Idealized models for one-dimensional elastoplastic material behaviour (Kelly, 2015)

An important phenomenon exhibiting some elastoplastic materials is the so-called Bauschinger effect. It describes the directional dependence or anisotropy of the yield strength after plastic deformation under cyclic loading, where the loading can be caused by a manufacturing process, or it can take place during the operation life of the part. The effect can be explained by the summation and self-obstruction of dislocations in the material. The microscopic stress distribution inside the material due to its past determines this behaviour. By plastic deformation, many dislocations are accumulated

at dislocation barriers like grain boundaries results in material hardening. The basic mechanism of Bauschinger effect can be explained as follows: during the initial plastic deformation (loading phase) and provoked by the applied loading, dislocations of the crystal structure of the material begin to move. They interact with different obstacles (e.g. other dislocations, grain boundaries and precipitates), which obstacles prevent their further propagation. This interaction generates back stress, which restricts further dislocation movement. During the reverse deformation (unloading phase), this back stress repels the dislocations from the obstacles in the opposite direction, namely in the direction of reverse strain. Thus, the back stress eases the movement of dislocations in the direction of reverse strain, and the reverse yield stress drops by the level of the back stress (Kostryzhev, 2009). It is important to note that the Bauschinger effect is strain-dependent, meaning higher strain will lead to stronger Bauschinger effect.
The Bauschinger effect can be advantageous or disadvantageous, e.g. the presence of a strong Bauschinger effect in the material can improve the sag resistance of spring steels by the production of springs (Yan, 1999). Although, strong Bauschinger effect can cause steel to become brittle at the point of plasticity after cyclic loading. An exemplary of elastoplastic material exhibiting Bauschinger effect under cyclic loading is shown in Figure 2-8, where in Figure 2-8 a), the initial loading direction is tension and in Figure 2-8 b), the initial loading direction is compression. In both cases, a reduction of the yield strength ($R_{p0.2}$') by unloading is observed, compared with the initial yield strength $R_{p0.2}$.

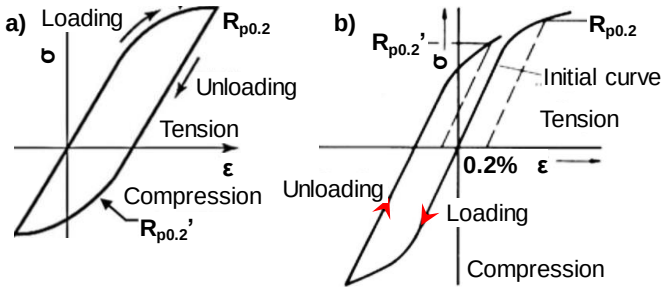

Figure 2-8: Elasto-plastic material exhibiting Bauschinger effect under cyclic loading: a) loading direction – tension (Schümann, et al., 2017) and b) loading direction – compression (Engel, 2005)

2.1.5 Microstructure

The material's microstructure in terms of grain size, -shape and –orientation, and the hardness can significantly influence the fatigue strength of the treated part.
Commonly known is that fatigue strength of steels is usually proportional to hardness and tensile strength, but this is only valid in a very general case. For example, by high strength steels, the hardness influences the fatigue strength only under certain conditions. In case the hardness is lower than an app. 400 HV, the fatigue limit is an app. half the ultimate tensile strength independent of the hardness values (Boardman, 1990). In (Hassan, 2018), it was proposed a model for prediction of the fatigue limit based on the Brinell hardness and the ultimate strength for high strength steels. The article investigated the correlation between Brinell hardness (HB from 163 to 536, means app. 163 HV to 570 HV), the ultimate strength (σ_u from 582 MPa to 2360 MPa)

and the fatigue strength for various materials. In contrary to the observations in (Boardman, 1990), the authors found out that for all investigated materials possessing Brinell hardness lower than 500 HB (app. 531 HV), the correlation between Brinell hardness in combination with the ultimate strength, and fatigue strength was almost linear. Still, the hardness, as a parameter in the proposed model, had much larger weight (factor 1.3), than the ultimate strength (factor 0.02).
The grain size is another microstructure factor that influences the fatigue strength. The presence of coarser/larger grain size and the corresponding larger grain boundaries/sliding paths between the grains promotes the appearance of surface cracks. Consequentially, the fatigue strength of fine-grain materials is higher than this of coarse grain materials. Besides, at fatigue with high loading cycles, the building of slip bands by coarse-grain materials eases the crack formation, while by the fine-grain materials, the higher dislocation density of the grains leads to crack formation below the surface (Calles, 1985).

2.2 Mechanical surface treatment by Deep Rolling

2.2.1 Mechanical surface treatments – an overview

The machining processes, like milling, turning, grinding, polishing, etc. induce in certain way plastic deformation and residual stresses at the rim zone. The mechanical surface treatments differ from the processes mentioned above by the targeted and controlled generation of plastic deformation and residual stresses. It is well known that the plastic deformation results in higher dislocation density, which is in favour of the fatigue life of the components. The impact of the residual stresses on fatigue life is also unavoidable. The mechanical surface treatments mentioned above are categorized in the norm DIN EN 8580 “Manufacturing processes – terms, classification” (DIN-EN 8580, 2003), as sub-class 6 “Material properties’ change”, which sub-class is divided into seven subclasses, namely: material’s strengthening by means of plastic deformation, heat treatments, thermo-mechanical treatments, sintering, magnetising, irradiation and photochemical processes. A central place in this categorisation takes the sub-class of the mechanical surface treatments, named in the norm “processes for material’s strengthening through plastic deformation”. Typical mechanical surface treatments are the rolling processes (deep-, deep cold rolling, low plasticity burnishing), the peening processes (shot-, piezo-, hammer peening), or the autofrettage processes (hydraulic or swage). Along with the selective generation of surface- and subsurface compressive residual stresses, some of those processes can reduce the surface roughness, can increase the surface and sub-surface hardness and thus can enhance the fatigue strength of the treated parts. The presented thesis focuses on the characterisation of deep rolling process, and therefore state of the art for this process will be discussed more extensively in a separate subchapter (see subchapter 2.2.2). Although, a general overview of the commonly used mechanical surface treatments will be done in this subchapter, as all those processes have a common principle and similar influence on the material’s properties. Thus, the knowledge about those influences can help for the

better understanding of the interdependencies between process parameters and the resulted material's properties by the investigated deep rolling process.

The mechanical surface treatments attracted the interest of the scientific community in the 1920s – 1930s. In 1929, Föppl (Föppl, 1929) found a correlation between surface finishing/rolling and the fatigue strength, where he compared deep rolled- versus polished surfaces and found the fatigue strength of the deep rolled specimens to be significantly higher than those of the polished specimens. In 1935, Thum (Thum, et al., 1935), stated that even by notched parts, the fatigue strength could be increased by means of surface treatment and mainly through work hardening. Here, for the first time, the residual stresses and the work hardening were separated as factors influencing the fatigue strength. In the USA, Horger (Horger, 1936) also debated about the influence of the surface hardening/rolling on the fatigue strength. In the 1920s – 1930s already established as process, deep rolling was utilised to strengthen axles of the Ford T and train axles.

Parallel to the development of the rolling processes, the peening processes appeared in the late 1920s, as peening referred to mechanical surface treatment where peening media with significantly higher hardness than the one of the treated part bombards the part creating plastic deformation and consequently residual stresses (DIN 8200, 1982). The precursor of the peening process named "cloudburst" was developed by Hebert in 1927 (Herbert, 1927), as the peening media was left to fall on the work piece using only the gravity. He observed a significant increase of the resulted by the processing hardness, but a clear relation to enhanced fatigue strength was not mentioned. Since the 1930s, the shot peening process was commercially used to treat valve- and suspension springs, where an increased fatigue life with up to factor 10 was reported (Koenecke, et al., 1982).

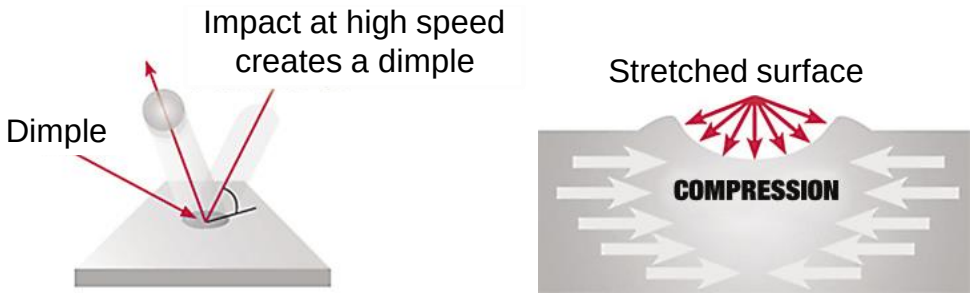

Figure 2-9: Shot peening principle (Hanson, 2015)

The modern shot peening process follows the same principle as the one from the 1920s. It uses a high-speed impact of peening media (usually air blasted) which induces elastoplastic material deformation leading to the generation of near-surface compressive residual stresses and work hardening (see Figure 2-9). The surface topography after shot peening is usually rough due to the dimples created by the peening media (O'Hara, 1999; Yao, et al., 2016). The residual stress distribution is relatively homogeneous by high coverage percentages, and it is not direction-dependent due to the stochastically distributed shots during processing (Dalaei, et al., 2010). The main process parameters influencing the surface integrity of the treated material are the

material state (elastoplastic material behaviour, hardness, and crystal structure), the work piece geometry (thickness, notches, etc.), the shot peening media (material type and hardness, media shape and size) and the peening parameters (shot velocity, peening time and coverage, and shot indentation angle). To avoid off-topic, only the parameters, which could be related to the deep rolling process, will be further discussed.

In (Holzapfel, et al., 1998), see Figure 2-10, was investigated the influence of the material state on the residual stress depth distribution and the work hardening state after shot peening. The material used was AISI 4140 high strength steel in the state: normalized (lower yield strength), quenched and tempered (tempering temperatures from 180 °C to 650 °C, higher yield strength than the normalised state) or only quenched (highest yield strength compared to normalized or quenched and tempered state). Using the normalised state, the lowest compressive residual stresses were generated. The quenched and tempered (180 °C) state delivered the highest maximal compressive residual stresses and the quenched state – similar maximal compressive residual stresses but slightly higher compressive near-surface stresses. The work hardening state was influenced by the material state as well. In the normalised state, the lowest work hardening state was observed, while the quenched state resulted in highest work hardening. The quenched and tempered state laid in between, where increasing the tempering temperature led to decreasing work hardening. The authors also found a correlation between the work piece's hardness (material AISI 4140) and the in-depth residual stress state, see Figure 2-10 b). Here, increasing the hardness from app. 220 HV to 600 HV increased the maximal compressive residual stresses (σ^{rs}_{max}). Still, the surface compressive residual stresses (σ^{rs}_{sur}) and the depth of the maximal compressive residual stresses (z_{max}) raised only up to 450 HV. The stress impact depth (z_0) decreased with increasing the hardness.

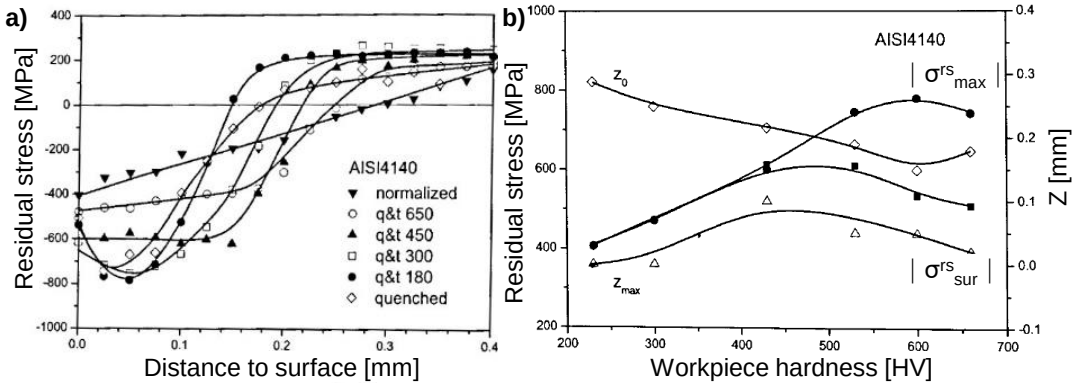

Figure 2-10: Influence of the material state and hardness on the residual stress in-depth distribution after shot peening (Holzapfel, et al., 1998)

The influence of the diameter of the shot media (0.2 mm to 1.4 mm) on the residual stress state in AISI 4140 steel was studied in (Schwarzer, et al., 2006). While the compressive residual stress maximum and surface magnitude remained unchanged, using larger diameter media raised the depth of the maximal compressive residual stress and the stress impact depth. Additionally, the authors discussed the impact of the shot

velocity (20 m/s to 80 m/s) on the residual stress state of AISI 4140 steel. They stated that raising the velocity has a minor effect on the maximal compressive residual stresses and the surface compressive residual stresses but has a significant influence on the depth of the maximal compressive residual stresses and the stress impact depth.

In (Vohringer, 1987), see Figure 2-11, was systematised the influence of the shot peening process parameters on the residual stress- and work hardening (by means of x-ray diffraction half width of the diffraction peaks and hardness investigation) depth distributions. The factors that raise the compressive residual stress maximum, see Figure 2-11 a), are the shot velocity and pressure, the hardness of the work piece and the shot media. Deeper distributed compressive residual stresses can be generated by using higher shot velocity and pressure, larger media size, higher coverage and harder shot peen media. Decreasing the work piece hardness leads to compressive residual stresses shifting towards work piece's surface. The higher work hardening amount can be achieved by higher shot velocity, higher pressure, larger shot media diameter and harder shot media. In contrary, increasing the work piece's hardness leads to reduced work hardening amount.

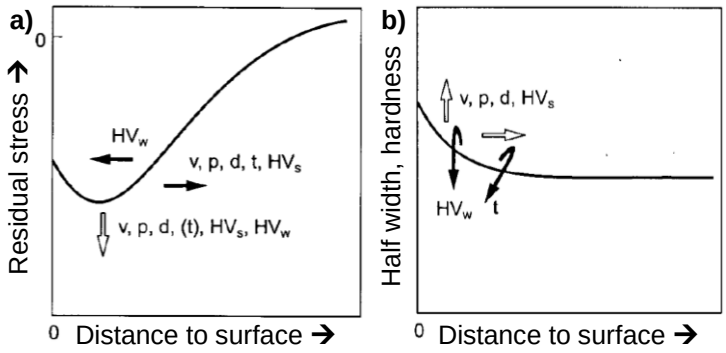

Figure 2-11: Influence of the shot peening process parameters on the residual stress depth distribution (Vohringer, 1987)

Even though shot peening contributes significantly to longer fatigue life of the treated parts above all due to the induced compressive residual stresses (Fabbro, et al., 1998; Scuracchio, et al., 2013; Kim, et al., 2013), the stress relaxation during the fatigue cycles should not be neglected. Independently on the loading case during fatigue, the material state is a crucial impact factor for the stability of the induced by shot peening residual stresses. Materials possessing low strength, exhibit large stress relaxation by both low- and high cycle fatigue. By the materials with medium strength, the residual stresses keep their stability by high cycle fatigue and the high strength materials exhibit no stress relaxation by both low- and high cycle fatigue (Löhe, et al., 2002).

An alternative peening process developed in the 1960s is the laser shock peening (Askar'yan, et al., 1963; Neuman, 1964; Gregg, et al., 1966). It uses a laser-utilized shock wave to modify the surface of the treated material without generating thermal effects. A transparent overlay on the work piece keeps the shock wave generated by the laser into the material. If the amplitude of the shock wave exceeds the dynamic yield strength of the material, the later begins to deform plastically during the treatment.

The magnitude of the plastic strain decreases in the material's depth as the peak pressure of the shock wave decreases. At higher depths, the resulted pressure falls below the dynamic yield strength generating only elastic deformation. After the shock wave passes, the residual plastic strain creates a compressive residual stress gradient with a maximum usually near the surface. The main process parameters influencing the surface integrity of the peened specimen are the work piece properties (elastoplastic material behaviour, the work piece's geometry/thickness, the laser pulse properties (pulse- energy, duration, focus and frequency) and the peening properties (overlapping, coverage, and overlay). The residual stresses generated by laser shock peening have usually significantly lower gradients compared to those generated by shot peening. They are directionally-independent, and in some materials, they can be compressive over one milimeter in depth. For example, the stress impact depth in AISI 4140 steel can exceed two milimeter (Menig, et al., 2003) and in TiAl6V4, the residual stresses can be compressive at over 1.2 mm depth (Prevéy, et al., 1997). The laser shock peening produces a very small amount of cold working compared to shot peening.

In (Sonntag, et al., 2015) was performed a comprehensive investigation of the surface integrity and the fatigue strength of Ti6Al4V hour-glass shaped rotationally-symmetric specimens exposed to different mechanical surface treatments like shot peening, laser shock peening, ultrasonic shot peening and deep rolling. The induced residual stress depth profiles are shown in Figure 2-12. It is visible that the shot peening induces high-gradient direction-independent residual stress profiles with a stress impact depth of app. 0.2 mm. The ultrasonic shot peening delivers in this case similar stress profiles. The laser shock peening generates similar magnitude but lower-gradient residual stress profiles with very high stress impact depth, exceeding 1.5 mm depth. Deep rolling induces strongly direction-dependent stress profiles with very high near surface compressive residual stresses in the axial direction, see Figure 2-12 a), and low to moderate compressive stresses in the tangential direction. The stress impact depth in both directions exceeds slightly 0.5 mm.

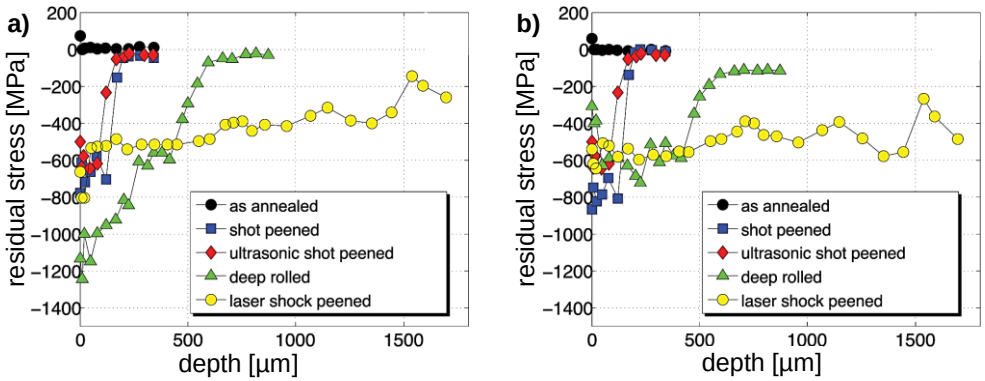

Figure 2-12: Residual stress depth profiles after different mechanical surface treatments in: a) axial direction and b) tangential direction (Sonntag, et al., 2015)

Additionally, the authors investigated the cold working amount by means of the x-ray diffraction peak width (FWHM), see Figure 2-13 a). They found that for the treated material, on the surface, the shot peening leads to higher cold working amount followed

by ultrasonic shot peening, laser shock peening and deep rolling (least work hardening amount). Both peening processes, followed by deep rolling, generated the steepest cold working gradients. The laser shock peening delivered significantly deeper cold working layer, which as amount was still larger than the base material state (as annealed) at over 1.5 mm depth. The Woehler graph, see Figure 2-13 b), which indicates the fatigue performance of the tested specimens (the fatigue loading was bending, applied for maximum 10^7 number of cycles, which corresponds to high-cycle fatigue). Compared to the material state “as annealed”, the greatest improvement of the fatigue strength delivered laser shock peening, followed by deep rolling, and lastly both peening processes.

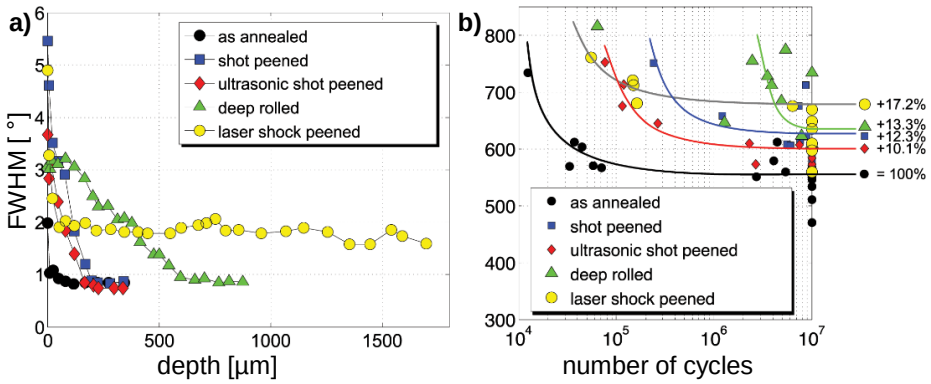

Figure 2-13: Different mechanical treatments, influence on the: a) work hardening amount and b) Woehler graph (Sonntag, et al., 2015)

In 1920, for military purposes was developed the autofrettage process to enhance the fatigue strength of cannon barrels (Jacob, 1920). The “swage” autofrettage was based on the elastoplastic deformation of the inner surface of the cannon barrel by means of inserting an oversized rigid mandrel into the cannon barrel. The mandrel creates elastoplastic deformation in the treated part, which causes the generation of compressive residual stresses in the inner surface of the treated cylindrical part. The “hydraulic” autofrettage uses the same principle but instead of mechanical tool utilises very high hydraulic pressure, which can reach up to 15 000 bar using the modern autofrettage systems (MAXIMATOR GmbH, 2015). Due to the absence of a rigid tool, the process is especially well-suited to treat internal- or difficult to reach surfaces. The main process parameters are the applied pressure and the work piece properties (elastoplastic material behaviour and work piece’s geometry/thickness). The autofrettage process is able to induce a thick layer of compressive residual stresses, e.g. in AISI 4140 steel the stress impact depth can reach up to 3.0 mm even after consecutive machining (Brünnet, et al., 2014 a); Brünnet, et al., 2014 b)). In contrary to the peening processes, here there is a typical directionality of the induced stresses, where the tangential residual stresses are significantly higher compressive than those in the axial direction (Brünnet, 2013). Similarly to the laser shock peening, the cold working induced by autofrettage process is very low. Still, in contrary to laser shock peening, autofrettage do not change in the surface roughness.

A comprehensive overview of the mechanical surface treatments classified by the type of contact between tool and work piece was given in (Schulze, 2005 a)), see Table 2-1.

Here, the processes were divided into static or impulsive, with- or without motion between work piece and tool. The movement of the tool was classified as singular or repetitive (regular or irregular).

Table 2-1: Overview of the mechanical surface treatments (Schulze, 2005 a))

<table>
<tr><td colspan="2" rowspan="3"></td><td rowspan="3">Without relative motion between tool and work piece</td><td colspan="4">With relative motion between tool and work piece</td></tr>
<tr><td colspan="2">Rolling contact</td><td colspan="2">Sliding contact</td></tr>
<tr><td>Without slip</td><td>With slip</td><td>Solid medium</td><td>Liquid medium</td></tr>
<tr><td rowspan="5">Static / Impulsive</td><td>Singular</td><td>Smooth-, size-, flat embossing</td><td colspan="2" rowspan="3">Deep-, finishing-, size rolling, deep cold rolling, low plasticity burnishing, ball burnishing</td><td rowspan="2">Swage autofrettage</td><td>Hydraulic Autofrettage</td></tr>
<tr><td>Repetitive regular</td><td>-</td><td>-</td></tr>
<tr><td>Singular</td><td>-</td><td rowspan="2">Spinning, smooth drawing</td><td>-</td></tr>
<tr><td>Repetitive regular</td><td>Hammering, laser shock peening, high pressure water peening</td><td colspan="2">-</td><td>-</td></tr>
<tr><td>Repetitive irregular</td><td>Shot peening, needle peening, ultrasonic peening</td><td>-</td><td>-</td><td>Brushing</td><td>-</td></tr>
</table>

Alternative mechanical surface treatments are the so-called stress-peening and stress-rolling processes, which include mechanical pre-stressing of the work piece to enhance the compressive residual stresses generated during the treatment. The mechanism of the pre-stressing is the following: external stress (tension, bending or torsion), causing elastic deformation is applied to the work piece, and then the mechanical surface treatment is performed. After processing, the resulting stresses are the algebraic sum of the pre-stress and the residual stress induced by the treatment. When the pre-stress is released, it causes a deformation in direction opposite to the initial pre-stressing. In case the pre-stress was positive/tensile, it will enhance the compressive residual stresses generated by the treatment, where the compressive stresses increase linearly from the depth of the specimen toward the treated/top surface. The result is shifting into higher depth the transition between compressive and tensile residual stresses resulting in thicker compressive residual stress layer. Stress-peening and stress-rolling are usually used to treat parts exposed to operational bending or torsion like leaf springs, belleville springs, coil springs, torsion bars, propeller shafts, etc. In 1949, in (Straub, et al., 1949) was introduced the stress peening process. The authors performed fatigue tests on not shot-peened, shot-peened and stress-peened specimens and observed an app. 350 % longer lifetime of the shot-peened specimens compared to the not shot-peened ones. The stress-peened specimens exhibited a remarkable 740 % longer lifetime than the shot-peened ones. An investigation of stress-peening on aluminium plates was done by (Barrett, et al., 1984). With bending pre-stress of an app. 87 % of the material's yield strength and consecutive shot peening on the convex-bent side of the work piece they achieved app. 47 % enhancement of the generated compressive residual stresses. However, the depth of those residual stresses re-

mained on the level of the only shot peened specimen. Moreover, the higher compressive residual stresses were measured only in the direction parallel to the bending. In the transverse direction, the compressive residual stresses were even lower than those measured in the only shot-peened specimen. In (Xu, et al., 1981) was performed stress-peening as the specimens were shot-peened either on the convex bent (tensile stressed) side or on the concave bent (compressive stressed) side of the specimens. The authors observed higher fatigue life only of the tensile pre-stressed specimens, while the compressive pre-stressing acted rather deteriorative on the fatigue life. The residual stresses of the tensile pre-stressed specimens were higher compressive and in greater depth compared to those of the only shot-peened specimens. In contrary, the compressive pre-stressed specimens exhibited low tensile residual stresses instead of compressive residual stresses.

A stress-rolling process was investigated by (Müller, 2005). Here, the work piece was bent, and the deep rolling process was performed on the tensile pre-stress side, along- or perpendicular to the bending direction. In case the deep rolling was applied in the direction perpendicular to the bending, the induced residual stresses on the surface remained on the same level as by the only deep-rolled specimen. In contrary, the pre-stressing led to deeper distributed compressive residual stresses (in some cases up to 1 mm depth). Stress rolling along the bending direction was then compared to stress peening and deep rolling without pre-stressing. The compressive surface residual stresses generated by the three processes compared to shot peening (without pre-stressing) are depicted in Figure 2-14. The abscissa axis corresponds to the longitudinal residual stresses (also along the bending direction). The perpendicular residual stresses (also perpendicular to the bending direction) are plotted on the ordinate axis. The isotropic stress state was achieved only by shot peening. Stress peening led to larger compressive surface residual stresses in the longitudinal direction, while by deep rolling considerable anisotropy in the residual stresses was observed. The stress rolling was able to induce the same magnitude of compressive stresses in the perpendicular direction and higher compressive stresses (than deep rolling) in the longitudinal direction.

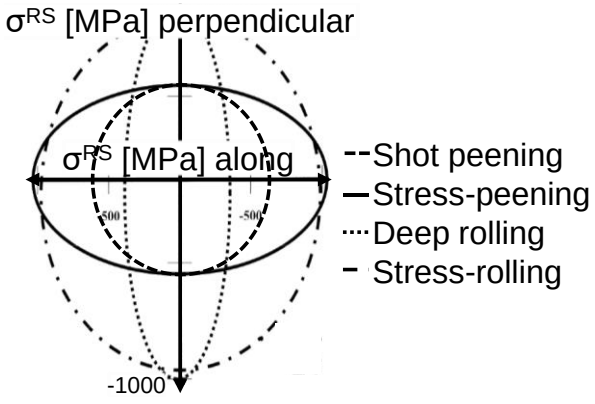

Figure 2-14: Surface residual stress distribution along- or perpendicular to the bending direction by stress-peening, stress-rolling or deep rolling without pre-stressing

A finite element modelling of stress rolling (pre-stressed deep rolling) was presented in (Lyubenova, et al., 2016), where a variation of the pre-stress amount and the DR pressure was realised. The essential results shown in this article are included in this thesis and will be discussed in chapters 5 and 7.2.

2.2.2 Deep rolling – principle, mechanism and scope of application

DR principle

Deep rolling, being a typical mechanical surface treatment, has a similar principle like the rest of the processes from this classification group. It is based on the elastoplastic deformation of the material, with the goal to create a smooth surface, a work hardening layer and favourable compressive residual stresses. The principle of DR can be explained as follows: once contact between the specimen and the tool is established, the tool is pressed with defined force/pressure/displacement against the specimen. As a result, a Hertzian pressure occurs. When the resulted stress is high enough to exceed the yield point of the treated material, the later begins to plastify. The amount of the resulted stress is a function of the applied pressure and the geometry of the DR tool. At the position of the maximal resulting stress occurs the initial yielding. In the general case, the resulted stress is not high enough to fully plastify the treated material, and therefore the layer below the plastified area remains only elastically deformed. Then, the tool begins its movement with a defined trajectory, to cover the whole treatment area. In case the tooltip rotates freely, a burnishing effect will appear, with resulting rolling friction between specimen and tool. If the tooltip is fixed, it will slide on the treated surface, resulting in sliding friction. After the tool moves away from the initial penetration area, the elastically deformed material layer, being not anymore under pressure, springs back. Nevertheless, the full recovery of this layer is prevented by the plastically deformed area, which leads to the generation of residual stresses. An exemplary setup of DR on a 3D surface is depicted in Figure 2-15.

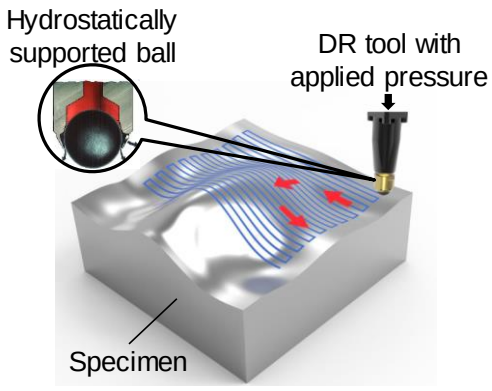

Figure 2-15: Principal setup of DR on a 3D surface with hydrostatically supported DR tool

Figure 2-16 illustrates a classification of the DR tools, differing by the setup of the predefined load application. The first type (see Figure 2-16 a)) uses hydrostatic pressure, and it is the most commonly employed DR tool. It has several advantages compared to other types like less number of components, thus reduced wear is ensured;

the hydraulic fluid, which creates the DR pressure, is used as a lubricant, thus additionally minimising the roughness of the treated part. Other tool types employ elastic force utilizing pre-stressed spring (see Figure 2-16 b) – e)) to define the loading. The most primitive tool type is depicted in Figure 2-16 f), where the loading is defined as a displacement of the tool against the treated part.

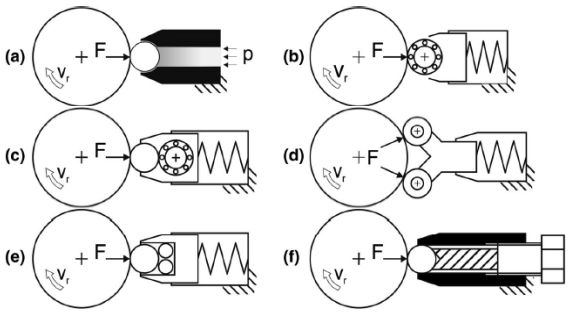

Figure 2-16: Classification of the DR tools by load definition: a) hydrostatic pressure, b) spring and bearing, c) spring, bearing and roller, d) spring and two bearings, e) spring and three balls and f) bolt and ball (Abrao, et al., 2014)

The elementary processes, which take place during DR, are the occurrence of Hertzian pressure and the plastic stretching and slipping, see Figure 2-17. The Hertzian pressure is a result of forces generated perpendicular to the surface, it causes the maximal plastic deformation, and compressive residual stresses beneath the surface. The plastic stretching is caused by both forces parallel and perpendicular to the surface, leading to maximal plastic deformation and compressive residual stresses on the surface. Usually, by hard materials (hardness > 600 HV), the effect of the Hertzian pressure predominates, while by soft materials (hardness < 300 HV), the plastic stretching causes the significant deformations. By materials with medium hardness (> 300 HV but < 600 HV), both effects combine. The slipping between tool and work piece results in slipping friction, which causes compressive residual stresses on the surface. Still, it cannot be considered as an isolated effect, as in combination with effects mentioned above, it can contribute to maximal compressive stresses on the surface, or at higher depths.

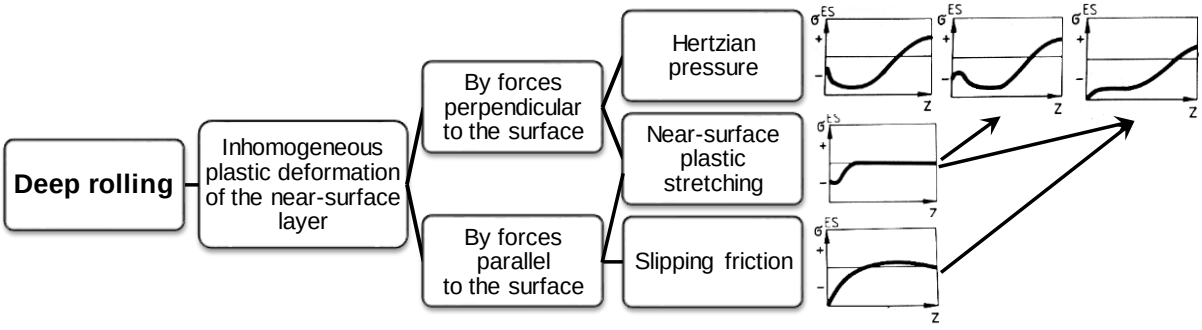

Figure 2-17: Schematic representation of the elementary processes, which take place during DR and their influence on the resulted residual stress depth distribution after DR (Scholtes, et al., 1986)

The friction between the DR tool and the work piece can be defined as the interdependency of the contact between both tool- and work piece's surfaces. At the beginning of the movement of the DR tool, static friction occurs, and during processing, a mixture of sliding and rolling friction occurs. This mixed friction (sliding and rolling) originates of the rotation of the DR tooltip combined with the steady work piece. In Figure 2-18 is depicted so-called "Stribeck curve" which describes the friction considering the lubrication type of the system "tool – work piece" and its influence on the resulted friction coefficient ($\mu = F_F$ – frictional force / F_N – normal force) as a function of the relative velocity between tool and work piece. The first case (on the left hand side) describes a boundary or "dry" lubrication means the surfaces of the tool and work piece are in contact by the absence of lubrication. Here, the velocity does not influence the magnitude of the friction coefficient. The second case (in the middle) depicts mixed lubrication, meaning that the roughness profile of both tool and work piece are low enough to let some lubrication to penetrate during load applied. This case results in dropping the friction coefficient by increasing the velocity. The third case (on the right hand side) characterises hydrodynamic lubrication, where the roughness profiles are lower than the thickness of the lubricating film. During loading, the whole normal load is born by the lubricating film, and no asperities of the tool or the work piece are in direct contact with each other. Here, increasing the velocity leads to higher friction, which even at high velocities is lower than the friction by boundary lubrication. Considering the mostly used DR tool with hydrostatic pressure (see Figure 2-16 a)), the mixed lubrication case should be valid, as the work piece can have a rough or smooth surface and the tooltip has in the most cases polished surface. Still, there is mechanical contact between the work piece and the tooltip.

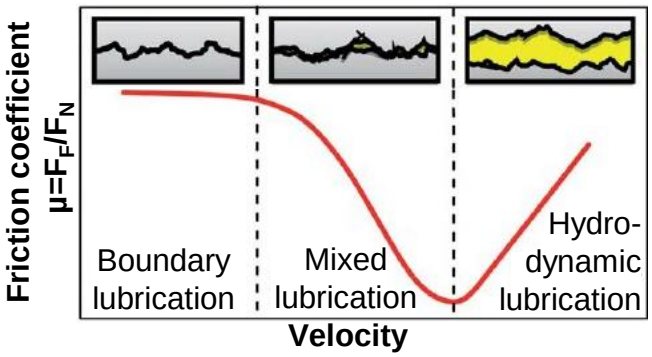

Figure 2-18: Typical Stribeck curve describing the friction coefficient as a function of the velocity and the type of lubrication between work piece and tool (Andablo-Reyes, et al., 2011)

Typical applications of DR process are in the automotive industry, where different engine components are deep rolled, e.g. engine valves, lobes of camshafts, journals of crankshafts, wheel flanges or gear shafts. In the aerospace industry, turbine blades and wheel rims are often treated using DR. In medical engineering, some parts of surgical instruments or implants are deep rolled. Typical application as post processing is the DR of welding structures, to reduce the tensile stresses produced by the welding process. Deep rolling is suitable for the treatment of external or internal surfaces,

where the internal surfaces should be accessible for the DR tool. Currently, bores with an inner diameter of a minimum 3.0 mm can be treated with DR (Röttger, et al., 2014).

Definition and development of deep rolling as a term

In the 30ties of the last century, when the research of the DR process was established, there were already several designations for processes, increasing the fatigue strength of components by local, continuous plastic deformation by keeping a constant the material volume. Typical examples were processes for (cold) rolling, work-hardening, strengthening, compressing, etc. Some terms like (cold) rolling were already occupied for sheet metal forming operations and therefore were no further used to describe DR in terms of unambiguousness. The definition “compressing” (to increase the material’s density) was also not suitable, as DR achieves no significant increase of the material’s macroscopic density unless the treated material has a porous structure. The term strengthening also did not adequately describe the process, even though an increase in the material’s strength is recognisable. Therefore, the following terms established during the past years: “deep (cold) rolling” in the manner of a process for increasing the material’s strength through local plastic deformation and “smooth rolling” in the manner of a process for improving the material’s surface quality through minor local plastification. Low plasticity burnishing is a derivation of DR, developed and patented by Lambda Technologies in 1996. The process utilises a hydrostatic pressurised tool and leads to stable compressive residual stresses but lower cold working than DR due to the lower process pressure (Prevey, 2000). Roller burnishing is also a derivation of the smooth rolling, having the main goal to achieve a smooth surface using a hydrostatic pressurised tool and low process pressure. Anyhow, the process also induces compressive residual stresses and cold working. Even though this thesis is focused on the DR process, these derivative processes will be discussed later as well, as they lead to changes in the surface integrity very similar to those induced by DR.

DR parameter influences

A comprehensive classification of the DR process parameters was done in (Schulze, 2005 b)), where the parameters were classified as DR tool, work piece, process- and machine parameters, see Figure 2-19. The most important DR tool parameters include the geometry of the tooltip (its diameter in case of a spherical tip or its profile in case of roller tip) and its elastic deformation behaviour. Tool’s roughness, geometrical accuracy and topography are usually neglected as influencing factors. The diameter of the DR tool has a significant influence on the elastoplastic deformed zone during processing which results in different residual stress distribution. In (Röttger, 2003) was investigated the impact of the DR tool diameter on the compressive residual stress maximum and depth by DR of 100Cr6V steel (hardness between 56 HRC and 61 HRC). It was found that larger tool does not significantly influence the maximal compressive residual stresses but shift them significantly to higher depth. The experiments were performed by different DR pressures (from 10 MPa to 40 MPa), and the observations mentioned above were valid for all DR pressures. Similar observations were

made in (Schuh, et al., 2007), where titanium rods were deep rolled with tool diameters of 4.0 mm, 6.0 mm and 13 mm. The induced by DR compressive residual stresses remained similar for the different tool diameters, but they were shifted into higher depth.

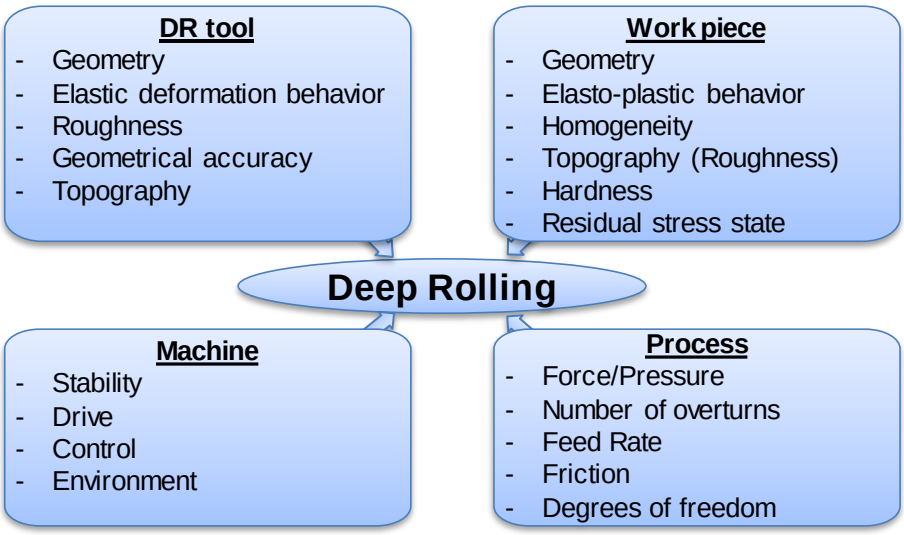

Figure 2-19: Classification of the deep rolling process parameters (Schulze, 2005 b))

The elastic behaviour of the DR tool is usually not a major investigation point, as the tooltip material possesses quite higher elasticity limit than the one of the work piece. Therefore, minor elastic deformations in the tooltip are expected. Typical materials used for the production of DR tooltips are tungsten carbide or ceramics (Meyer, et al., 2011; Meyer, et al., 2018).

The next parameter group is the one describing the process itself. Here, the main influencing factors are the applied pressure, the number of overturns (similarly to the coverage above 100 % by shot peening, the parameter describes how many times the same area was treated) and the feed rate or the so-called overlapping (the first term is valid by treatment of axis-symmetrical parts, and the latter is used in case of treatment of complex 3D parts or flat surface). The friction is an influencing factor in case of application DR with non-rotational tooltip or DR without lubricant. The different degrees of freedom in terms of tool fixation will not be discussed, as the DR setup employed in this thesis uses only one type of tool with defined degrees of freedom. The most crucial impact factor of this parameter group is the applied pressure. It directly influences the amount of the elastoplastic material deformation and thus the amount and depth of the induced residual stresses, the portion of cold working and the surface roughness. In Figure 2-20 is described the influence of the DR pressure/force on the resulted residual stress depth profiles.

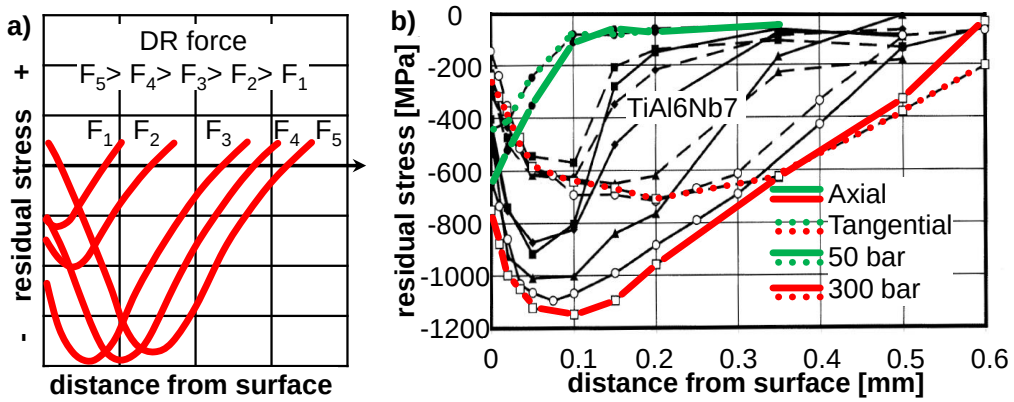

Figure 2-20: Typical dependence of the residual stress depth profiles, by variation of the DR force: a) qualitative representation (Berstein, 1979) and b) quantitative representation (Schuh, et al., 2007)

Figure 2-20 a) shows a quantitative representation of the depth profiles by applied low- (F_1) to high (F_5) DR force. It is visible that up to F_3, the magnitude of the compressive stresses and their depth increases and further enhancement of the DR force shifts the compressive stress maximum to higher depths. Nevertheless, higher DR force leads also to decreasing compressive stresses on the surface and in the shown case, by force F_5, even minor tensile stresses are present on the surface. In Figure 2-20 b) is plotted similar study, as here the profiles were generated by DR with increasing pressure from 50 bar (the green profile) to 300 bar (the red profile). Here, a similar tendency is observed as in Figure 2-20 a). Additionally, the typical for DR anisotropy of the residual stresses in axial (full lines) and tangential (dashed lines) direction is visible. Increasing the DR pressure also leads to stronger anisotropy. In the tangential direction, the compressive stress maximum remains almost the same by increasing the DR pressure, but it is shifted to higher depths. In the axial direction, enhancing the DR pressure leads to higher magnitude- and deeper distributed compressive stresses.

In (Rodríguez, et al., 2012) was also observed a strong residual stress anisotropy by deep ball burnishing with pressures of 100 bar to 200 bar. This phenomenon is caused by the complex three axial plastic deformation mechanism during processing, which results in different plastic stretching and shrinking in the directions along- and perpendicular to the DR.

The DR pressure also influences the hardness directly. Materials prone to strain hardening usually get harder by treatment with DR and increasing the DR pressure leads to higher hardness values (Rodríguez, et al., 2012), while others, typically very hard materials, can exhibit even strain softening at high DR pressures. In (Berstein, et al., 1982) was described the influence of the applied DR force on the resulting change of the work hardening layer, see Figure 2-21 a). It is visible that the higher DR force leads to deeper work hardening layer, where the hardness maximum is shifted to higher depth when raising the DR force. Although, at certain force level (F_8), the hardness on the surface even decrease, compared to those of the untreated material. Also, no further raise of the hardness maximum below the surface is observed. This decrease of the surface hardness is characterised by the so-called disruption damage that in extreme cases, can lead to surface flanking. The disruption damage is a wearing mechanism typical for ball bearings, which appears due to the applied cyclic loading. As a

result, on the surface appear micro-cracks and pitting. The authors also systematised the change of the hardness by DR for different material types, see Figure 2-21 b). Soft materials with ferritic or ferritic-perlitic microstructure exhibit the highest enhancement of the hardness, followed by hard materials with martensitic microstructure. Quenched and tempered steels (hardness range 350 HV to 450 HV) exhibit the lowest increase of the hardness.

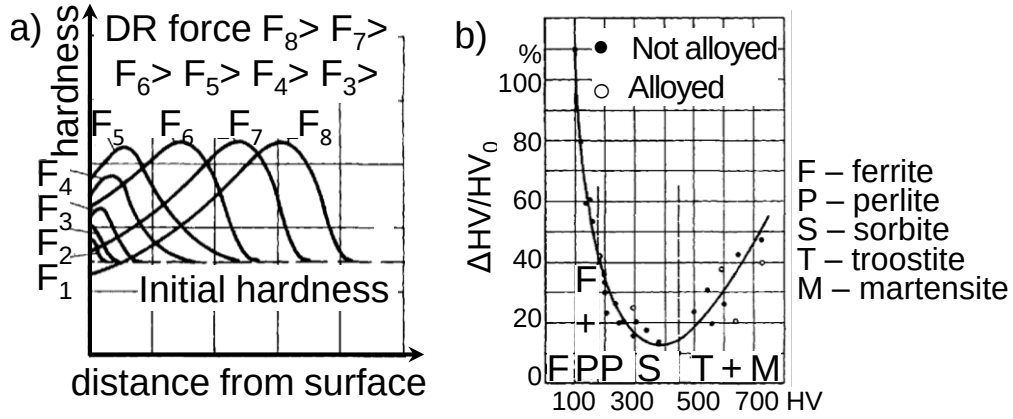

Figure 2-21: a) typical dependence of the hardness, by variation of the DR force and b) increase of hardness by deep rolling as a function of different microstructures (Berstein, et al., 1982)

The DR pressure/force has a major impact on the surface topography, especially by treatment of soft materials. In (Magalhaes, et al., 2016) was studied the change of the surface roughness by DR with variable pressure (50 bar to 300 bar) on AISI 1060 steel in annealed state (HV 290) or quenched and tempered state (HV 750). The treatment of the soft material state led to higher roughness by increasing the DR pressure, while the hard material state was only minor influenced. In contrary, (Röttger, 2003) observed reduced surface roughness of up to 70 % by increasing the DR pressure from 100 bar to 400 bar in high strength steel 100Cr6V. The same observations were made for TiAl6Nb7 in (Schuh, et al., 2007). In (Zoch, 1995) was reported for surface roughness achieved by DR of under 1 µm, thus comparable with the roughness induced usually by electropolishing. Nevertheless, it is essential to note that the initial surface quality has to be considered as well, as it is the pre-condition influencing the surface roughness after DR.

The number of overturns is another process parameter that has a significant impact on the surface integrity after DR. The application of several overturns on the same area, can lead to increased work hardening with every next overturn (in case the material is prone to work hardening). As a result, the plastic deformation amount decreases by every next overturn until a saturation point is reached. By multiple overturns, a cyclic loading takes place, and the corresponding material behaviour has to be considered (Achmus, 1999). The same author investigated the axial residual stress depth distribution after DR with one to five overturns applied on a rotation-symmetric work piece with a transitional radius. The author found that the generated compressive- and tensile residual stresses increase for DR with three overturns compared to single overturn. Still, further change in the residual stress state was not observed. In (Magalhaes, et

al., 2016) was employed single or triple DR on AISI 1060 steel in annealed- or quenched and tempered state. The annealed state showed almost no change in the surface residual stress state, but the annealed- or quenched state exhibited slightly higher near-surface compressive stresses by triple overturn compared to single overturn.

The next group of process parameters are those describing the work piece properties (geometry, material elastoplastic behaviour, hardness, roughness, residual stress state, etc.). The work piece's geometry will not be discussed, as it is not directly connected to the topic of this thesis. The material's elastoplastic behaviour and its hardness were considered already, as they interact with other process parameters, leading to complex interdependencies. The material's ultimate strength (Rm), even by the same material type, can lead to quite different residual stress depth distributions (see Figure 2-22).

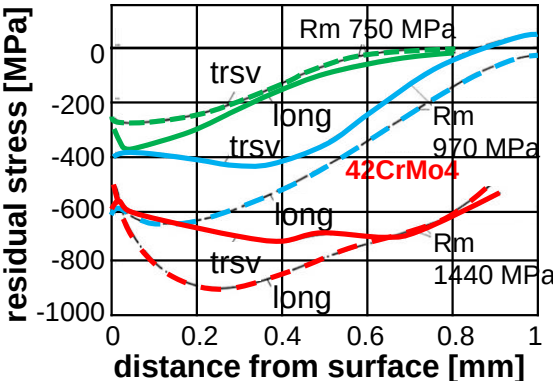

Figure 2-22: Influence of the material's ultimate strength on the residual stress depth distribution after DR (Scholtes, 1990)

The initial residual stress state of the work piece (usually caused by previous machining/manufacturing operations) can lead to unpredictable residual stress state after DR. In (Lyubenova, et al., 2019) was performed a comprehensive investigation of the surface- and depth residual stress state after DR by variation of the pre-machining state of the work piece and several process parameters. The results of this article will be discussed in subchapter 7.3.

The last group of process parameters describes the influence of the DR machine, like its stability, the type of driving mechanisms, environment (temperature influences on its precision). Usually, these process variables are not comprehensively discussed, as DR is performed using standard CNC machines, which possess nowadays very good stability.

2.3 Methods for modelling of Deep Rolling

The previous chapter emphasised the influence of the numerous deep rolling process parameters on the resulted surface integrity. Even though the process was investigated since decades and despite its relatively simple principle, the knowledge about the exact prediction of the generated residual stress state, the cold working amount or

the surface topography is still not achieved. Often, the influences of the process parameters interact with the material's properties inherited from previous manufacturing stages, thus leading to difficult to distinguish interdependencies. For this reason, the analytical- and the finite element modelling of DR is attracting the scientific interest since long time ago. In (Broszeit, 1984) was attempted to describe the near-surface residual stress state using the Hertzian theory. Nevertheless, the developed model did not consider the non-linear elastoplastic material deformations and the friction conditions. In (Magalhaes, et al., 2016) were compared three analytical models (Hertz, 1882; Bouzid, et al., 2004; Li, et al., 2012) for prediction of the surface roughness after DR. The authors proposed their analytical model for prediction of the surface residual stress state and the hardness. The surface roughness after DR (single or triple overturns) on AISI 1060 steel in three different material states (annealed, sub-critical annealed and quenched and tempered) was calculated and compared by all three models. In the sub-critical annealed and the quenched and tempered state, the modelled roughness was comparable to the measured. Anyhow, the modelled roughness after triple overturns of the quenched and tempered state underestimated the measured values. The stated reason was neglecting the plastic deformation or the elastic recovery during DR. The hardness after DR was calculated with proposed by the authors analytical model, based on a linear regression correlation between initial material hardness, DR pressure and number of overturns. The model predicted well the hardness by low pressure but led to some discrepancies at high pressures and by triple overturns. The near-surface residual stress was calculated based on empirically derived initial material hardness, yield strength and intimate tensile strength. The model considered strain hardening as well. The comparison with measured stress values showed an agreement between 3 % and 47 % with no systematic deviations. Nevertheless, the model was able to calculate only the near-surface residual stresses and did not consider contact and friction.

The finite element analysis (FEA), being able to deal with more aspects of the DR process, compared to the analytical approaches, was employed to predict mainly the residual stresses and deformations after DR since the 1980s. The FEA is an approach, able to simulate different physical problems like structural loading, heat transfer, fluid flow, etc., using the numerical technique finite element method (FEM). This technique is based on the description of the problem by partial differential equations and by given boundary conditions. The object of interest is represented as an assembly of finite elements. The FEM formulation of the problem results in a system of algebraic equations. The simple equations that model these finite elements are then assembled into a larger system of equations that models the entire problem. The FEM consists of four main stages:

1. Discretising the continuum – in this stage, the object of interest is divided into finite elements. The finite elements form a mesh, typically generated by a pre-processor program.
2. Selecting the interpolation functions – they are used to interpolate the field variables over the element. Often, polynomials are selected as interpolation functions, and the degree of the polynomial depends on the number of nodes assigned to each element.

3. Finding the element properties – in this stage, the matrix equation for the finite element should be established. It relates the nodal values of the unknown function to other parameters.
4. Assembling the element equations – here, all of the element equations should be assembled to find the global equation system for the whole solution region.
5. Solving the global equation system – the finite element global equation system is typically sparse, symmetric and positive definite. Direct and iterative methods can be used for the solution. The nodal values of the sought function are produced as a result of the solution.
6. Computing additional results – for the cases, typically by mechanical problems, where instead of the calculated displacements, the stresses and strains are of interest, the last parameters are obtained after the solution of the global equation system.
The description of the modelled problem can be divided into six stages:
1. Choice of equation system solver – dependent on the linearity of the problem (linear static or dynamic)
2. Definition of the geometries of the objects of interest
3. Defining the material data for the objects of interest – a crucial modelling stage, as the material properties define the response of the material to the applied loads.
4. Designation of the modelling steps, boundary conditions (BC), loads and interactions – similar to the description of a physical process, the simulated process is divided into several steps, defined by the changes in the process's input variables. Description of the fixations and the applied loads; interaction definitions (e.g. friction behaviour). This stage is accompanied by unavoidable simplifications of the boundary conditions of the physical process, which simplifications can lead under certain conditions to misleading results.
5. Meshing strategy - discretisation of the objects of interest, mesh and element types definition.
6. Post processing – visualisation of the calculated results; types of output parameters displayed (e.g. displacements, stresses, strains) and location of the calculated values.
In this chapter, several from the modelling aspects mentioned above will be considered in the context of modelling of the DR process. A focus will be put to the definition of the material data and the influence of the applied boundary conditions on the calculated post processing variables (stresses, strains, etc.).
Figure 2-23 presents a classification of the commonly used material models for FE simulations. The models are classified by linearity, time- and temperature dependence, cyclic loading and hardening.

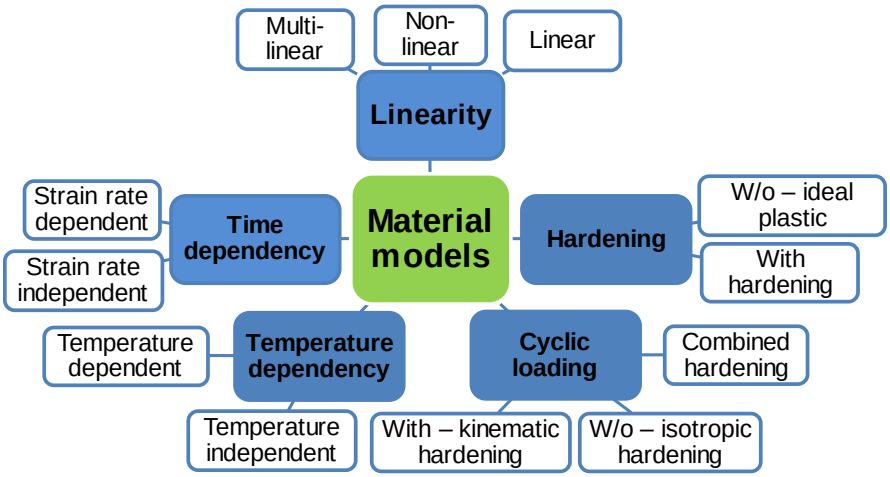

Figure 2-23: Classification of the material models used for FE simulation of DR

For the DR process, the multi-linear models are commonly used, as they can represent more realistically the physical non-linear material behaviour. Under real conditions, materials do exhibit strain hardening/softening as well, and as DR generates strain hardening/softening, including a hardening rule to the material model is highly recommended. The behaviour of the material under cyclic loading should be considered as well even that usually, DR does not generate cyclic loading. Under certain conditions like applying multiple overturns or a high percentage of overlapping and when the material is prone to exhibit strong Bauschinger effect (see subchapter 2.1.4), not including the behaviour of the material under cyclic loading can lead to wrongly calculated stress values.

In case a temperature boundary condition is added to the DR model, to simulate DR by elevated temperatures, temperature-dependent material data needs to be included. Strain dependent material data can be included, but this is not stringently necessary for DR (in contrary to shot peening) as the process is typically supported by low to medium strain rates (Altenberger, 2002).

In (Liebisch, 1991) was done one of the first endeavours to model the DR process using FE modelling. The author simulated the process as a static, two-dimensional one, and the goal was to calculate the residual stresses. Nevertheless, as the DR generates strongly direction-dependent stresses, the two-dimensional modelling did not deliver plausible results. The first detailed work focused on the three dimensional FE modelling of DR was done by (Jung, 1996). The author employed the FE software MARC to model the DR process on a rod with transitional radius (the work piece's geometry corresponds to those of crankshaft's transitional radius between hub and cheeks) or a rod without transitional radius. The discretisation was performed with only 20 000 elements in total. The material (42CrMo 4 steel) was described as elastic-plastic with isotropic hardening, the friction between work piece and tool was neglected. By the rod without radius, the calculated axial residual stress depth profiles after single- or triple overturns were in a very good agreement with the x-ray diffraction measured values (corrected with the method of (Moore, et al., 1958)). The DR simulation using rods with radius also delivered consistent results, up to higher depths, where the model

predicted higher tensile stresses than measured. The author suggested loss of sensitivity due to the stress correction with the method of (Moore, et al., 1958). The calculated tangential residual stress depth profiles, in contrary to the axial stress depth profiles, were in a relatively large discrepancy to the measured ones, especially near the surface (app. -300 MPa measured vs app. -800 MPa calculated). In (Achmus, 1999) was employed the explicit module of ABAQUS CAE to obtain a dynamic simulation of DR using similar work piece's geometry as in (Jung, 1996). The author proved that employing a rigid body as a tool did not influence the resulted stresses, so the elasticity of the tool can be neglected. He also investigated the influence of scaling the material density (high scaling factors significantly reduce the calculation time) on the resulted stresses and stated that up to factor 1000^2 the scaling has no significant impact. The employed Chaboche material model (Broggiato, et al., 2008), a model with a nonlinear combined isotropic-kinematic hardening rule, compared to the material model with isotropic hardening rule delivered very similar residual stress values. The FE model also showed almost no sensitivity to change of the friction coefficient from 0 to 1.0. Several process parameters were investigated (DR force, number of overturns, different work piece geometries, etc.) but a comprehensive validation of the FE model was unfortunately not presented. (Schaal, 2002) contributed to the development of the FE modelling of DR. The author established a 3D model of a rotation-symmetrical notched work piece (42CrMo 4 steel) and a 3D roller tool. The employed FE software was MARC. An isotropic material hardening rule was defined, and friction between work piece and tool was assigned (Coulomb Friction). The comparison between the FE calculated and measured depth profiles (using x-ray diffraction and stress relaxation correction according (Moore, et al., 1958)) showed a relatively good agreement in the axial direction. Here, increasing the DR force led to higher magnitude compressive residual stresses, shifted deeper into the material, and balanced with higher tensile stresses in depth. In contrary to the good agreement in the axial direction, the FE calculated stresses in the tangential direction showed a significant discrepancy compared to the measured values. Here, near the surface, the FE calculated stress values reached app. -1000 MPa, where the measured ones – only app. -300 MPa. The author pointed as possible reason uncertainties by the x-ray measurements, caused by the discontinued measurement procedure due to the electropolishing material removal for determining the stress depth profiles. In the 2000s, with the development of computer technologies, which offered more computing power for reasonable calculation time, the FE modelling of DR made its further progress. Most of the researches employed rotational-symmetric work pieces (Balland, et al., 2013; Beghini, et al., 2014; Perenda, et al., 2014; Perenda, et al., 2015; Klocke, et al., 2016; Majzoobi, et al., 2016), while very few were focused on modelling of DR on flat/complex work piece's geometry. In (Manouchehrifar, et al., 2012) was performed a dynamic simulation of DR process on flat work piece using ABAQUS CAE 6.10. The Johnson-Cook material model was employed (Johnson, et al., 1983). This model is suitable to describe material behaviour by large strains, high strain rates and elevated temperatures (although, the modelled DR was at room temperature). The established DR model was unrealistically sensitive to change of the friction coefficient or of the overlapping percentage and almost non-sensitive to change of the applied DR force. Validation of the FE calculated residual stress depth profile

with x-ray diffraction measurements was presented but neither the direction of the residual stresses was noted, nor the conditions of the stress measurements (they were taken from the available literature). The authors stated a very good agreement between calculated and measured values.
In (Lim, et al., 2016) a quasi-static FE approach and a flat work piece (Ti6Al4V material) were chosen for the modelling of DR. A material model with isotropic hardening rule was defined, the tool was modelled as a rigid body, and the DR pressure was varied (20 MPa or 38 MPa). The FE model was verified by means of residual stress in-depth measurements using hole drilling method. The verification showed that the FE model could predict very well the stress impact depth by both DR pressures. Nevertheless, near the surface, there were some discrepancies between calculated and measured values. At DR pressure of 20 MPa, the DR model was not able to describe the strong anisotropy of the near-surface stresses in longitudinal and transverse directions. At DR pressure of 38 MPa, the FE model overestimated the near-surface stresses in both directions (deviations of the depicted normalized stress of 0.2 to 0.4 were reported). As a possible reason for the discrepancy was pointed the relatively low accuracy of the hole drilling method for near-surface stress determination.
In (Lyubenova, et al., 2015 a); Lyubenova, et al., 2015 b); Lyubenova, et al., 2015 c)) was developed an FE model of DR on flat geometry using the FE code ABAQUS (versions 6.12 – 6.14). The modelled results of these articles will be discussed in detail in subchapter 7.1. A continuation of this work, in (Lyubenova, et al., 2017 a)), the calculated from the FE model surface residual stresses were compared to the surface stress profiles determined by x-ray diffraction. The comparisons will be shown in subchapter 7.3. In (Lyubenova, et al., 2017 b)) was additionally discussed the influence of the material model on the residual stress state after DR with variable process pressure. The results of this article will be presented in chapter 6.

2.4 Experimental methods for characterisation of the surface integrity after deep rolling

2.4.1 Residual stress determination methods

This subchapter addresses the choice of technique for the determination of the residual stress state after DR. As discussed in subchapter 2.1.3, the residual stresses can be considered as one of the crucial material properties, because of their significant impact on the fatigue strength. Due to the specifics of the residual stresses, most of the available measurement techniques are non-direct, as typically strains, displacements or magnetic fields are measured and base on these measurements, the residual stresses are calculated. In Figure 2-24 is presented a classification of the residual stress determination techniques by measurement depth in steel and level of material removed. The group of the non-destructive techniques consists of several diffraction methods, like the most commonly used x-ray method, synchrotron x-ray and neutron diffraction. The classical x-ray diffraction method can offer a very good precision, with a very low spatial resolution (using special optics, measurement spot in the micrometer range is possible) and relative short measurement time. The technique is limitedly considered

as a non-destructive, as the x-ray beam penetrates typically less than 10 µm in streel and therefore can provide stress determination near the surface. Due to the low x-ray penetration, plane stress is usually considered. For the determination of the residual stresses in depth, a material layer removal needs to be performed. Even when the material removal procedure does not induce additional residual stresses, it can lead to notable stress redistribution and stress relaxation. A back-calculation of the residual stresses removed together with the material is possible, but it does not always adequately consider the realistic conditions.

The synchrotron x-ray technique is similar to the standard x-ray one, with the difference that the x-rays of the former have higher intensity and energy, thus penetrating deeper into the material (up to several hundred micrometer in streels). Due to the higher penetration depth, a measurement gauge volume must be considered, i.e. the full three-dimensional stress condition. In contrary to the standard x-ray method, the one using synchrotron radiation compares the measured strains to strain-free reference, and this can be a source of precision uncertainty. The measurement costs by synchrotron x-ray diffraction are generally higher than those by the standard x-ray one.

The neutron diffraction, compared to the other diffraction methods, offers significantly higher penetration depth (up to several milimeter in steels), which classify it as an unlimited non-destructive method. Similarly to the synchrotron method, here, a strain-free reference is required. The measurement costs by neutron diffractions are high, as the determination of the strains in a single measurement gauge volume (usually app. 1 mm^3) lasts longer time compared to the x-ray methods. The measurement resolution by neutron diffraction is lower compared to the x-ray methods.

The Magnetic Barkhausen Noise is a non-destructive stress determination technique based on the inductive measurement of a noise-like signal, generated when a magnetic field is applied to a ferromagnetic sample. The intensity of the Barkhausen noise is sensitive to elastic stresses available in the measured sample. Anyhow, the relatively low measurement resolution (in the range of 1 mm), the low stress sensibility (around ±300 MPa) and the need for calibration with a nearly identical test sample, severely compromises and restricts the usage of this technique for precise determination of high gradient residual stresses.

The next group of measurement techniques describes the semi-destructive ones. Here, the most commonly used technique is the hole drilling one (includes center-hole drilling, ring coring and deep-hole drilling methods), with significantly lower measurement costs, compared to those by the diffractions methods. It is based on the drilling of a small hole in the surface of the specimen and measuring the deformations of the surrounding surface, i.e. it considers the stress relaxation indirectly. Typically, strain gauges are employed to obtain the strain changes and more recently, the optical technique called Electronic speckle pattern interferometry. The hole drilling method has limited application for near-surface stress determination and reduced sensitivity for measurements at higher depths. High stress gradients are also difficult to interpret.

The group of fully destructive methods consists of the slitting, contouring, BRSL (Block Removal, Splitting and Layering), Sachs boring and inherent strains methods. All of those techniques are based on the determination of the deformations after cutting the stressed specimen. Based on the measured deformations, stress relaxation can be

calculated. The great advantage of these techniques is their simple principle and low measurement costs. Depending on the type of cutting (drilling or slitting/full in-plane cutting), different stress tensor determination limits are observed. E.g., by slitting and contour methods, the stress can be determined only in the direction normal to the cutting plane, which for the case of stress anisotropy is a severe disadvantage.

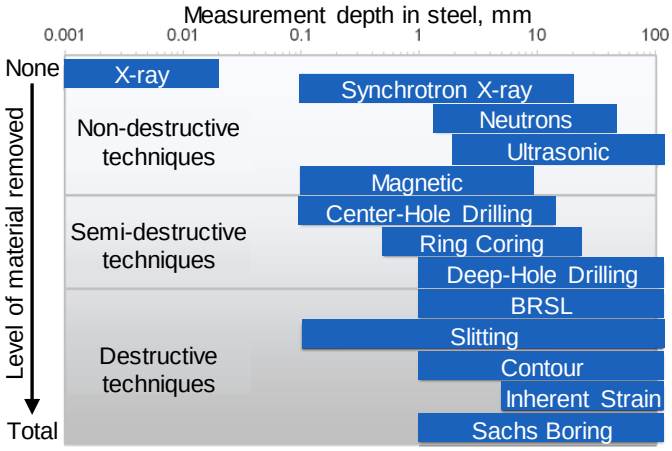

Figure 2-24: Classification of the residual stress determination techniques by measurement depth and level of material removed (Schajer, 2015)

Table 2-2 gives a general overview of the stress measurement methods mentioned above, including information about their suitability to measure different objects, their availability, the measurement speed, and the generalised costs. Based on the discussed advantages and disadvantages of the presented stress determination methods, the experimental residual stress analysis shown in this thesis was performed using classical x-ray diffraction technique.

Table 2-2: Classification of the residual stress determination techniques (Kandil, et al., 2001)

Techniques	**Parts ***	**Contact**	**Destructive**	**Availability**	**Speed**	**Cost**
Hole Drilling	S, A, C	Yes	Semi	Widespread	Fast/ Med	£50-200
X-Ray Diffraction	S, A, C	No	No	Generally available	Fast/ Med	£50-200
Synchrotron	A, C	No	No	Specialist	Fast	High
Neutron Diffraction	A	No	No	Specialist	Med/ Slow	£10-1500
Curvative and Layer Removal	A, C	Yes	Yes	Generally available	Med	£50-200

* S – structures, A – artefacts, C – coatings

X-ray diffraction method

The x-ray diffraction technique, when employed for residual stress determination, is based on the measurement of the strain in the crystal lattice. The related residual stress is determined from the material elastic constants assuming a linear elastic distortion of the appropriate crystal lattice plane. Since a whole area of the specimen is exposed to x-rays, many grains and crystals will contribute to a single measurement.

Although the measurement is considered as near-surface, x-rays do penetrate the material: the penetration depth is dependent on the anode of the x-ray tube, the material and angle of incidence. Hence, the measured strain is essentially the average over a few microns depth under the surface of the specimen. The measurement of the strain in the crystal lattice is performed as the specimen is exposed to focused radiation (typically x-rays). The radiation interacts with atoms or crystallites of the specimen that are arranged in a regular array, for example, atoms in crystals and then, diffraction of electromagnetic radiation occurs. The focused radiation is absorbed and then reradiated with the same frequency such that strong emissions occur at certain lattice orientations and minimal emissions at other lattice orientations. The angle at which the strong emissions occur are described by the Bragg's Law:

$$n\lambda = 2D^{\{hkl\}}sin\theta^{\{hkl\}} \qquad \textit{Equation 2-1}$$

Where:
n – whole number of wavelengths
λ – wavelength
$D^{\{hkl\}}$ – inter-planar (lattice plane) spacing
$\theta^{\{hkl\}}$ – Bragg's angle
A simplified x-ray diffraction case of only two lattices with a spacing of $\mathbf{D^{\{hkl\}}}$ and two x-ray beams with a length of $\mathbf{I_0}$ (primary) and **I** (reflected) is illustrated in Figure 2-25. The primary beam $\mathbf{I_0}$ collides with the atom, and the x-ray wave of the beam (with wavelength **λ**) interacts elastically and excites the atom, forcing it to emit own radiation with the same wavelength **λ**. The lower beam depicted in the figure needs to travel a longer distance than the upper until it reaches the lower atom. If the path difference of the lower beam to the upper one is equal to **λ** or the integral multiple of **λ**, then the emitted (reflected) x-ray will be in phase. If the beam path difference is not equal to **λ** or the integral multiple of **λ**, the x-ray will cancel each other. When considering the general case, where a big number of atoms are exposed to x-rays, those x-rays that are in phase will produce a diffraction maximum and those who cancel each other will produce a diffraction minimum.

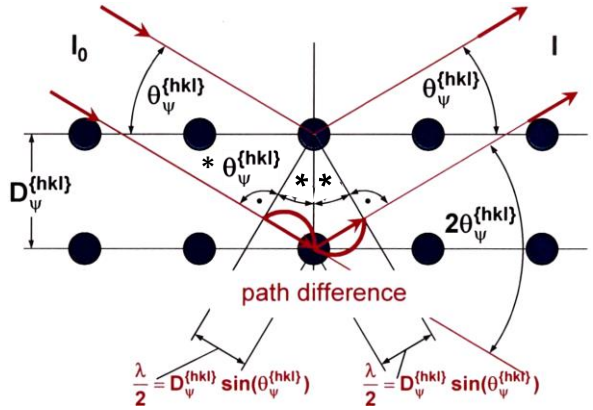

Figure 2-25: Schematic diffraction interference of x-rays of wavelength λ at lattice plane {hkl} (Hoffmann, 2011)

Considering that the inter-planar lattice plane spacing $\mathbf{D^{\{hkl\}}}$ will change when applied- or residual strain exists in the measured specimen, if the unstrained lattice plane spacing $\mathbf{D_0^{\{hkl\}}}$ is known, then the applied- or residual strain can be quantitatively characterised. The connection between macro- and atomic strain is represented in Figure 2-26.

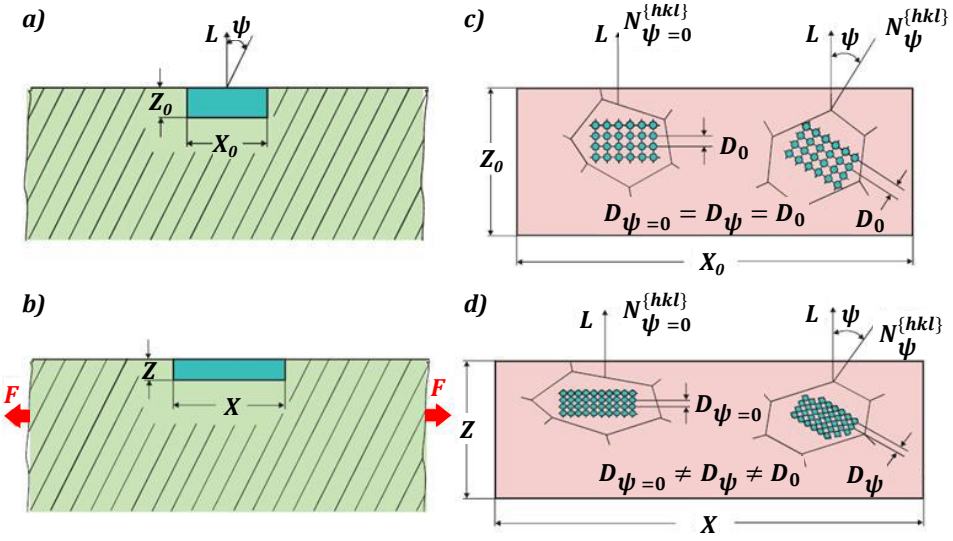

Figure 2-26: Schematic representation of macro and micro strain (Macherauch, et al., 2011)

Figure 2-26 a) and b) depicts a not-deformed and deformed specimen. When a force **F** is applied, the dimensions of the illustrated rectangle will change from $\mathbf{Z_0/X_0}$ to **Z/X**, where $\mathbf{Z_0 > Z}$ and $\mathbf{X_0 < X}$ (the rectangle becomes longer and narrower). If considering the resulted deformation in z direction at ψ = 0, the macro strain in the same direction $\boldsymbol{\varepsilon_Z}$ is equal to:

$$\varepsilon_Z = \frac{Z - Z_0}{Z_0}$$ *Equation 2-2*

Following this consideration, the atomic strain $\boldsymbol{\varepsilon_{\psi=0}}$ at ψ=0 (see Figure 2-26 c) is equal to:

$$\varepsilon_{\psi=0} = \frac{D_{\psi=0} - D_0}{D_0}$$ *Equation 2-3*

In case no deformation exists, see Figure 2-26 c), the lattice plane spacing $\mathbf{D_{\psi=0}}$ will be equal to $\mathbf{D_0}$ (for the corresponding hkl lattice plane) and when tilting the specimen at ψ angle, it will remain the same ($\mathbf{D_\psi = D_{\psi=0} = D_0}$). If the specimen is deformed, see Figure 2-26 d), then the lattice plane spacing at $\mathbf{D_{\psi=0}}$ will differ from this of the not-deformed state ($\mathbf{D_0}$), and when tilting the specimen at ψ angle, the lattice plane spacing $\mathbf{D_\psi}$ will differ to this at ψ = 0 ($\mathbf{D_{\psi=0}}$).
For every ψ angle, the atomic strain ε_ψ can be calculated as follows:

$$\varepsilon_\psi = \frac{D_\psi - D_0}{D_0}$$ *Equation 2-4*

Considering the Bragg's law, see Equation 2-1, for $\mathbf{D^{\{hkl\}}}$ and for arbitrarily **ψ** angle, the total derivative of the Bragg's law is:

$$2dD_\psi sin\theta_0 + 2D_0 cos\theta_0 d\theta_\psi = 0 \qquad \textit{Equation 2-5}$$

The change in the Bragg's angle and the following displacement of the interference lines are:

$$d\theta_\psi = -\frac{D_\psi - D_0}{D_0} tan\theta_0 = -\varepsilon_\psi tan\theta_0 \qquad \textit{Equation 2-6}$$

To calculate the stress, the measured atomic strain is combined with the elasticity theory. In Figure 2-27 a) is represented a coordinate system with three axial stress/strain state, where $\boldsymbol{\varepsilon_1, \varepsilon_2, \varepsilon_3, \sigma_1}$ and $\boldsymbol{\sigma_2}$ are the principle strain/stress directions ($\boldsymbol{\sigma_3}$ is considered as zero, as the penetration depth of x-rays is very low → plain stress is assumed). The elasticity theory gives the possibility to determine strain $\boldsymbol{\varepsilon_{\varphi,\psi}}$:

$$\varepsilon_{\varphi,\psi} = \varepsilon_1 cos^2\varphi sin^2\psi + \varepsilon_2 cos^2\varphi sin^2\psi + \varepsilon_2 cos^2\psi \qquad \textit{Equation 2-7}$$

where:

$$\varepsilon_1 = \frac{1}{E}(\sigma_1 - \sigma_2);\ \varepsilon_2 = \frac{1}{E}(\sigma_{2-}\vartheta\sigma_1);\ \varepsilon_3 = -\frac{\vartheta}{E}(\sigma_1 + \sigma_2)$$

Considering the Voigt constants $\boldsymbol{s_2}$ and $\boldsymbol{s_1}$:

$$\frac{1}{2}s_2 = \frac{\vartheta + 1}{E};\ s_1 = -\frac{\vartheta}{E} \qquad \textit{Equation 2-8}$$

Combining the Bragg's law, and substituting the Voigt constants to Equation 2-7, the fundamental equation of the x-ray diffraction method can be derived:

$$\varepsilon_{\varphi,\psi} = -cot\theta_0 d\theta_{\varphi,\psi} = \frac{1}{2}s_2 sin^2\psi + s_1(\sigma_1 + \sigma_2) \qquad \textit{Equation 2-9}$$

When considering the plain stress state, for fixed **φ** angle, the strain distribution over the sinus square ψ function can be graphically illustrated as shown in Figure 2-27 b). In practice, the gradient of the strain over sinus square ψ gives the value of the required stress value $\boldsymbol{\sigma_\varphi}$. The standard deviation of the stress value results from the deviation of every single $\boldsymbol{\varepsilon_\psi}$ measurement and it origins usually from the specimen's geometry, the measurement uncertainty or the material's properties.

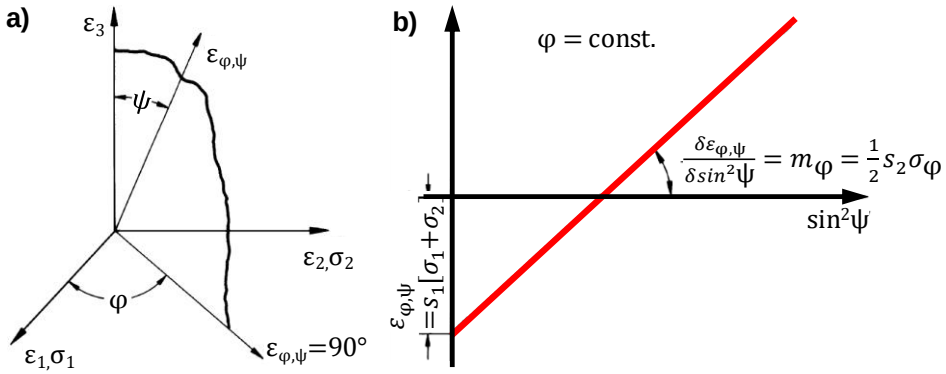

Figure 2-27: a) coordinate system representing 3 axial stress/strain state; b) strain distribution over sinus square ψ function (Macherauch, et al., 2011)

Due to the specifics of the x-ray diffraction technique, there are many measurement accuracy-influencing factors, which needs to be considered. Such factors include faulty mechanical adjustment of the x-ray diffractometer, imprecise positioning of the measured specimen, measurement surface issues and material properties specifics. Some of these factors will be considered below.

Specimen's height adjustment

The false specimen's height adjustment can lead to significant shifting of the position of the diffraction peak. As it additionally leads to misalignment of the tilting axis, this may also lead to ψ-splitting. In Figure 2-28 is schematically outlined such specimen's misalignment. Usually, the source of this error is a false adjustment of the specimen's surface or/and poor diffractometer alignment. Equation 2-10 describes the amount of the caused 2θ shifting, where it is visible that due to the cosine function, the effect is more pronounced at lower θ values.

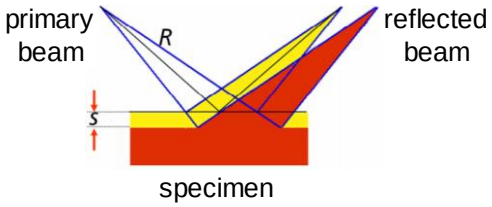

Figure 2-28: 2θ shifting caused by a false specimen's height adjustment (Panalytical, 2013)

$$\Delta 2\theta(°) = \frac{2s\ cos\theta}{R}\frac{180}{\pi}$$ *Equation 2-10*

where:
s – error of the height adjustment
R – radius of the diffractometer operational circle

Specimen's surface roughness

The increased specimen's surface roughness can also be a source of measurement uncertainty. In Figure 2-29 is represented the primary and the reflected beam directions by a change of the specimen's surface topography. The roughness peaks and valleys can lead to the generation of diffraction signals from differing specimen height and can displace the focus of the reflected beam. This can result in shifting of the diffraction peak and thus to false stress values.

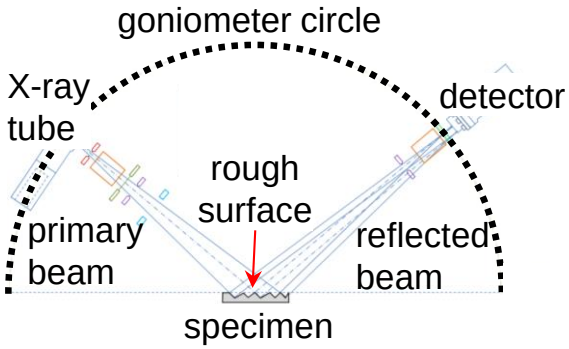

Figure 2-29: 2θ shifting caused by specimen's rough surface (Döbelin, 2013)

ψ splitting

Previously in this subchapter, it was mentioned that the stress determination by x-ray diffraction includes obtaining the lattice plane spacing (2θ angle or strain as well) as a function of sinus square ψ angle, which builds the characteristic linear slope (see Figure 2-27 b)). The determined stress value is based on the calculation of the steepness of this slope with the corresponding standard deviation. In Figure 2-30 are represented different cases of this function. Figure 2-30 a) illustrates the regular case, where the lattice plane spacing has a linear distribution over sinus square ψ angle. Figure 2-30 b) depicts the so-called "ψ splitting", which is characterised by higher lattice plane spacing values for positive ψ angles and vice versa. Such splitting can be an indication of shear stress presented in the material or it can have a geometry origin as well. For example, when measuring in a curvature, tilting the specimen at ψ angle (only when the direction of the ψ tilting corresponds to the curvature direction) will cause the calculated stress value for the positive ψ angles to be higher than this for the negative ψ angles. This can lead to equidistant shifting of the measured values, where the measured tensile stress is shifted towards higher positive value, and the measured compressive stress is shifted in the negative direction towards higher negative value.

Figure 2-30 c) depicts the last case of untypical lattice plane spacing distribution, called oscillating distribution. It indicates the presence of inhomogeneous stress within the material, which is usually a sign of a presence of preferred crystallographic orientation (texture).

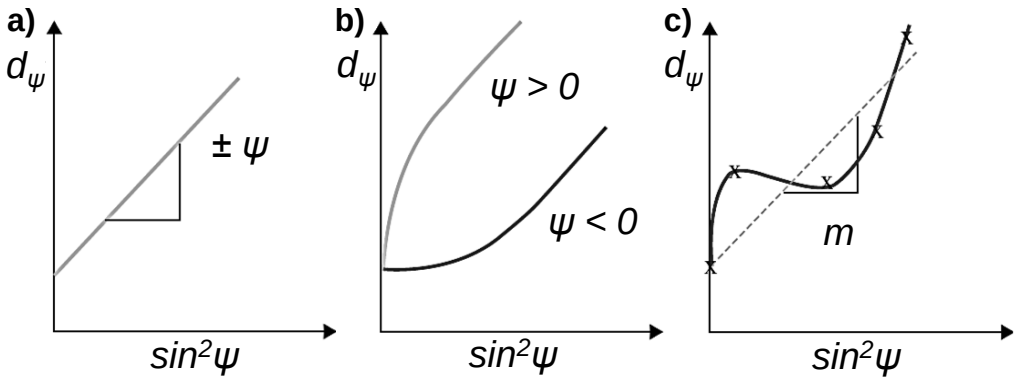

Figure 2-30: Representation of the lattice plane spacing (d_ψ) over sinus square ψ function: a) regular case, b) ψ splitting and c) oscillating lattice plane spacing distribution (Schajer, 2015)

2.4.2 Methods for characterisation of the surface topography and the hardness

In subchapters 2.1 and 2.2 was discussed the importance of the surface topography and the hardness of the material for its fatigue behaviour. Therefore, a part of this thesis, see chapter 8, is focused on the characterisation of the material properties mentioned above. For the experimental characterisation of the surface topography, two kinds of measurement techniques: contact and non-contact are commonly available. The mechanical stylus method is one of the most popular contact methods for measurement of the surface roughness. Figure 2-31 shows the schematic view of this method, where on the left hand side, an example of a measurement object is depicted and a part of the measurement device, called perthometer. The measurement of the surface roughness is performed using a stylus with a defined tip radius. The stylus is brought in contact with the measured surface using a defined force, and then, it is dragged on the surface, thus tracing the surface profile. The disadvantage of this method is the deviation of the traced profile compared to the original one, which deviation results from the radius of the stylus tip (see the right hand side of Figure 2-31). Although, due to its simplicity and reasonable reliability, this method was employed to investigate the surface topography of pre-machined and deep rolled specimens (see subchapter 8.1). More specific information regarding the measurement setup can be found in subchapter 4.4.

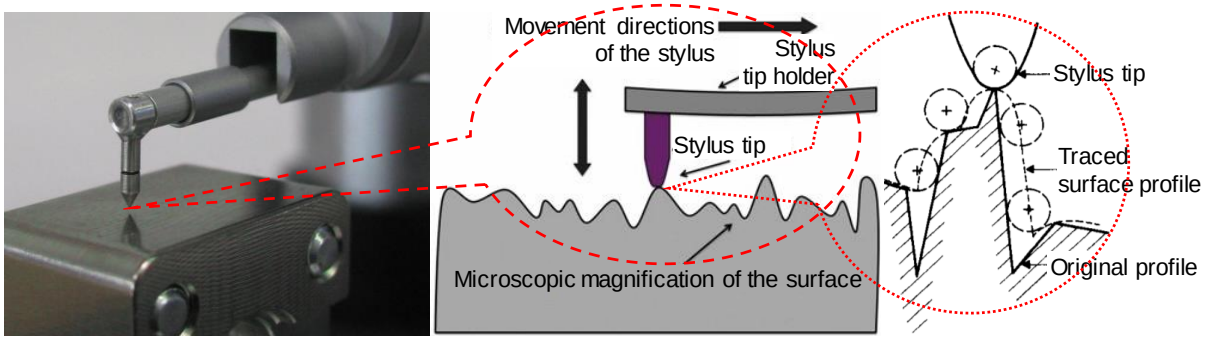

Figure 2-31: Schematic view of the mechanical stylus method

For the characterisation of the material's hardness (defined as the resistance of a solid object against the indentation of another object), several measurement techniques are available. All technical hardness-testing methods are based on the penetration of a sufficiently hard indenter with pre-determined geometric shape into the work piece with a certain force during a specified time. The indenter creates a high local contact pressure to the examined material that causes a multiaxial elastic-plastic deformation. It is assumed that the indenter bears only elastic deformations. As a measure of the hardness is considered either the resulted from the indenter surface projection of the imprint related to the applied test force (Brinell hardness, Vickers hardness), or the depth of the imprint left by the indenter (Rockwell hardness). The different measurement techniques use different material- and shape of the indenter, namely: the Brinell hardness method employs a sintered-carbide spherical indenter, the Vickers method – a diamond pyramid-shaped one and the Rockwell – diamond cone one. For the micro-hardness analysis presented in subchapter 8.2.1, the Vickers method was employed. Detailed information about the method and the measurement setup can be found in subchapter 4.5.

To conclude this chapter, the following can be summarised: the current state of the art regarding the mechanical surface treatments was presented, and their advantages as fatigue enhancers were revealed, especially in the cases, where the material (as type) and the geometry of the treated part are already fully optimised. In general (with some exceptions), the mechanical surface treatments improve the surface integrity by inducing favourable compressive residual stresses on the surface and in depths from several tenths of milimeter to several milimeter. Often, those treatments create a layer of work-hardened material and reduce surface roughness. The presented literature overview focused on one mechanical surface treatment called deep rolling – a treatment, which combines all three features mentioned above for improving surface integrity. Due to its relatively simple operating principle, DR is an established finishing process. Nevertheless, the numerous process variables lead to difficult to predict residual stress state, surface topography and amount of work hardening. In combination with material characteristics, inherited from processes employed at previous stages of the manufacturing chain, the surface integrity generated by DR becomes even more challenging to predict. Therefore, the modelling techniques, especially the finite element analysis, became very attractive in the past decades as a design tool to predict the material changes generated by DR. This thesis presents another endeavour to model the DR process using FEA, but in contrary to the most available researches in this direction, the DR was applied on a flat surface and as single-trace setup, with a goal to represent the basic residual stress state and deformations (uninfluenced by other process parameters) generated by the process. The established FE model was employed for the prediction of the surface- and in depth residual stress distributions, as well as for the investigation of the surface topography and the plastic deformations. The FE model was validated using several experimental researches like residual stress measurements by x-ray diffraction, topography measurements by mechanical stylus method, micro-hardness indentation measurements and x-ray diffraction peak intensity investigations.

3 Objective and scientific approach

The goal of this thesis is to expand the existing knowledge and to contribute to the more comprehensive understanding of the complex interdependencies by deep rolling as a single process, or as part of a process chain. The surface integrity after DR, described by the residual stress state, the surface topography and the cold working, will be investigated by means of experimental work as well as finite element analysis.
This chapter aims to clarify the scientific approach for the modelling and experimental investigations presented in the thesis. It will serve as a guideline regarding the chapter structure and the included studies. The following chapter 4 gives an overview of the experimental setup, including the material data, specimens' preparation (subchapter 4.1.1), material mechanical characterisation (subchapter 4.1.2), the DR setup (subchapter 4.2), the x-ray diffraction setup (subchapter 4.3), the experimental setup for the topography investigations (subchapter 4.4) and the arrangements for the micro-hardness measurements (subchapter 4.5). The FE modelling setup was presented in chapter 5.
Figure 3-1 illustrates schematically the scientific approach, which can be divided into three main stages:

1. Preliminary investigations by finite element modelling (see chapter 6) – include the residual stress investigations by optimising several input variables, mentioned in the figure below.
2. Residual stress analysis by finite element modelling and x-ray diffraction, see chapter 7 – includes residual stress surface and in depth distributions by several process parameter variations. Subchapter 7.1 presents the results obtained by the optimised FE model; subchapter 7.2 proposes a FE model of pre-stressed DR for further exploitation of the process. In subchapter 7.3 is presented a comprehensive experimental investigation of the residual stress state using x-ray diffraction method after different pre-machining states and consecutive DR. Several measurement uncertainties are additionally discussed. Subchapter 7.4 is devoted to the verification of the FE model utilizing x-ray diffraction residual stress determination.
3. The surface topography and the cold working investigations are shown in chapter 8, as FE modelling, x-ray diffraction, mechanical stylus method and indentation hardness techniques are employed. Subchapter 8.1 is focused on the surface topography, where in subchapters 8.1.1 and 8.1.2 the mechanical stylus method is employed to represent the surface roughness and the profile of the DR trace. The FE modelling is also used to represent the profile of the DR trace, see subchapter 8.1.3, and the results are compared to those delivered by the mechanical stylus method. Subchapter 8.2 is devoted to the investigation of the cold working changes due to pre-machining and / or DR. In subchapter 8.2.1 is performed an experimental study of the depth distributions of micro-hardness and indentation modulus of pre-machined and DR specimens utilizing indentation hardness method. The x-ray diffraction peak widths as an indication of the cold working are investigated in subchapter 8.2.2. The FE model is employed

in subchapter 8.2.3 to analyse the plastic strain after DR with variable process parameters.

In chapter 9, the most significant results from chapters 6, 7 and 8 are discussed, and conclusions are drawn. The last chapter 10 summarises the findings of this thesis and gives an outlook.

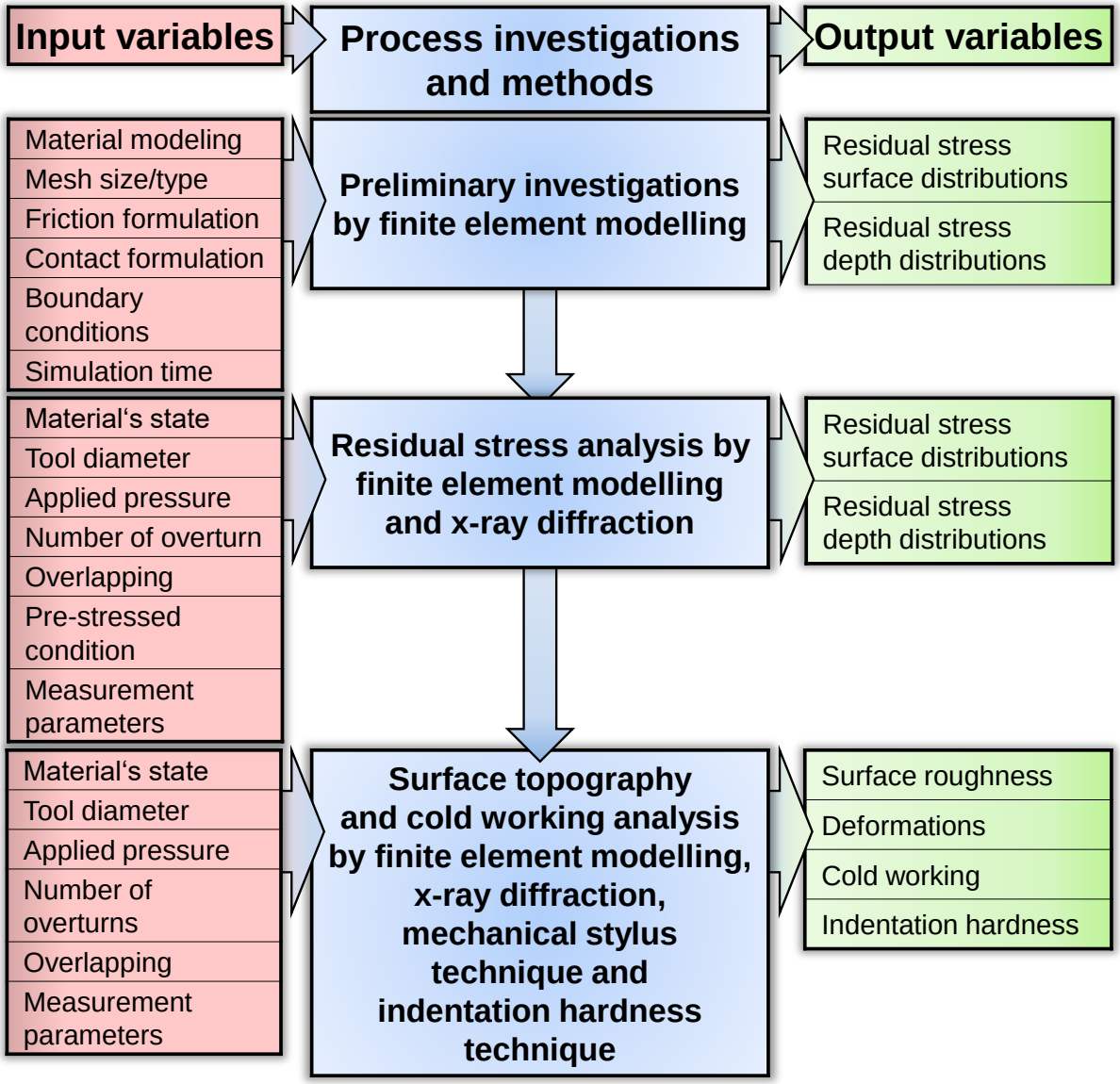

Figure 3-1: Scientific approach

4 Experimental setup

The following chapter aims to clarify the most significant aspects of the designed experimental setup. In the first subchapter 4.1 is described the experimental approach for the characterisation of the used material, in the manner of material data, specimens' preparation and mechanical characterisation. The subchapter 4.2 focuses on the description of the deep rolling process setup and the variation of the process variables, arranged in different process sequences. Subchapter 4.3 illustrates the x-ray diffraction measurement setup, including the specimens' characteristics, the hardware configuration of the two different x-ray diffractometers employed for residual stress measurements and the determination of the full-width-at-half-maximum values shown in subchapters 7.3 and 8.2.2. The corresponding measurement orientations and the measurement and evaluation parameters are also listed. The subchapter 4.4 depicts the setup for the topography characterisation in terms of roughness and DR trace geometry of specimens after different pre-machining and consecutive DR treatment. The results of this characterisation are displayed in subchapter 8.1.
The last subchapter of the experimental setup (see 4.5) describes the micro-hardness measurement procedure for the investigation of the micro-hardness depth profiles in- and out of the trace for milled and consequently DR specimens.

4.1 Characterisation of the used material – mechanical- and chemical data; material mechanical characterisation setup (tensile compressive tests)

4.1.1 Material data and specimens' preparation

The material used in all of the experiments and described in the FE modelling was a high strength martensitic steel of grade AISI 4140 (USA designation) or 42 CrMoS 4 (DIN designation). It is a chromium-molybdenum alloy with increased sulphur percentage for improved machinability. The steel is widely used in the automotive and the aircraft industries due to its high ductility in combination with high strength and good air corrosion resistance.
The material's heat treatment was as follows: austenitised (hardened) at 860 °C for 60 minutes, quenched in polymer and tempered at 560 °C for 120 minutes. In the end, it was cooled down to room temperature in air. To prepare the specimens, square rods of 25 mm x 25 mm were cut to a length of 40 mm, and the top surface on which the DR was later applied was milled with the parameters shown in Table 4-1. The side surfaces were milled to achieve a specimen width of 20 mm. The next part of the process chain was different single-trace DR or DR with overlapping (see chapter 4.2), performed by ECOROLL Company. Some of the specimens were additionally ground (removed layer of minimum 100 µm) and polished after the milling procedure, and lastly deep rolled. This additional procedure was accomplished to reduce the influence of the milling procedure on the residual stress state after DR. The parameters of the corresponding polishing procedure are plotted in Table 4-2.

Table 4-1: Milling parameters

Parameter	Value
Type of milling	Perpendicular face milling
Spindle speed - n	600 rpm
Feed - Vf	100 mm/min
Removed layer	3 x 1 mm + 2 x 0.5 mm
Cooling lubricant	Yes

Table 4-2: Polishing procedure

Parameter	Value
Applied force	25 N
Velocity	150 rpm
Coarse grinding	at least 100 µm removed
Fine grinding	SiC paper: 120; 320; 600 and 1200
Polishing	Polishing cloth Delta + diamond suspension 3 µm; Polishing cloth Zeta + diamond suspension 1 µm;

4.1.2 Mechanical characterisation

Specimens' preparation and test setup

To characterise the mechanical properties of the used material, tensile- and tensile-compressive tests by DIN EN ISO 6892-1 norm were performed at the School of Engineering, HTW Saar in Saarbrücken. The dimensions of the test specimens are depicted in Figure 4-1. To avoid buckling during the compression, shorter, non-standard specimens, see Figure 4-1 a), were used for tensile-compressive tests. The DIN norm mentioned above regulates the gauge length of the test specimens, and the minimal recommended length for this specimen type is 50 mm, therefore the short specimens were designated as non-standard. They were also used for some additional tensile tests, to compare the mechanical data obtained with the short and the long specimens. Additionally, the tests were completed using two test methods differing from the way of controlling the load's velocity. Test type A is strain rate controlled, where the recommended strain rate varies from 0.00007 s^{-1} to 0.002 s^{-1}. Test type B is stress rate controlled, and for materials with Young's modulus over 150 GPa, the recommended stress rate is from 6 to 60 MPa/s. Both test methods can be considered as quasi-static. The machine used for the tests was ZWICK- Z250 RED with a maximal applicable single-axis test force of 25 kN.

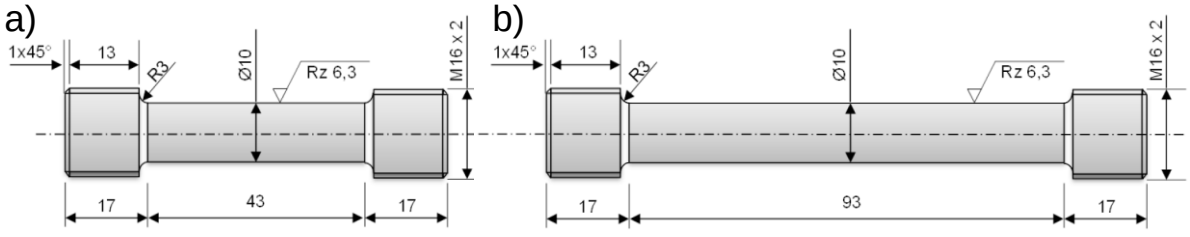

Figure 4-1: a) short, non-standard specimen for tensile and tensile-compressive tests and b) long, standard specimen for tensile tests (Brünnet, 2013)

Test data derivation

During the tests, the resulting force and the elongation of the specimens were measured. The elongation measurement was used to calculate the technical strain **ε_{tech}**, derived as follows:

$$\varepsilon_{tech} = \frac{l - l_0}{l_0} = \frac{\Delta l}{l_0} \qquad \textit{Equation 4-1}$$

where:
l final gauge length,
l_0 – initial gauge length and
Δl – change in gauge length.

The force data was employed to calculate the technical stress, **σ_{tech}**, using the following equation:

$$\sigma_{tech} = \frac{F}{A_0} \qquad \textit{Equation 4-2}$$

where:
F – current force
A_0 – initial gauge cross-section
When implementing the stress-strain data into the FE modelling, the technical strain and stress need to be converted into true strain **ε_{true}** and true stress **σ_{true}**. The difference between the technical and the true stress is that the technical one is related to the initial gauge cross-section and the true one – to the current gauge cross-section. Therefore, in the case of large plastic deformations, significant discrepancies between the technical and the true stress can occur. The technical data can be calculated using the equations Equation 4-3 and Equation 4-4 only when assuming incompressible material's plasticity, and in case the plastic deformation is significantly larger than the elastic one. The following procedure was employed to convert the technical into true data:
1. The true strain **ε_{true}** was calculated with the following equation:

$$\varepsilon_{true} = ln(1 + \varepsilon_{tech}) \qquad \textit{Equation 4-3}$$

2. The true stress **σ_{true}** was derived as follows:

$$\sigma_{true} = \sigma_{tech}(1 + \varepsilon_{tech}) \qquad \textit{Equation 4-4}$$

3. The Young's modulus **E** was calculated:

$$E = \frac{\sigma_{true,Yield}}{\varepsilon_{true,Yield}} \qquad \textit{Equation 4-5}$$

where:
$\sigma_{true,Yield}$ is the calculated true stress at the yield point
$\varepsilon_{true,Yield}$ is the calculated true strain at the yield point.

4. The technical stress-strain data were converted into true stress-strain data.
5. The true plastic strain was subtracted from the true total strain, as in ABAQUS CAE only the plastic data is needed. The true total strain at the yield point is equivalent to the true elastic strain, and the true plastic strain at this point is zero.

In Figure 4-2 is plotted schematically, the difference in the stress-strain plots when using the technical versus the true material data. One can notice that up to the yield point, the curve's evolution remains the same, following by a slightly higher true data up to the ultimate strength. The true data is calculated up to the technical ultimate strength. Simulation codes usually assume that the material is perfectly plastic after this point (i.e. the strain will continue to increase without an increase in stress). This is valid only in case no fracture is defined.

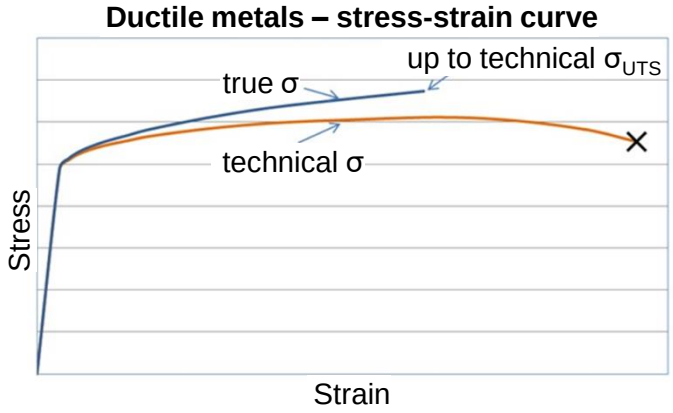

Figure 4-2: Technical vs true stress-strain plots (CAE Associates, 2013)

Tensile tests

The tensile tests were accomplished with short (43 mm gauge length) and long (93 mm gauge length) specimens, by variation of the test method (A and B). In Figure 4-3 are plotted the stress-strain curves for all of the variations made and in Table 4-3 the corresponding mechanical data.

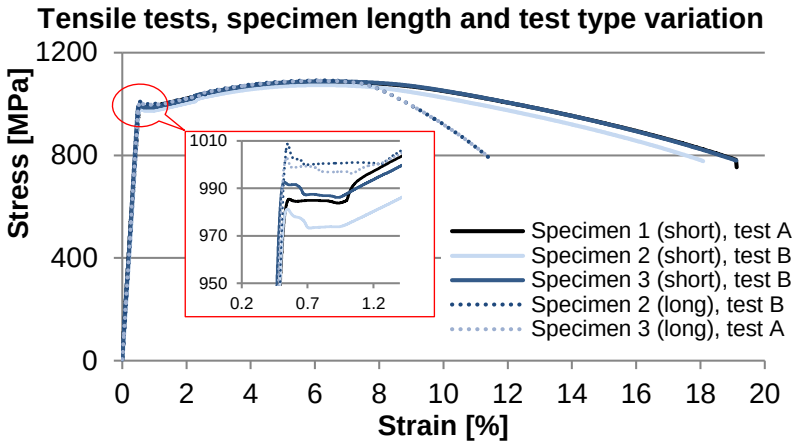

Figure 4-3: Tensile tests – stress-strain curves by variation of the specimen's length (short = 43 mm and long = 93 mm, and the test type (A – strain rate controlled and B – stress rate controlled)

After reaching the elastic-plastic limit, all of the tested specimens exhibit almost an ideal plastic behaviour up to a strain of 1.0 %, with a pronounced upper (**REH**) and lower (**REL**) yield strength. The Young's modulus's **E** is about 198 GPa and no particular tendency between the values for the different specimen's length or the test method can be observed. The yield strength for the long specimens is only about 2 % higher than this of the short specimens. The tensile strength $\mathbf{R_m}$ of ca. 1086 MPa is also randomly distributed, without signs of tendency. The main difference between the measured values is in the fracture strain, $\mathbf{A_{35}}$/$\mathbf{A_{85}}$ ($\mathbf{A_{35}}$ – short specimens; $\mathbf{A_{85}}$ – long specimens). This can be expected, as the necking length is the same for both specimens' lengths but the strain, increases for the longer gauge length, as it is referred to the initial gauge length.

Table 4-3: Tensile tests - mechanical properties of AISI 4140 by variation of the specimen's length (short = 43 mm and long = 93 mm, and the test type (A – strain rate controlled and B – stress rate controlled)

	E (GPa)	**R_{EH} (MPa)**	**R_{EL} (MPa)**	**A_E (%)**	**R_m (MPa)**	**A_g (%)**	**A_{35}/A_{85} (%)**
Specimen 1 (short), test A	198	985	984	0.43	1085	5.80	18.76
Specimen 2 (short), test B	192	981	973	0.50	1074	5.62	17.68
Specimen 3 (short), test B	201	993	986	0.43	1088	5.78	18.73
Specimen 2 (long), test B	197	1009	1000	0.71	1092	5.58	11.07
Specimen 3 (long), test A	200	1003	996	0.50	1090	5.45	10.96

Tensile-compressive tests

To investigate if and at which amount the material exhibits Bauschinger effect (see chapter 2.1.4) tensile-compressive tests were performed by variation of the strain as a reversal point. In Figure 4-4 are depicted the corresponding stress-strain curves. Here, the specimen's length was fixed to 43 mm (short) to avoid buckling and the test method applied was strain-controlled (test A) in the tensile area and stress-controlled (test B) in the compression area. The reverse strain values were chosen based on the strain by the yield strength $\mathbf{A_E}$ and the strain by the tensile strength $\mathbf{A_g}$. Therefore, the lowest reversal strain selected was 1 % (well above the measured $\mathbf{A_E}$ values), and the highest reversal strain was 5.5 %, which corresponded almost to the $\mathbf{A_g}$ value, where it was expected the material to exhibit the strongest Bauschinger effect. From the accomplished tests, the Bauschinger factor (BF) as the ratio between the yield strength under tension and compression can be derived. The BF is material dependent and sensitive to the initial strain amount. It has values typically between 0.3 and 1 (Huang, 2005), where 1 means the material does not exhibit Bauschinger effect and the reducing BF value describes increasing Bauschinger effect. In Figure 4-4 (the top right corner), the BF is plotted versus the reverse strain values. It is visible that higher strain causes quadratic potentially decreasing of the BF, which reaches at strain close to $\mathbf{A_E}$, the value of an app. 0.65. Based on the typical values for the BF (Huang, 2005), it can be concluded that the tested material does not exhibit a very strong Bauschinger effect. Nevertheless, at high strain (near the A_g value), the reduction of the yield strength by reverse compression of up to 30 % should not be neglected.

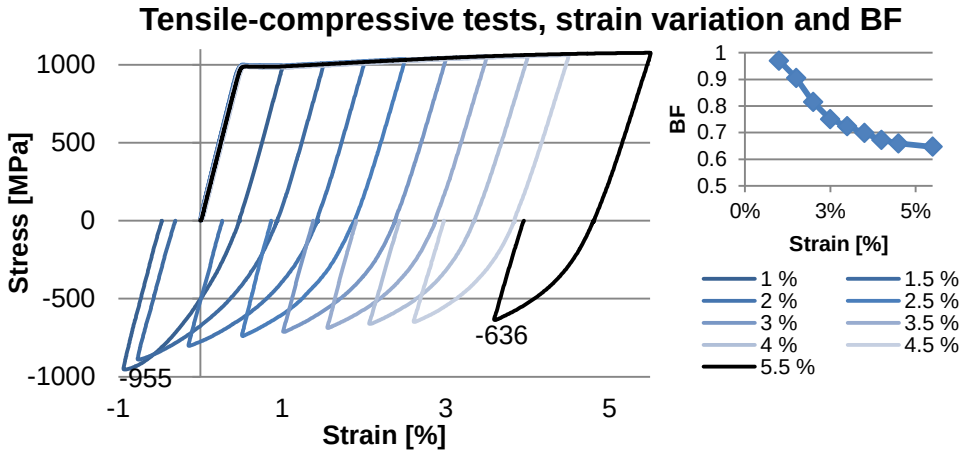

Figure 4-4: Stress-strain curves of the tensile-compressive tests by variation of the strain and BF dependent on the strain

4.2 Experimental deep rolling setup and process chains

The tools used for the deep rolling were ECOROLL HG6 with a diameter of 6.35 mm or HG3 with a diameter of 3.175 mm. Both are equipped with hydrostatically pressurised roller burnishing sphere, which allows the tip of the tool to move freely in the axial direction and the sphere to rotate freely in all directions. The treatment was realised with low viscosity oil. The DR pressure, supplied by a hydraulic aggregate, was kept constant during the treatment and it could not exceed 400 bar with the currently used device. An exemplary scheme of such DR tool is plotted in Figure 4-5.

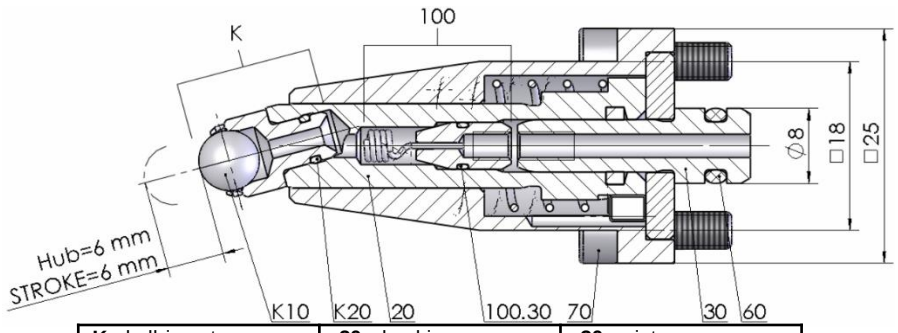

K - ball insert	**20** - bushing	**30** - piston
K10 - hydrostatic ball	**100.30** - O-ring	**60** - O-ring
K20 - O-ring	**100** - throttle	**70** - allen screws

Figure 4-5: Scheme of DR tool type HG 6 (Ecoroll GmbH, 2010)

The work piece was mounted on a milling vice, fixed from both long sides (see Figure 4-6) and the DR treatment was done in -y, +x and +y directions.

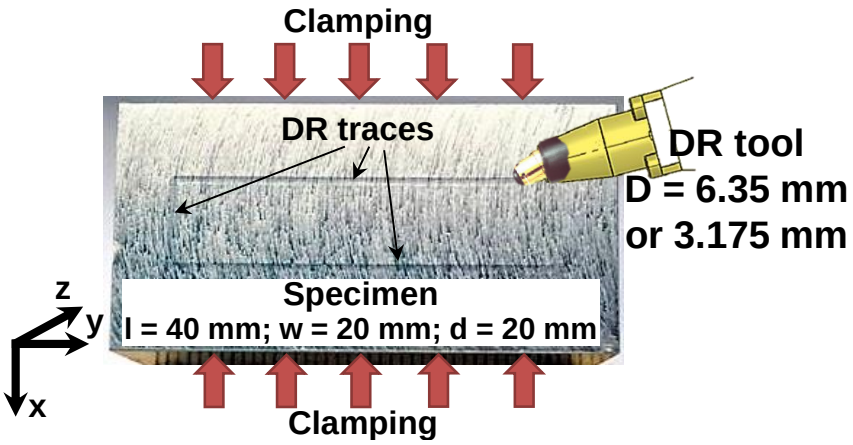

Figure 4-6: Exemplary picture of the DR setup and the specimen's fixture

For the experimental investigations, described in subchapter 7.3 and chapter 8, several process chains were designed, by variation of the specimens' pre-machining state (see chapter 4.1.1, Table 4-1 and Table 4-2) and the DR process parameters.
The specimens used for the x-ray diffraction measurements (see subchapter 7.3 and subchapter 8.2.2) were treated with a DR tool of diameter 6.35 mm. The pre-machining sequence was either milling (specimens designated with M) or milling and polishing (designation P). After that, the DR parameters were varied, as shown in Table 4-4. Important to note is the choice of the DR pressure as a process parameter which mostly influences the final residual stress state. For the used material, the process pressure from 20 MPa to 40 MPa can be considered as a low to high range. The further increase of the DR pressure should not lead to greater change in the residual stress state due to the reached saturation level. In all tables describing the process chain design, with yellow is marked the varied parameter.

Table 4-4: Specimens' process chain design for x-ray diffraction measurements

Specimen No (milled + DR)	Specimen No (milled + polished + DR)	Process parameters		
		DR pressure	Overturn (o.t.)	Overlapping (o.l.)
M12	P11	20 MPa	1	0 %
M15	P8	40 MPa	1	0 %
M18	-	40 MPa	5	0 %
M19	P4	40 MPa	7	0 %
M22	P2	40 MPa	1	75 %

For the roughness and the topography investigations (see subchapter 8.1.1 and 8.1.2), specimens treated with DR tool of diameters 3.00 mm or 6.35 mm were used in a pre-machined condition "milled". The process chains resulted from the variation of the DR tool diameter, and the DR process parameters are listed in Table 4-5. The specimens' designation D3 or D6 means DR treatment with tool HG3 (3.00 mm) or HG6 (6.35 mm).

Table 4-5: Specimens' process chain design with DR tool HG3 (milled condition) for roughness and topography measurements

Specimen No (tool HG3)	Specimen No (tool HG6)	Pre-machining	Process parameters		
			DR pressure	Overturn	Overlapping
D3M12	D6M12	milling	20 MPa	1	0 %
D3M13	D6M13	milling	25 MPa	1	0 %
D3M14	D6M14	milling	32 MPa	1	0 %
D3M15	D6M15	milling	40 MPa	1	0 %
D3M16	D6M16	milling	40 MPa	2	0 %
D3M17	D6M17	milling	40 MPa	3	0 %
D3M18	D6M18	milling	40 MPa	5	0 %
D3M19	D6M19	milling	40 MPa	7	0 %
D3M20	D6M20	milling	40 MPa	1	25 %
D3M21	D6M21	milling	40 MPa	1	50 %
D3M22	D6M22	milling	40 MPa	1	75 %

Additionally, an analysis of the roughness of some specimens (see chapter 8.1.1) in the pre-machined condition milled + polished was accomplished, where the applied DR tool was HG6 and the process parameters were varied according to Table 4-6.

Table 4-6: Specimens' process chain design with DR tool HG6 (milled + polished condition) for roughness measurements

Specimen No	Pre-machining	DR tool	Process parameters		
			DR pressure	Overturn	Overlapping
P11	milling + polishing	HG6	20 MPa	1	0 %
P9	milling + polishing	HG6	25 MPa	1	0 %
P8	milling + polishing	HG6	40 MPa	1	0 %
P4	milling + polishing	HG6	40 MPa	7	0 %
P2	milling + polishing	HG6	40 MPa	1	75 %

The micro-hardness investigation, shown in chapter 8.2.1, was obtained on the milled specimens, with a DR tool HG 6, with the parameter variables plotted in Table 4-7.

Table 4-7: Specimens' process chain design with DR tool HG6 (milled condition) for micro-hardness measurements

Specimen No	Pre-machining	DR tool	Process parameters		
			DR pressure	Overturn	Overlapping
D6M12	milling	HG6	20 MPa	1	0 %
D6M15	milling	HG6	40 MPa	1	0 %
D6M19	milling	HG6	40 MPa	7	0 %
D6M22	milling	HG6	40 MPa	1	75 %

4.3 X-ray diffraction experimental setup

The x-ray diffraction measurements were performed in two laboratories: at the Chair of Functional Materials, Saarland University, where a diffractometer PANalytical Empyrean was available and at the Department of Materials Science and Materials Testing, University of Applied Sciences in Kaiserslautern, where a diffractometer Seifert,

XRD 3000 PTS was currently in use. These independent measurements were accomplished to compare the measurement parameters- and the accuracy influences when using different measurement devices.
Some of the specimens treated under the process chain “milling + DR” were measured on the surface using the PANalytical Empyrean diffractometer and after that using the Seifert, XRD 3000 PTS. This allowed comparing the surface residual stress determined by both devices. The specimens treated under both process chains (“milling + DR” or “milling + polishing + DR”) were measured in depth with diffractometer Seifert, XRD 3000 PTS which allowed investigating the pre-processing and DR influence by constant measurement conditions.

4.3.1 Specimen geometry and measurement directions

The geometry and the material state of the specimens used for the x-ray diffraction measurements are described in chapter 4.1.1. Here, the material state after two different process chains was investigated. The first process chain consisted of pre-machining (milling) and consecutive deep rolling. Some of the specimens with this treatment were measured only on the surface with the diffractometer PANalytical Empyrean. The same specimens were consequently measured on the surface and in depth with diffractometer Seifert, XRD 3000 PTS. This allowed comparing the surface measurements determined with both measurement devices. The exact experimental design with the specimens’ designation can be found in chapter 4.2. The measurement directions and the measurement points used for the surface measurements with the diffractometer PANalytical Empyrean, are plotted in Figure 4-7.

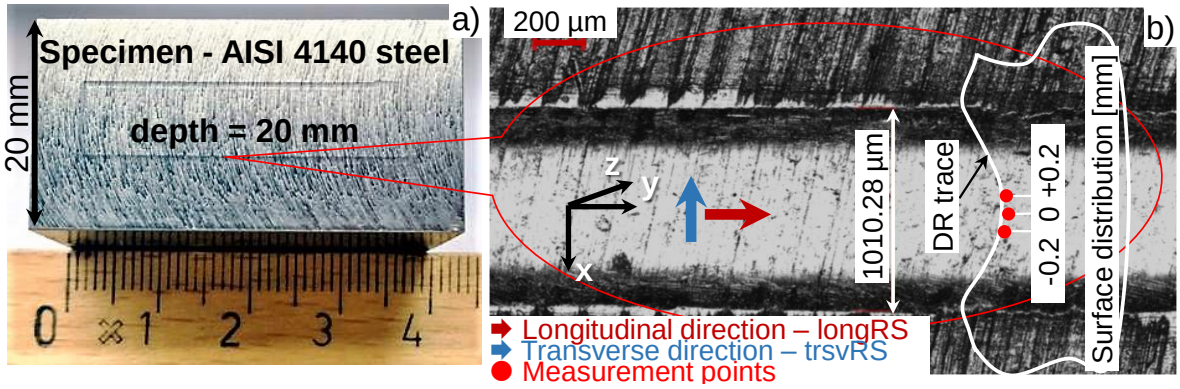

Figure 4-7: a) specimen’s geometry and material designation and b) microscope image of the DR trace and measurement directions for diffractometer PANalytical

The second process chain consisted of pre-machining: milling, (see Table 4-1), polishing, (see Table 4-2), and deep rolling. Here, the diffractometer Seifert, XRD 3000 PTS was employed, and measurements on the surface and in depth were accomplished. The experimental design is described in chapter 4.2 and the measurement directions- and the surface path is depicted in Figure 4-8.

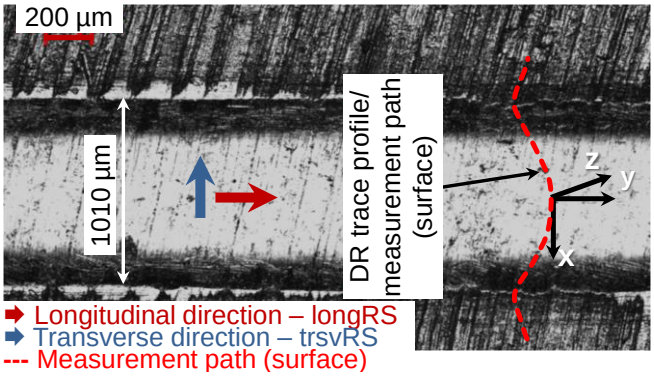

Figure 4-8: Microscope image of the DR trace and measurement directions for diffractometer Seifert

The distance between the surface measurement points in the DR trace was 100 µm to 200 µm and out of the DR trace – 500 µm to 1000 µm. The surface measurement path was assigned transverse to the DR trace, i.e. in ± x direction and with 0 was designated the center of the trace. The residual stress depth profiles were obtained in the center of the DR trace, in +z direction through successive layer removal with electropolishing. The shape of the removed layer was square (10 mm x 10 mm) and thickness of the removed layers was variable: 10 µm, 25 µm and 50 µm for a depth up to 625 µm and increased to 250 µm - 500 µm for a depth up to 1500 µm.
It is well known that the successive layer removal leads to a redistribution of the residual stress field and eliminates the residual stresses located in the removed layer. Therefore, the mathematical formulations of Moore and Evans for the correction of stress in removed layers (Moore, et al., 1958) were used. Their formulations are widely spread, and their correction method is recommended in the SAE HS-784 2003 (residual stress measurement by X-ray diffraction) standard. The residual stresses determined in longitudinal and in transverse direction were corrected as follows:

$$\sigma(z_1) = \sigma_m(z_1) + 2\int_{z_1}^{H}\frac{\sigma_m(z)}{z}dz - 6z_1\int_{z_1}^{H}\frac{\sigma_m(z)}{z^2}dz \qquad \textit{Equation 4-6}$$

where:
σ - corrected stress,
σ_m - measured stress,
H – nominal thickness of the specimen,
z - current thickness of the specimen,
z_1 – current distance from the surface
Even widely used, the formulations mentioned above need to be applied with attention, as they cannot accurately correct the determined stresses due to several reasons. The corrections are meant to back-calculate the residual stress removed with the material, but they are not able to predict the residual stress redistribution and relaxation due to the removed material. Very often under real conditions, the removed layer is not the complete surface but just a small portion of the whole surface. Thus, at the edges of the removed layer appears a notch effect, creating artificial stress gradients and additional stress redistribution. The formulations of Moore and Evans cannot deal with this

issue, as they do not consider the shape of the removed layer but just its thickness. In (Surtee, et al., 2017) was investigated the influence of the removed layer shape on the corrected residual stress and it was found that the percentual redistribution by square-shaped layer was significantly higher than the redistribution in case of a strip-shaped layer. Wasniewski et al. (Wasniewski, et al., 2014) compared different correction formulations as measuring the stresses in a three-point bending test. They found that the corrections of Moore and Evans deliver the nearest to the theoretical stress profile values. Nevertheless, when varying the shape of the removed layer, the corrected stress profiles using the formulations of (PedersenaI, et al., 1989) showed at higher depth a discrepancy of up to 30 % compared to the theoretical stress profile.
Lastly, yet importantly, the Moore and Evans formulations consider the stresses in the different directions to be independent; means the stress relaxation and redistribution in one direction can be only affected by previous stresses removed in the same direction. In subchapter 7.3., the residual stress correction due to layer removal redistribution will be investigated more detailed.

4.3.2 X-ray surface residual stress measurements with PANalytical Empyrean

The residual stress surface measurements from chapter 7.3.1 were obtained at the Chair of Functional Materials, Saarland University with a diffractometer PANalytical Empyrean in θ-θ configuration. The measurement parameters are plotted in Table 4-8. To ensure the accuracy and the reproducibility of the measurements, several disturbing factors were considered. First, the accurate in-plane positioning of the specimen was provided as adjusting the device's alignment camera. The adjustment was crucial due to the available stress gradients in the direction transverse to the DR trace. On the PANalytical diffractometer, it was accomplished by longitudinal and transverse scanning of a 130 µm thin plate and analysing the measured diffraction peak intensity. The resulted from the scanning Gaussian shaped curve of the intensity was used to align the peak of the curve with the center of the specimen (it was assumed the specimen was symmetrical). The difference between the position of the alignment camera and the position of the intensity peak was considered as an alignment error and hence corrected. With this adjustment, a positioning accuracy of ± 50 µm was achieved. Another disturbing factor considered was the adjustment of the specimen in the vertical (z) direction to ensure that it was positioned in the center of the goniometer's circle. With the available measurement gauge, the exact vertical positioning for measurements in the trace was not possible. Therefore, white light interferometry (WLI) was used to measure the DR trace depth profile, and the vertical positioning was accordingly corrected.
One diffractometer's feature needs to be considered, and this is the ability of the specimen's manipulator to tilt only in positive ψ angles. This limitation will not influence the measured values only in case the 2θ over $\sin^2\psi$ distribution is linear. When measuring in a curvature (i.e. the DR trace), there is a geometrical ψ splitting (Hoffmann, 1984) which cause the calculated stress value for the positive ψ angles to be higher than this for the negative ψ angles. This can lead to equidistant shifting of the measured values, where the measured tensile stress will be shifted in the positive direction to a higher

positive value and the measured compressive stress will be shifted in the negative direction to a higher negative value.

Table 4-8: X-ray diffraction setup - PANalytical Empyrean

Hardware data:	
Detector	Proportional counter
Radiation	Cr-K_a
K_b-Filter	Vanadium
Primary slit	Polycapillary glass mini-lens
Primary beam diameter (focused)	0.05 mm (manufacturer's data)
Measurement parameters:	
Measured lattice plane	{211}
Diffraction angle $2\theta_0$	156.5 °
Measurement range 2θ	151.7 ° to 161.3 °
Measurement time (per ψ)	390 sec
Number of ψ tiltings	7 equidistant, 0 - 50 °, with $\sin^2 y$
Measurement directions φ	Longitudinal (0 °), Transversal (90°)
Oscillation around φ axis	none
Evaluation parameters:	
Evaluation software	PANalytical Stress
Evaluation method	$\sin^2\psi$
Elasticity constant $s_1^{\{211\}}$	-1.36 x10^{-6} mm²/N
Elasticity constant ½ $s_2^{\{211\}}$	6.10 x10^{-6} mm²/N
Peak positioning	Center of gravity 20 %

4.3.3 X-ray surface and depth residual stress measurements with Seifert XRD 3000 PTS

The residual stress surface and depth measurements of the milled + DR and the milled + polished + DR specimens, as well as FWHM values (see chapters 7.3.3, 7.3.4 and 8.2.3), were determined at the Department of materials science and materials testing at the University of Applied Sciences in Kaiserslautern, with the means of x-ray diffractometer Seifert, XRD 3000 PTS. The corresponding hardware features, measurement and evaluation parameters are plotted in Table 4-9, and the diffractometer's configuration is depicted in Figure 4-9.

Table 4-9: X-ray diffraction setup - Seifert, XRD 3000 PTS

Hardware data	
Diffractometer	Seifert, XRD 3000 PTS, Goniometer TS-4, ψ-type
Detector	Meteor 1D, 2011
Radiation	Cr-K_a
K_b Filter	Vanadium
Primary slit	Polycapillary mini-lens, 2016
Primary beam diameter (focused)	0.05 mm (manufacturer's data); 0.1 mm own measurement
Measurement parameters	
Measured lattice plane	{211}
Diffraction angle $2\theta_0$	156.084 °
Measurement range 2θ	147 ° to 159.5 ° or 141 ° to 161 °
Measurement time (per ψ)	120 sec
Number of ψ tiltings	27 equidistant, ± 50 °, with $\sin^2\psi$
Measurement directions φ	Longitudinal (0 °, 180 °), Transversal (90 °, 270 °)
Oscillation around φ axis	± 5 °
Evaluation parameters	
Evaluation software	Analyze (up-date 2017)
Evaluation method	$\sin^2\psi$
Elasticity constant ½ $s_2^{\{211\}}$	5.81 x10^{-6} mm²/N
Young's modulus	$E^{\{211\}}$ = 220000 MPa
Poisson's ratio	$\nu^{\{211\}}$ = 0.28
Peak positioning	Center of gravity 70 %

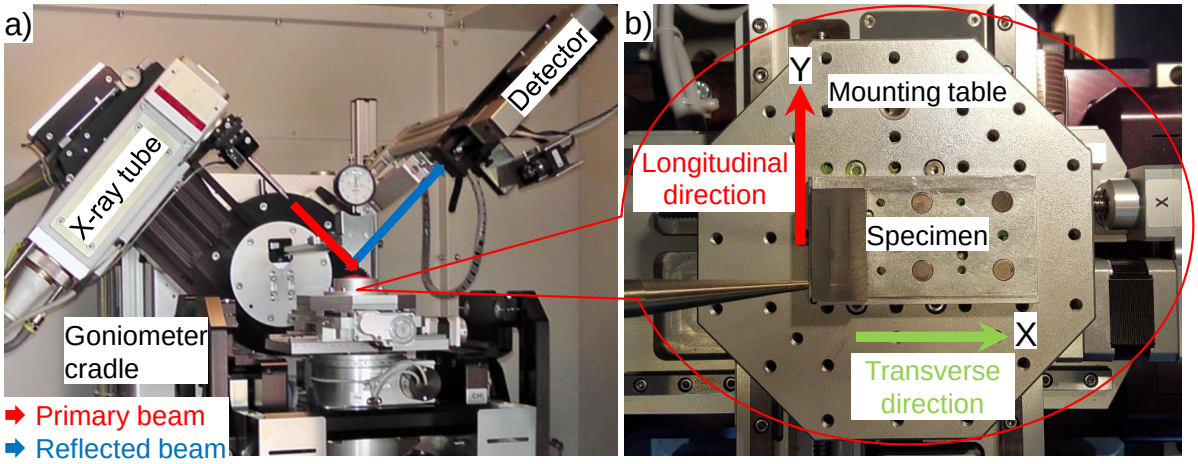

Figure 4-9: X-ray diffractometer Seifert, XRD 3000 PTS: a) general view and b) closer view and measurement directions

For these measurements, several precautions were taken to ensure accurate and reproducible results. The in-plane measuring position on the specimen's surface was set with the positioning camera. To improve the positioning accuracy, the crosshair of the camera needed to be precisely adjusted in the center of the goniometer's circle. This was accomplished by using a sample with adhered fluorescent paper with a marking point on it. When rotating the sample around the z-axis, the deviation of the crosshair's

position in x-y direction was visible as a movement of the sample's marking point. The deviation was corrected until the position of the crosshair aligned with the center of the goniometer's circle. Afterwards, the position of the x-ray beam was also checked and precisely adjusted with the aid of the adjusted camera crosshair image on the fluorescent paper with the marking point.
The vertical (z) positioning in the DR trace was done with the available measurement gauge equipped with a sharp tip. The exact in-plane position of the measuring gauge tip was ensured by producing an imprint with the tip. The imprint was compared with the current coordinates of the positioning camera and the difference between the current coordinates, and those of the imprint was then corrected. After that, the specimen's height adjustment was obtained. The measurement points were defined at 300 µm far from the place where the gauge's tip touched the specimen's surface to avoid misleading stress values due to possible plastic deformation of the touched area.
The absolute height adjustment of the specimen's manipulator was additionally controlled by determining the stress in iron powder. This is a standard control/adjustment procedure, intending to determine no residual stresses, as in powder state, no residual stresses can exist between the iron grains.
In contrary to the PANalytical Empyrean diffractometer, the specimen's manipulator of Seifert XRD 3000 PTS can tilt in positive and in negative ψ angles, thus eliminating the possible positive shifting of the measured values due to the geometrical ψ splitting discussed in chapter 4.3.2.
When comparing the parameters listed in Table 4-8 and in Table 4-9, it is visible that the hardware features are similar for both devices, except the ψ tilting degree of freedom and the primary beam diameter. The primary beam diameter for both diffractometers (focused in the center of the goniometer's circle and related to the FWHM of the diffraction peak) was specified from the manufacturer to 50 µm. A control measurement on the Seifert diffractometer showed the beam diameter of 100 µm but related to the complete width of the diffraction peak. No comparable data for the beam diameter of the PANalytical diffractometer was available, so a direct comparison of both beam sizes cannot be made. Nevertheless, it should be noted that a greater beam diameter means that in a larger area, the determined stresses are averaged.
The measurement parameters are also comparable, and they were defined considering several criteria. E.g., achieving a reasonable intensity of the reflection peak for adequate exposure time; ensuring good statistical reliability with means of decent ψ tiltings and using oscillation during the measurement (only on Seifert XRD 3000 PTS); applying the narrowest 2θ measuring range, without cutting the reflection peak, thus reducing the measurement time additionally. The evaluation parameters are also similar, as for both devices were used the parameters' configuration "by default".
The influence of Young's modulus on the determined residual stress values can be considered based on the Hooke's law, which states that the stress is linearly proportional to the strain by the Young's modulus. As the x-ray diffraction determines residual stresses by measuring strains, the difference of the determined stress value when changing the Young's modulus can be calculated. E.g., if the stress value is 1000 MPa at Young's modulus 210 GPa, increasing the Young's modulus to 220 GPa will shift the stress value to 1047 MPa. This discrepancy can be considered as minor.

4.4 Topography measurement setup

To characterise the surface topography after different pre-machining (milling or milling + polishing) and consecutive deep rolling, roughness- and DR trace geometry measurements were obtained.
The roughness measurements were done using a mechanical stylus method and were performed on Taylor Hobson perthometer at the Department of materials science and materials testing, University of Applied Sciences in Kaiserslautern as well as at the Institute of Production Engineering, Saarland University. An exemplary picture and principle setup of such method are illustrated in Figure 4-10. Its principle can be described as follows: a stylus holds a small measurement tip that is pulled horizontally across the surface of the object. As the tip follows the surface (roughness) profile, the cantilever moves vertically. The current vertical position is recorded and depicted in the figure below as red profile.

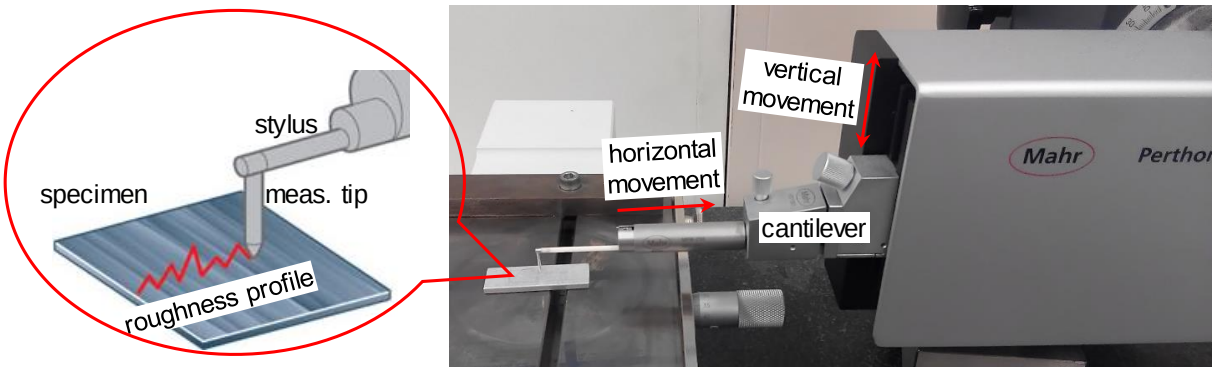

Figure 4-10: Principle setup of mechanical stylus method

The roughness measurements shown in this subchapter were divided into: out of the DR trace - to investigative the milling and polishing influences and in the DR trace - to investigate the DR influence. The orientations and directions for the in-trace roughness measurements are plotted in Figure 4-11.

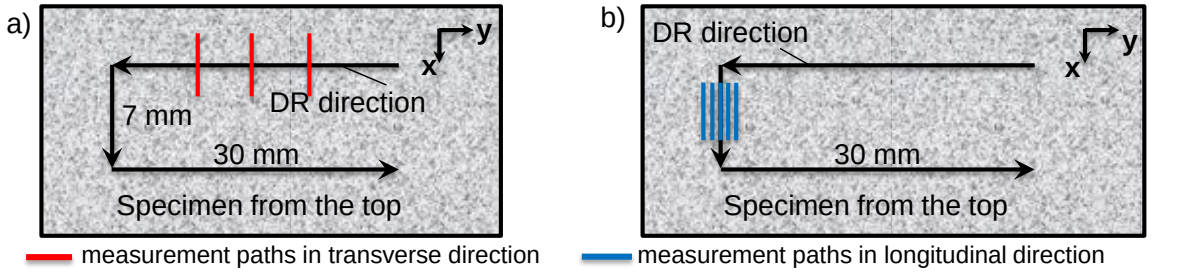

measurement paths in transverse direction
Distance between the measurement paths = 5 mm
Measurement path length = 2 mm

measurement paths in longitudinal direction
Distance between the measurement paths = 0.1 mm
Measurement path length – variable according DIN 4287

Figure 4-11: Measurement setup for roughness and DR trace profile shape investigations

The length of the measurement paths was fixed to 2 mm in the transverse direction. In the longitudinal direction, the sampling length varied from 0.08 mm to 0.80 mm, see Table 4-10, according to DIN EN ISO 8785 norm. In the transverse direction, due to the curved surface, the proper selection of the sampling length is important because

the sampling length defines the length of the primary filter effectivity and therefore, can influence the measured values.

Table 4-10: Classification of the sampling- and the evaluation lengths for roughness measurements depending on the expected roughness values by DIN EN ISO 8785

Rz [µm]	**Ra [µm]**	**Cut-off λc [mm]**	**Sampling length [mm]**	**Evaluation length [mm]**
Up to 0.1	< 0.02	0.08	0.08	0.40
> 0.1 – 0.5	> 0.02 – 0.10	0.25	0.25	1.25
> 0.5 – 10.0	> 0.1 – 20	0.80	0.80	4.00
> 10.0 – 50.0	> 2.00 – 10.00	2.50	2.50	12.50
> 50.0	> 10.00	8.00	8.00	40.00

The topography measurements of the DR trace's width and depth were obtained with Taylor Hobson perthometer at the Institute of Production Engineering, Saarland University. Here, the cut-off length, the sampling length and the evaluation length were not chosen according to the DIN EN ISO 8785 norm. The measurement path length was tailored to fit the maximal DR trace width, and the resulted measurement profiles were manually evaluated. The measurement setup was the same as the one shown in Figure 4-11.
Additionally, White Light Interferometry topography measurements of the trace's width and depth were done at the Institute of Functional Materials, Saarland University. As both techniques showed very similar values, in chapter 8.1 are shown only the results obtained by the tactile device.

4.5 Micro-hardness measurements

For the characterisation of the micro-hardness depth distributions of the milled + DR specimens, indentation micro-hardness measurements were accomplished with a Fischerscope HM2000 device at the Department of materials science and materials testing, University of Applied Sciences in Kaiserslautern. The specimens were cut perpendicular to the DR trace and consecutively polished, thus allowing the full specimen's cross-section to be investigated. An exemplary microscopy picture of the cross-section with the imprints resulted from the measurements is depicted in Figure 4-12. Here, with x direction is described the direction transverse to the DR trace and with z – the depth from the surface. The origin of the coordinate system is in the middle of the DR trace, on the top surface. In the figure are plotted five measurement paths in depth, where the distance between the measurement points was 0.025 mm in depth up to 0.175 mm, 0.050 mm in depth up to 0.625 mm and 0.200 – 0.250 mm in depth up to 1.500 mm. The smallest measurement points' distance was calculated according to BS EN ISO 14577 norm (DIN 14577, 2015). In the results plotted in chapter 8.2.1, paths consisted of the mean values of the three measurement paths in the middle of the DR trace were compared for the different DR treatments. Both measurements paths out of the DR trace were positioned on the places, where the highest compressive residual stresses on the surface were measured (see chapter 7.3.3), aiming to

investigate the possible micro-hardness changes due to the high compressive residual stresses presented in this area. As the position of this compressive residual stress maximum varied for the specimens treated with different DR process parameters, the position of these two measurement paths was explicitly defined for every single specimen. However, both paths were always symmetrically positioned to the middle of the DR trace. In the results shown in chapter 8.2.1, the values of both paths were averaged.

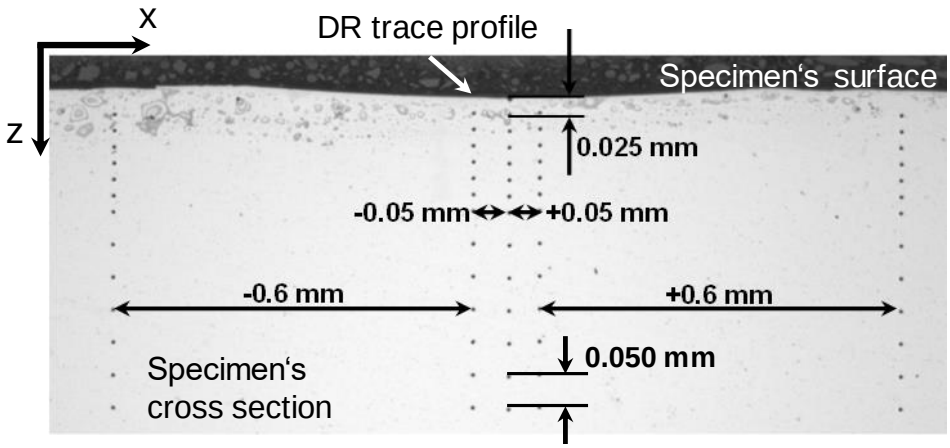

Figure 4-12: Exemplary microscopic picture of the micro hardness measurements

In general, the employed for these investigations indentation hardness can be described as the resistance of a material to penetration with a defined force **F** of another, harder material (DIN 14577, 2015). The calculation of the indentation hardness takes place based on the dimensions of the resulted imprint and the applied force. A schematic representation of the force **F** – displacement **h** curve during loading and unloading by a hardness test is plotted in Figure 4-13 a).

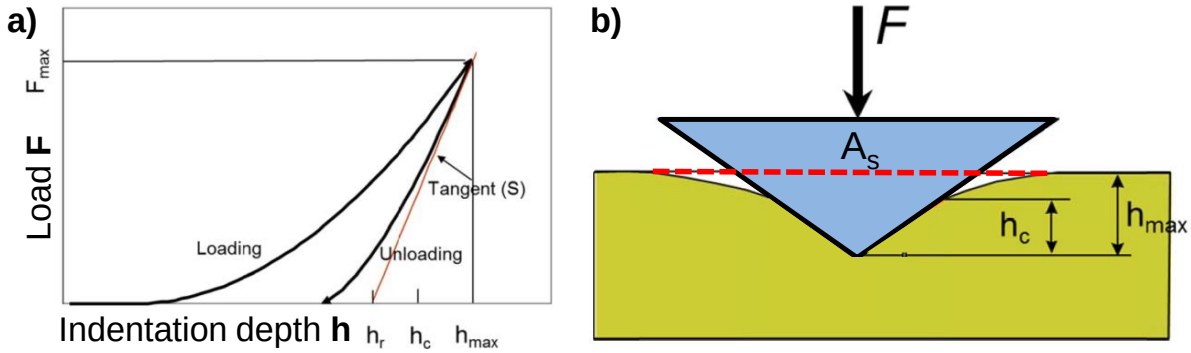

Figure 4-13: a) typical force-displacement curve showing measured and derived parameters and b) scheme of indentation showing the displacements observed during testing

The displacement of the indenter **h**, which describes the indentation depth, is depicted throughout the testing cycle, and this allows measuring the elastic-plastic deformation in the test specimen. Apart from the indentation depth, the indentation modulus $\mathbf{E_{IT}}$ can be calculated from the slope of the unloading curve as follows:

$$E_{IT} = (1 - \vartheta_{IT}^2) / \left(\frac{2}{\sqrt{\pi}} \frac{\sqrt{A_{hc}}}{S} - \frac{1 - \vartheta_{indenter}^2}{E_{indenter}} \right) \qquad \textit{Equation 4-7}$$

where:
ν_{IT} – Poisson's ratio of the test piece
$\nu_{indenter}$ – Poisson's ratio of the indenter
S – slope of the tangent of the force/indentation curve during the unloading cycle
h_c – the contact depth value, which is dependent on the shape of the indenter
For homogeneous and isotropic materials, the measured value of $\mathbf{E_{IT}}$ approaches the Young's modulus of the tested material. For an isotropic material, this value is the 3D average of the crystallographic moduli.
An important hardness test parameter is the shape of the indenter. It can be chosen based on the scale and the application case. For macro-indentation tests, the widely used is the Vickers indenter (pyramid-shaped), as it has the widest scale and is suitable for all kind of metal materials. The Brinell indenter (sphere-shaped) is also in standard usage for macro tests with high loads.
The presented in subchapter 8.2.1 results were obtained with a Vickers indenter, and the corresponding Vickers hardness (**HV**) was calculated as follows:

$$HV = \frac{F}{g_n A_S} \qquad \textit{Equation 4-8}$$

where:
F – applied force
g_n – gravity
A_S – indentation imprint area

The maximal test force was chosen to be in the micro range, according to DIN EN ISO 14577-2:2015-11 (see Table 4-11). The micro-range scale was chosen based on the thickness of the layer affected by the DR process. As it was only several hundreds of micrometer thick, the distance between the imprints should not exceed 50 µm, to follow the changes of the hardness. Initially, several loading forces were tested, see Table 4-12, and the resulting imprint measured to obtain the most suitable imprint size. The results showed imprint diagonals of an app. 4 µm – 20 µm (HV 0.01). The highest measurement resolution could be achieved with the smallest imprint (in this case, HV 0.01). Still, the material's grain size as an influencing factor cannot be neglected, as the smaller the size of the imprint is, the higher the possibility is that the imprint is positioned on a grain edge, thus delivering unusual hardness value. Therefore, the test force was fixed on 49.05 mN (HV 0.05).

Table 4-11: Scale ranges and test forces for instrumented indentation method by DIN EN ISO 14577-2:2015-11

Scale	Force/indentation depth
Macro range	2 N < F < 30 000 N
Micro range	2 N > F and h > 0,000 2 mm
Nano range	0,000 2 mm ³ ≥ h

Table 4-12: Testing parameters used for the indentation hardness measurements

Test force:	98.1 mN (HV 0.1), 49.05 mN (HV 0.05) or 9.81 mN (HV 0.01)
Loading duration	20 s
Maximal force kept for	10 s
Unloading duration	20 s

5 Finite element modelling and material data modelling setup

In the following chapter will be described the major aspects of the finite element (FE) modelling, employed for the investigations shown in subchapters 7.1, 7.2, 7.4, 8.1.3 and 8.2.3. The classification of the modelling phases represented in Table 5-1 aims to systematise and to clarify the information regarding the corresponding modelling steps. For all FE modelling, the commercially available software ABAQUS CAE (versions 6.12 – 6.14) was employed. The FE simulations were obtained on a PC equipped with Intel Core 7 processor (2nd generation) with 16 GB RAM (DDR3).

Table 5-1: Classification of the finite element modelling stages

Modelling phases	**Description**
1. Choice of equation system solver	Which kind of solver was used (implicit or explicit)
2. Geometries	Representation of the geometries of the work piece and the tool
3. Material data	Information about the material data and material model assigned to the work piece and the tool
4. Modelling steps, boundary conditions (BC), loads and interactions	Similar to the description of a physical process, the simulated process is divided into several steps, defined by the changes in the process's input variables. Description of the fixations and the applied loads to both work piece and tool; interaction definitions (e.g. friction behaviour) between work piece and tool.
5. Meshing strategy	Discretisation of the work piece and the tool, mesh and element types used
6. Post processing	Visualisation of the calculated results; types of output parameters displayed (e.g. displacements, stresses, strains) and location of the calculated values

Finite element models - preliminary investigations

1. Choice of equation system solver

For all of the FE simulations of the DR process, the explicit equation system solver of ABAQUS CAE was employed. As the DR process was considered as a quasi-static process divided into several time steps, the application of the implicit equation system solver (suitable for solving static problems) was considered as inappropriate.
The DR model was realised as a full 3D, in order to analyse the resulted output parameters in all three dimensions.

2. Geometries

The geometries of the work piece and the DR tool, simplified to a sphere are plotted in Figure 5-1.

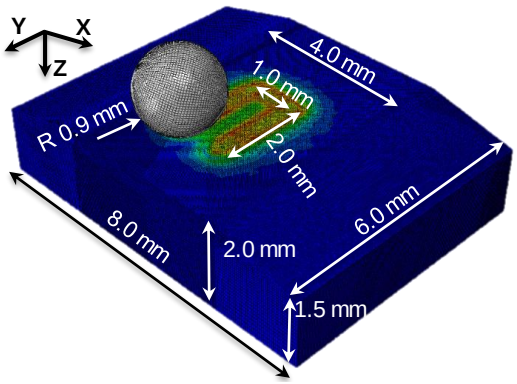

Figure 5-1: Work piece and DR tool geometries; length of the DR traces

3. Material data

The material of the work piece, exhibiting during the DR strong elastoplastic deformations, needed to be defined as a deformable body. Here, the most important definitions were the elasticity and the plasticity of the material. The elasticity was defined as linear, isotropic with Young's modulus and Poison's ratio. For modelling the plasticity, as represented in Figure 2-23 (chapter 2.4) there are several suitable material models. From particular interest were the linear and multi-linear, with isotropic or kinematic hardening as well as the Johnson Cook material representation. Temperature-dependent material data can be neglected as the DR process was accomplished at room temperature. The strain rate dependent material data can be included if the treatment velocity is high, as the material's behaviour differ strongly at high strain rates. In the presented modelling, the treatment velocity was kept very low, i.e. 1 mm/s; therefore, it can be considered that the valid material properties will be those at very low strain rates.

The material assigned on the work piece was steel with Young's modulus of 210 GPa, Poisson's ratio 0.28, Yield strength of 997 MPa and ultimate strength of 1144 MPa. A material model with bi-linear kinematic hardening was defined, where the elastic limit of the material and the ultimate strength were specified, with the corresponding plastic strain.

No material was assigned to the DR tool, as it was defined as a rigid body. The application of a rigid body has several advantages, e.g. the concept of application of boundary conditions and the computation efficiency. The rigid body is considered as a system of nodes, elements, and surfaces whose motion is governed by the motion of a single node called the rigid body reference node. The relative positions of the rigid body's nodes and elements toward the reference node remain constant throughout a simulation. Therefore, they do not deform but can undergo motion as they are not fixed in the modelling coordinate system. The motion of a rigid body can be realised by applying boundary conditions directly at the rigid body reference node. There is another principal advantage of using rigid bodies rather than deformable bodies, and this is the computational efficiency. Despite the required computational effort to update the motion of the nodes of the rigid body, the motion of the rigid body is determined completely by a maximum of six degrees of freedom at the reference node. Consequently, the lower

number of nodes requiring calculation of the motion, the less calculation effort needed. (Dassault Systèmes, 2011).
In the presented simulations, the modelling of the DR tool as a rigid body should not have a significant influence on the process (Mori, et al., 1995), as under real conditions the yield strength of the tool's material (tungsten carbide) is more than double the yield strength of the work piece material. Besides, the Young's modulus of the tool material with app. 700 GPa value is much higher than the Young's modulus of the treated material, which is app. 200 GPa (Klumpp, et al., 2016).

4. Modelling steps, boundary conditions (BC), loads and interactions

The defined modelling steps and the boundary conditions of the DR tool are listed in Table 5-2. The first modelling step aimed to establish contact between the work piece and the tool. Therefore, a small force in z direction was applied, as the movement of the sphere in z direction was correspondingly allowed. All other degrees of freedom (DoF) were fixed. In the second step, the DR force was applied and kept constant during the DR process. The force was considered as a process input variable and varied for the different models, to compare its influence on the resulted output variables, e.g. stresses, displacements, strains, etc. The DR force was calculated based on a defined DR pressure as follows:

$$F = \pi r^2 p \quad \text{(Röttger, 2003)} \qquad \textit{Equation 5-1}$$

where:
F – applied DR force
r – radius of the DR tool
p – applied DR pressure

In the last step "DR force releasing", the force was kept inactive, thus leaving the material to relieve elastically from the applied force. The BC applied on the work piece were kept constant throughout the modelling steps, where only the bottom surface was fixed in all directions.

Table 5-2: Modelling steps and boundary conditions of the DR tool

Steps for DR	**Translational DoF**			**Rotational DoF**			**Applied force**
	X	Y	Z	RX	RY	RZ	
1. Contact establishing	fixed	fixed	free	fixed	fixed	fixed	5 N in z direction
2. DR force application	fixed	fixed	free	fixed	fixed	fixed	variable
3. DR process	fixed	1mm/s	fixed	free	fixed	fixed	active
4. DR force releasing	fixed	free	fixed	fixed	fixed	fixed	inactive

In the modelling phase "interactions", the contact between the DR tool and the work piece was defined. The proper modelling of the contact between both components is crucial, as this can lead to different surface deformations and near-surface stress distributions. The FE code ABAQUS offers different possibilities to define a contact; one

of these is the “contact pair” option. Here, both surfaces, which will be in contact with each other, have to be assigned and defined as master and slave surfaces. Generally, the nodes of the master surface are allowed to penetrate to the slave surface but not contrariwise. There are several requirements for the master surface, i.e. if a rigid body is in contact with a deformable body, the rigid body needs to be defined as master. In this case, the DR sphere was chosen to be master- and the work piece - slave surface. After setting the contact pairs, the friction between them can be formulated. The used friction model is based on the Coulomb friction model, as described in Figure 5-2 a) and b). Equation 5-2 shows the dependence of the applied normal force **N** on the resulted frictional force $\mathbf{F_f}$, whereas the applied tangential force **F** is equal to the $\mathbf{F_f}$. The friction coefficient **μ** is a scalar that describes the ratio of friction between two surfaces. For all of the presented FEM models, the friction coefficient was fixed to 0.1.

$$F_f = \mu N \qquad \textit{Equation 5-2}$$

The Coulomb friction model in ABAQUS is extended to fit different simulation cases. One of those extensions is the penalty formulation (see Figure 5-2c)). It describes the stiffness of friction that allows a relative motion, i.e. elastic slip **γ**, of the contacted surfaces when they should remain sticking. The elastic slip is an important parameter as it affects the friction behaviour before the slipping phase occurs. The elastic slip is defined as the distance where the slipping phase begins.

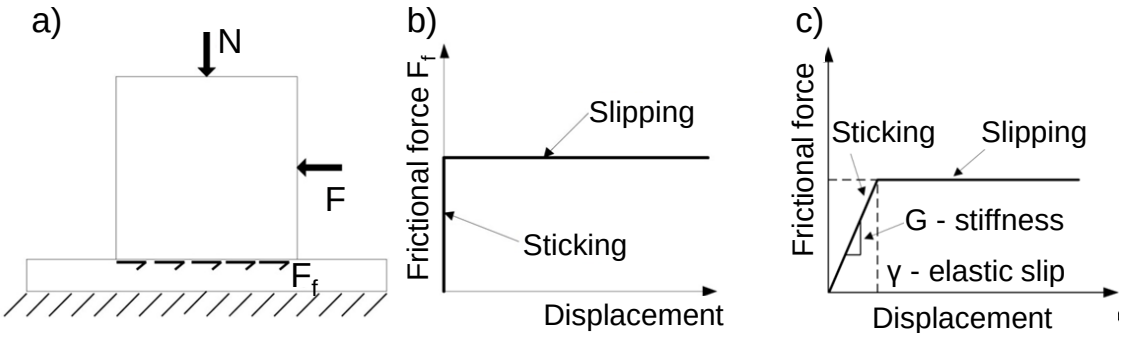

Figure 5-2: a) Basic Coulomb friction model, b) Coulomb friction ideal curve and c) Friction curve with defined sticking (Dassault Systèmes, 2014)

Under realistic conditions, the elastic slip can be contributed to the existing elastic displacements in the surface roughness. In ABAQUS, the elastic slip can be defined as a fracture of the element length or as an absolute distance. In the presented investigations, the first option was applied, and the elastic slip was fixed to 0,005%. The application of small elastic slip is recommended in the ABAQUS User’s manual, as it improves the solution accuracy. Regarding the frictional directionality, the isotropic option was applied.

5. Meshing strategy

A convergence study was accomplished for the optimal discretisation of the work piece. The element type was fixed as C3D8R, i.e. eight-node brick element with reduced integration, to increase the computational efficiency. The smallest element size was varied from 0.1 mm to 0.025 mm, resulting in calculation time from 3 minutes to over 2 hours. Reducing the element size below 0.040 mm did not influence further the calculated maximal von Mises stress and therefore could be used. Although based on the calculated surface and in depth stress profiles, a smaller element size was fixed at the area where the DR treatment was applied. Using a progressive meshing strategy, the work piece was meshed with 1 720 800 elements, where the smallest element was 0.025 mm. The DR tool was meshed with R3D4 4-node 3D bilinear rigid quadrilateral elements; the size of the elements was maximal 0.05 mm, resulting in element number of 7380.

The DR treatment was realised as single-trace, meaning the DR tool produced only one trace instead of the whole area. For statistical plausibility, initially, two traces in -y and +y direction were modelled, and the values of the generated stress profiles were compared. As no significant difference in the results was observed, the models shown later in this chapter were realised only with a single trace. For some models, an overlapping process parameter was established, as under real conditions the DR process usually produces a whole surface, not only a single trace. The overlapping definition is described in Figure 5-3.

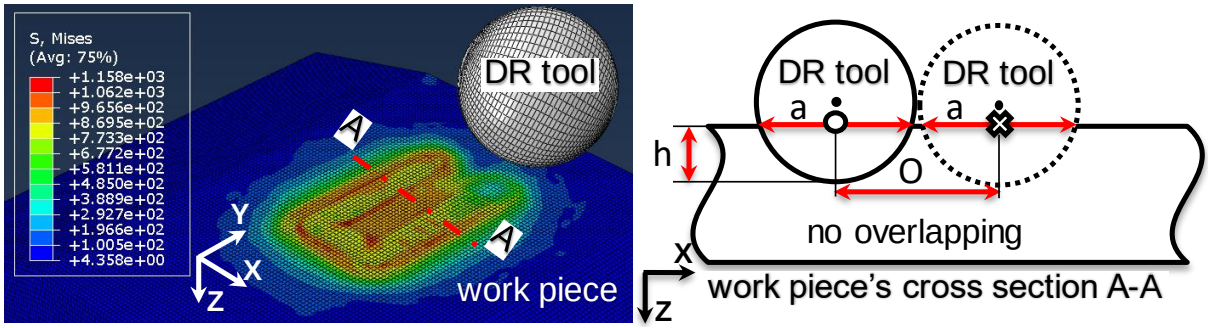

Figure 5-3: Definition of the overlapping parameter by DR process

Considering that the DR force applied on the tool results in certain penetration depth **h** of the tool into the work piece, the corresponding diameter **a** of the tool imprint can be calculated:

$$a = 2\sqrt{h(2r - h)} \qquad \textit{Equation 5-3}$$

Where:

a – diameter of the imprint resulting from the DR tool during its penetration into the work piece

r – radius of the DR tool

h – depth of indentation

The overlapping **A** in percentage can be defined as a process variable, and the overlapping in milimeter, i.e. the distance **O** between the tool paths in x direction can be calculated:

$$O = (100\,\% - A\,\%).a \qquad \textit{Equation 5-4}$$

Where:
O – overlapping in mm
A – overlapping in %

6. Post-processing

The last part of the simulation, after the DR process was modelled, was the post-processing, i.e. the visualisation of the calculated values. In general, two kinds of plots were displayed: on the surface and in depth, as the output variables stresses, displacements and strains were analysed. The surface plots were defined as an evaluation path was created on the surface, in x direction (perpendicular to the DR trace), similar to the position of the cross-section A-A from Figure 5-3. The depth plots were realised as creating an evaluation path in the middle of the DR trace, starting at the deepest point of the DR trace profile on the surface and continuing throughout the work piece in z direction. The evaluated parameters, in case of direction dependency, were designated as “long”, meaning in the direction along the DR trace and “trsv”, meaning in the direction transverse to the DR trace.

Finite element models for experimental verification

The finite element models which were verified by means of x-ray diffraction measurements and experimental topography characterisation (see the results in subchapters 7.1, 8.1.3 and 8.2.3) were built in a similar approach as the one used for the preliminary investigations. Nevertheless, several aspects were optimised and adapted to fit the conditions of the experimental verifications. Figure 5-4 depicts the work piece and DR tool geometries, as well as the length of the DR trace(s).

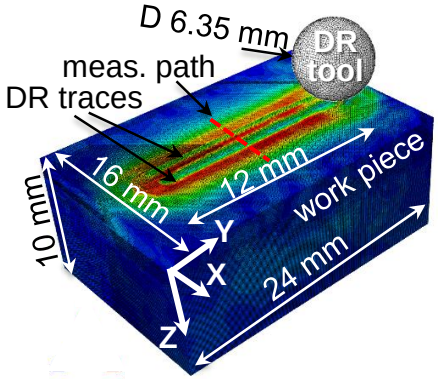

Figure 5-4: FE work piece and DR tool geometries; length of the DR traces

A comprehensive material data was gathered by means of the tensile and tensile-compressive tests described in subchapter 4.1.2. The commercially available MCalibration® software from Veryst Engineering was employed to implement the material data obtained from the tensile tests. The software is a calibration tool for different material models, which allows a row material-data extraction and its implementation to several native material models available for ABAQUS CAE, ANSYS, etc. The ABAQUS models of interest were: Johnson and Cook, Elastic-plastic-isotropic-hardening and Elastic-plastic-kinematic-hardening. In Figure 5-5 is depicted an example of the software users interface, where on the left (see Figure 5-5 a)) is plotted the experimentally derived versus the predicted stress-strain material data with implemented Elastic-plastic-isotropic-hardening model. In this example, the prediction fits almost entirely to the experimental data. More detailed investigations of the curve fitness and the material model variations are shown in chapter 6.2., where a DR process parameter study was conducted by varying the DR force and the material model definition. In Figure 5-5 b) can be seen the derived material model parameters which can be directly implemented in ABAQUS. As the material parameters used in ABAQUS should always be upwards increasing, the derived data only until the Ultimate strength can be used. After this point, the material will behave ideally plastic, as no fracture behaviour was additionally defined.

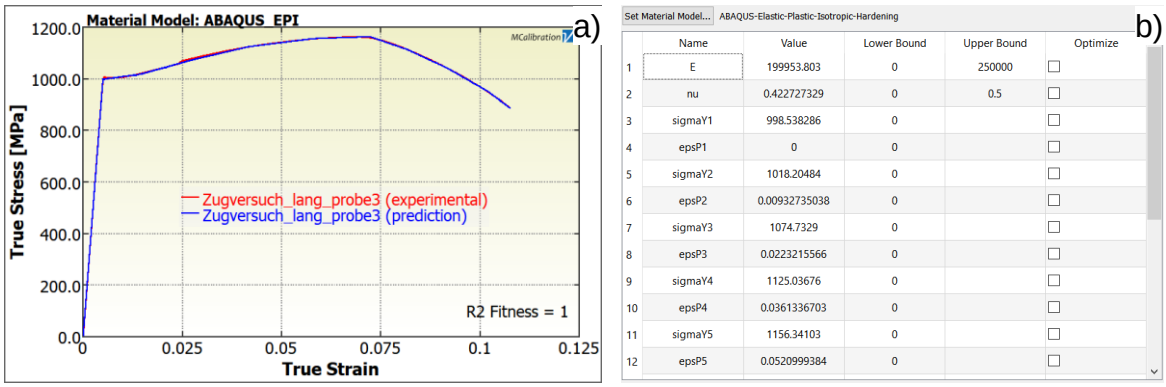

Figure 5-5: MCalibration user interface: a) true stress-strain plot, comparison between experimental vs predicted material data; b) material model parameter calibration

The boundary conditions of the work piece and the DR tool remained unchanged, but the application of the DR force was defined by assigning a fixed displacement of the DR tool in z direction. The reason for this change was that the DR sphere was modelled as a rigid body, and this means it possesses infinitely high elasticity modulus. Under real process conditions, the sphere would have Young's modulus of an app. 700 GPa, meaning it will elastically deform when the DR force is applied. This will result in a slightly larger contact area, compared to the area formed if the sphere has an infinitely high elasticity modulus. The larger contact area will change the indentation depth of the sphere and thus will influence the macroscopic topography of the resulted DR trace. Therefore, using the contact mechanics and the formulation of the Hertzian pressure between two spheres (here, the work piece has infinite radius), the indentation

depth of the DR tool was calculated and applied as BC instead of DR force. Based on Equation 5-5, the indentation depth **h** was calculated.

$$F = \frac{4}{3}E^*\sqrt{R}\sqrt[3]{h^2}, where\ E^* = \frac{1-\vartheta_1^2}{E_1} + \frac{1-v_2^2}{E_2} \qquad \textit{Equation 5-5}$$

Where:
F – applied force
E* – composite Young's modulus
R – radius of the tool
h – indentation depth
v_1 and v_2 – Poisson's ratio of the work piece and the tool
E_1 and E_2 – Young's moduli of the work piece and the tool
The work piece was meshed using progressive seeding option, enabling the smallest element size of 0.08 mm at the place of interest, growing to a size of 0.16 to 1.0 mm. The total element number was 1 297 200, which led to a calculation time of app. 12 hours (by the single-trace model). The visualisation of the calculated results was similar to this of the models for preliminary investigations.

Finite element models for pre-stressed DR

The model used for the analysis in subchapter 7.2 consists of three parts. First, an elastic four-point bending at levels 30 %, 60 % and 70 % of the material's yield strength was performed using the standard module of ABAQUS CAE 6.14. Then, using a pre-defined field, a pre-stress was determined as an initial stress state for the DR treatment, performed in ABAQUS CAE 6.14 explicit. The final spring back operation was made in ABAQUS standard, using the pre-defined field from the DR operation. The geometries of the work piece and the DR tool (sphere) are depicted in Figure 5-6.

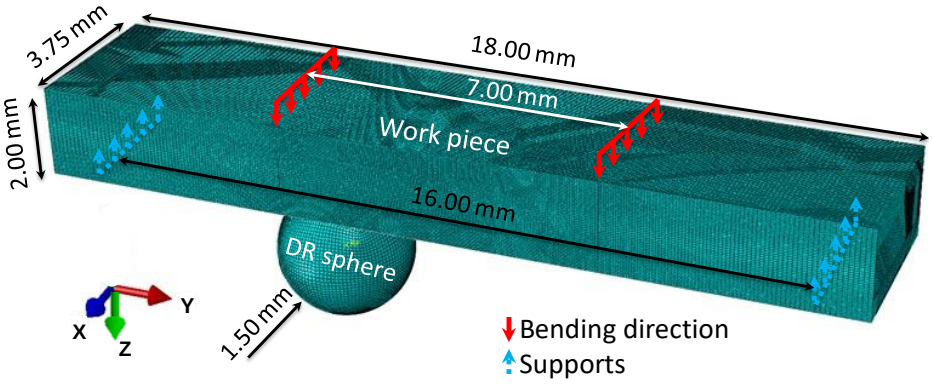

Figure 5-6: Pre-stressed DR – work piece and tool geometries

The material assigned to the work piece was AISI 4140 steel with Young's modulus of 210 GPa, Poisson's ratio 0.28, Yield strength of an app. 997 MPa and ultimate strength of an app. 1144 MPa. The applied material model was elastic-plastic with bi-linear kinematic hardening. No material was assigned to the DR sphere, as it was modelled as

a rigid body. The designed modelling steps reflected the physical realisation of the pre-stressed DR process. The model consisted of steps and boundary conditions listed in Table 5-3 and Table 5-4.

Table 5-3: Pre-stressed DR – boundary conditions of the work piece

Step	**Translation**			**Rotation**			**Bending force**
	X	Y	Z	RX	RY	RZ	
1. Bending (pre-stressing)	fixed	free	fixed	free	free	fixed	active
2. DR	fixed	fixed	fixed	fixed	fixed	fixed	active
3. Bending spring back	free	free	free	free	free	free	inactive

Table 5-4: Pre-stressed DR – boundary conditions of the DR tool (sphere)

Steps for DR	**Translation**			**Rotation**			**Applied force**
	X	Y	Z	RX	RY	RZ	
2.1. Contact establishing	fixed	fixed	free	fixed	fixed	fixed	5 N
2.2. DR force application	fixed	fixed	free	fixed	fixed	fixed	variable
2.3. DR process	fixed	1mm/s	fixed	free	fixed	fixed	active
2.4. DR force releasing	fixed	fixed	free	fixed	fixed	fixed	inactive

The applied bending pressure, as a percentage of the material's yield strength, was calculated as follows:

$$\sigma = \frac{M_x y}{I_x}, where\ I_x = \frac{bh^3}{12}, \qquad \textit{Equation 5-6}$$

Where:
σ – Resulting stress
M_x – Torque around x axis
I_x – Moment of inertia around x axis
$R_{P0.2}$ – Yield strength of the material
b – width of the work piece
h – height of the work piece

As both supports and the applied bending force are symmetrical to the work piece's middle:

$$\sum F_z = 0 \rightarrow F_{left\ supp.} = F_{right\ supp.} = F \qquad \textit{Equation 5-7}$$

$$M = \sum F \,.\, L \rightarrow M_x(middle) = 4.5F \qquad \textit{Equation 5-8}$$

Where:
F_z – sum of the forces in z direction
M – torque
L – length

In Table 5-5 are plotted the calculated pre-stress and bending force as a percentage of the material's yield strength.

Table 5-5: Applied bending Force, calculated as percentage of the material's yield strength

% from yield strength	Pre-stress [MPa]	Bending force [N]
30	299.1	166.2
60	598.2	332.3
70	697.9	443.1

Considering the design of the pre-stressed DR, four different boundary conditions set-ups can be configured, depending on the direction of the applied DR process and the side of the bending set-up. In Figure 5-7 are depicted the possible variations, where in chapter 7.4 (FEA - Pre-stressed deep rolling) not all of the variations are shown but just the most favourable (tensile side, longitudinal direction).

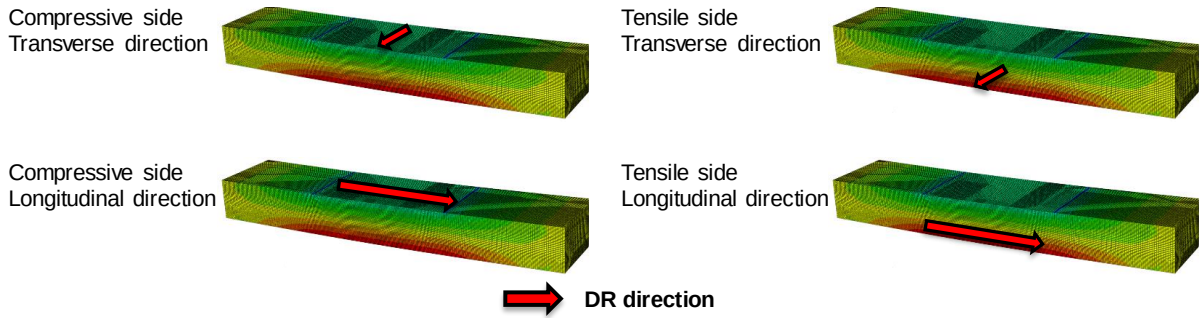

Figure 5-7: Application of the DR process by variation of the DR- and the pre-stress directions

The meshing of the work piece was done with structured C3D8R hexahedral elements, and a convergence study was accomplished, where the analytically calculated bending stress was compared with the FE calculated one. The work piece was discretised with an app. 1 400 000 elements, using a progressive meshing strategy, resulting in a simulation time of app. 24 hours, with smallest element size of 0.04 mm and a calculation error of 2.25%.
The results were displayed as an evaluation path in depth (-z direction) was defined in the middle of the work piece; starting from the bottom surface, where the DR process was applied and ending at the top surface.

6 Finite element simulations - preliminary investigations

In this chapter will be represented the preliminary investigations of the finite element analysis of deep rolling. These investigations have the goal to establish a plausible and stable FE model of DR process, which enables several process parameter variations and delivers realistic results. Some critical boundary conditions like friction, mesh type and density were varied, and their influence on the calculated stresses by several different DR process parameters was investigated. Special attention was drawn on the representation of the elastoplastic material behaviour, which, according to state of the art considered in subchapter 2.3, plays a critical role in the realistic residual stress predictions.

6.1 Establishing of the finite element model with DR tool diameter 1.8 mm

Initially, the FE model of the DR process was realised using geometry and meshing, according to Figure 6-1.

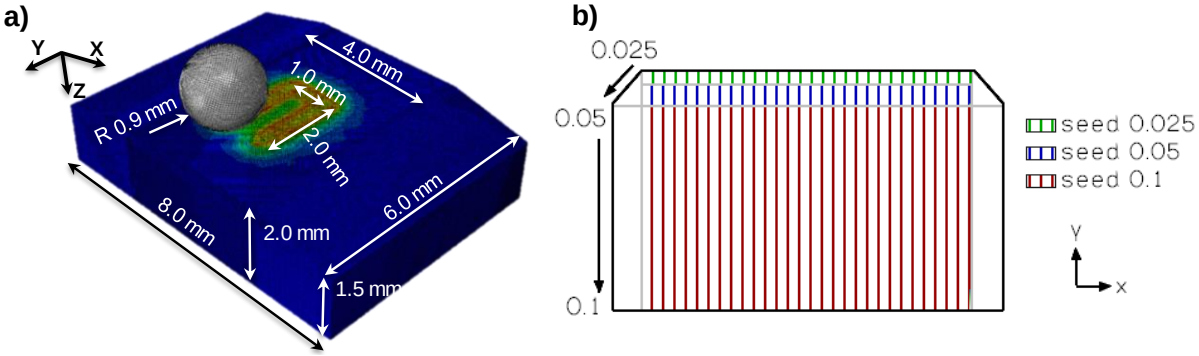

Figure 6-1: Finite element model of DR with tool diameter 1.8 mm: a) geometry of the work piece and the tool and b) progressive meshing strategy

A flat surface was deep rolled with a sphere of diameter 1.8 mm, using a trajectory visible in Figure 6-1 a). For the single-trace DR, the distance between two traces was relatively large, so that the stresses generated in both traces do not significantly influence each other. The calculated stresses in both traces were very similar. The results shown in this subchapter were obtained as for the surface residual stress distribution, a stress determination path was defined on the surface, in x direction, through the whole work piece's surface, in the middle of both DR traces. The stress depth profiles were obtained in the middle of one trace starting from the surface in z direction. The stresses were determined in longitudinal (longRS) or transverse (trsvRS) to the DR trace direction (referred to both traces placed in y direction).

A convergence study was performed to optimise the mesh density so that the highest calculation precision for the most reasonable time and a sufficient resolution can be achieved. The element size was varied from 0.1 mm to 0.03 mm for the whole work piece, or a progressive mesh size was employed as meshing strategy. The latest combines a coarse meshing at regions out of interest with very fine meshing at the near-surface layer, where the stress gradients generated by the DR process are highest.

Figure 6-1 b) depicts the mesh size distribution in the work piece's depth. On the surface in x and y directions, the mesh size was fixed to 0.25 mm.
Table 6-1 gives an overview of the maximal calculated stress von Mises and the resulting calculation time for the corresponding mesh size. The calculated stress stabilises by the mesh size of 0.04 mm, resulting in a calculation time of 20 minutes. The progressive meshing gives a higher near-surface resolution, resulting in 36 minutes calculation time, and therefore it was employed as an optimal one.

Table 6-1: Convergence study of the work piece's meshing accuracy of DR FE model with tool diameter 1.8 mm

Element size [mm]	Number of elements	Maximal von Mises Stresses [MPa]	Approximate time of completion
0.1	7200	1580	3 minutes
0.08	142500	1660	3 minutes
0.05	576000	1200	10 minutes
0.04	1157100	1170	20 minutes
0.03	2690000	1180	More than 2 hours
Progressive meshing	1720800	1170	36 minutes

A variation of the friction coefficient between tool and work piece was performed by fixed DR force of 100 N. The calculated residual stress depth profiles are depicted in Figure 6-2. In both directions, changing the friction coefficient did not significantly influence the calculated values. As praxis-near, the value of 0.1 was chosen for the later represented results.

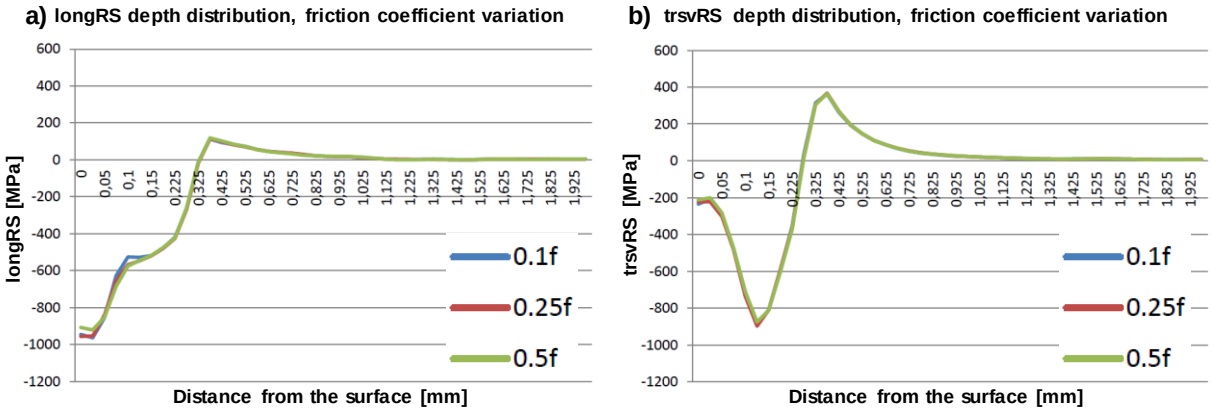

Figure 6-2: FE calculated residual stress depth distributions after DR with tool diameter 1.8 mm with constant DR force of 100 N and variable friction coefficient between work piece and tool: a) longitudinal direction and b) transverse direction

The treatment velocity, i.e. the velocity of the motion of the sphere in the direction of the treatment was varied from 1 mm/s to 20 mm/s and the resulted calculation time, see Figure 6-3 a) and the stress depth profiles in the transverse direction, see Figure 6-3 b) were investigated. Higher velocity resulted in lower calculation time, but the calculated depth profiles were not-realistically sensible to the change of this parameter. Therefore, the DR treatment was kept quasi-static using a velocity of 1 mm/s. Further

decrease of the velocity delivered very similar stress depth profiles like the one by a velocity of 1 mm/s.

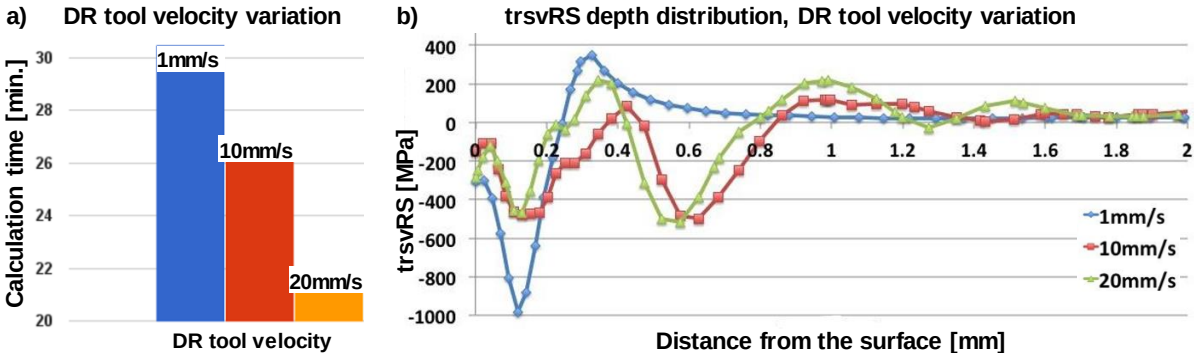

Figure 6-3: Variation of the DR tool velocity by constant DR process parameters: a) influence of the DR tool velocity on the calculation time and b) RS depth distribution after DR with variable tool velocity

During non-linear simulations, large deformations in the whole structure can result in abnormally mesh elements' distortion. To avoid such abnormality, an adaptive meshing (AM) technique was implemented to reduce the mesh distortion at every increment. This technique allows the mesh to move simultaneously with the direction of the calculated deformation, thus reducing the generation of artificial element displacements. In Figure 6-4 is illustrated the influence of the adaptive meshing on the resulted by DR deformations, where the surface topography after DR along the DR trace with- (red line) or without (blue line) AM is depicted in Figure 6-4 a).

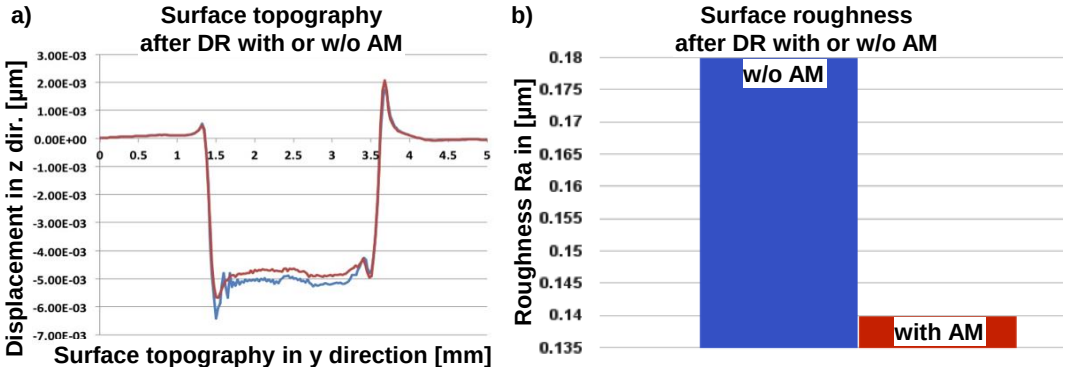

Figure 6-4: Influence of the adaptive meshing on the resulted by DR deformations; DR model with tool diameter 1.8 mm: a) deformations along the DR trace (y direction) and b) calculated surface roughness Ra

The middle section of the diagram describes the vertical displacements of the elements along the DR trace. Here, the AM led to slightly smaller deformations. The calculated average roughness Ra with- or without AM is plotted in Figure 6-4 b), where the AM deliver lower roughness value. It is important to note that the calculated roughness is based only on the displacements of the elements resulting from the DR process. In contrary to the realistic conditions, it does not reflect the initial surface roughness, as the FE defined surface of the work piece was perfectly smooth before the treatment.

Due to the delivered smoother surface, the AM was employed in the results shown later.

The residual stress surface profiles of the optimised FE model are shown in Figure 6-5, where a variation of the applied DR force was performed. For the assigned material and the sphere diameter, the force varied from low to high. In both directions, see Figure 6-5 a) for longitudinal and Figure 6-5 b) for transverse direction, the DR force variation delivered plausible results. The shape of the surface stress profiles and the influence of the DR force on the resulted stresses will be discussed more comprehensively in subchapter 7.1.

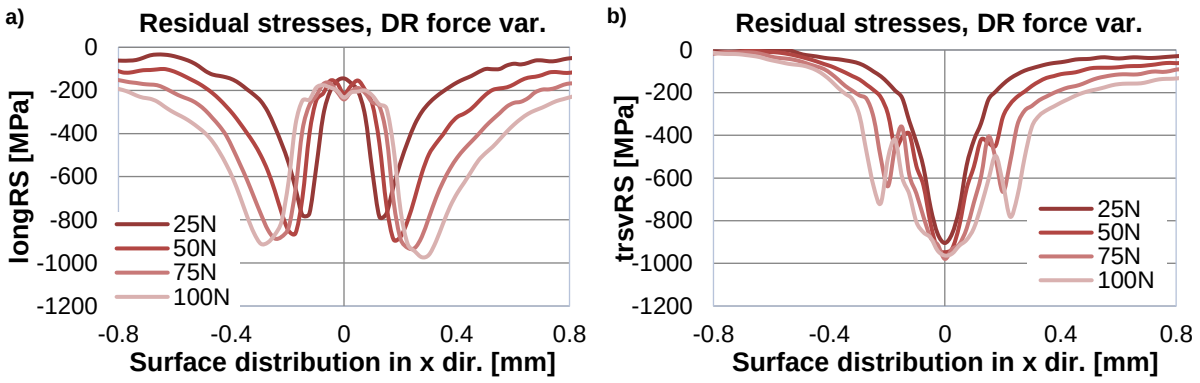

Figure 6-5: FE calculated residual stress surface distributions after DR with tool diameter 1.8 mm, by variation of the applied DR force: a) longitudinal direction and b) transverse direction

The overlapping variation between two traces by fixed DR force of 100 N was performed, and the calculated surface stress profiles are plotted in Figure 6-6.

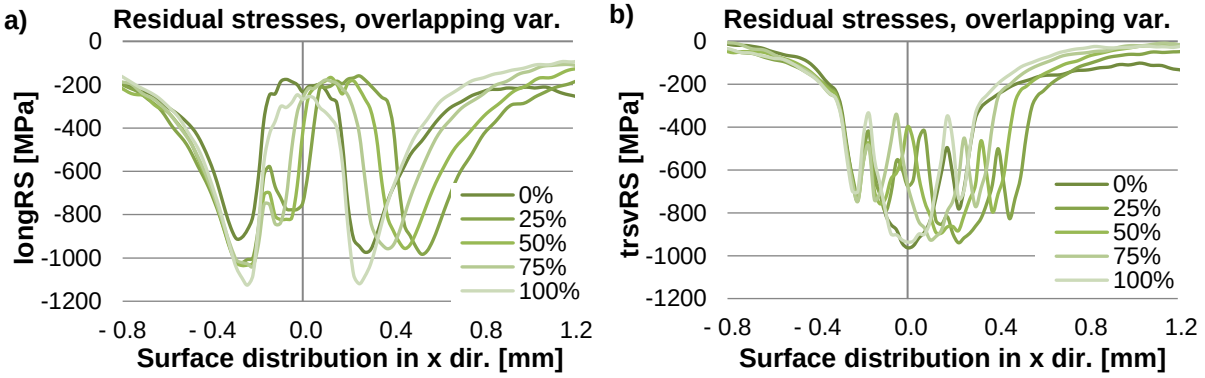

Figure 6-6: FE calculated residual stress surface distributions after DR with tool diameter 1.8 mm, by fixed DR force of 100 N and overlapping variation: a) longitudinal direction and b) transverse direction

In the longitudinal direction, see Figure 6-6 a), the treatment without overlapping and with 100 % overlapping led to a similar width of the stress affected zone. Still, the maximal compressive stress increased from an app. -900 MPa for 0 % overlapping to an app. -1100 MPa for 100 % overlapping, which practically means double treatment of the same area. The low overlapping percentage led to larger stress affected zone, which was expected due to the definition of the overlapping parameter (see chapter 5).

In the transverse direction, see Figure 6-6 b), the overlapping resulted in some artificially scattered stress values, which scatter was reduced by using several modelling techniques, e.g. optimising the mesh of the sphere, etc.
The stress depth profiles after variation of the DR force, see Figure 6-7, and the percentual overlapping, see Figure 6-8, look qualitatively plausible and the influences of the varied process parameters on the resulted stresses will be discussed more detailed in subchapter 7.1.

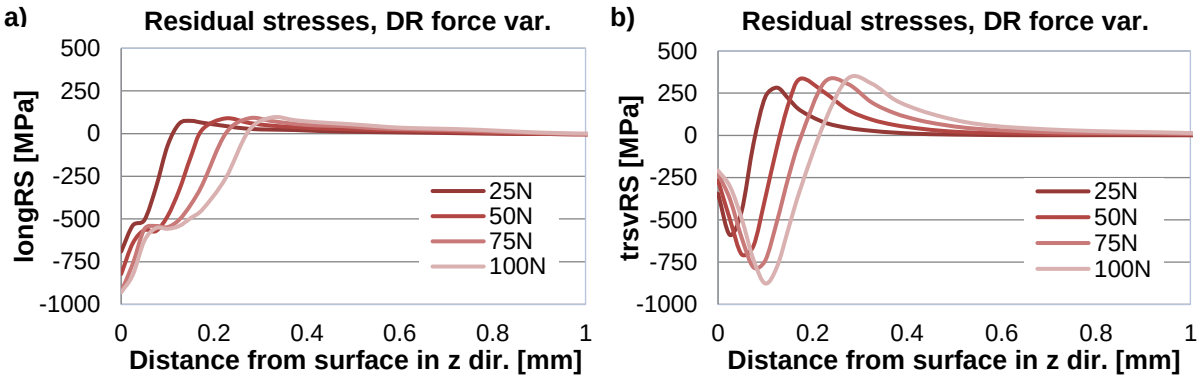

Figure 6-7: FE calculated residual stress depth distributions after DR with tool diameter 1.8 mm, by variation of the applied DR force: a) longitudinal direction and b) transverse direction

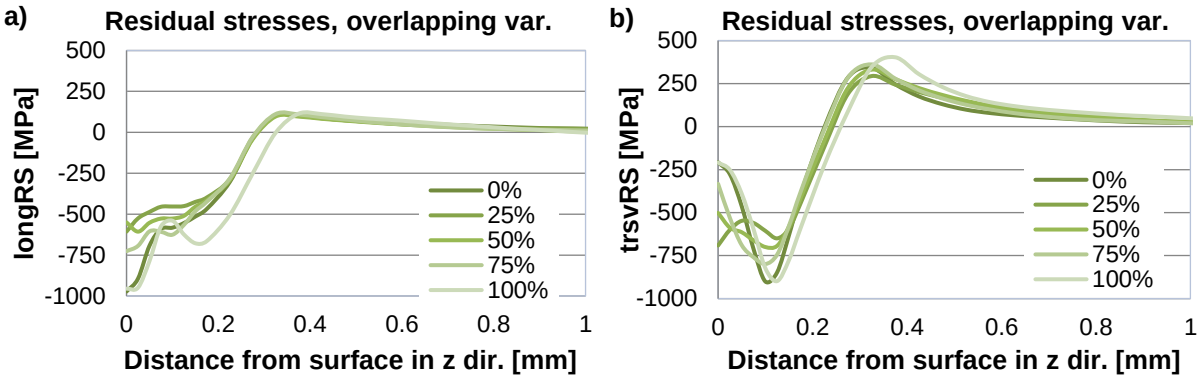

Figure 6-8: FE calculated residual stress depth distributions after DR with tool diameter 1.8 mm, by fixed DR force of 100 N and overlapping variation: a) longitudinal direction and b) transverse direction

The stress depth profiles after DR with a fixed force of 100 N and single- or multiple overturns are plotted in Figure 6-9. In the longitudinal direction, see Figure 6-9 a), the multiple treatment did not lead to an increase of the maximal compressive residual stress, which even slightly decreased. Still, as a positive effect, it can be observed that the multiple treatment led to deeper compressive residual stresses, reached a depth of app. 0.53 mm at six overturns. The stress impact depth is with 0.2 mm higher compared to those achieved with a single overturn. In the transverse direction, see Figure 6-9 b), a similar observation can be made and additionally, the low compressive stresses in depth were shifted by treatment with six overturns toward zero stress.

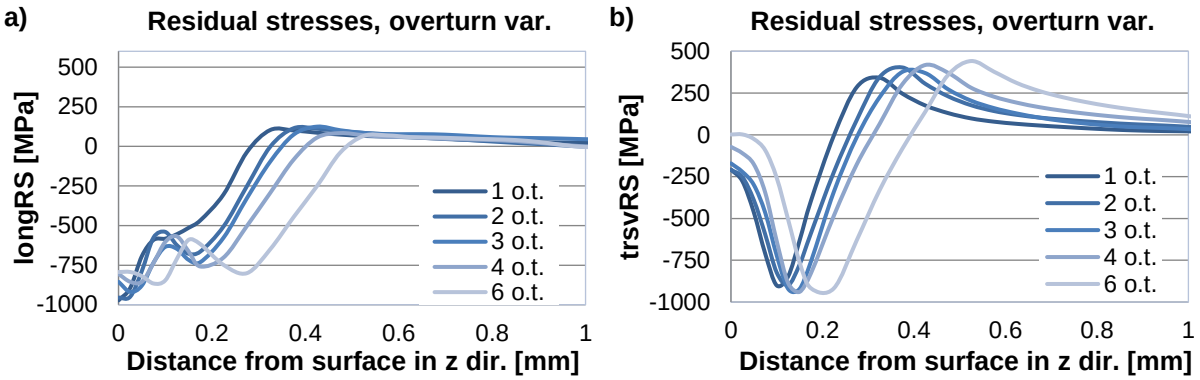

Figure 6-9: FE calculated residual stress depth distributions after DR with tool diameter 1.8 mm, by fixed DR force of 100 N and overturn variation: a) longitudinal direction and b) transverse direction

6.2 Influence of the material modelling and the material calibration on the calculated residual stresses - DR modelling with tool diameter 1.8 mm

In this subchapter, special attention will be drawn to the representation of the material behaviour of the work piece in the FE model. To implement the experimental tensile-compressive test data, which describe the material's elastoplastic behaviour into ABAQUS CAE, the software MCalibration was employed. After several material models were calibrated using the experimental data, those material models were implemented in ABAQUS CAE, and FE simulations of DR were performed by fixed process parameters and by different material model definitions. The calculated residual stress depth profiles were compared accordingly.

Material data implementation and model calibration

The experimentally derived tensile-compressive test material data was implemented in the software MCalibration, and three material models were employed to describe the material's behaviour: multi-linear elastic-plastic with kinematic hardening, multi-linear elastic-plastic with isotropic hardening and Johnson Cook model (Johnson, et al., 1983).

The elastic-plastic model with kinematic hardening is an ABAQUS CAE native material model that uses a discrete number of material parameters to describe a non-linear hardening behaviour. The material model can be formulated with multiple back-stress parameters. In Figure 6-10 is visualized the calibration of the material data using the multi-linear elastic-plastic material model with kinematic hardening, where Figure 6-10 a) depicts the whole test/calibrated data range, the Figure 6-10 b) takes a closer look on the tensile range and Figure 6-10 c) focuses on the compression range. For each tensile-compressive loop, one test specimen was used. In the tensile range, the model with kinematic hardening rule slightly overestimates the yield stress and the ultimate strength. In contrary, in the compressive range, the modelled values are quite lower than the test data, especially at low strains.

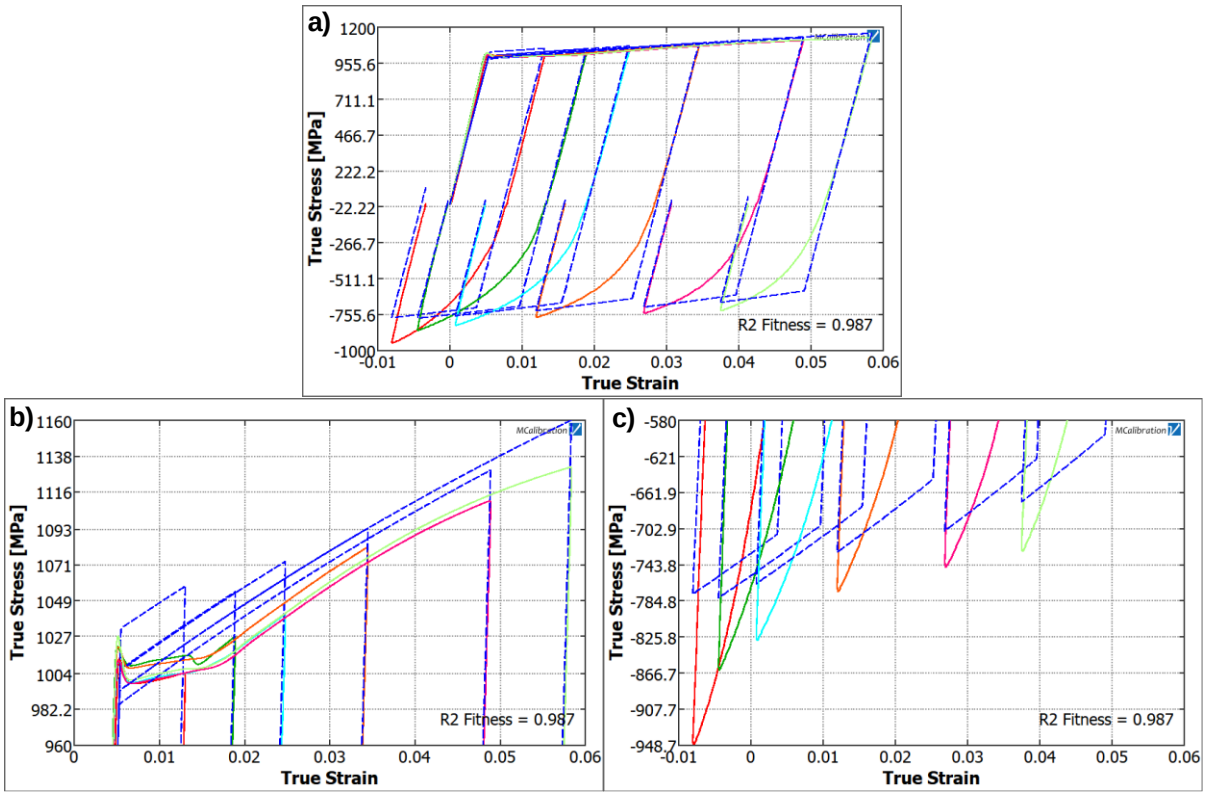

Figure 6-10: Material model calibration - elastic-plastic with kinematic hardening, based on tensile-compressive tests; experimental (full lines) vs calibrated (dashed lines) stress-strain curves: a) full range; b) tensile range and c) compressive range

The next calibrated material model was multi-linear elastic-plastic with isotropic hardening. It delivers similar results to the one with kinematic hardening. The important difference here is that in the compressive range, the isotropic hardening model predicts the material data very well but only at low strains and overestimates the material data at high strains, predicting higher compressive stress than the test data. This happens as a result of the interpolation of the yield stress from the tensile range.

The last calibrated material model was Johnson Cook (Johnson, et al., 1983), which is capable of describing the characteristics of materials subjected to large strains, high strain rates and high temperatures. The flow stress von Mises (σ) can be expressed as follows:

$$\sigma = (A + B\varepsilon^{n})(1 + C ln\varepsilon^{*})(1 - T^{*m}) \qquad \textit{Equation 6-1}$$

where **ε** is the equivalent plastic strain, **ε*** is the dimensionless plastic strain rate for $\boldsymbol{\varepsilon^{0} = 1.0\ s^{-1}}$, expressed in Equation 6-2.

$$\varepsilon^{*} = \varepsilon/\varepsilon_{0} \qquad \textit{Equation 6-2}$$

T* is the homologous temperature, expressed in Equation 6-3.

$$T^{*} = (T - T_{r})/(T_{m} - T_{r}) \qquad \textit{Equation 6-3}$$

$\mathbf{T_m}$ is the melting temperature of the material, and $\mathbf{T_r}$ is the room temperature. The parameters **A**, **B**, **n**, **C** and **m** are material constants. The first brackets of the equation represent the stress as a function of strain for $\boldsymbol{\varepsilon^* = 1}$ and $\mathbf{T^* = 0}$. The second and third brackets indicate the effects of strain rate and temperature, respectively. For simulating the DR process, the temperature and the strain-rate dependent material data was neglected. In Figure 6-11, is shown the corresponding model calibration. Here, the last delivers similar results to the test data at lower strains but at high strains underestimates the test data at the tensile range, see Figure 6-11 b), and overestimates the test data at the compressive range, see Figure 6-11 c). The determination coefficient $\mathbf{R^2}$, compared to the material model with kinematic hardening ($R^2 = 0.987$) is here lower ($R^2 = 0.948$).

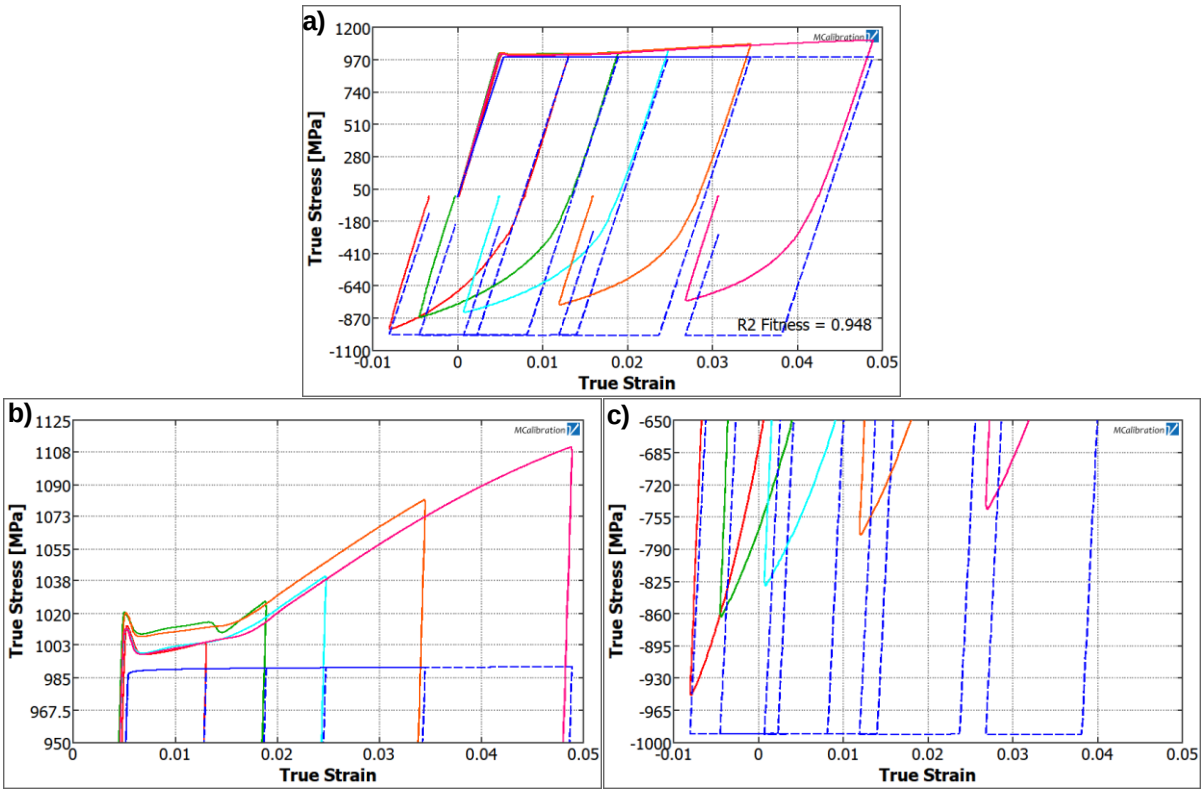

Figure 6-11: Material model calibration – Johnson Cook model, based on tensile-compressive tests; experimental (full lines) vs calibrated (dashed lines) stress-strain curves: a) full range; b) tensile range and c) compressive range

The results shown above emphasise the importance of the material representation and the fitness of the most commonly used material models to different loading cases like tensile, compression, and various strains. As the calibrated data from the material models do not fit the test data in all considered loading cases, the utilisation of each of them should be taken with caution.

The next data calibration was performed using tensile test data performed with two different test specimens' lengths. The influence of the specimens' length on the calculated material parameters was investigated, see Table 6-2. All material parameters are similar for both long- and short specimens. Only the strain before necking differs, as it

is defined based on the total length of the specimen, which for the short or long type differs.

Table 6-2: True stress-strain MCalibration isotropic hardening model parameters derived from tensile tests on long or short specimens

	Young's modulus [GPa]	**Yield strength [MPa]**	**Ultimate strength [MPa]**	**Strain before necking [%]**
Long specimens	198.9	1006.0	1164.0	0.0621
Short specimens	198.9	990	1160.0	0.0740

Figure 6-12 and Figure 6-13 compare the experimental with the predicted material data for both specimens' lengths (Figure 6-12 a) – long specimens complete range, Figure 6-12 b) – short specimens complete range, Figure 6-13 a) – closer look yield strength range and Figure 6-13 b) – closer look ultimate strength range). A very good agreement between predicted and test data for the whole range is visible, and for both specimens' lengths, the maximal deviation is not higher than ± 10 MPa.

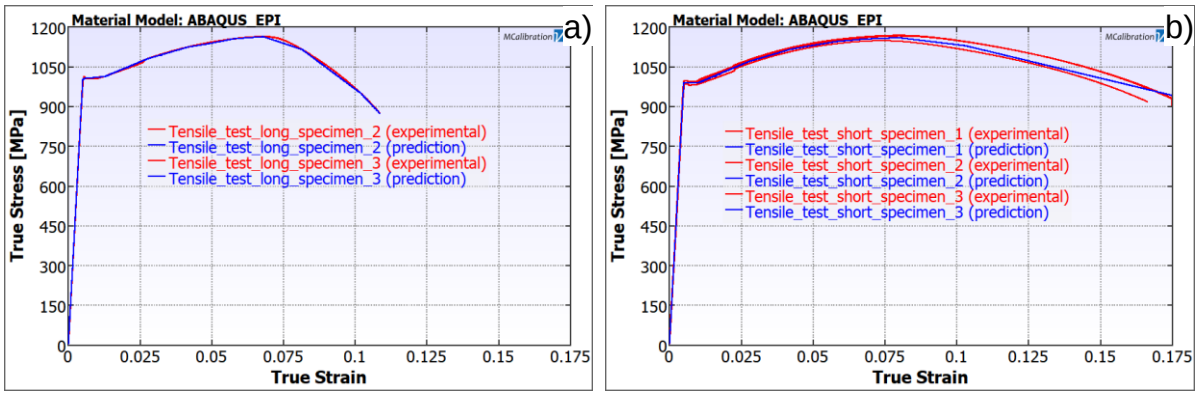

Figure 6-12: Material model calibration – elastic-plastic with isotropic hardening, based on tensile tests; experimental (red lines) vs calibrated (blue lines) stress-strain curves; a) long specimens and b) short specimens

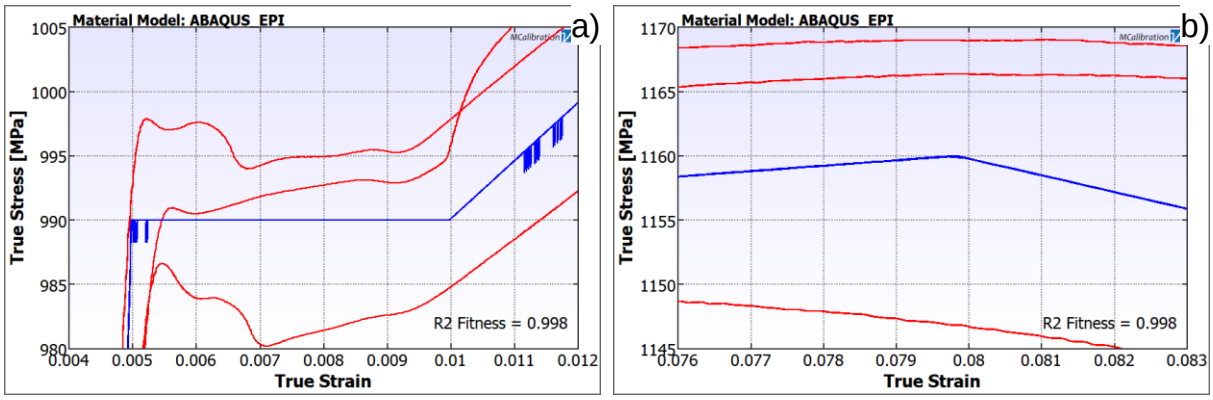

Figure 6-13: True stress-strain curves short specimens; blue curves – predictions and red curves – experimental data; a) yield strength region and b) ultimate strength region

FEM of deep rolling by variation of the material model

Utilising the material calibrations from the previous section, material data was implemented in ABAQUS CAE using the material model formulations listed in
Table 6-3. After that, DR process simulations were performed by fixed process parameters and variable material model definition. Two DR forces: 50 N or 100 N were employed, to investigate the sensitivity of the material model to different loading magnitudes.

Table 6-3: Designation of the varied material models

Abbreviation	Designation
Iso_pp_bi_lin	Bi-linear elastic- perfect plastic
Iso_bi_lin	Elastic-plastic with bi-linear isotropic hardening
Iso_non_lin	Elastic-plastic with non-linear isotropic hardening
Kin_bi_lin	Elastic-plastic with bi-linear kinematic hardening
Johnson	Johnson Cook

Figure 6-14 depicts the FE calculated residual stress depth profiles by variable material model and DR force of 50 N. In the longitudinal direction, see Figure 6-14 a), the bi-linear models with isotropic elastic-perfect plastic- or kinematic hardening deliver similar results with pronounced compressive stress maximum on the surface. Both models with bi-linear and non-linear isotropic hardening shift the compressive stress maximum deeper into the material. The Johnson Cook model deliver different shape stress profile, which compared to the profiles seen in the available literature and the later shown x-ray experimental data, can be considered as unrealistic. In the transverse direction, see Figure 6-14 b), all four material models with isotropic or kinematic hardening deliver similar stress profiles with the greatest difference of app. 150 MPa. The Johnson Cook model lead again to different stress profile, shifting the maximal compressive stress towards the surface and reducing the stress impact depth.

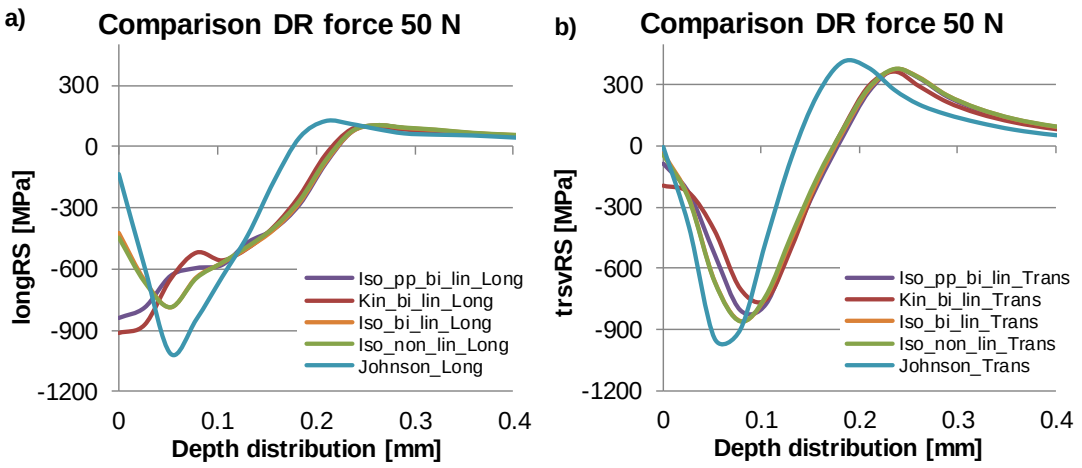

Figure 6-14: FE calculated residual stress depth distributions after DR with force of 50 N by variation of the material model; a) longitudinal residual stresses and b) transverse residual stresses

Figure 6-15 describes the FE calculated residual stress depth profiles by the same material model variation and DR force of 100 N. In the longitudinal direction, see Figure 6-15 a), the bi-linear models with isotropic hardening or kinematic hardening deliver the highest stress impact depth. The bi-linear isotropic elastic-perfect plastic and the bi-linear kinematic models lead to maximal compressive residual stress on the surface. The bi-linear and non-linear isotropic models shift the compressive stress maximum deeper into the material, and the Johnson Cook model predicts again quite different stress profile with very high compressive stress maximum. In the transverse direction, Figure 6-15 b), the near-surface stresses are similar for all material models, and the maximal compressive stress differs with less than 150 MPa. The Johnson Cook model deliver the compressive stress maximum closest to the surface followed by the non-linear and bi-linear elastic-perfect-plastic models with isotropic hardening, the bi-linear isotropic and lastly the bi-linear kinematic model. The stress impact depth was similar for the models Johnson Cook, isotropic non-linear and bi-linear elastic-perfect plastic. The bi-linear kinematic and isotropic models shift the stress impact depth deeper into the material.

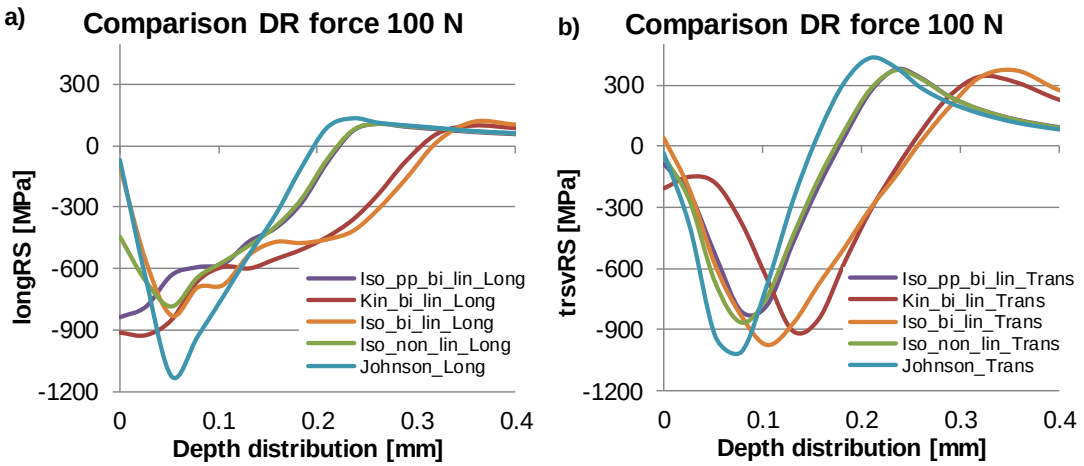

Figure 6-15: FE calculated residual stress depth distributions after DR with force of 100 N by variation of the material model; a) longitudinal residual stresses and b) transverse residual stresses

It can be concluded that the linearity of the material model, as well as its definition, plays an important role in the calculation of the residual stresses after DR, especially at higher DR force. The shape of the stress depth profiles was similar for all material models but the Johnson Cook, which considering the model calibration from the previous section, did not fit as good as the rest models to the test data. Still, near the surface (up to 50 µm depth), the models with isotropic or kinematic hardening deliver stresses differing with up to -800 MPa. This observation emphasises the material behaviour description as one of the most crucial factors for the FE prediction of the residual stresses after DR. Commonly for all material models is the FE calculated moderate tensile residual stresses in the transverse direction at higher depths. The FE calculated stress depth profile shapes from this section were qualitatively compared to the presented in subchapter 7.3 x-ray diffraction residual stress depth profiles shapes, and it was found that the non-linear model with isotropic hardening fitted the best the experimental data and therefore was employed for the FE analysis described in subchapter 7.1

7 Residual stress analysis of pre-machining and deep rolling by finite element modelling and x-ray diffraction

It is known that residual stresses are crucial for fatigue strength. I.e. tensile stresses promote crack formations, thus leading to premature parts' failure, and compressive stresses retard crack formations and propagations, thus contributing to more extended parts' lifetime. Accordingly, the focus of this thesis lay on the residual stress analysis of pre-machined and deep rolled specimens performed using two different approaches: finite element modelling and x-ray diffraction.

Subchapter 7.1 deals with the finite element analysis of the surface and depth residual stress distributions after DR with a tool diameter of 6.35 mm and by variable DR process parameters. In subchapter 7.2 was attempted the further utilisation of the DR process using mechanical pre-stressing of the work piece. Here, the pre-stressing was defined as a percentage of the material's yield strength, and the pre-stressing direction was varied. Additionally, the interdependencies between variable pre-stress state and DR pressure were investigated.

Subchapter 7.3 focuses on the experimental x-ray diffraction determination of the residual stress state of pre-machined and/or deep rolled specimens. Here, two different measurement devices with similar configurations were employed to analyse the influence of the measurement devices on the determined residual stress values. Additionally, some measurement parameters were varied, and their effect on the results was discussed. The pre-machining state (milling or milling + polishing) and the DR process parameters: pressure, overlapping percentage and number of overturns were varied. For all states and parameter variations, the surface and depth residual stress profiles were determined.

In the last subchapter 7.4, the most significant parameter cases from both finite element analysis and x-ray diffraction were compared together, and the plausibility of the FE models and the x-ray diffraction measurements was discussed.

7.1 Finite element analysis of the surface and depth residual stresses after DR

Subchapter 7.1 deals with the finite element modelled DR parametrical study by fixed DR tool diameter of 6.35 mm. In Table 7-1 is plotted the FE modelling design with the corresponding parameter variations. For a better visibility, the varied process parameter is marked in yellow. The residual stress surface distribution was determined in the middle of the DR trace in perpendicular to the trace direction, where the zero x-coordinate describes the middle of the DR trace. By DR with overlapping, the zero x-coordinate depicts the middle of the first (later overlapped) trace.

Table 7-1: FE modelling design - DR with HG 6

Process parameters	
DR pressure	**Overlapping**
20 MPa	0 %
25 MPa	0 %
32 MPa	0 %
40 MPa	0 %
40 MPa	25 %
40 MPa	50 %
40 MPa	75 %
40 MPa	90 %

The first results shown in Figure 7-1 depicts the residual stress surface distribution by variable DR pressure. In Figure 7-1 a) are plotted the surface profiles in the longitudinal direction (longRS). Here, it is visible that the surface area affected by the DR expands with increasing the DR pressure (at 20 MPa – app. ± 0.43 mm and at 40 MPa – app. ± 0.52 mm). Notable is that at 20 MPa DR pressure, the highest compressive stresses were determined and the surface profile's shape of this pressure level differs from the rest profiles.

In Figure 7-1 b) are represented the residual stress surface profiles in the transverse direction (trsvRS). Here, all profiles compared to those in the longitudinal direction differ significantly as shape. This deviation can be explained by the anisotropic plastic flow of the material during treatment. Initially, when the contact pressure between the DR tool and the work piece is established, the material flows in both longitudinal and transverse directions. When the DR tool starts to roll over the work piece, it pushes material out of the generated DR trace in the direction perpendicular to the DR trace. This leads to low tensile stresses in the trace. The pushed material (so-called "peel out") is compressed in the direction out of the generated DR trace leading to compressive residual stresses at the regions of the peel outs (see (Schulze, 2015 c)).

In the transverse direction, the similar observation was made as in longitudinal direction; namely, the surface zone affected by the DR process expands with increasing the DR pressure (at 20 MPa – app. ± 0.43 mm and at 40 MPa – app. ± 0.62 mm). The maximal compressive residual stress is very high, app.-929 MPa, which is very close to the yield strength of the material (modelled as 1002 MPa). It is also notable that a saturation point was achieved at DR pressure of 32 MPa, where the maximal compressive residual stress was determined. At DR pressure of 40 MPa, the stress affected zone still expands, but the maximal compressive residual stress is lower compared to the treatment with 32 MPa DR pressure.

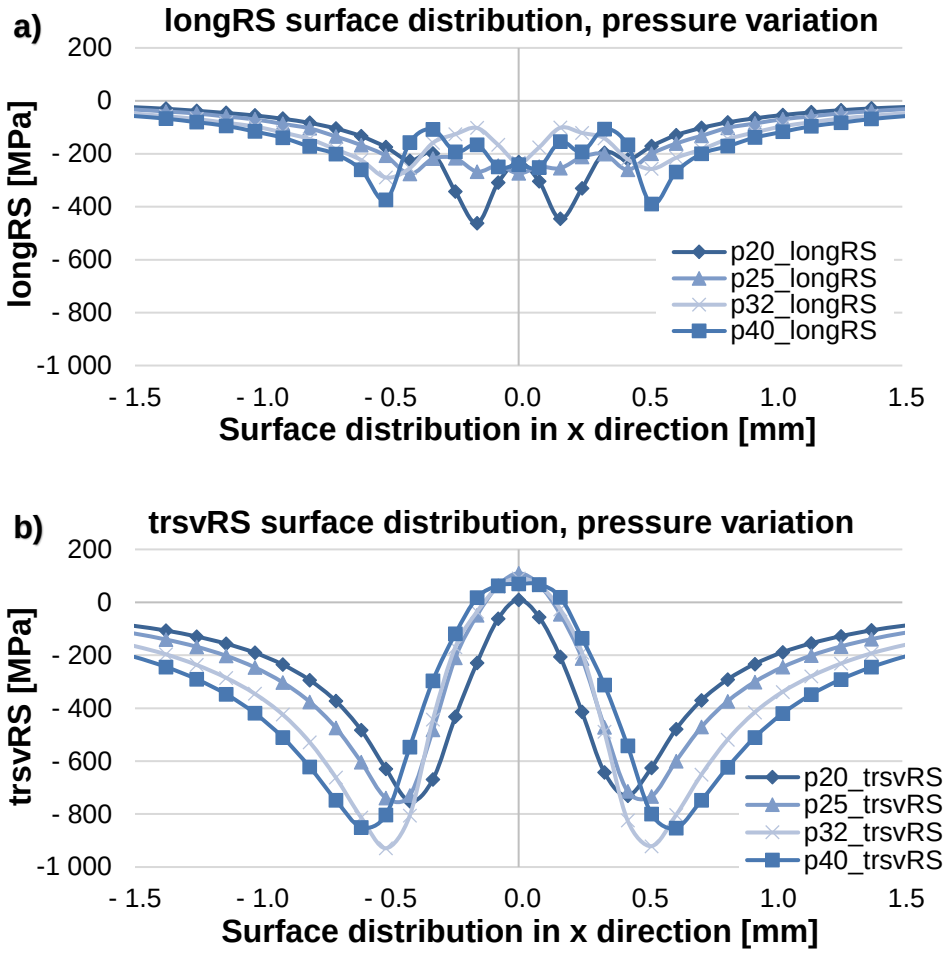

Figure 7-1: FEM surface residual stresses after DR with variable pressure: a) longitudinal direction and b) transverse direction

The next process variation was done as fixing the DR pressure to 40 MPa and varying the overlapping percentage. In Figure 7-2 are plotted the longitudinal residual stress surface profiles by overlapping from 25 % to 50 % (Figure 7-2 a)) and overlapping from 75 % to 90 % (Figure 7-2 b)), where the 90 % overlapping was realised by defining two or three traces (designation 90%o.l._2). As expected, due to the geometrically defined overlapping parameter, lower overlapping percentage generates wider affected DR zone (25 % - app. 1.66 mm; 90 % - app.1.14 mm). Notable is that up to 75 % overlapping, the residual stress distribution is significantly inhomogeneous with a maximal compressive value of an app. -600 MPa. The 90 % overlapping (both variations with two or three traces) deliver quite different profile shape, with single compressive stress peak of an app. -1060 MPa. When comparing both 90 % overlapping variations, with two (90%o.l.) or three (90%o.l._2) traces, the profile with three traces has compressive stress peak shifted to the +x direction side of the profile, thus forming a small plateau region in the zone of the overlapping (x-coordinates -0.25 mm to 0.0 mm). Therefore, if applying more overlapping traces so that an entire surface will be treated, this compressive stress peak will be shifted in the direction out of the treated zone. If this assumption is correct, the treatment with 90 % overlapping could generate relatively homogeneous stress zone at the level of an app. -500 MPa.

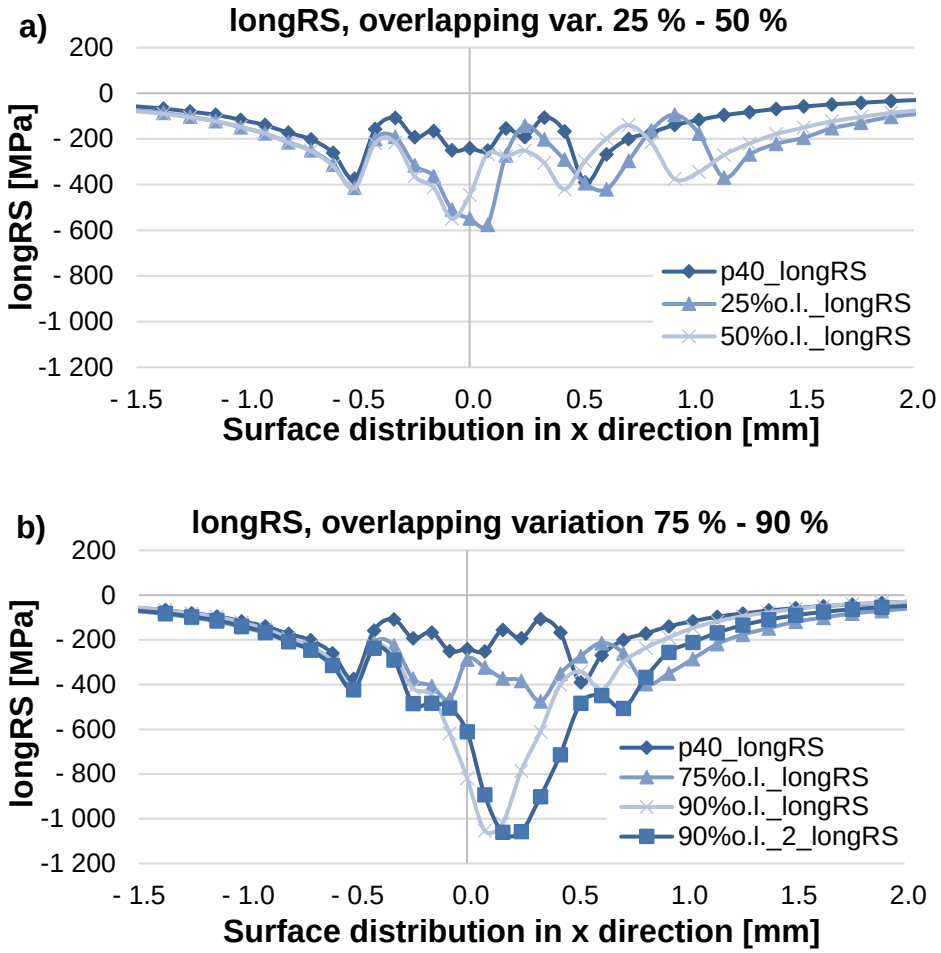

Figure 7-2: FEM longitudinal surface residual stresses after DR with variable overlapping: a) 25 % and 50 % overlapping and b) 75 % and 90 % overlapping

Figure 7-3 describes the surface transverse residual stress profiles by the same overlapping variation as shown in Figure 7-2. Here, up to 50 % overlapping (see Figure 7-3 a)), the surface profiles exhibit double stress peak. Such abrupt change in the residual stress state is in general disadvantageous for the fatigue strength of the treated component. The treatment with 75 % or with 90 % overlapping induces in the overlapping zone (see Figure 7-3 b), x-coordinates -0.62 mm to -0.16 mm) relatively smooth residual stress zone with very high compressive stresses of up to -1090 MPa, which is close to the assigned ultimate strength of the material of 1144 MPa. Compared to the 75 % overlapping treatment, both treatments with 90 % overlapping shift the maximal compressive stress to higher compression and shift the peak values (see x-coordinate app. +0.25 mm) from slight tensile to slight compression. If following the same hypothesis as for the longitudinal profiles, it could be considered that when employing an overlapping of 90 % and treating an entire surface, the final surface residual stress state could be on the level of an app. -800 MPa to -1000 MPa.

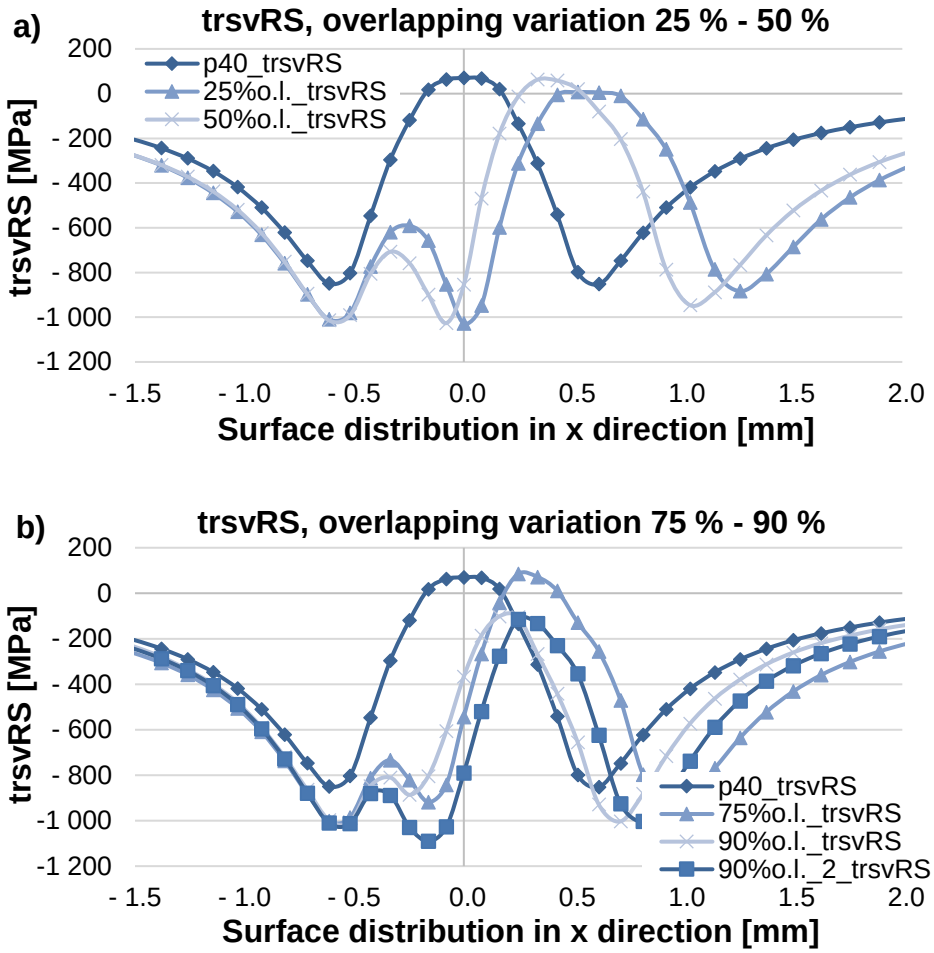

Figure 7-3: FEM transverse surface residual stresses after DR with variable overlapping: a) 25 % and 50 % overlapping and b) 75 % and 90 % overlapping

The next part of this parametrical study focuses on the investigation of the residual stress depth distributions by the same parameter variations, as shown in Figure 7-2 and Figure 7-3.

It is important to note that the information for the residual stress depth distribution is in general crucial for the prediction of the fatigue behaviour of the treated parts and cannot be substituted only by surface residual stress profiles determination. The so-called stress impact depth is an important parameter, which characterises the depth where the residual stresses tend to zero. The presence of compressive residual stresses deeper into the material, not only high as an amount, can improve fatigue strength. This happens because compressive stresses can retard the propagation of existing cracks and can prevent cracks formation even by the presence of tensile residual stresses on the surface. The definition “crack arrest/closure” describes this phenomenon (Gardin, et al., 2005).

Figure 7-4 depicts the stress depth profiles of DR specimens with variable pressure. In the longitudinal direction, Figure 7-4 a), increasing the DR pressure does not influence the magnitude of the maximal compressive residual stress, which for all variations lays at app. -750 MPa. In contrary, the stress impact depth increase from an app. 0.55 mm for DR pressure of 20 MPa to 0.71 mm for 40 MPa DR pressure.

In the transverse direction, Figure 7-4 b), the shape of the depth profiles differs significantly to this of the profiles in the longitudinal direction. Here, the near-surface stress is slightly tensile instead of moderate compressive, and the maximal compressive stress reaches an app. -900 MPa for DR pressure 40 MPa. In higher depth, for all variations, there is a presence of moderate tensile stress of app. 350 MPa to 430 MPa. The higher DR pressure raises the maximal compressive stress, the sub-surface tensile stress and the stress impact depth.
The anisotropy of the stress depth profiles in both directions should have the same source as the anisotropy of the stress surface profiles, namely the plastic flow of the material during processing.

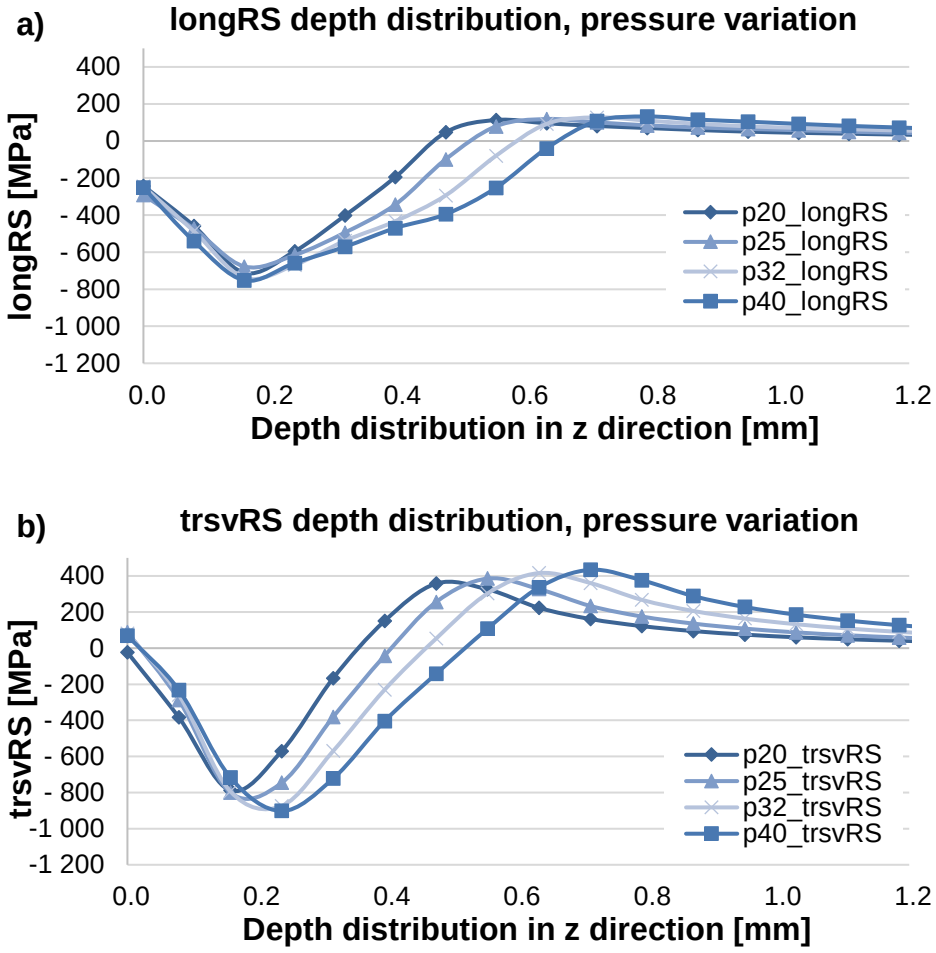

Figure 7-4: FEM residual stress depth distribution after DR with variable pressure: a) longitudinal direction and b) transverse direction

Figure 7-5 depicts the stress depth profiles in the longitudinal direction of DR specimens by fixed DR pressure of 40 MPa and variable overlapping percentage. Here, the depth profiles were determined in the middle of the first (later overlapped) trace, Figure 7-5 a), or in the middle of the second (overlapping) trace, Figure 7-5 b). The aim was to characterise the stress field generated by the complex material flow during the overlapping. The depth profiles in the first trace show sporadically distributed near-surface stresses, where the highest compressive stress exhibit the work piece treated with

90 % overlapping with the app. -800 MPa (compared to single-trace treated – app. -280 MPa). The shape of the near-surface stress profiles changes from parabolic (single-trace) with maximal compressive stress in 0.6 mm depth (app. - 740 MPa), through plateau-near for the overlapping 25 % - 75 % (compressive stress on the level of an app. -500 MPa) and to exponential for the overlapping 90 %, with maximal compressive stress on the surface (app. -800 MPa). The stress impact depth is very similar for all depth profiles: app. 0.71 mm.
The stress depth profiles determined in the second trace are plotted in Figure 7-5 b). Here, all profiles up to overlapping of 75 % showed similar stress distribution with near-surface values of an app. -250 MPa to -380 MPa, the maximal compressive stress of app. -800 MPa and stress impact depth of app. 0.71 mm to 0.78 mm. The profile of the treatment with 90 % overlapping differs significantly near the surface, exhibiting very high compressive stress of app. -1060 MPa.

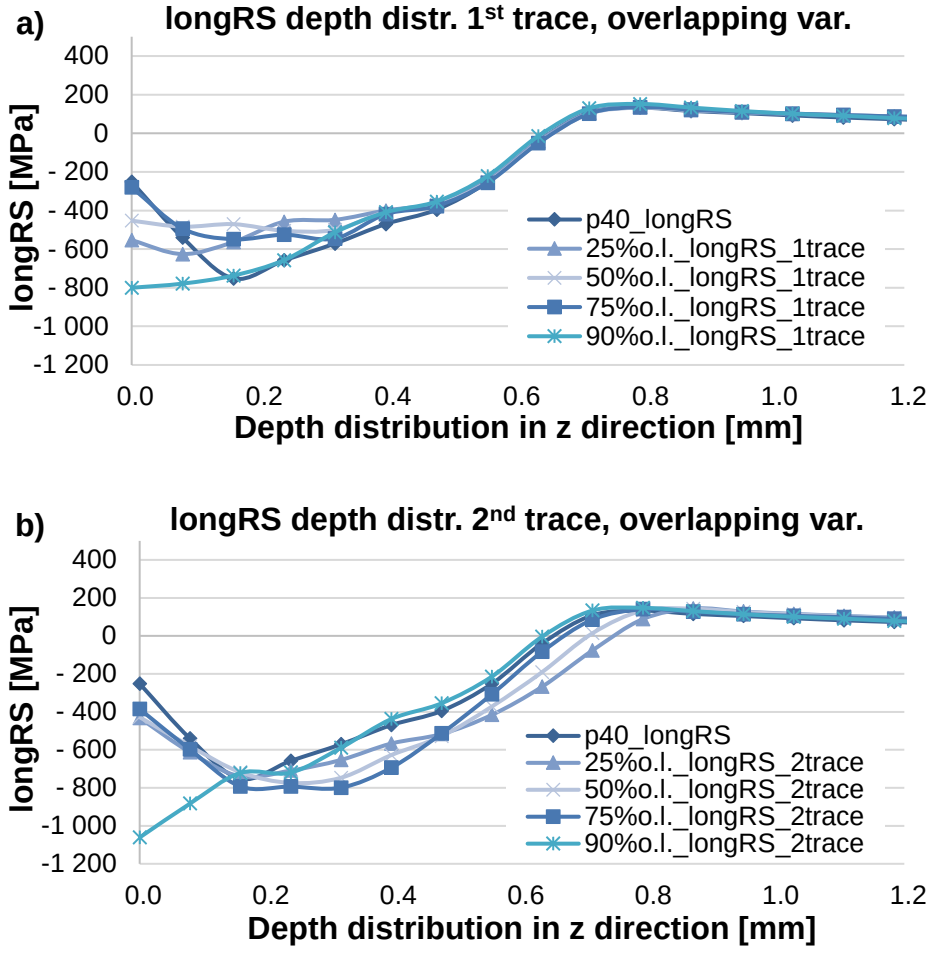

Figure 7-5: FEM longitudinal residual stress depth distribution after DR with variable overlapping: a) determined in the 1st DR trace and b) determined in the 2nd DR trace

Figure 7-6 illustrates the depth profiles of the same overlapping variations, but the stresses were determined in the transverse direction. In the first trace, near the surface, the stress distribution for the different overlapping percentages is very different, from an app. +70 MPa (single-trace) to -1040 MPa for 25 % overlapping. The near-

surface stress values decrease (from high to low compression) with increasing the overlapping percentage. For treatment with 90 % overlapping, the value is still higher compressive compared to single-trace treatment, but it is lowest compressive compared to the rest treatments with overlapping.
In the second trace, all profiles are relatively similar: near the surface, the stress values for all specimens but 90%o.l. are minor tensile of an app. +60 MPa to +100 MPa and only the 90%o.l. has compressive stress of app. -200 MPa. In depth, all profiles have a maximum of an app. -920 MPa to -1080 MPa and the stress impact depth is similar as well.

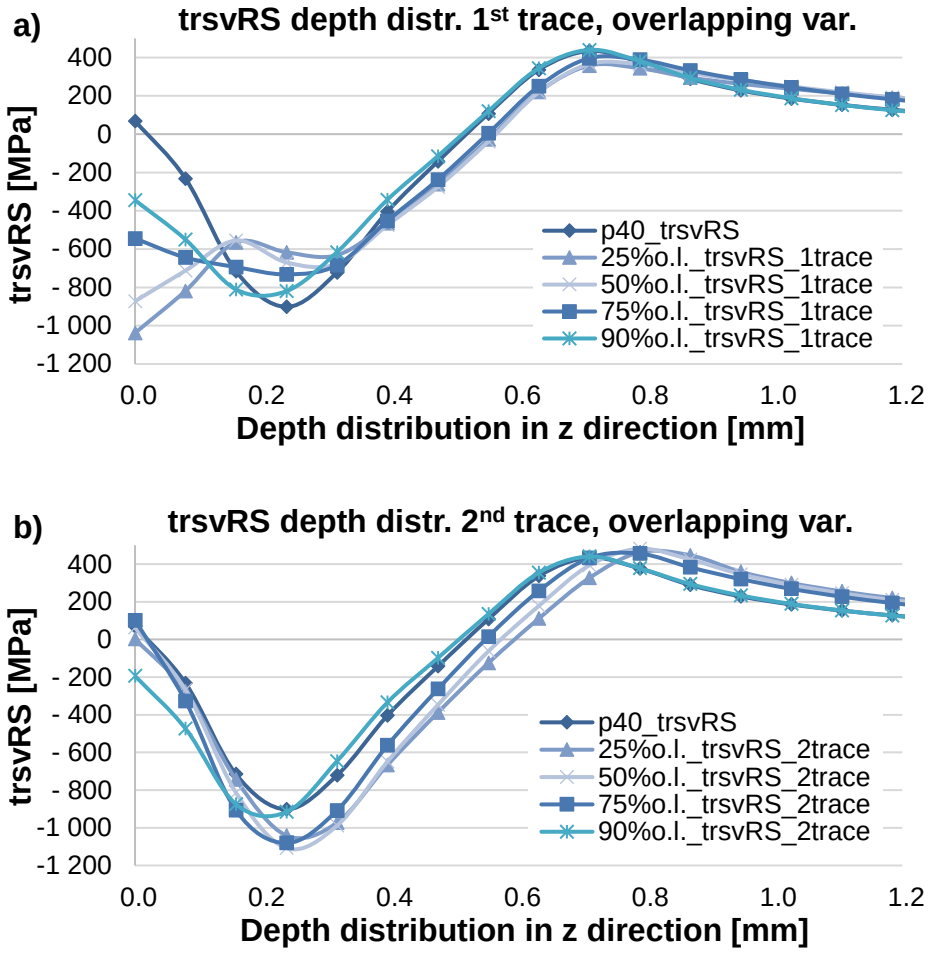

Figure 7-6: FEM transverse residual stress depth distribution after DR with variable overlapping: a) determined on the 1st DR trace and b) determined on the 2nd DR trace

The results from Figure 7-5 and Figure 7-6 confirm that the overlapping parameter has a significant influence on the residual stress near-surface distribution (up to a depth of 0.3 mm) and the place for the stress determination is crucial. Therefore, from the FE output databases of the performed FE simulations, 2D graphics were extracted (see Figure 7-7), where the surface- and depth residual stresses in longitudinal and transverse directions for all overlapping variations and the single-trace treatment can be compared. The scales were kept constant for easier comparison (longitudinal direction: red = +200 MPa, blue = -1150 MPa; transverse direction: red = +550 MPa,

blue = -1150 MPa). The top four graphics show the longitudinal residual stress distribution by single-trace treatment or with overlapping of 25 % to 75 %. On the surface, the residual stresses are slight compressive and become more homogenous with increasing the overlapping percentage. In depth, only the treatment with 75 % overlapping lead to relatively homogenous stress field at the overlapped zone. Still, the double light-blue spots under the surface are a hint for a not uniform stress field. The four graphics below those of the longitudinal stress distribution illustrate the transverse stress distribution of single-trace treatment or with overlapping of 25 % to 75 %. On the surface, a highly disordered stress field can be observed, where only the 75 % overlapping generated relative uniform stress field at the overlapped zone (left hand side light- and dark blue zone, stresses app. -700 MPa to -1000 MPa). Below the surface, the tensile stress zone becomes wider for lower overlapping percentage, with maximal tensile stress shifted to the area of the second (overlapping) trace.

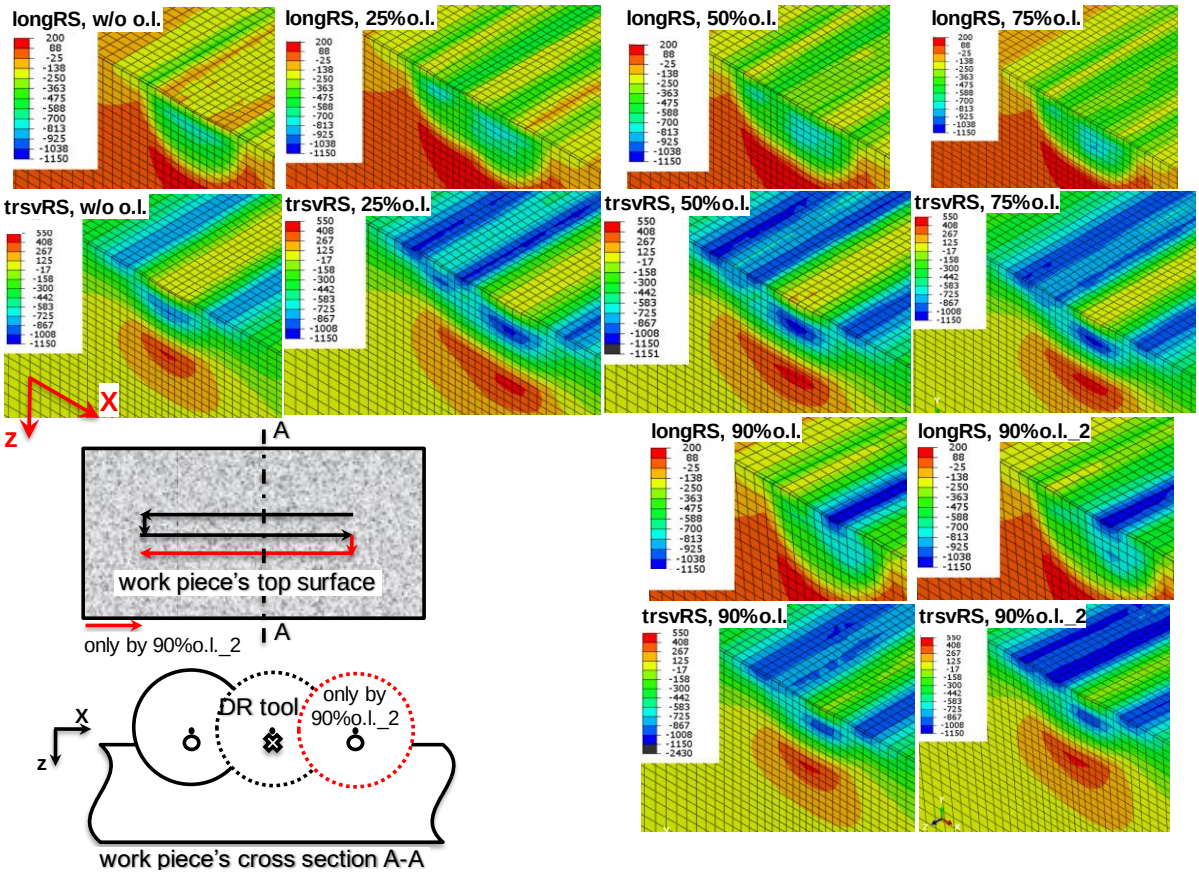

Figure 7-7: FEM overview of the surface and depth residual stresses in longitudinal (long) and transverse (trsv) direction after DR without overlapping (w/o o.l.) or with variable overlapping of 25 %, 50 %, 75 % and 90 %

The 90 % overlapping realised as two or three traces is depicted in the lower right corner in Figure 7-7. In the longitudinal direction, on the surface at the overlapped zone, the stress distribution is relatively smooth with moderate negative values. The compressive stress peak is shifted towards out of the trace, meaning when treating an entire plane surface, this stress peak will be shifted to the edge of the specimen. In the

transverse direction, the 90 % overlapping with three traces leads to high compressive and relatively smooth stress zone on the surface, and in depth, the tensile stress zone is shifted in the direction out of the trace.

To conclude this parametric study, the following can be summarised:

- Residual stress surface distribution
    - Pressure variation – a significant stress anisotropy was observed in longitudinal compared to transverse directions → anisotropic plastic flow of the material during treatment.
    - Pressure variation – in both directions, the surface area affected by the DR expanded with increasing the DR pressure.
    - Pressure variation – in the transverse direction, the maximal compressive residual stress was very high, up to app.-929 MPa, which was very close to the yield strength of the material.
    - Pressure variation – in the transverse direction, a stress saturation point was achieved at DR pressure of 32 MPa.
    - Overlapping variation – up to 90 % overlapping led to inhomogeneous stress field, which became smoother by increasing the overlapping percentage.
    - Overlapping variation – in the longitudinal direction, up to 75 % overlapping generated moderate compressive stress field, and only 90 % overlapping exhibited a compressive stress peak, which was shifted towards out of the trace.
    - Overlapping variation – in the transverse direction, all overlapping variations but this of 90 %, generated not uniform stress field at the overlapped area.
- Residual stress depth distribution
    - Pressure variation – a significant stress anisotropy was observed in longitudinal compared to transverse directions → anisotropic plastic flow of the material during treatment.
    - Pressure variation – in both directions, the stress impact depth expanded with increasing the DR pressure.
    - Overlapping variation – in both directions, there was a complex 3D stress field, which profoundly differed by changing the overlapping percentage or the place of determination.
    - Overlapping variation – the 90 % overlapping with three traces lead to relatively smooth stress field in depth, and the presented sub-surface tensile stress peak in the transverse direction was shifted towards out of the trace.
    - For all variations, in some areas were determined very high compressive residual stresses, which had an amount slightly over the defined yield strength of the treated material.

7.2 Finite element analysis of pre-stressed deep rolling

The current chapter employs the finite element analysis to utilise further the deep rolling process as applying a pre-stressing the work piece. This unpopular process, called pre-stressed deep rolling or stress rolling, has the aim to increase the induced by the DR compressive residual stresses by adding a defined static mechanical load on the work piece during treatment. After the DR treatment, the work piece is unloaded, and the stress relaxation from the unloading superimpose with the stress relaxation from the DR process. This superimposed relaxation could lead to the generation of larger compressive residual stresses. When using the pre-stressed deep rolling, the residual stress state depends on the DR process parameters themselves, and additionally on the pre-stress amount, the pre-stress direction and the DR treatment direction related to the pre-stress direction. In the preliminary parametrical study, all parameters mentioned above were varied and here, only the most significant results will be discussed. In Table 7-2 is represented the FE modelling design for the pre-stress deep rolling, where a combination between all listed process parameters was accomplished. The pre-stress on the work piece was realised as a four-point bending, and the bending amount was defined as a percentage of the material's yield strength (it is essential that the applied pre-stressing is below the material's elastic limit). The DR process was accomplished on the tensile stressed side of the work piece. An exemplary picture of the pre-stressed DR setup can be seen in Figure 7-8.

Table 7-2: FE modelling design – overview of the process parameters by pre-stressed DR

DR pressure	Bending amount
20 MPa (DR 20 MPa)	0 %
30 MPa (DR 20 MPa)	30 % (PS 30%)
40 MPa (DR 20 MPa)	60 % (PS 60%)
	70 % (PS 70%)

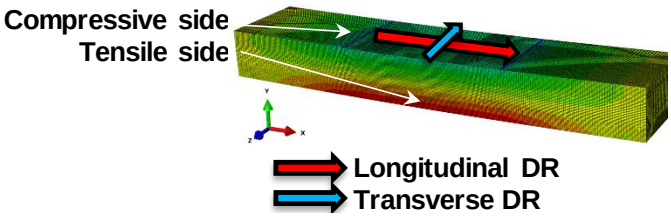

Figure 7-8: FEM pre-stressed DR setup

The first results, see Figure 7-9, illustrate the stress depth profiles after longitudinal tensile pre-stressed DR, by DR pressure of 40 MPa and variable pre-stress amount. The direction of the determined residual stresses refers to the direction of the DR process. The longitudinal stress depth profiles are plotted in Figure 7-9 a). Near the surface, the pre-stressing slightly enhances the compressive residual stresses from an app. -730 MPa for the not pre-stressed work piece to -910 MPa for the 70 % pre-stressed one. The maximum compressive stress remains on the level of app.-950 MPa for all variations (only for longitudinal residual stresses). Still, it is shifted to higher depth

when applying pre-stressing (app. 0.10 mm for not pre-stressed and app. 0.17 mm for 70 % pre-stressed). In depth, the pre-stressing increase slightly the presented low tensile stresses, but the stress impact depth also increases when applying pre-stress (app. 0.67 mm for not pre-stressed and app. 0.87 mm for 70 % pre-stressed).
The transverse stress depth profiles derived by the same pre-stress variations are depicted in Figure 7-9 b). When applying pre-stress, the near-surface residual stresses are shifted from zero to minor tensile (maximum +250 MPa), the maximal compressive stress reduced slightly (app. -890 MPa for not pre-stressed and app -810 MPa for 70 % pre-stressed). Still, the sub-surface tensile stresses remain the same for all variations, but the stress impact depth increase when applying pre-stress (0.69 mm for not pre-stressed and app. 0.87 mm for 70 % pre-stressed).

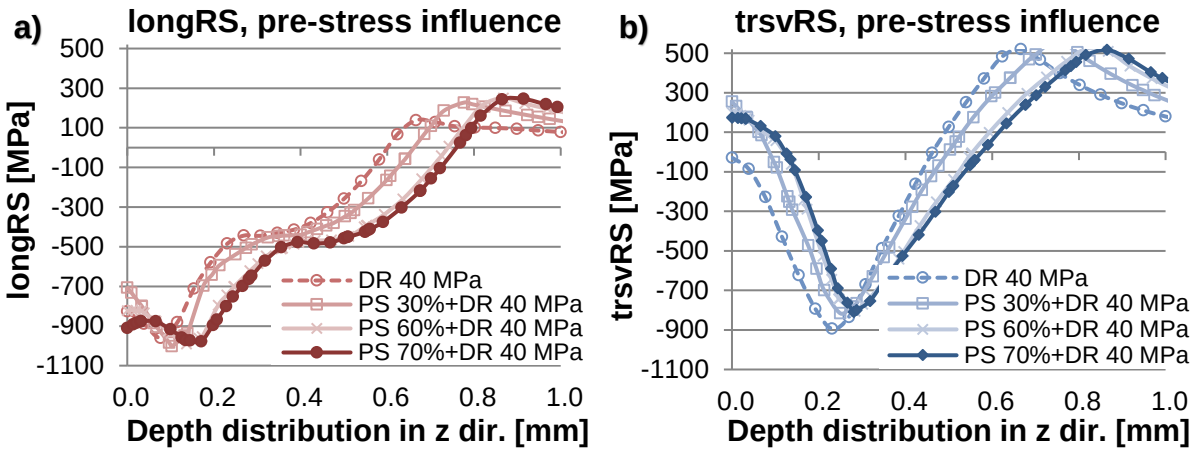

Figure 7-9: FEM influence of the pre-stress (PS) amount on the residual depth profiles after longitudinal pre-stressed DR: a) longitudinal direction and b) transverse direction

Figure 7-10 displays the stress depth profiles by a fixed pre-stress amount (70 %) and by variable DR pressure, and compare them to the not pre-stressed residual stress state. Figure 7-10 a) shows the longitudinal residual stress depth profiles. Near the surface, all profiles show compressive stress of app. -790 MPa to -990 MPa. The pre-stressing shifts the maximal compressive stress to higher depth and significantly enhance the stress impact depth (for DR with 20 MPa: w/o pre-stress – 0.38 mm, with pre-stress – 0.69 mm; for DR with 40 MPa: w/o pre-stress – 0.67 mm, with pre-stress – 0.87 mm). The more significant relative improvement (comparison w/o vs with pre-stress) was achieved by DR with a pressure of 20 MPa.
The transverse stress depth profiles are depicted in Figure 7-10 b). Near the surface, the pre-stressing shifts slightly the stresses from minor compressive to minor tensile. In depth, the maximal compressive stress is reduced insignificantly, and the presented tensile stress at higher depth remains almost the same for all profiles. Still, the pre-stressing leads to deeper maximal compressive stress and significantly higher stress impact depth (for DR with 20 MPa: w/o pre-stress – 0.38 mm, with pre-stress – 0.69 mm; for DR with 40 MPa: w/o pre-stress – 0.67 mm, with pre-stress – 0.87 mm). The more significant relative improvement (comparison w/o vs with pre-stress) was achieved again by DR with a pressure of 20 MPa.

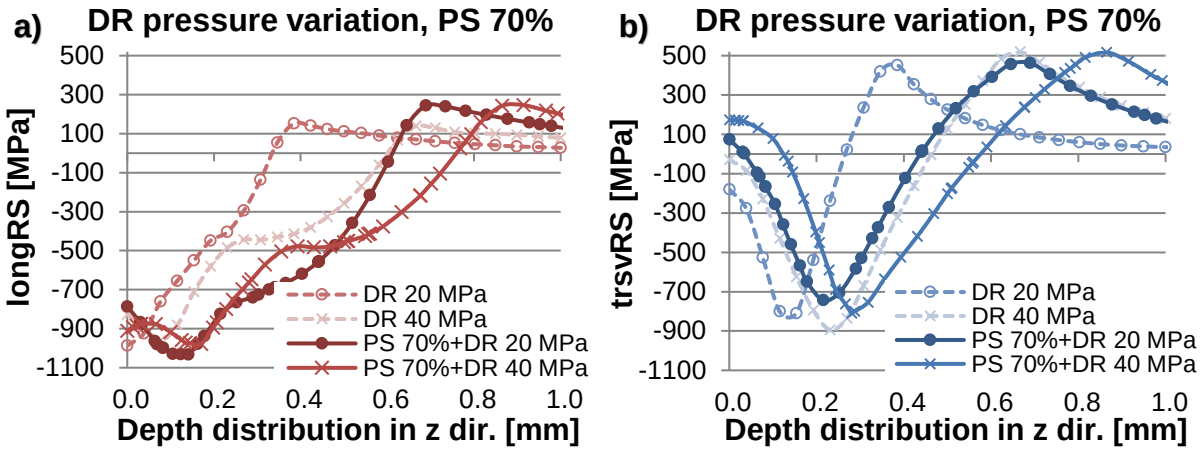

Figure 7-10: FEM influence of the DR pressure by fixed pre-stress (PS) amount on the RS depth profiles after pre-stressed DR: a) longitudinal direction and b) transverse direction

For easier comparison of the varied parameters and their influence on the residual stress depth distribution, based on the results from Figure 7-9 and Figure 7-10, the integral tensile- and compressive stress areas as a function of the depth were calculated for both longitudinal and transverse residual stress depth profiles. The explanation scheme is plotted in Figure 7-11.

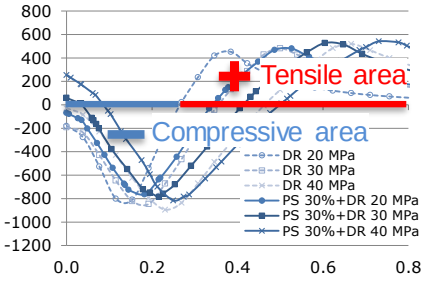

Figure 7-11: Scheme for the calculation of the tensile and compressive integral areas of the residual stresses after pre-stressed DR

In Figure 7-12 are illustrated the calculated integral residual stress areas by variation of the pre-stress and the DR pressure. Figure 7-12 a) describes the longitudinal compressive and tensile stress areas. Concerning the compressive areas, the most significant nominal improvement shows the treatment with 70 % pre-stress (compared to not pre-stressed). For all pre-stress variations (including w/o pre-stressing), higher DR pressure leads to greater compressive stress area. Still, the relative enhancement of the compressive stress is greater by DR without pre-stressing (although, as nominal much lower than the improvement by DR with 70 % pre-stress). The tensile stress areas for all variations (only from Figure 7-12 a)) are much lower than the compressive areas and vary from an app. 68 MPa.mm to 126 MPa.mm.

Figure 7-12 b) depicts the transverse compressive and tensile stress areas. Here, the highest compressive stress area has the specimen treated with DR pressure of 40 MPa without pre-stressing. For all pre-stress variations (incl. w/o pre-stress), increasing the DR pressure leads to a larger compressive stress area. Increasing the

pre-stressing amount (not compared to w/o pre-stressing) slightly enhance the compressive stress areas. Still, when compared to the not pre-stressed state, as nominal, the compressive stress areas are higher with pre-stressing only for DR pressure of 20 MPa. The tensile stress areas are approaching as values the compression ones and in case of pre-stressing, are even higher as an amount. The higher DR pressure leads in almost all cases (only for Figure 7-12 b)) to larger tensile stress areas, where the relative difference is highest by DR without pre-stressing. As nominal, by DR with 20 MPa and 30 MPa, the largest tensile stress areas possess the specimens treated with DR with 70 % pre-stress. Only for DR pressure 40 MPa, increasing the pre-stressing do not influence the amount of the tensile stress areas.

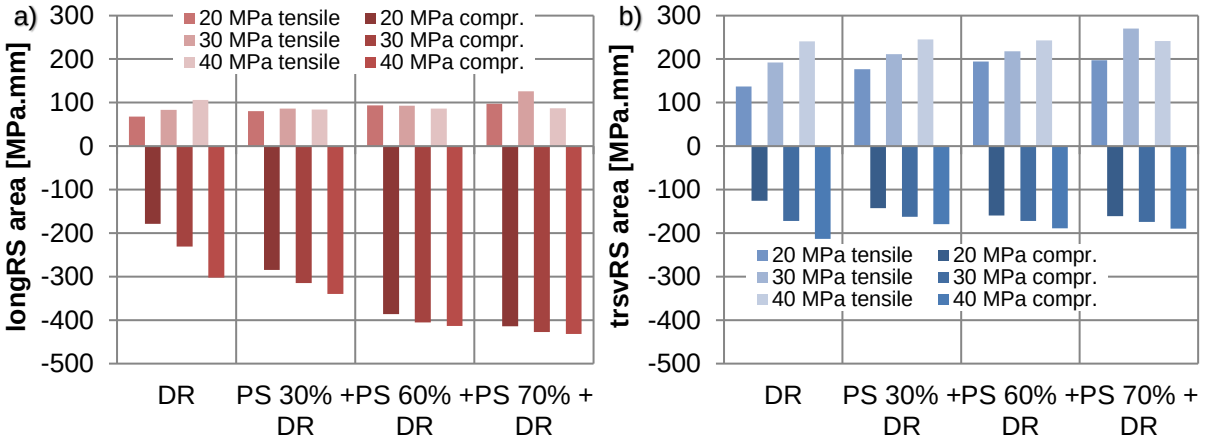

Figure 7-12: Integral residual stress areas by variation of the PS and variation of the DR pressure: a) longitudinal direction and b) transverse direction

Additionally to the results shown in this chapter, the stress depth profiles were investigated by pre-stressed DR on the compressive side of the work piece and by pre-stressed DR transverse to the pre-stressing (see Figure 7-8). All these variations were more unfavourable compared to the presented results.

To summarise, pre-stressing the work piece during DR process can have a favourable effect on the residual stress field, where the pre-stress direction and the DR direction play a significant role by the generation of the residual stresses. In the investigated case, applying longitudinal DR on the tensile pre-stressed side of the work piece greatly enhanced the longitudinal compressive residual stresses in depth, by mainly increasing the stress impact depth. The maximal compressive residual stress values were for all variations very high (between app. -920 MPa and -1030 MPa). The transverse stress depth profiles had as usual different shape (compared to the longitudinal stress depth profiles), and the pre-stressing additionally enhanced this anisotropy. The pre-stressing caused here slightly lower compressive stress maximum, but again the stress impact depth was positively influenced. As a conclusion, it can be stated that applied pre-stressing had a positive effect on the residual stress depth distribution. However, stress anisotropy has to be considered when using this hybrid process.

7.3 X-ray diffraction residual stress determination of pre-machined and deep rolled specimens

The following subchapter takes a central place in this thesis, as the comprehensive characterisation of the residual stress state after different pre-machining treatments and consecutive deep rolling by variable process parameters aims to contribute to better understanding the investigated process and the considered process chains.
In Table 7-3 is depicted the experimental design of the XRD residual stress determination of milled + deep rolled specimens, with the corresponding specimens' designation and the varied process parameters. For this parametrical study, two different diffractometers were employed to investigate the possible devices' influence on the determined residual stress profiles.

Table 7-3: Experimental design of the XRD residual stress determination of milled + DR specimens

Specimen No	Process parameters		
	DR pressure	Overturn	Overlapping
M12	20 MPa	1	0 %
M13	25 MPa	1	0 %
M14	32 MPa	1	0 %
M15	40 MPa	1	0 %
M16	40 MPa	2	0 %
M17	40 MPa	3	0 %
M19	40 MPa	7	0 %
M20	40 MPa	1	25 %
M21	40 MPa	1	50 %
M22	40 MPa	1	75 %

Table 7-4: Chapter location of the XRD parametrical study of milled + DR specimens

Specimen No	Residual stress determination, measurement devices and chapter location		
	PANalytical, RS-surface	Seifert, RS-surface	Seifert, RS-depth
M12	7.3.1	7.3.3	7.3.4
M13	7.3.1	x	x
M14	7.3.1	7.3.3	x
M15	7.3.1	7.3.3	7.3.4
M16	7.3.1	x	x
M17	7.3.1	x	x
M19	x	7.3.3	7.3.4
M20	7.3.1	x	x
M21	7.3.1	x	x
M22	7.3.1	7.3.3	7.3.4

Table 7-4 serves as an orientation map regarding the residual stress determination (surface or depth), the employed measurement devices and in which sub-chapter the corresponding results can be found.

In Table 7-5 is described the experimental design of the XRD residual stress determination and chapter location of milled + polished + DR specimens.

Table 7-5: Experimental design of the XRD residual stress determination and chapter location of milled + polished + DR specimens

Specimen No	Process parameters			Residual stress surface/depth determination and chapter location	
	DR pressure	Overturns	Overlapping	Seifert RS-surface	Seifert RS-depth
P11	20 MPa	1	0 %	7.3.3	7.3.4
P8	40 MPa	1	0 %	7.3.3	7.3.4
P4	40 MPa	7	0 %	7.3.3	7.3.4
P2	40 MPa	1	75 %	7.3.3	7.3.4

The subchapter 7.3 consists of 6 subchapters, where the following investigations were performed: subchapter 7.3.1 focuses on x-ray diffraction the surface residual stress determination of milled + DR specimens realised with diffractometer PANalytical Empyrean. The residual stresses in longitudinal and transverse directions were determined in the middle of the DR trace, by variable DR pressure, number of overturns or overlapping percentage. In subchapter 7.3.2 were investigated some influences of the measurement and evaluation parameters on the measurement accuracy with diffractometer Seifert, XRD 3000 PTS. The surface residual stress state of DR specimens with variable process parameters and different pre-machining states determined with diffractometer Seifert, XRD 3000 PTS, was presented in subchapter 7.3.3. The same specimens and the same diffractometer were employed for the study of the in-depth residual stress state, and the corresponding stress depth profiles are shown in subchapter 7.3.4. Subchapter 7.3.5 presents the influence of the measurement device on residual stress surface distribution of milled + DR specimens by variable process parameters. In subchapter 7.3.6 were compared the residual stress surface and depth profiles treated with fixed process parameters but with variable pre-machining sequence and thus the influence of the pre-machining state on the final residual stress state after DR was investigated.

7.3.1 X-ray diffraction surface residual stress determination of milled and DR specimens – diffractometer PANalytical Empyrean

Subchapter 7.3.1 focused on the x-ray diffraction the surface residual stress determination of milled + DR specimens by fixed tool diameter of 6.35 mm and variable DR pressure, number of overturns or overlapping percentage. The stress values were determined with diffractometer PANalytical Empyrean.

Figure 7-13 shows the in-trace surface residual stress distribution of milled + DR specimens, where the longitudinal (designation “long”) and the transverse (designation “trsv”) residual stresses were plotted together for easier comparison. In Figure 7-13 a) are illustrated the surface stress values by varying DR pressure. As already seen by the FE residual stress analysis from subchapters 7.1 and 7.2, the typical anisotropy of

the stresses in longitudinal and transverse directions is confirmed by the XRD measurements. In the longitudinal direction, for all specimens there is a presence of low to moderate compressive stresses (between app. -145 MPa and -321 MPa) and in the transverse direction, the stresses are low to moderate tensile (between app. 0 MPa and +350 MPa). The shape of the profiles also differs in both directions, as in the longitudinal direction, there is plateau-near stress distribution, and in the transverse direction, the profile shape is slightly convex. All stress values in the corresponding direction are very close to each other, and when comparing the profiles of the different DR pressure variation, considering the measurement error bars, no clear tendency can be observed. Some asymmetry of the profiles in the transverse direction is visible, which is a sign of possible surface imperfection (especially the value of M12, trsv, at -200 µm) and/or measurement positioning issue.

In Figure 7-13 b) are plotted the surface stress profiles in longitudinal and transverse directions by fixed DR pressure (40 MPa) and by variable number of overturns. Treatment with multiple overturns leads in the longitudinal direction to higher compressive residual stresses and in the transverse direction to lower tensile residual stresses. Still, the stress values of the specimens treated double (M16) or triple (M17) are very similar.

The last parameter variation, namely the overlapping percentage, was performed by fixed DR pressure of 40 MPa and a single overturn, see Figure 7-13 c). Here, the measurement path was adjusted so, that with zero x-coordinate was designated the middle of the first (later overlapped) trace. In both directions, the surface stress profiles for all specimens (overlapping: M20 = 25 %, M21 = 50 % and M22 = 75 %) are asymmetric, without showing a clear tendency, even though the measurement error bars are very small. Still, there is an indistinct trend by overlapping with 75 % of higher compressive residual stresses in the longitudinal direction and lower tensile residual stresses in the transverse direction, compared to the values of the specimens treated with 25 % and 50 % overlapping.

In conclusion, this study confirmed the stress anisotropy in longitudinal and transverse directions. The stress values from the pressure variation did not show any distinct trend, as all laid very close to each other. The multiple overturn positively influenced the stresses in both directions, enhancing the compressive stresses in the longitudinal direction and reducing the tensile stresses in the transverse direction. The surface profiles of overlapping variations were relatively asymmetrical. Still, a vague trend was observed for the 75 % overlapping, compared to 25 % and 50 % overlapping, by the higher compressive stresses in the longitudinal direction and the lower tensile stresses in the transverse direction. Considering the surface stress profiles derived by the finite element models from subchapter 7.1, where the area influenced by the DR was by some parameter variations over 1.5 mm long, a wider surface area for the XRD stress determination needs to be defined.

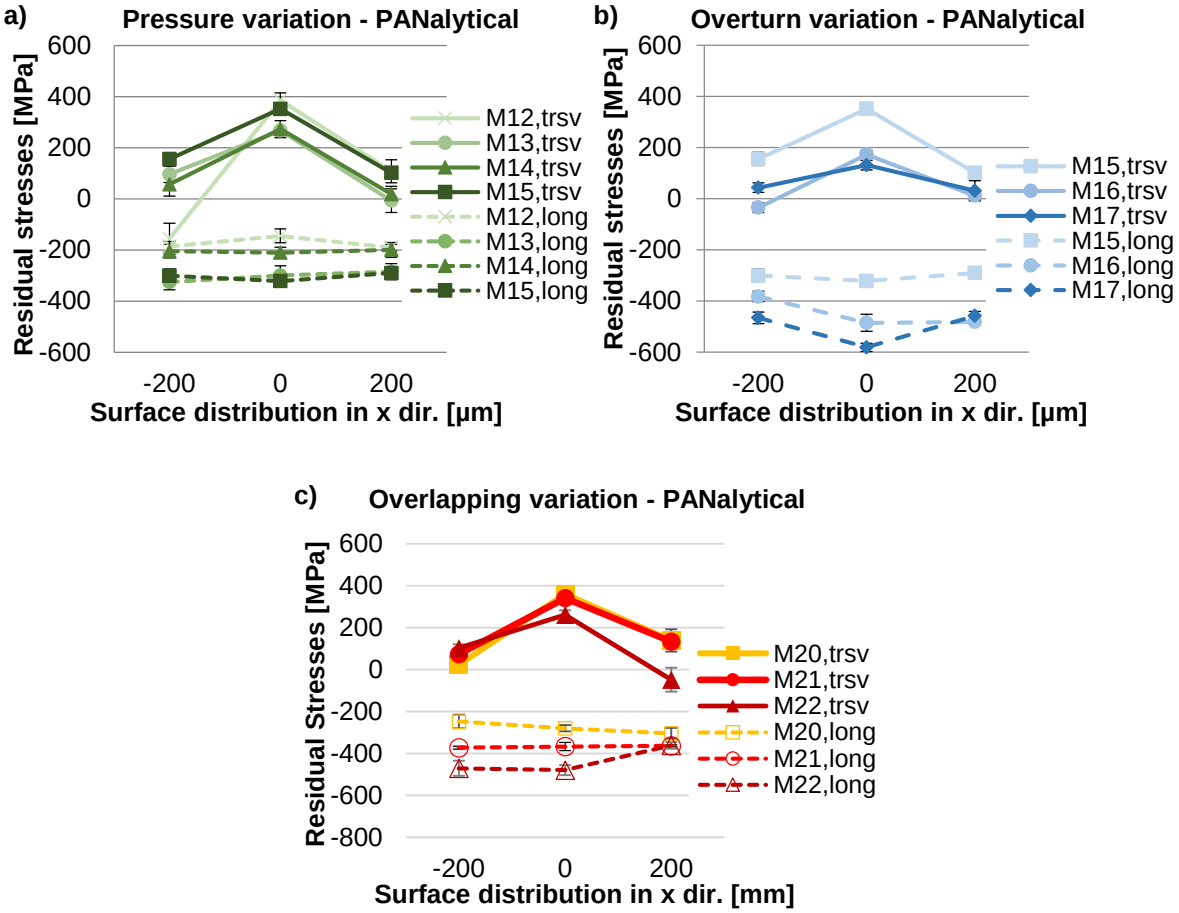

Figure 7-13: XRD residual stress surface distributions of milled + DR specimens measured with diffractometer PANalytical Empyrean by variable process parameters: a) DR pressure variation, b) number of overturn variation and c) overlapping variation

7.3.2 Influences of the measurement and evaluation parameters on the measurement accuracy – diffractometer Seifert, XRD 3000 PTS

In the current chapter, the possible impact of several measurements and evaluation parameters on the XRD residual stress determination will be discussed.

Determination of the diffraction peak position

It is known that the XRD residual stress measurements are based on the determination of the diffraction peak positions by two or more tiltings of the specimen at different angles. Therefore, the correct determination of the peak position is crucial for the precise stress calculation, particularly when the shape of the diffraction peak is asymmetric. For the stress measurements in this section, two methods were chosen, namely the center of gravity (CoG) at 20 % or 70 %. On one randomly chosen specimen, both methods were directly compared, and the depth profiles in the transverse direction were plotted in Figure 7-14. It is important to note that for both depth profiles, the same measurement data was used and only the evaluation of the diffraction peaks positions was different. Here, both profiles differ insignificantly, as only a few measurement points have a deviation of under 100 MPa. Most of the measurement points show almost identical values.

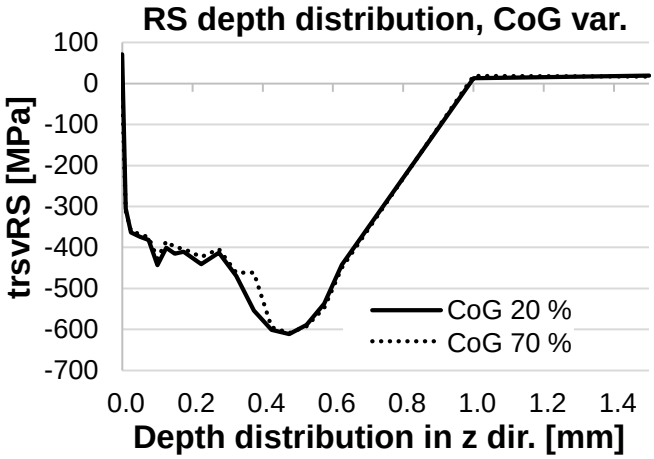

Figure 7-14: XRD residual stress depth distributions in the transverse direction obtained by variable diffraction peak determination: center of gravity (CoF) at 20 % or 70 %

φ position accuracy

Another measurement uncertainty can occur when rotating the specimen at the different φ angles. As the residual stresses produced by the DR process are anisotropic in longitudinal and transverse directions, to obtain both stress values with one specimen placement, the specimen needs to be rotated. In this device's configuration, the rotation is around the φ axis: from φ = 0° (longRS) to φ = 90° (trsvRS). If the axis of the rotation φ does not lay in the center of the diffractometer's circle, then rotating the specimen around it will result in shifting of the measurement position. Considering the in-plane stress gradients, this may lead to inconsistent values. Therefore, on a randomly chosen specimen, the stress measurements were taken in both φ = 90° and φ = 270° (180 ° difference). The measurement point after the rotation should remain the same, and correspondingly identical measurement values for both φ angles should be expected. It is important to notice that for the determination of stresses in both directions (longitudinal and transverse), different measurements were performed, where the in-plane position of the specimen (in x-y direction) was fixed, and it was rotated only around the φ axis. In Figure 7-15 are plotted the transverse stress depth profiles determined at φ = 90° or φ = 270°. It is visible that both profiles are in a very good agreement and the maximal deviation is lower than 50 MPa.

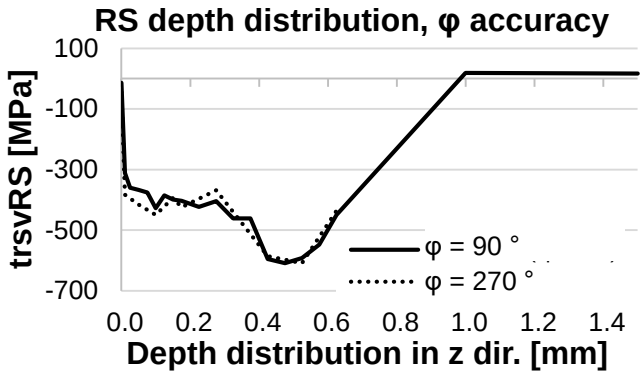

Figure 7-15: XRD residual stress depth distributions obtained by 180 ° differing φ angles

2θ measurement range influence

The choice of the 2θ measurement range directly reflects the measurement time at each ψ tilting and the quality of the diffraction peak. Therefore, the 2θ measurement range was optimised during the stress determination and even the narrowest 2θ measuring range delivered enough diffraction background, so that a reasonable peak to background ratio was available. Comparison measurements with the narrowest and the largest reasonable scanning ranges, see Figure 7-16, confirmed in this case, that narrowing the scanning range did not affect the results.

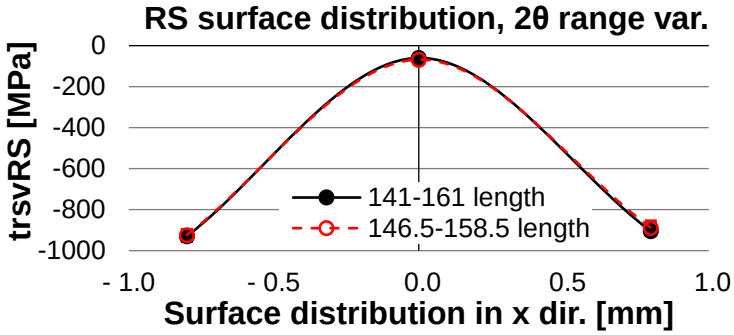

Figure 7-16: XRD residual stress surface distributions obtained by variable 2θ range, measured with Seifert

Homogeneity of the residual stresses along the DR trace

In the present chapter, the XRD residual stress measurements were performed, as either surface measurement path was defined perpendicular to the DR trace, or in-depth path was assigned in the center of the DR trace. In both cases, the measurement paths were assigned in the middle of the treated area, with the assumption that the DR process produces homogeneous residual stresses along the DR trace. To confirm this assumption, on a randomly chosen specimen (M14, milled + DR, pressure 32 MPa), the surface longitudinal- and transverse residual stresses were measured in the middle of the DR trace, where the measurement path was assigned along the DR trace (y direction), see Figure 7-17. In contrary to the assumption made, both longitudinal and transverse stress profiles showed some non-negligible deviations: in the longitudinal

direction, the stresses fluctuated from an app. -170 MPa to -405 MPa and in the transverse direction from an app. +300 MPa to +410 MPa. This deviation could have several issues, like surface imperfections of the treatment itself, or the high roughness generated by the pre-machining and still presented after DR. A specimen- or device misalignment could be an issue as well.

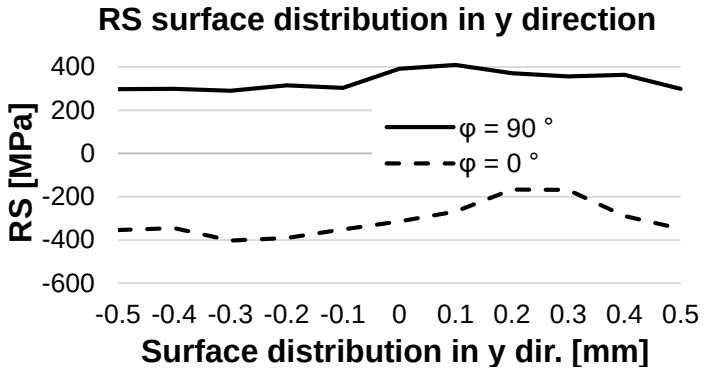

Figure 7-17: XRD residual stress surface distributions of milled + DR specimen in y direction (along the DR trace), measured with Seifert

Mathematical correction of the removed material and the determined in depth residual stress

It is known that the x-ray diffraction technique is classified as a non-destructive measurement technique. When considering the x-ray penetration depth in steels of several micrometers only, the technique is directly applicable only for surface stress determination. A standard procedure for acquiring stress depth profiles is successive material layer removal after each one the corresponding stress determination is performed. The material removal always leads to stress redistribution and relaxation, even when the employed technique does not generate additional residual stresses. The stress relaxation could be back-calculated with certain plausibility in case the defined boundary conditions are fulfilled (for more information, see chapter 4.3.1). In Figure 7-18 is shown a comparison between the longitudinal- and transverse stress depth profiles of specimen M15 (DR pressure 40 MPa) in the state “as measured” or “corrected” (designation “corr.”) utilizing the mathematical correction of stress relaxation by removed layer published by Moore and Evans. In the “corrected” state, the stress profiles in both directions exhibit minor difference near the surface, which increase in depth of 0.4 mm to 0.5 mm (maximal deviation of 190 MPa in longitudinal- and 205 MPa in the transverse direction) and decrease again at higher depths. Despite the observed deviations, the mathematical correction was not used in the later illustrated stress depth profiles due to several reasons explained in detail in chapter 4.3.1.

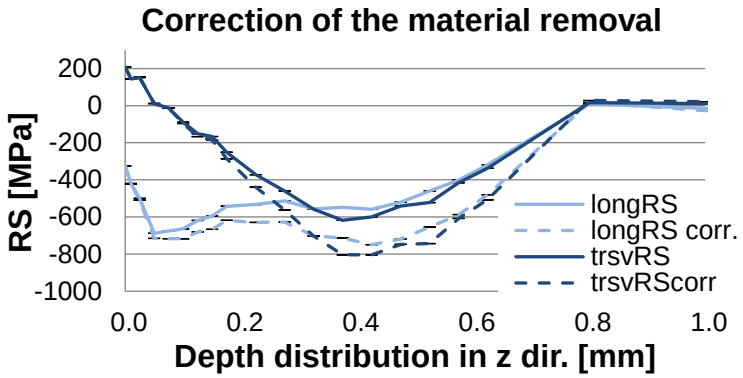

Figure 7-18: XRD stress depth profiles of specimen M15, measured with Seifert XRD 3000 PTS, in the state "as measured" or corrected (corr.) with the mathematical definition for the removed material by Moore and Evans (Moore, et al., 1958)

Influence of the measurement device

The characterisation of the residual stress profiles after DR can be still an issue, even when employing similar measurement- and evaluation parameters, due to some specific measurement procedure characteristics. Often, using the same measurement techniques is not a guarantee for consistent results, as the precision- and the devices' setup can vary. Therefore, the current section presents results of residual stress surface profiles measured on the same specimens using different diffractometers (PANalytical Empyrean (PAN) or Seifert, XRD 3000 PTS (Seifert)). Besides, some of the most significant DR process parameters were varied, and the resulting residual stress profiles were compared. In Figure 7-19 are plotted the surface residual stress distribution of milled + DR specimens, where the DR pressure was varied from 20 MPa (M12) to 40 MPa (M15); with fixed DR pressure of 40 MPa, one specimen was treated with 7 overturns (M19) and another one with overlapping of 75 % (M22). The same specimens were measured using Seifert and Panalytical diffractometers, with measurement parameters and orientation plotted in subchapters 4.3.2 and 4.3.3. For the pressure variation, in the both measured directions: longitudinal (see Figure 7-19 a)) and transverse (see Figure 7-19 b)), the difference between the values derived by both diffractometers laid between 50 MPa and 150 MPa. The higher DR pressure (see specimen M15_p40) led to a slight shifting of the transverse residual stresses towards higher compression. It is also visible that the stress distribution is not always as expected symmetrical to the center of the DR trace; this can be a sign of a measurement position misalignment. Figure 7-19 c) and d) show the surface residual stress distribution in longitudinal and in the transverse direction, by treatment with 7 overturns (o.t.) or the 75 % overlapping (o.l.). Here, both measurement devices deliver again similar results but some moderate asymmetry in the stress profiles in the longitudinal direction (see Figure 7-19 c)) is present. In the transverse direction, the DR with 7 overturns (M19_7o.t., Figure 7-19 c)), compared with the single overturn (M15_p40, Figure 7-19 b)), lowers the tensile residual stresses found in the middle of the DR trace. The DR with overlapping (M22_75%), compared with DR without overlapping (M15_p40) deliver similar residual stress profiles.

The results shown in Figure 7-19 confirm that in this particular case the employment of different measurement devices, when applying similar measurement techniques and parameters does not lead to a considerable inconsistency of the determined residual stress values. Nevertheless, when investigating very similar residual stress states, the observed here discrepancy of up to 150 MPa could be a crucial factor for the correct interpretation of the determined values.

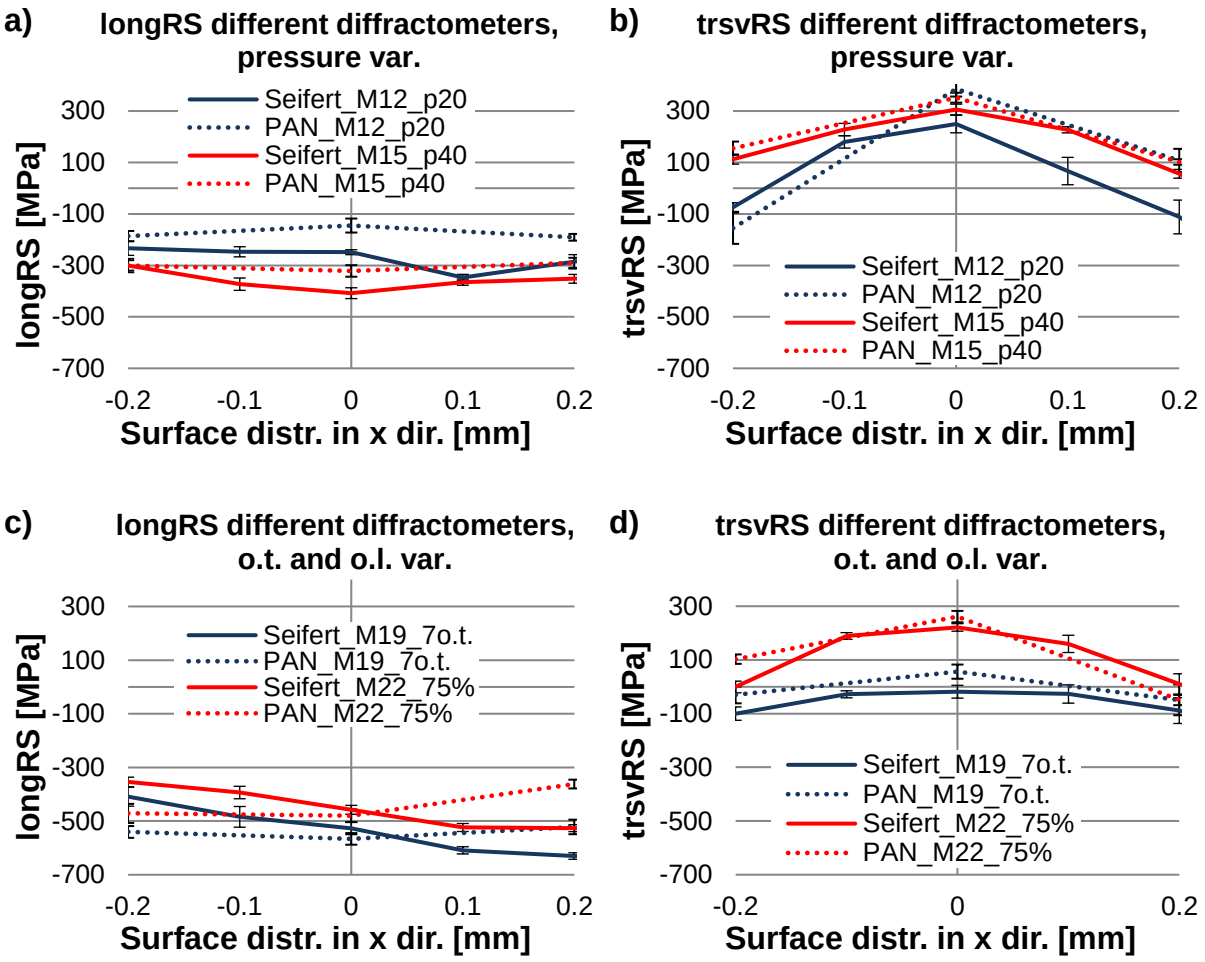

Figure 7-19: XRD surface residual stress distributions of milled + DR specimens measured with diffractometers PANalytical Empyrean (PAN) or Seifert, XRD 3000 PTS (Seifert), by variable DR process parameters: a) longitudinal direction variable pressure, b) transverse direction variable pressure, c) longitudinal direction overturns or overlapping variation and d) transverse direction overturns or overlapping variation

The comparison measurements shown in this subchapter showed just very few aspects of the possible XRD measurement uncertainties. It is important to note, that the incorrect choice of some measurement- and evaluation parameters can have a considerable impact on the residual stress determination. The specimen's imperfections can also play an important role and could be a source of error as well. The precise adjustment of the diffractometer is also extremely important for the proper data acquisition. Although, for the presented in this chapter results, the measurement- and evaluation parameters were carefully considered, and the measurement device was regularly adjusted and calibrated, so that plausible and reliable results were obtained.

7.3.3 X-ray diffraction residual stress surface distributions after DR with variable process parameters and different pre-machining states

Subchapter 7.3.3 is focused on the XRD surface residual stress determination of specimens treated with differing pre-machining sequences, i.e. milling + DR or milling + polishing + DR. For the presented results, the diffractometer Seifert XRD 3000 PTS was employed, and an identical measurement path was defined – perpendicular to the DR trace (in the x direction).

XRD residual stress surface distribution of milled + DR state

Figure 7-20 illustrates the surface residual stress distribution of milled + DR specimens, by varied pressure, overlapping or number of overturns (M12 – pressure 20 MPa; M15 – pressure 40 MPa; M19 – pressure 40 MPa and 7 overturns and M22 – pressure 40 MPa and 75 % overlapping). Figure 7-20 a) describes the stresses in the longitudinal direction. Here, it can be seen that higher DR pressure increase the stress affected zone but do not essentially increase the maximal compressive stress. The treatment with 7 overturns (M19) significantly increase the maximal compressive stress from an app. -410 MPa for single overturn to -630 MPa, but the determined profile is strongly asymmetric. The 75 % overlapping compared to single trace treatment, also enhance the maximal compressive stress from an app. -410 MPa to -530 MPa, which can be explained by the double treatment at the area of the overlapping. The stress profile is, as expected, asymmetric, as the zero x-coordinate was defined in the middle of the first (later overlapped) DR trace.

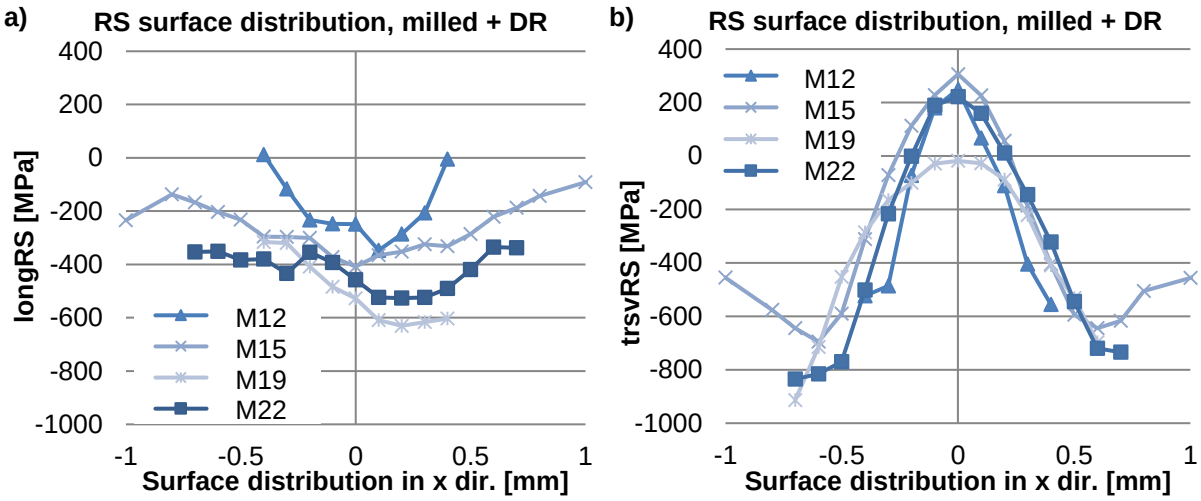

Figure 7-20: XRD residual stress surface distributions of milled + DR specimens measured with Seifert XRD 3000 PTS, by variable process parameters: a) longitudinal direction and b) transverse direction

In Figure 7-20 b) are plotted the surface transverse stress profiles. Here, the profile shape is very similar to this of the FEM derived transverse stress profiles. The higher DR pressure (M12 vs M15) expands the stress affected zone. Still, due to the lack of measurement data from ± 0.4 mm for M12, no comparison can be made regarding the maximal compressive stress generated. The results of M19 (7 overturns) compared to

M15 (single treated) show a shifting of the tensile stresses in the middle of the trace towards minor compression (from an app. +306 MPa to -20 MPa); the stress affected zone expands as well and the maximal determined compressive stress increase from an app. -715 MPa for M15 to -915 MPa for M19. The treatment with 75 % overlapping (M22) increases the maximal determined compressive stress from an app. -715 MPa to -835 MPa.

XRD residual stress surface distribution of milled + polished + DR state

In Figure 7-21 are illustrated the surface stress profiles of milled + polished + DR specimens by variable process parameters (P11 – pressure 20 MPa; P8 – pressure 40 MPa; P4 – pressure 40 MPa and 7 overturns and P2 – pressure 40 MPa and 75 % overlapping).

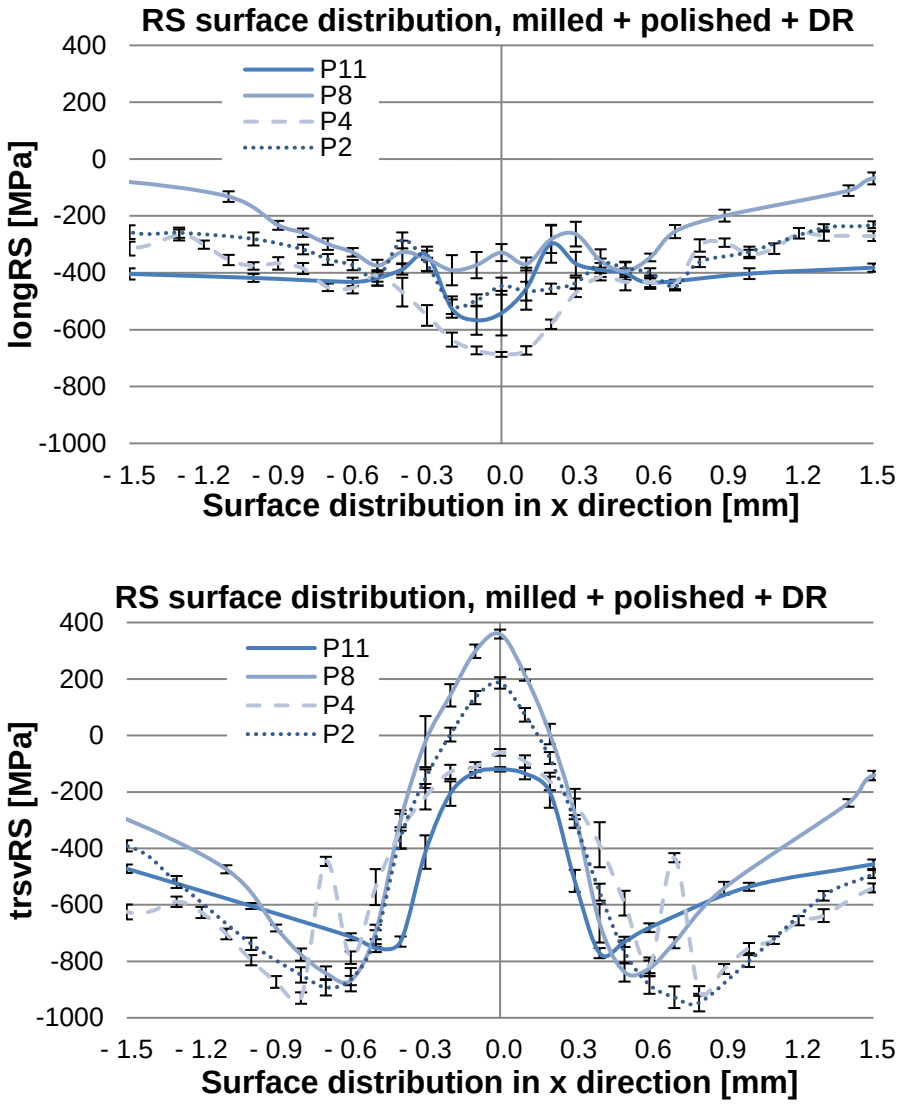

Figure 7-21: XRD residual stress surface distributions of milled + polished + DR specimens measured with Seifert XRD 3000 PTS, by variable process parameters: a) longitudinal direction and b) transverse direction

Here, the measurement path was expanded to represent the whole stress affected zone. The longitudinal stress profiles can be seen in Figure 7-21 a). Here, the higher pressure (P11 vs P8) increases the stress affected area but decrease the compressive stresses in the middle of the trace (for P11 app. -560 MPa and P8 app. -330 MPa). The stress values of P11 from ± 0.6 mm towards out of the trace were not expected. They remained on the level app. -400 MPa even at ± 1.5 mm out of the trace's middle. Considering the low applied DR pressure (20 MPa), it is unlikely that this stress field was generated by the DR process. It could be contributed rather to the pre-machining procedure. The 7 overturns treatment (P4) enhanced the compressive stress in the middle of the trace from an app. -330 MPa (P8) to -690 MPa. The 75 % overlapping treatment (P2) generated undefined stress profile with a maximal compressive stress of app. -515 MPa (i.e. higher compressive than the single trace treatment). This comparison showed that apart of the larger investigated surface area, the stress profiles still have different shapes, without showing some particular trend, i.e. some have a rather concave shape (P11 and P4), as other have an undefined shape (P8 and P2).
Figure 7-21 b) show the stress profiles in the transverse direction. In the middle of the trace, the measured stresses for all specimens but P11 are moderate tensile. Here, the P11 differs again from the rest of the specimens, exhibiting slightly compressive instead of tensile stresses. When comparing P11 (pressure 20 MPa) and P8 (pressure 40 MPa), the stress affected area is greater for P8 and the maximal compressive stress raise from -750 MPa for P11 to -865 MPa for P8. Significant is also the difference of the stresses in the middle of the trace: -120 MPa for P11 and +359 MPa for P8. Remarkable for the results of specimen P4 (7 overturns) are the two local stress peaks at x = ± 0.7 mm, which differed from all other results plotted in the diagram. It is difficult to assume the origin of this local stress peaks, but they are unlikely due to local microstructure imperfection or treatment failure, as they are symmetrical to the trace's middle. Apart from these local stress peaks, the specimen P4 exhibit significantly wider stress affected area than P8 (single treated). The 75 % overlapping (P2) compared to no overlapping (P8) show similar stress profile, with slightly lower tensile stresses in the middle of the trace.
To conclude this subchapter, the following can be summarized:

- Milled + DR state longitudinal direction
    - ↗ DR pressure = ↗ stress affected zone; → the maximal compressive stress.
    - 7 overturns = ↗↗ the maximal compressive stress
    - 75 % overlapping = ↗ maximal compressive stress
- Milled + DR state transverse direction
    - Similar profile shape to this of the FEM derived transverse stress profile
    - ↗ DR pressure = ↗ stress affected zone
    - 7 overturns = ↘ tensile stresses in the middle of the trace; ↗ the stress affected zone; ↗ maximal compressive stress
    - 75 % overlapping = ↗ maximal compressive stress
- Milled + polished + DR state longitudinal direction

  - ↗ DR pressure = ↗ stress affected zone; ↘ compressive stress in the middle of the trace
  - Moderate compressive stresses out of the stress affected zone by DR with 20 MPa pressure → unlikely generated by the DR process, rather contributed to the pre-machining procedure.
  - 7 overturns treatment = ↗ compressive stress in the middle of the trace
  - 75 % overlapping treatment generated undefined stress profile; ↗ maximal compressive stress
- Milled + polished + DR state transverse direction
  - ↗ DR pressure = ↗ stress affected zone; ↗ maximal compressive stress; ↗ tensile stress in the middle of the trace.
  - 7 overturns - two local stress peaks at x = ± 0.7 mm, unlikely presented due to local microstructure imperfection or treatment failure, as symmetrical to the trace's middle; ↗↗ stress affected zone
  - 75 % overlapping = ↘ tensile stress in the middle of the trace; → stress affected zone; → maximal compressive stress.

7.3.4 X-ray diffraction residual stress depth distributions of DR specimens with variable process parameters and different pre-machining states

In this subchapter, the specimens investigated in subchapter 7.3.3 were used to determine the in-depth residual stress distributions. As in the previous subchapter, here the studies were also divided by the pre-machining state of the specimens, i.e. milled + DR or milled + polished + DR. The stress determinations were obtained with diffractometer Seifert XRD 3000 PTS.

XRD residual stress depth distributions of milled state

In this section will be shown the stress depth profiles of two randomly chosen milled specimens before the DR treatment was investigated, see Figure 7-22, where the milling procedure was performed with identical milling parameters. Here, with longitudinal- and transverse stress direction was meant the direction of the later DR trace and not the cutting direction by the milling process. Considering the position and the form of milling traces on the specimen (see Figure 4.10 and Figure 4.11), the direction of the measured residual stresses cannot be designated as along or transverse to the cutting direction.
The stress depth profiles in longitudinal and transverse direction for both specimens were very similar with a maximum difference of 80 MPa at depth below 25 µm. Although, near the surface (up to 25 µm depth), the stress values in longitudinal and in transverse directions differ with up to 200 MPa. Considering the milling type (perpendicular face milling), no significant difference of the induced near-surface stresses along and transverse to the cutting direction should be expected (Scholtes, 1990). Nevertheless, the undefined to the cutting direction measurement setup invalidates this assumption. The observed discrepancy in the near-surface residual stresses has to be considered when investigating the surface residual stress state after the DR treatment. There, the residual stresses generated by the milling can affect those produced

by the DR. In depth, the milling should not have a significant impact on the residual stresses after DR.

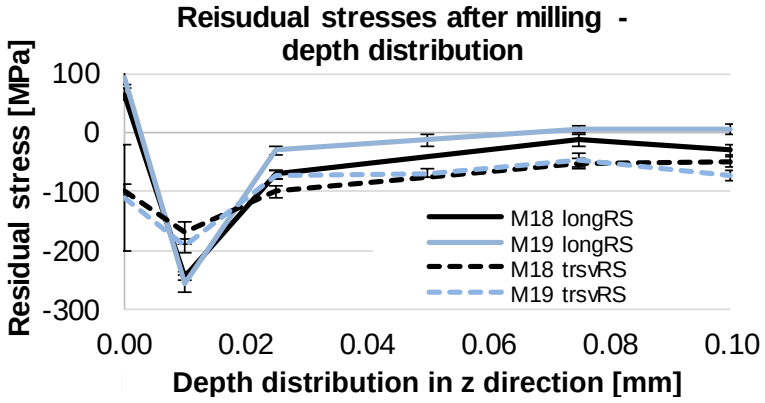

Figure 7-22: XRD residual stress depth distributions of milled specimens

<u>XRD residual stress depth distributions of milled + DR state by variable DR parameters</u>

The next results depict the residual stress depth profiles of milled + DR specimens by variable DR parameters (M12 – pressure 20 MPa; M15 – pressure 40 MPa; M19 – pressure 40 MPa and 7 overturns and M22 – pressure 40 MPa and 75 % overlapping). The measurement path was defined in the middle of the DR trace in +z direction, and the consecutively measured surfaces were obtained as the corresponding material layer was removed using of electropolishing.

In Figure 7-23 are plotted the stress depth distributions of DR specimens by variable DR pressure (M12 = 20 MPa and M15 = 40 MPa) or with a constant pressure of 40 MPa but with 7 overturns (M19) or with 75 % overlapping (M22). The Figure 7-23 a) shows the stress depth profiles in the longitudinal direction, where it can be observed that for all specimens the magnitude of compressive stress is similar and the maximum is found about 75-100 µm below the surface. In contrary, the stress impact depth is quite different, namely the stresses of the specimens treated with 40 MPa pressure reach zero at app. 0.7 mm depth, and those of the specimens treated with 20 MPa tend to zero at just 0.45 mm depth. When comparing specimens M19 (7 overturns) and M22 (75 % overlapping) with the specimen M15, it is notable that the magnitude and the position of the compressive stresses are similar. Although, the stress impact depth reaches about 1.0 mm for specimens M19 and M22, where the M15 (also treated with 40 MPa DR pressure but only once and without overlapping) has a smaller stress impact depth of 0.8 mm. These observations confirm the favourable effect of the multiple-overturn DR treatment on the one hand and emphasis the change in the stress state if applying DR with- or without overlapping on the other hand.

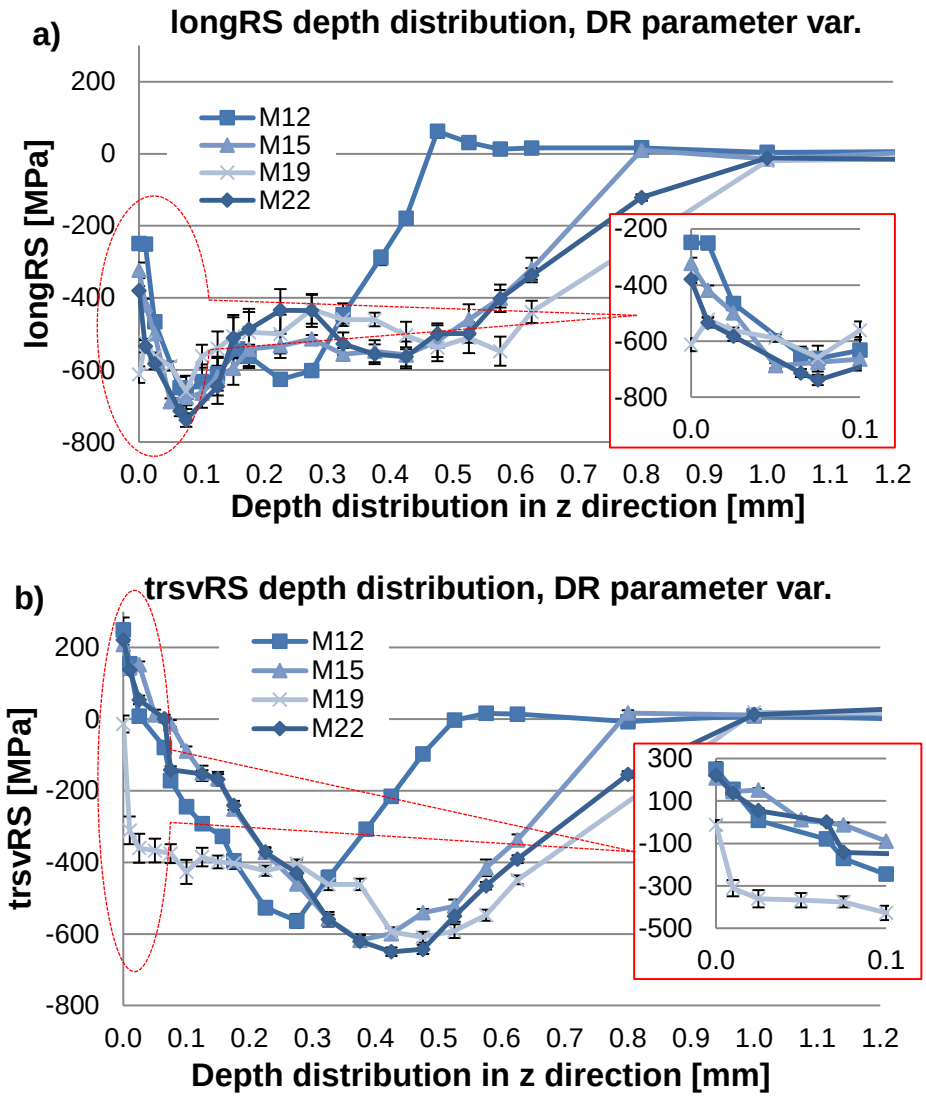

Figure 7-23: XRD residual stress depth distributions of milled + DR specimens measured with Seifert XRD 3000 PTS, by variable process parameters: a) longitudinal direction and b) transverse direction

In Figure 7-23 b) are depicted the stress depth profiles in the transverse direction, by variable DR parameters. Similarly to the results in Figure 7-23 a), the higher DR pressure (M15) did not lead to enhancing the amount of the compressive residual stress, but it positively affected the stress impact depth, increasing it with about 0.30 mm from 0.45 mm (M12) to 0.75 mm (M15). The shape of the transverse residual stress profile differs from this in the longitudinal direction, similar to the FE determined transverse stress depth profiles, and having a maximum of the compressive residual stresses shifted into higher depth of 0.3 mm to 0.4 mm.

Near the surface, the treatment with 7 overturns (M19) compared with single overturn (M15) generates near-zero- instead of tensile stresses. Besides, the stresses develop more rapidly towards higher compression than those generated by the single overturn. The compressive stress maximum remains almost the same as amount but it is shifted to higher depth with an app. 0.1 mm and the stress impact depth is greater namely app. 1.0 mm, compared with this generated by the single treatment of 0.8 mm.

The depth profile of the specimen M22 (75 % overlapping) is almost identical with this of M15. The only difference is in the stress impact depth, which in case of treatment with overlapping reaches 1.0 mm, where the stress impact depth without overlapping is about 0.8 mm.

XRD residual stress depth distributions of milled + polished + DR state by variable DR parameters

In the current section, specimens treated with the same DR parameters, as shown in the previous section, were employed for the in-depth residual stress analysis. Here, the pre-machining state was milling and consecutive polishing (P11 – pressure 20 MPa; P8 – pressure 40 MPa; P4 – pressure 40 MPa and 7 overturns and P2 – pressure 40 MPa and 75 % overlapping). The polishing procedure had the aim to smooth the surface and to eliminate the roughness peaks, which could negatively influence the residual stress surface determination. Although surface stress profiles from subchapter 7.3.3 (see Figure 7-21) showed in some cases (specimen P11) not negligible change in the surface stress state at zones beyond the stress-affected areas of DR. Therefore, in continuation to these observations, the stress depth profiles of the same specimens were determined. Figure 7-24 illustrates the stress depth profiles of milled + polished + DR specimens measured with Seifert XRD 3000 PTS by variable process parameters.
In the longitudinal direction, see Figure 7-24 a), the higher DR pressure (P11 vs P8) leads to higher maximal compressive stress (app. -560 MPa for P11 and app. -710 MPa for P8) and higher stress impact depth (0.53 mm for P11 and 0.85 mm for P8). The 7 overturns treatment compared to single treatment (P4 vs P8), results in a similar level of maximal compressive stress at the app. -700 MPa. Although, the stresses by P4 develop more rapidly towards higher compression than those generated by the single overturn (P8). The stress impact depth also increases from 0.85 mm for P8 to almost 1.00 mm for P4. The 75 % overlapping (P2) compared to no-overlapping (P8), generates very similar stress impact depth and maximal compressive stress but the stress profile has an abrupt drop at 0.16 mm depth from -730 MPa to -410 MPa. This could be caused by the complex plastic deformations due to the overlapping. Although, a measurement position misalignment is also possible.
The stress depth profiles in the transverse direction are plotted in Figure 7-24 b). The DR pressure variation (P11 vs P8) show similar maximal compressive stress of app. - 560 MPa, which is shifted to greater depth for the higher DR pressure (P8). The stress impact depth also increases by higher DR pressure from 0.53 mm for P11 to 0.85 mm for P8. The treatment with 7 overturns (P4) compared to single overturn (P8), increase the maximal compressive stress from -530 MPa to -660 MPa and the stress impact depth is higher for P4, app. 1.08 mm, compared to P8 (app. 0.85 mm). The 75 % overlapping (P2) has a very similar stress depth profile to P4, meaning slightly higher and deeper compressive stresses than P8 (w/o overlapping).

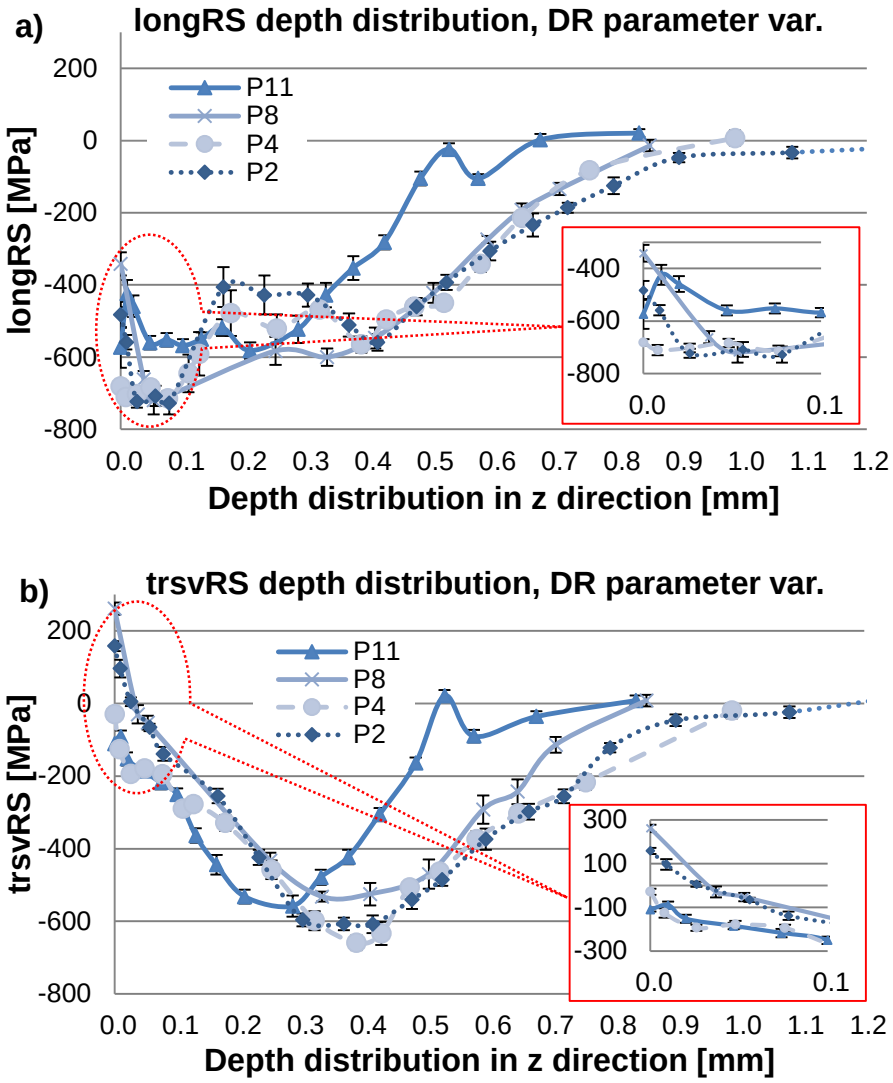

Figure 7-24: XRD residual stress depth distributions of milled + polished + DR specimens measured with Seifert XRD 3000 PTS, by variable process parameters: a) longitudinal direction and b) transverse direction

In summary, the following observations can be stated:

- Residual stress depth profiles after milling (w/o DR) – in depth higher than 25 µm - very similar stress depth profiles in longitudinal and transverse directions; near the surface - discrepancy in the longitudinal and the transverse directions with up to 200 MPa. The milling process should not have a significant impact on the residual stress depth profiles after DR. Only near-surface effects should be expected.
- Residual stress depth profiles of milled + DR specimens - longitudinal direction
  - similar maximal compressive stress (app. -650 MPa to -750 MPa) for all specimens at about 75-100 µm below the surface
  - ↗ DR pressure = ↗ stress impact depth
  - 7 overturns = ↗ stress impact depth
  - 75 % overlapping = ↗ stress impact depth
- Residual stress depth profiles of milled + DR specimens - transverse direction
  - ↗ DR pressure = → maximal compressive stress; ↗ stress impact depth

  - 7 overturns = → maximal compressive stress; ↘ tensile near-surface stresses; ↗ stress impact depth
  - 75 % overlapping = → maximal compressive stress; ↗ stress impact depth
- Residual stress depth profiles of milled + polished + DR specimens - longitudinal direction
  - ↗ DR pressure = ↗ maximal compressive stress; ↗ stress impact depth
  - 7 overturns treatment = → maximal compressive stress; ↗ stress impact depth; stronger near-surface stress gradient
  - 75 % overlapping = → maximal compressive stress; → stress impact depth; abrupt stress drop at 0.16 mm depth from -730 MPa to -410 MPa (could be caused by the complex plastic deformations due to the overlapping or by measurement position misalignment)
- Residual stress depth profiles of milled + polished + DR specimens - transverse direction
  - ↗ DR pressure = → maximal compressive stress; ↗ stress impact depth
  - 7 overturns = ↗ maximal compressive stress; ↗ stress impact depth
  - 75 % overlapping = ↗ maximal compressive stress; ↗ stress impact depth

7.3.5 X-ray diffraction residual stress surface and depth distributions – influence of the pre-machining state

In this subchapter, the pre-machining treatment of the later DR specimens was varied, where specimens labelled with “M” were milled + deep rolled and those labelled with the “P” were milled, polished and deep rolled. Some changes in the residual stress profiles were expected due to the variable roughness (on the milled specimens much higher than on the polished ones) and the corresponding change in the contact surface between work piece and tool during the initial penetration of the DR tool. The DR process parameters were varied in the same manner as in the previous subchapter: applied pressure, number of overturns or overlapping percentage. The residual stress surface- and depth profiles in longitudinal and transverse directions were investigated.

XRD residual stress surface distributions – influence of the pre-machining state

Figure 7-25 a) represents the surface residual stress profiles and the trace width of DR specimens with variable pressure. The residual stresses in the longitudinal direction are plotted in red. Here, the highest difference exhibit the stresses of the milled vs polished specimens treated with DR pressure of 20 MPa. It was assumed that the polished + DR specimens should exhibit lower compressive residual stresses than the milled + DR specimens due to the resulted difference in the contact force caused by the variable surface roughness. Considering the applied DR pressure is in general constant when the contact area between specimen and DR tool decreases due to high roughness of the specimen, the contact pressure will increase proportionally to the

decreasing of the contact area. This should lead to a higher amount of plastic deformation and higher compressive stress values. In contrary to this assumption, the milled + polished + DR specimen (P11_p20) exhibit higher compressive stress than the milled + DR (M12_p20) and even than the specimens treated with 40 MPa pressure (M15_p40 and P8_p40). Nevertheless, it is notable that the residual stresses of the untreated material (see the results from ± 0.6 mm towards out of the DR trace) are significantly higher compressive, app. -400 MPa than those of the rest specimens. This can be an indication of higher compressive residual stresses generated by the polishing process or residual stresses inherited from previous process chain steps. The width of the DR trace (dashed vertical lines) increases with increasing the DR pressure, an indication of expanding plastic deformation zone. On the other hand, the stresses measured on the specimens treated with 40 MPa pressure are similar for both pre-machining states, where those measured on the milled + polished + DR specimen are at some places up to 100 MPa higher compressive than those measured on the milled + DR specimen.

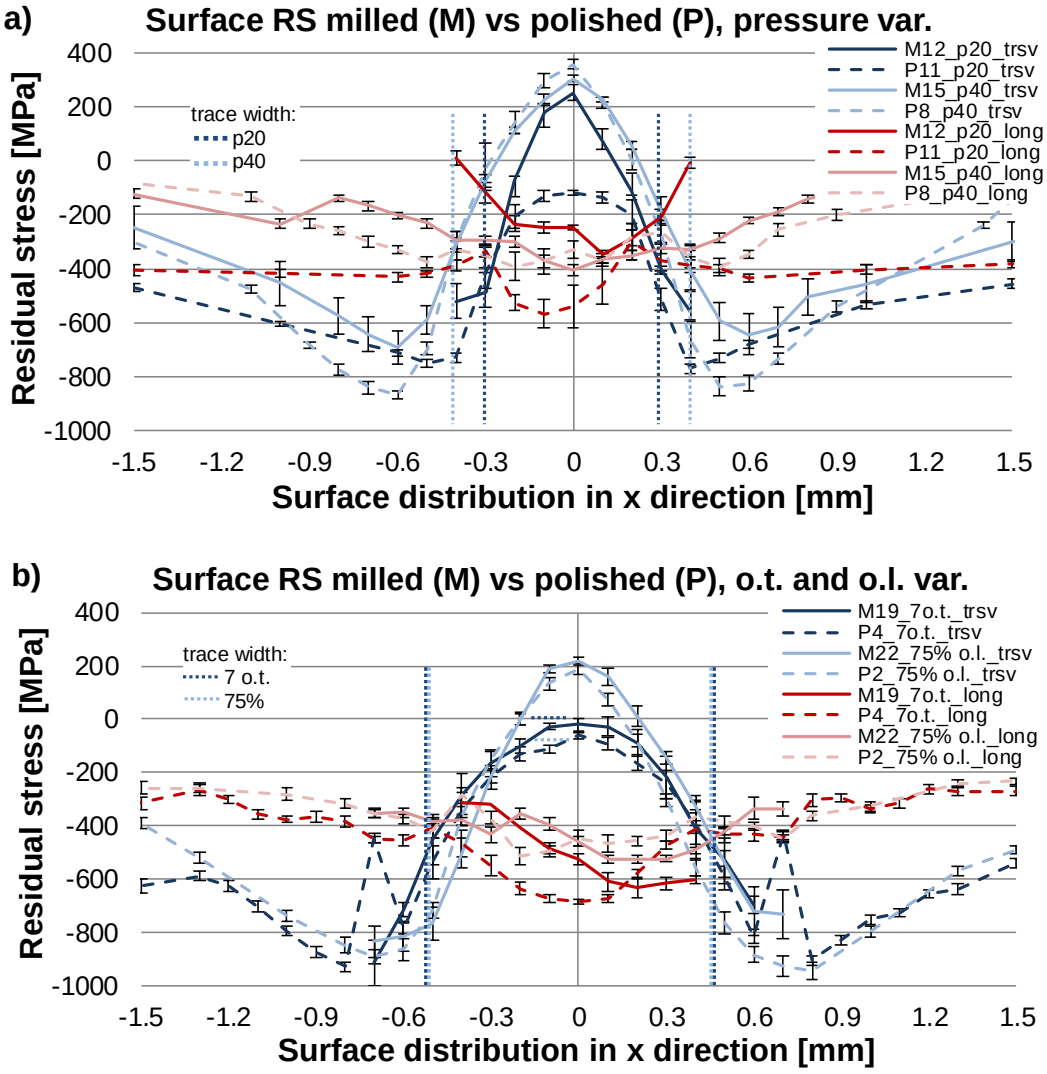

Figure 7-25: XRD residual stress surface distributions of milled + DR or milled + polished + DR specimens measured with diffractometer Seifert, XRD 3000 PTS, by variable DR process parameters: a) DR pressure variation and b) overturn or overlapping variation

In Figure 7-25 a) with blue lines are plotted the transverse surface stress profiles. The compressive residual stress maximum, located out of the DR trace is higher for the polished specimens (P11 and P8) than the milled specimens (M12 and M15). In the middle of the trace, the measured stresses for all specimens but P11 are moderate tensile. Here, the P11 differs again from the rest specimens, exhibiting slight compressive instead of moderate tensile stresses.
Although, it remains unclear if the differing the surface stress profile of the P11 specimen is due to inconsistency of the residual stress state caused by the pre-machining or it is an effect of the DR treatment. A superposition of both factors is also possible.
The next process parameters' variation was done as fixing the DR pressure at 40 MPa and applying 7 overturns (o.t.) or 75 % overlapping (o.l.) on different pre-machining states (milled or milled + polished), see Figure 7-25 b). For the specimen treated with overlapping, the zero-x coordinate in the diagrams describes the center of the overlapping (2^{nd}) trace. The surface stress profiles are plotted in red for longitudinal direction and in blue for transverse direction. In the longitudinal direction, an asymmetry of the stress profile of M19 (7 o.t.) is observed (up to 200 µm), where it is not clear if the shifting is caused by a faulty DR treatment or it is due to positioning misalignment during the stress determination. Regardless the asymmetry, it is visible that the DR treatment with 7 overturns (M19 and P4) enhanced the maximal compressive stress in comparison with the single overturn (M15 and P8, Figure 7-25 a)) with 250-300 MPa. The stresses obtained by DR treatment with overlapping of 75 % (M22 and P2) do not significantly differ from those generated by the single trace DR (M15 and P8, Figure 7-25 a)). It was additionally observed that the different pre-machining (milling or milling + polishing) did not significantly affect the final residual stress distribution.
The surface stress profiles in the transverse direction are plotted in blue, see Figure 7-25 b). Here, similarly to the results from Figure 7-25 a), there is a presence of tensile, tending to zero residual stresses in the middle of the DR trace and the maximal compressive stress are located out of the DR trace. The DR treatment with 7 overturns shifted the tensile stresses towards compression, to achieve a stress state near zero in the middle of the DR trace, where the highest compressive stresses remained at the level of the single treated polished specimen (P8 from Figure 7-25 a)). Although, the difference between the milled + DR with single- or with 7 overturns specimens (M15, Figure 7-25 a)) and M19, Figure 7-25 b)) is notable: the highest compressive stress measured on M15 was about -700 MPa, where for M19 was about -900 MPa. This means that the multiple overturn DR treatment is in this case, more favourable than the single overturn treatment.
It was also observed that the stress profile of specimen M19 is symmetric, in contrary to the one measured in a longitudinal direction. This can be an indication about misalignment of the primary x-ray beam. The stress state of the specimens treated with 75 % overlapping (M22 and P2, Figure 7-25 b), blue lines) and of those treated without overlapping (M15 and P8, Figure 7-25 a), blue lines) is similar, and the pre-machining (milled vs milled + polished) did not significantly affect the final residual stress state.

XRD residual stress depth distributions – influence of the pre-machining state

The same specimens, shown in the previous subchapter, were employed to investigate the in-depth residual stress state by variable pre-machining states and DR process parameters. In Figure 7-26 are shown the depth stress profiles of specimens treated with 20 MPa or 40 MPa DR pressure and with variable pre-machining. Figure 7-26 a) illustrates the stress depth profiles, measured in a longitudinal direction, where almost no discrepancy between the profiles of the different pre-machining state can be observed. The only significant difference between the results for the different pre-machined states of M12 and P11 of an app. 300 MPa is present only at the surface and at about 50 µm depth diminished. The depth distributions in the transverse direction for the same specimens are plotted in Figure 7-26 b). Here, it is visible that the only significant discrepancy (M12 and P11) of the stresses between the different pre-machining states occurs on the surface (app. 350 MPa difference), this difference diminishes drastically at about 75 µm depth.

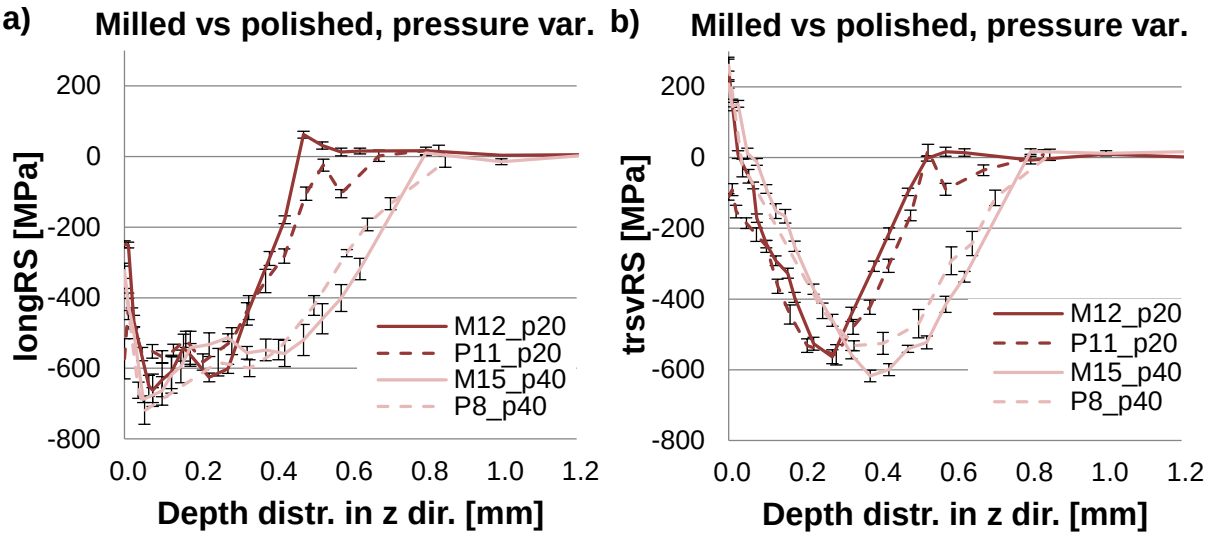

Figure 7-26: XRD residual stress depth distributions of milled + DR or milled + polished + DR specimens measured with diffractometer Seifert, XRD 3000 PTS, by variable DR pressure: a) longitudinal direction and b) transverse direction

The next results (see Figure 7-27) display the stress depth profiles in longitudinal- (Figure 7-27 a)) and in transverse (Figure 7-27 b)) directions, by a fixed DR pressure of 40 MPa and treatment with 7 overturns (o.t.) or with 75 % overlapping (o.l.). The depth distributions in both directions are relatively consistent for all specimens with a maximal deviation of an app. 200 MPa, which cannot be systematically classified.

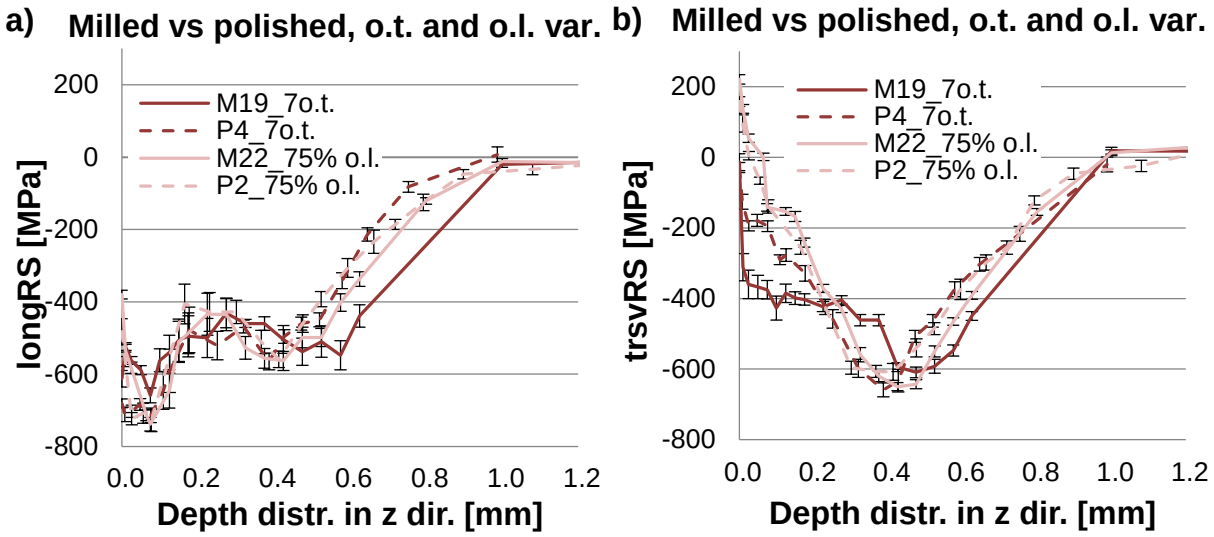

Figure 7-27: XRD residual stress depth distributions of milled + DR or milled + polished + DR specimens measured with diffractometer Seifert, XRD 3000 PTS, by overturns or overlapping variations: a) longitudinal direction and b) transverse direction

As a summary of this subchapter, the following can be noted:

- XRD residual stress surface distributions - influence of the pre-machining state
  - Longitudinal direction
    - DR pressure 20 MPa – by milled state significantly lower compressive stresses than by milled + polished state → high possibility of stresses inherited from the pre-machining procedure
    - DR pressure 40 MPa - the polished state partially led to slightly higher compressive stresses than the milled state
    - 7 overturns or 75 % overlapping – no difference between the surface stress profiles of milled or polished state, except the profile asymmetry observed by 7 overturns
  - Transverse direction
    - DR pressure 20 MPa and 40 MPa – the polished state led to higher maximal compressive residual stress than the milled specimens; DR pressure 20 MPa polished state led to slight compressive stresses in the trace, in contrary to milled state, where moderate tensile stresses presented.
    - 7 overturns or 75 % overlapping – no difference between the surface stress profiles of the milled or the polished state was observed, except the two local stress peaks observed by 7 overturns
- XRD residual stress depth distributions – influence of the pre-machining state
  - DR pressure variation: in both measurement directions, the stress depth profiles by the milled or polished specimens differed mainly near the surface. At app. 50 µm to 75 µm the differences diminished.
  - 7 overturns or 75 % overlapping – the depth distributions in both directions were relatively consistent with a maximal deviation of an app. 200 MPa, which deviation could not be systematically classified.

7.4 Verification of the finite element models by x-ray diffraction

In this subchapter, a verification of the finite element models presented in subchapter 7.1. is done using the x-ray diffraction residual stress determination presented in subchapter 7.3. For this verification, the FEM derived surface and depth stress profiles are compared to the surface- and depth stress profiles determined experimentally by the x-ray diffraction. In subchapter 7.3, the stress profiles by variable DR parameters and two pre-machining states were compared, and it was observed that near the surface, the pre-machining state influenced the surface stress profiles. Considering no pre-machining was defined to the FE models, it is necessary to compare the stress profiles of both pre-machining states (experimentally derived) to the FE determined stress profiles. In Table 7-6 are listed the experimental- and the modelling design for the residual stress comparisons shown in this subchapter.

Table 7-6: Experimental and modelling design of the residual stress determination of milled + DR (M), milled + polished + DR (P) specimens and FEM DR

Specimen‘s designation	**Process parameters**	
	DR pressure	**Overlapping**
M12/P11/FEM_p20	20 MPa	0 %
M15/P8/FEM_p40	40 MPa	0 %
M22/P2/FEM_p40_75%o.l.	40 MPa	75 %

7.4.1 Comparison between FEM and XRD - residual stress surface distributions

The following subchapter focuses on the comparison between the FEM- and XRD derived residual stress surface profiles by variable DR pressure or overlapping and different pre-machining states. Figure 7-28 depicts the FEM vs XRD surface stress profiles of specimens treated with DR pressure of 20 MPa, where the experimentally determined stress profiles were in milled + DR (M12) or milled + polished +DR (P11) state. In the longitudinal direction, see Figure 7-28 a), in the trace, the FE derived surface profile lays between the experimentally derived profiles. The FE profile exhibits two symmetrical local compression peaks, which are missing by the experimental profiles. Out of the trace, a comparison between the three profiles is very difficult, due to lack of information for the M12, and due to the unusually high compressive stresses exhibited by P11. In the transverse direction, see Figure 7-28 b), all three profiles have a very similar shape. In the trace, the FE derived profile lay again between both experimental profiles. The FE maximal compressive stress is on the level of the polished specimen (P11), and out of the trace, the FE profile tends to zero stress due to absence of pre-machining or any other stress-inducing process.

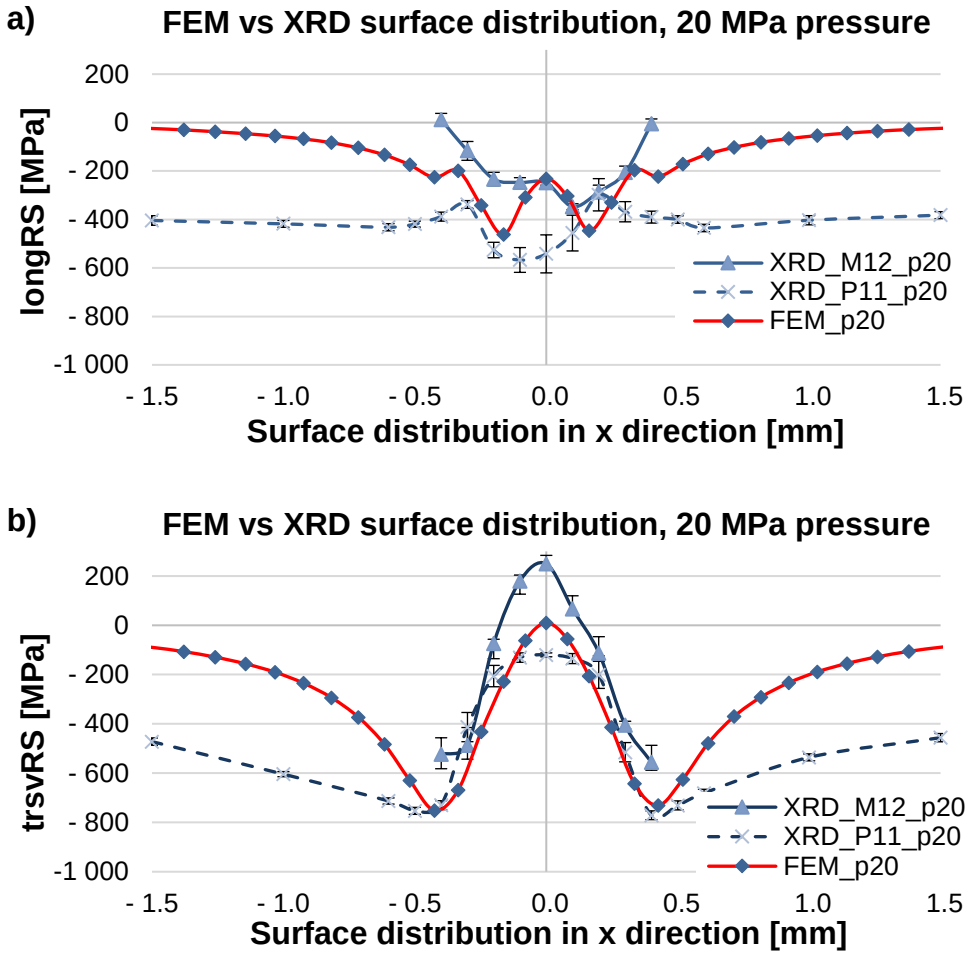

Figure 7-28: FEM vs XRD residual stress surface distributions, DR pressure 20 MPa: a) longitudinal direction and b) transverse direction

Figure 7-29 depicts the FEM vs XRD surface stress profiles of specimens treated with DR pressure of 40 MPa. Figure 7-29 a) describes the stress profiles in the longitudinal direction. In the trace, the FE derived values were slightly lower compared to the XRD determined with a maximal deviation of under 200 MPa. Out of the trace, all profiles tend to zero stress. The transverse surface stress profiles are illustrated in Figure 7-29 b). In the trace, the FEM moderately underestimates the experimentally determined tensile stresses (with maximum 290 MPa). Although, the other sections of the profile are in a very good agreement with the experimental profiles.

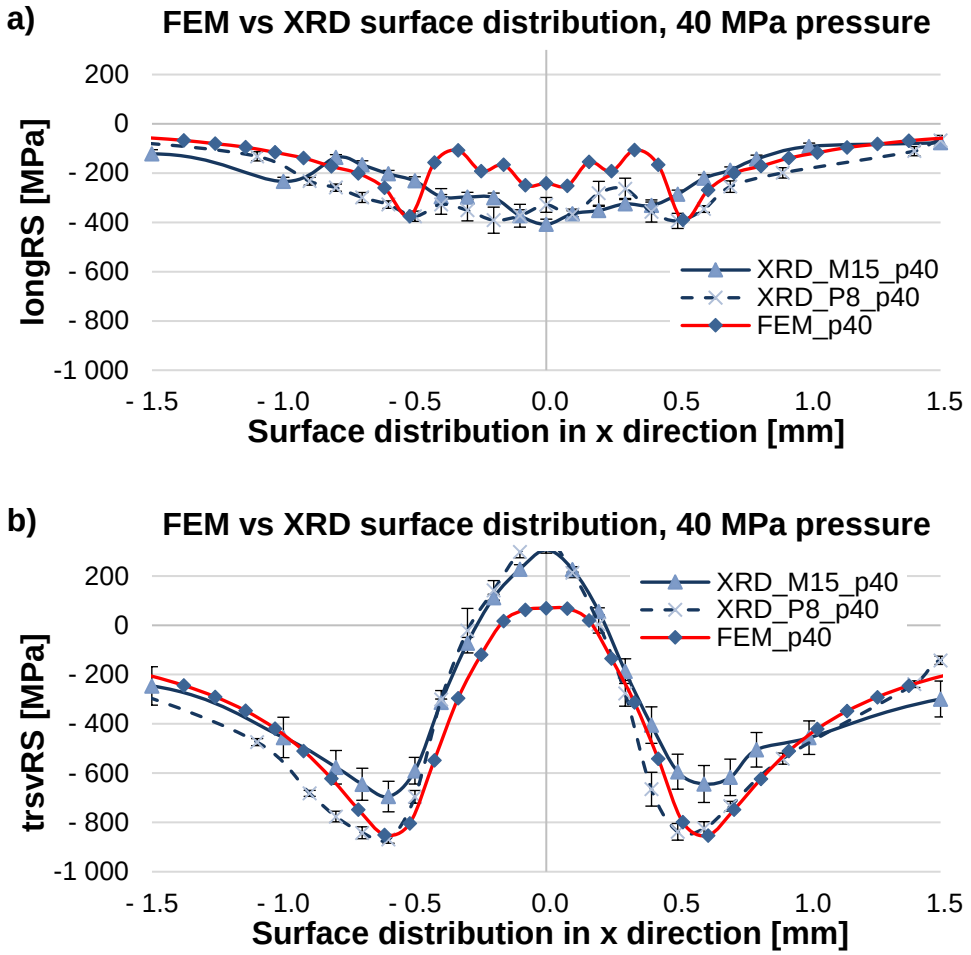

Figure 7-29: FEM vs XRD residual stress surface distributions, DR pressure 40 MPa: a) longitudinal direction and b) transverse direction

The last comparison in this subchapter was made between both FEM- and XRD determined surface stress profiles of DR specimens with 40 MPa pressure and 75 % overlapping (see Figure 7-30). In the longitudinal direction, see Figure 7-30 a), the FE stress profile shows some scattered stress values with a deviation of maximum 250 MPa. As a magnitude, the stress values lay very close to the XRD determined ones. The stress profiles in the transverse direction are plotted in Figure 7-30 b). Here, the FE profile shape agrees very well with the experimental profiles, with the only exception of the zone between the x-coordinates -1.0 mm and -0.5 mm, where the FE stress profile exhibit a small local peak. All FE stress values differ from the experimental ones with maximal 200 MPa.

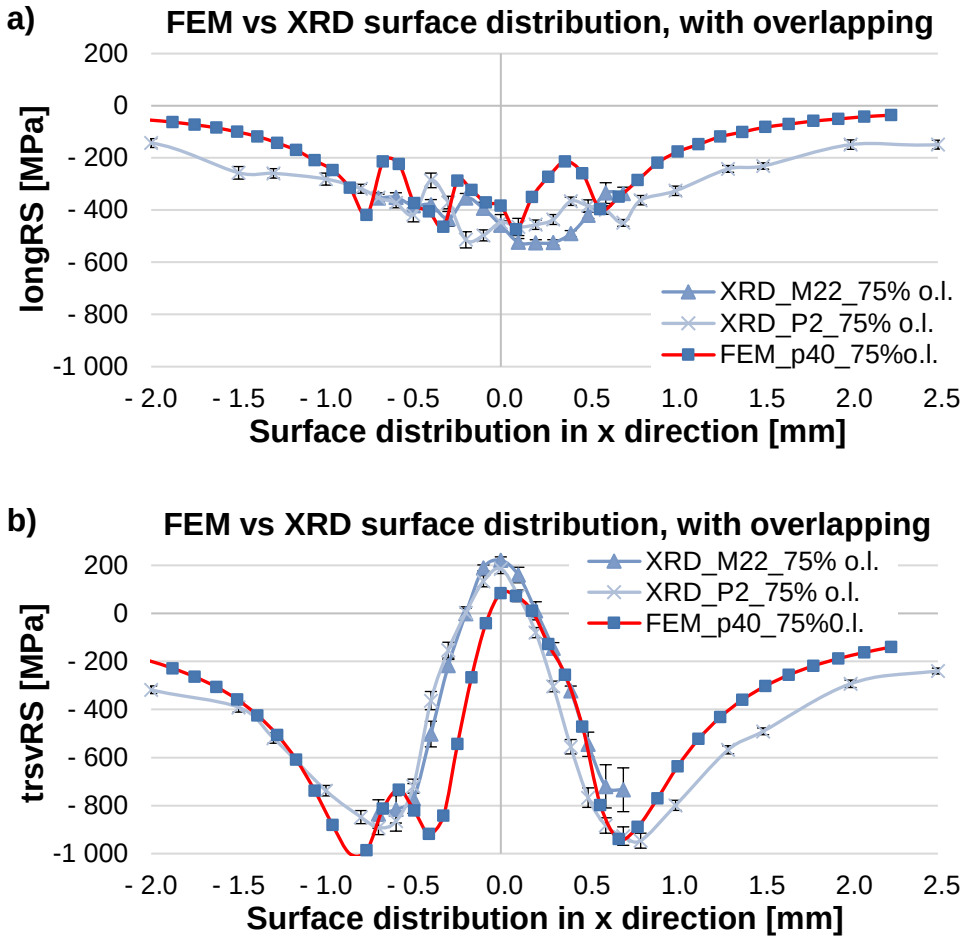

Figure 7-30: FEM vs XRD residual stress surface distributions, DR pressure 40 MPa, overlapping 75 %: a) longitudinal direction and b) transverse direction

7.4.2 Comparison between FEM and XRD - residual stress depth distributions

The next subchapter is focused on the comparison between FEM- and XRD residual stress depth profiles of DR specimens by variable DR pressure, or with overlapping and by different pre-machining state (experimental). Figure 7-31 depicts the longitudinal stress depth profiles by DR with 20 MPa or 40 MPa. The comparison of the 20 MPa treatment, see Figure 7-31 a) show a good agreement between FEM and XRD, with slightly differing profile shapes, as the FE profile exhibit a single compressive stress maximum, while the XRD profiles have double compressive stress peaks. Still, the stress values near the surface, the maximal stress and the impact stress depth for all three profiles are very similar. The stress depth profiles of the specimens treated with 40 MPa pressure are shown in Figure 7-31 b). Here, the FE derived profile differs slightly from the experimental two, having again only a single compressive stress maximum, in contrary to the double peak by the experimental profiles. The near-surface stress values and the maximal compressive stress is well comparable, and only the impact stress depth is minor underestimated by the FEM.

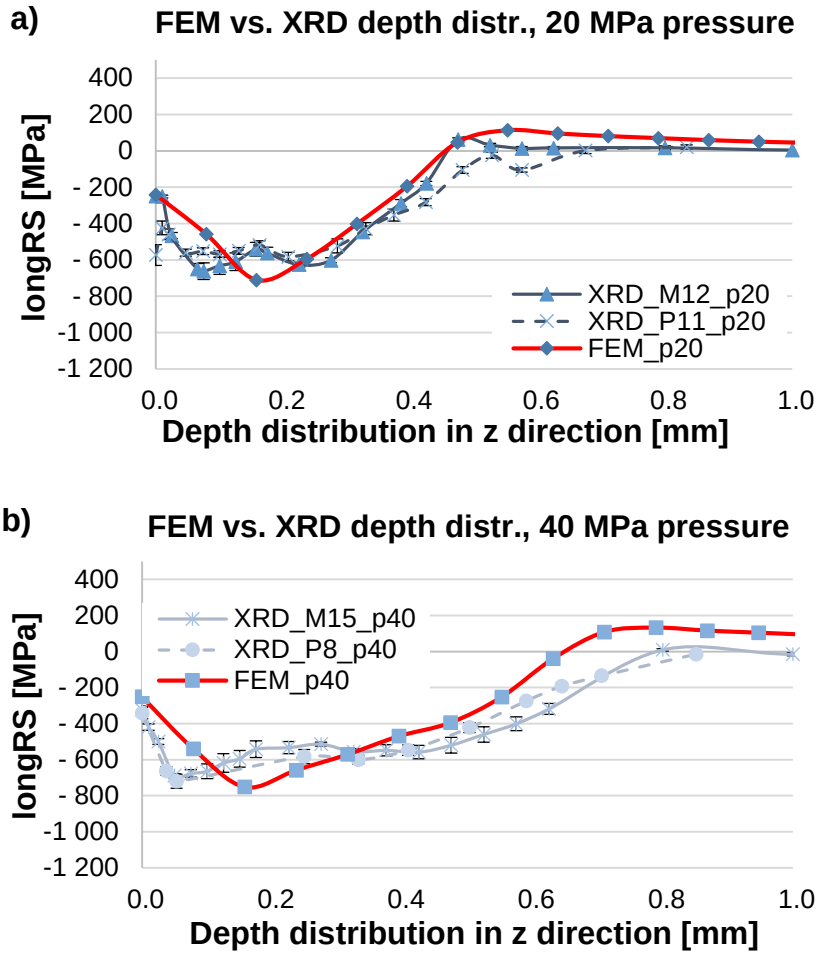

Figure 7-31: FEM vs XRD residual stress depth distributions in longitudinal direction: a) DR pressure 20 MPa and b) DR pressure 40 MPa

The transverse stress depth profiles of the specimens treated under the same conditions as those from Figure 7-31 are plotted in Figure 7-32. The profiles of the treatment with 20 MPa can be seen in Figure 7-32 a). Here, the FE derived profile has a similar shape compared to the XRD derived ones. Although the calculated maximal compressive stress is with an app. 200 MPa higher (in compression) and in depth, the FEM calculated moderate tensile stresses (app. +350 MPa) instead of the measured near-zero stresses. The calculated tensile stresses shift the stress impact depth deeper as measured.

Figure 7-32 b) illustrates the comparison between FEM and XRD for DR pressure of 40 MPa. Here, the trend seen by the DR pressure of 20 MPa is enhanced, so that the calculated maximal compressive stress is an app. 280 MPa higher (in compression) than the measured and in depth tensile stresses up to +430 MPa were calculated, while near-zero stresses were measured. This affects calculated the stress impact depth as well.

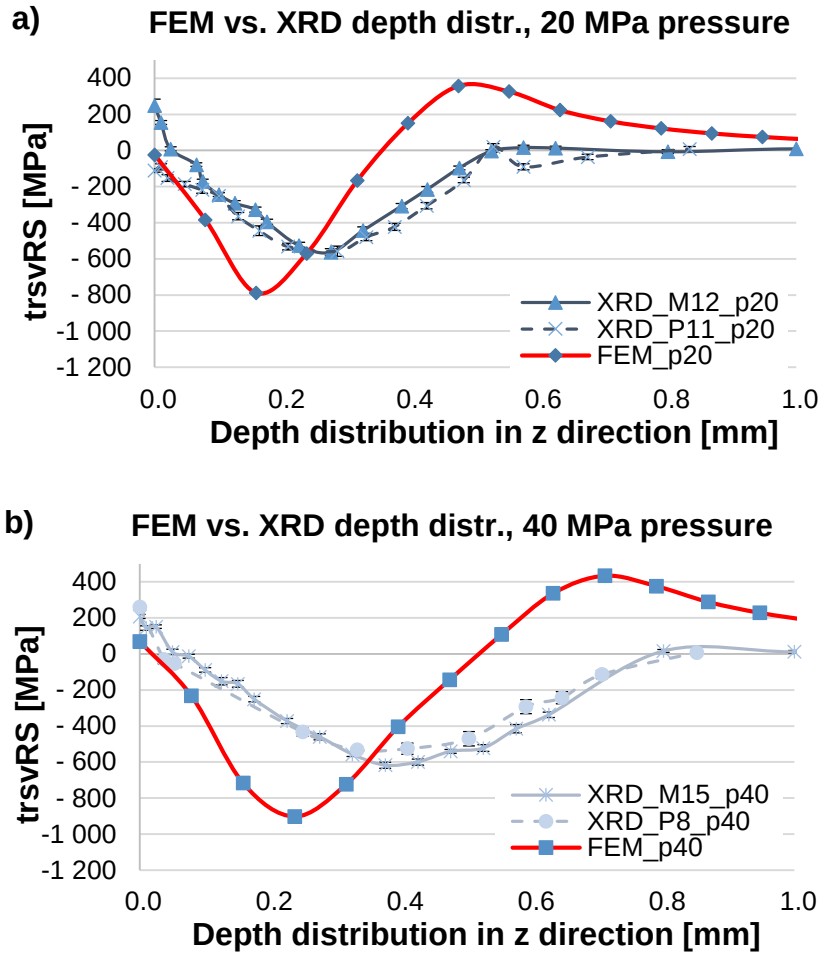

Figure 7-32: FEM vs XRD residual stress depth distributions in transverse direction: a) DR pressure 20 MPa and b) DR pressure 40 MPa

The last comparison in this subchapter shows the FEM and XRD stress depth profiles of DR specimens with pressure of 40 MPa and 75 % overlapping, see Figure 7-33. The FEM depth profiles were determined in the middle of the first (overlapped) or the second (overlapping) trace, where the XRD depth profiles were defined in the middle of the second trace. A direct comparison should be made only with the depth profiles determined in the second trace. Nevertheless, the FEM investigations shown in subchapter 7.1 showed that the measurement position by DR with overlapping has a crucial impact on the near-surface stress distribution. For this reason but not as direct comparison, the FEM depth profiles determined in both traces are depicted.

Figure 7-33 a) illustrates the longitudinal stress depth profiles. Near the surface, the FEM 2nd trace profile exhibit almost identical stresses as measured. The maximal compressive stress as magnitude is very similar to the measured one. Still, at depth from 0.16 mm to 0.32 mm the FEM overestimates the compressive stresses with up to 360 MPa and underestimates the stress impact depth with an app. 0.1 mm. The FEM 1st trace profile has lower compressive stress maximum (app. -510 MPa) but similar stress impact depth.

In the transverse direction, see Figure 7-33 b), similarly to the previous results, there is a larger discrepancy between FEM and XRD derived stress depth profiles. The FEM

overestimated the compressive maximum with up to 400 MPa (when compared FEM 2nd trace with both XRD). Under the surface, tensile stresses up to +450 MPa were calculated, compared to the measured near-zero stress values. The subsurface tensile stresses influenced the calculated stress impact depth and the shape of the stress profile in depth.

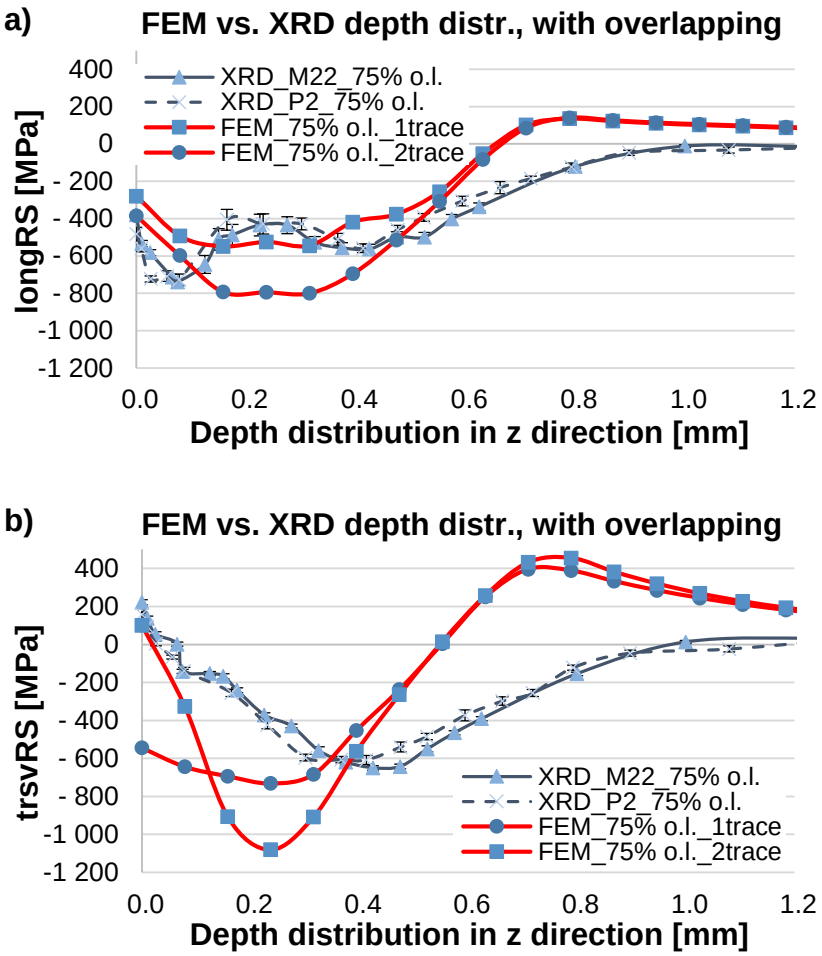

Figure 7-33: FEM vs XRD residual stress depth distributions, DR pressure 40 MPa, overlapping 75 %: a) longitudinal direction and b) transverse direction

To summarise this subchapter, the following can be concluded:

- residual stress surface distributions – the FE calculated surface stress profiles were in a good agreement to the XRD determined ones. Only one exception was observed: by DR with low pressure, due to the high discrepancy of both experimentally derived profiles, a conclusion about the agreement of the FE calculated profile to the XRD derived could not be drawn (nevertheless, the FE calculated profile laid in between). The rest FE profiles deviated from the XRD ones by maximum ± 145 MPa.
- residual stress depth distributions
    - longitudinal direction – the FE calculated depth profiles were in a very good agreement to the XRD derived, especially by single DR and for both low and high DR pressure (maximal deviations of below ± 100 MPa). For

DR with overlapping, the FE calculated profiles in the first or the second trace differed by the compressive stress maximum with app. ± 150 MPa. This fact noted that (at least for this overlapping percentage), no homogeneous stress state in depth can be achieved and emphasised the importance of the position for the stress determination.

- transverse direction
  - single trace DR – the FE predicted stress profile shape fitted well to the XRD derived. Still, quantitatively there were some discrepancies like the maximal compressive stress was overestimated by the FE with up to ± 140 MPa and the stress impact depth was underestimated with roughly 100 µm. The most significant misfit was observed by the stress distributions in depth, where the FE calculated moderate tensile stresses (up to +430 MPa) compared to the near-zero measured values.
  - DR with overlapping – the FE predicted stress depth profiles determined at the first or the second trace differed profoundly from each other, as shape, as near-surface stress and as maximal compressive stress. The comparison between the FE and XRD stress profiles determined in the second trace showed a notable discrepancy of the maximal compressive stress (overestimated by the FE with an app. ± 200 MPa) and presence of moderate tensile stresses in depth (FE) versus near-zero stresses (XRD).

8 Analysis of the surface topography and the cold working

In the following chapter, a comprehensive analysis of the surface topography of pre-machined and/or deep rolled specimens was accomplished as well as the cold working of deep rolled specimens was investigated. It is well known that the surface topography is a substantial part of the surface integrity, as it influences the fatigue life of the treated specimens. The roughness profile, consisting of micro peaks and valleys, forms micro-cracks that can open during operational loading and thus can directly deteriorate the fatigue strength. It is proved that polished specimens (with the goal to minimise the surface roughness) have higher fatigue strength than rough specimens. Chapter 8.1 is focused on the investigation of the surface topography after different pre-machining state, i.e. milling or milling + polishing and/or consecutive deep rolling with variable process parameters like the diameter of the DR tool, applied pressure, the number of overturns and the overlapping percentage. The chapter 8.1.1 shows experimentally derived surface roughness of specimens treated as mentioned above; chapter 8.1.2 deals with the shape of the DR trace (width and depth) by variable process parameters. The FE modelling was employed in chapter 8.1.3 to plot the shape of the DR trace, thus proving the capability of the finite element model to predict the surface topography after DR.

The cold working change after DR, in terms of hardness and indentation modulus, diffraction peak widths and plastic strain, was analysed in chapter 8.2. Chapter 8.2.1 focuses on the experimental investigation of the micro-hardness- and indentation modulus depth distributions after DR with variable applied pressure, number of overturns and overlapping percentage. The diffraction peak widths, a characteristic property of every x-ray diffraction measurement and a non-direct indication for the presence of cold working, was studied in chapter 8.2.2. The last subchapter 8.2.3 investigated the induced during- and after DR plastic strain using FEM. This measure can also be considered as a non-direct indication of the amount of the induced cold working.

8.1 Surface topography

In chapter 8.1 was analysed the surface roughness after different pre-machining states and/or following DR process. The shape of the DR trace in terms of trace width and depth was investigated through experimental measurements with White Light Interferometry method and utilizing FEM. In Table 8-1 are plotted all varied process parameters, where in yellow are noted the current process variables. Additionally, the DR tool was varied from 3.0 mm (HG3) to 6.35 mm (HG6). The examined specimens were not additionally designated, as only one process parameter was varied. For clearer representation, the varied process parameter was plotted in the diagrams' abscissa axis, instead of the specimen's designation.

Table 8-1: Experimental design of the surface roughness of pre-machined and/or DR specimens

DR pressure	Number of overturns	Overlapping percentage
20	1	0
25	1	0
32	1	0
40	1	0
40	2	0
40	3	0
40	5	0
40	7	0
40	1	25 %
40	1	50 %
40	1	75 %

8.1.1 Experimental investigation of the surface roughness of pre-machined and/or DR specimens by mechanical stylus method

The chapter 8.1.1 presents an experimental investigation of the surface roughness after pre-machining (milling or milling + polishing) and/or consecutive DR with variable parameters plotted in Table 4-1. The classical mechanical stylus method was employed, and the roughness parameters Ra (the arithmetical mean deviation of the assessed profile) and Rz (the average distance between the highest peak and lowest valley in each sampling length) were analysed.

In Figure 8-1 are plotted the roughness values after milling or milling + DR with tool HG3. Figure 8-1 a) shows the Ra (in blue) and Rz (in red) after milling (dotted lines) and after milling + DR (full lines) with variable DR pressure from 20 to 40 MPa. The roughness after milling for both Ra and Rz is much higher than after the consecutive DR independent of the applied DR pressure. After DR, a slight tendency is present, where both Ra and Rz decrease with increasing the DR pressure, reaching at 40 MPa pressure Rz value of under 2 µm. Figure 8-1 b) depicts the Ra and the Rz values for a variable number of overturns (DR pressure was fixed at 40 MPa). The randomly distributed roughness after milling (Rz = 7 – 8 µm) significantly reduces after DR, where the higher number of overturns reduces it even further to reach after 7 overturns a value for Rz below 1.0 µm. The last parameter variation is plotted in Figure 8-1 c), where the specimens were treated with constant DR pressure of 40 MPa, single overturn and variable percentual overlapping. The roughness after milling is again in the range of Rz = 7 – 8 µm with a minimal standard deviation (based on three measured profiles for each value), indicating a reproducible milling process in terms of achieved roughness. There is a significant improvement of the surface quality after DR, but the overlapping up to 50 % does not influence the achieved roughness. At 75 % overlapping, there is a slight improvement of the Ra and Rz (compared with lower overlapping), which reached very low values of 0.16 µm and 0.9 µm. This can be attributed to the fact that at higher overlapping, a certain part of the investigated trace is practically double treated. Considering the DR process is usually applied with certain overlapping

to treat a whole surface, the achieved surface roughness is comparable with those after using a polishing process.

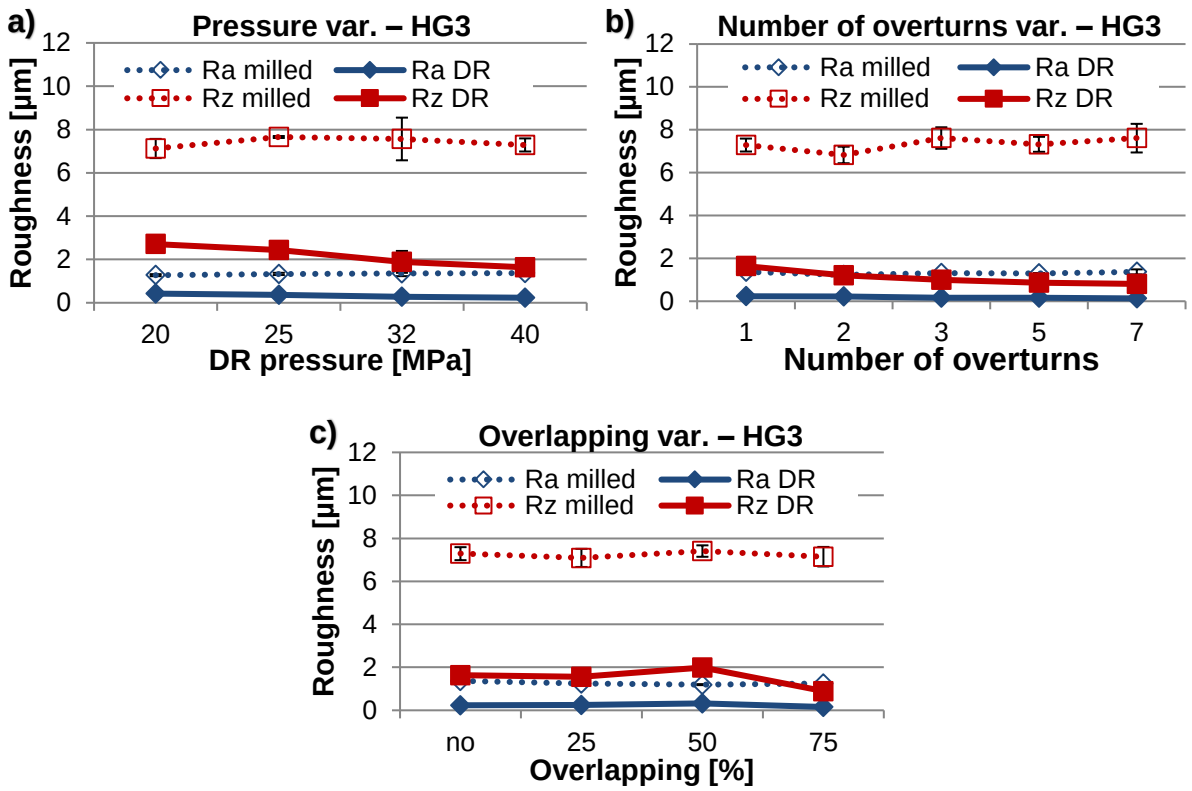

Figure 8-1: Experimental roughness comparison of milled or milled + DR specimens with DR tool HG3 by variation of: a) DR pressure, b) number of overturns and c) percentual overlapping

Figure 8-2 depicts the roughness after milling and/or following DR with the same parameters varied as in Figure 8-1 but with employed DR tool with a diameter of 6.35 mm (HG6). The results after milling and/or variable DR pressure are plotted in Figure 8-2 a). Differently as in Figure 8-1 a), the values of Rz after milling are relatively higher reaching 11 – 12 µm, whereas the Ra values are just slightly higher as those of Figure 8-1 a). Nevertheless, after DR, the Rz values reduce to an app. 2 µm but do not show the tendency observed in Figure 8-1 a) for decreasing at higher DR pressure. A possible reason can be the much higher and fluctuating initiate roughness after the milling procedure. Figure 8-2 b) represents the Ra and Rz after milling and/or DR with constant DR pressure of 40 MPa and a variable number of overturns. The initial roughness (Rz) after milling is also higher compared with the results in Figure 8-1 b) and vary between 9.0 – 12 µm. The following DR treatment reduces these values to below 2 µm reaching a minimum of below 1 µm for the treatment with 7 overturns. Anyhow, the apparent tendency for reducing roughness with an increasing number of overturns is compromised by the variable initial values. Figure 8-2 c) shows the roughness of milled and/or DR specimens with constant DR pressure of 40 MPa, single overturn and variable overlapping. The initial Rz values after milling vary from 7.0 – 11 µm and are quite higher than those of Figure 8-1 c). Considering all the specimens used for the investigations in Figure 8-1 and Figure 8-2 were treated with identical milling parameters, it

is clear that in this particular case the milling process did not deliver reproducible surface quality. After applying the DR process, the roughness, as already expected, diminished to values for Rz below 2 µm and reached a minimum of Rz 0.8 µm and Ra 0.08 µm at the higher overlapping percentage. Still, the Rz values after the milling are lower for the later treated with DR with overlapping of 50 % and 75 %, so this tendency cannot be distinguished.

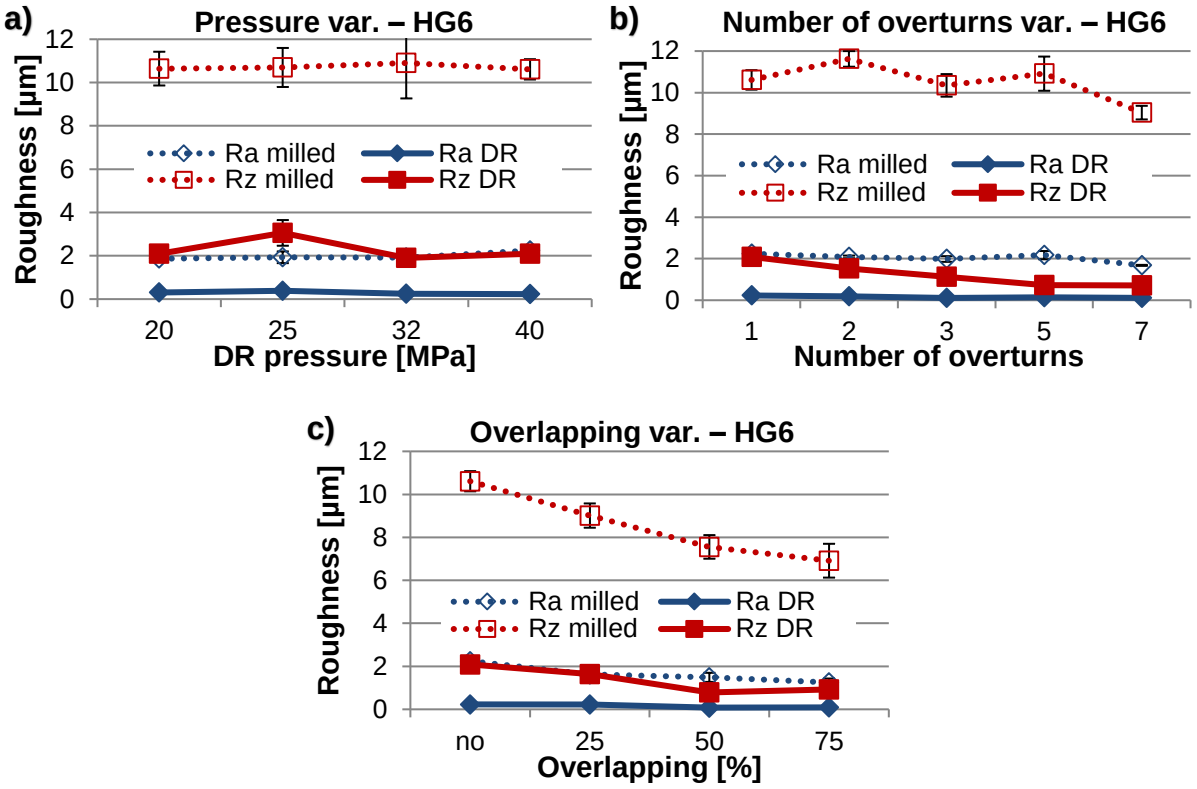

Figure 8-2: Experimental roughness comparison of milled or milled + DR specimens with DR tool HG6 by variation of: a) DR pressure, b) number of overturns and c) percentual overlapping

The next investigation shows the roughness (Rz) of specimens treated with variable pre-machining and/or following DR with variable process parameters (the DR tool diameter was fixed at 6.35 mm). Figure 8-3 depicts the Rz values of milled or milled + polished specimens before the DR process, where the milling and polishing parameters were kept constant. The roughness of the milled specimens fluctuates significantly from an app. 8 to 14 µm, whereas the following polishing procedure diminishes these differences and reduces the Rz values to ca. 0.05 µm.

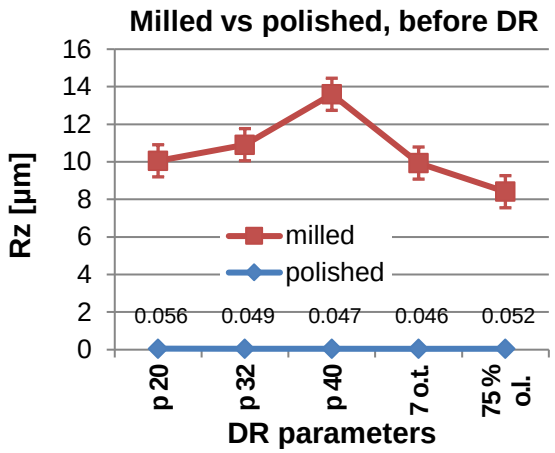

Figure 8-3: Experimental roughness of milled or milled + polished specimens before DR

After performing the roughness measurements plotted in Figure 8-3, the same specimens were treated with DR. The induced roughness is shown in Figure 8-4, where the Figure 8-4 a) depicts the Rz values along the DR trace and Figure 8-4 b) transverse to the DR trace (the same measurement setup as for the measurements shown in Figure 8-1 and Figure 8-2). In the longitudinal direction (see Figure 8-4 a)), the milled + DR specimens (red line) show tendency of decreasing Rz with increasing the DR pressure despite the higher roughness before DR (see Figure 8-3). The multiple overturns, or overlapping of 75 % reduce further the Rz values, but the initial roughness after milling was lower for the specimens treated later with 7 overturns or with 75 % overlapping. The specimens treated with milling + polishing + DR (blue line) show quite different tendency. Considering the very low initial roughness Rz of an app. 0.05 µm, after the DR treatment the Rz values slightly increase with increasing the DR pressure or when applying an overlapping. The multiple overturn notably deteriorate the surface quality increasing the Rz values from 0.05 µm (after pre-machining) to 0.6 µm (after DR). The Rz values in the transverse direction are plotted in Figure 8-4 b). Here, the milled + DR state shows in general, much lower Rz values compared to the milled condition (see Figure 8-3). Still, the DR pressure variation does not show a clear trend. The treatment with 7 overturns or with 75 % overlapping decrease, even more, the Rz values compared to those with variable DR pressure. The lowest Rz value of 0.25 µm was achieved by treatment with 75 % overlapping. Still, it must be considered that the difference between all milled + DR specimens is an app 1.4 µm.

The milled + polished + DR specimens show almost no change in the Rz values compared with the only milled + polished state. The only deviation exhibit the specimen treated with 7 overturns, where the Rz value is much higher (0.6 µm) than before the DR (0.05 µm).

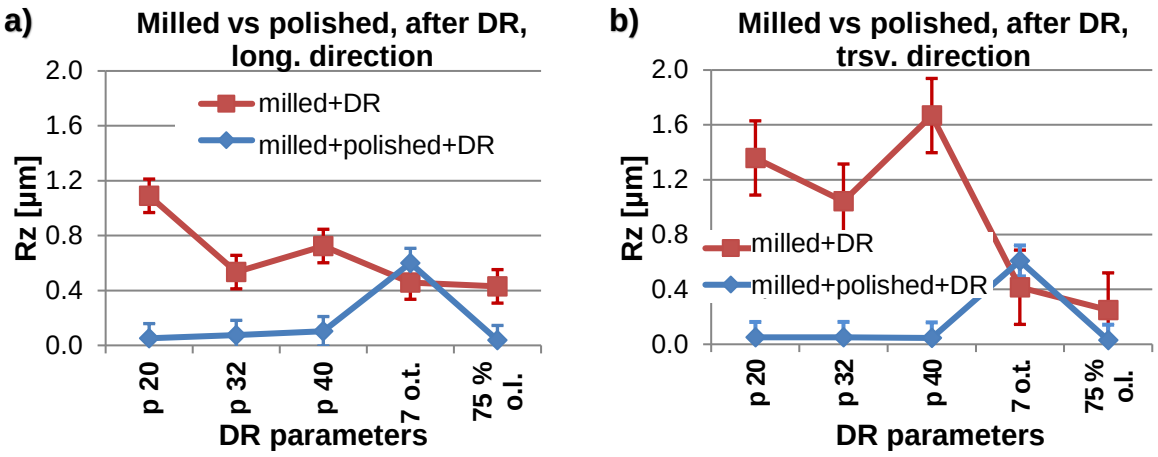

Figure 8-4: Experimental roughness of milled + DR or milled + polished + DR specimens by variation of DR process parameters; measurement path in: a) longitudinal direction and b) transverse direction

The observations from Figure 8-2 and Figure 8-4 b) show that the influence of the DR process cannot be distinguished from the pre-machining state. In case of high initial roughness, the DR process can be used as a smoothing operation, as it smashes the roughness peaks. In contrary, when the initial roughness is very low, the plastic deformation created by the DR can induce artificial roughness, thus deteriorating the surface quality. This occurrence was observed, especially when applying severe DR conditions like, e.g. multiple overturns.

The findings in this chapter show that the pre-machining state has a significant impact on the resulted roughness after DR. Treatment with DR tool with a bigger diameter (HG6) compared with a smaller diameter (HG3) led to a higher reduction of the induced after DR roughness for all process parameters variations. An overview of the pre-machining and process parameters interdependencies can be found in Figure 8-5.

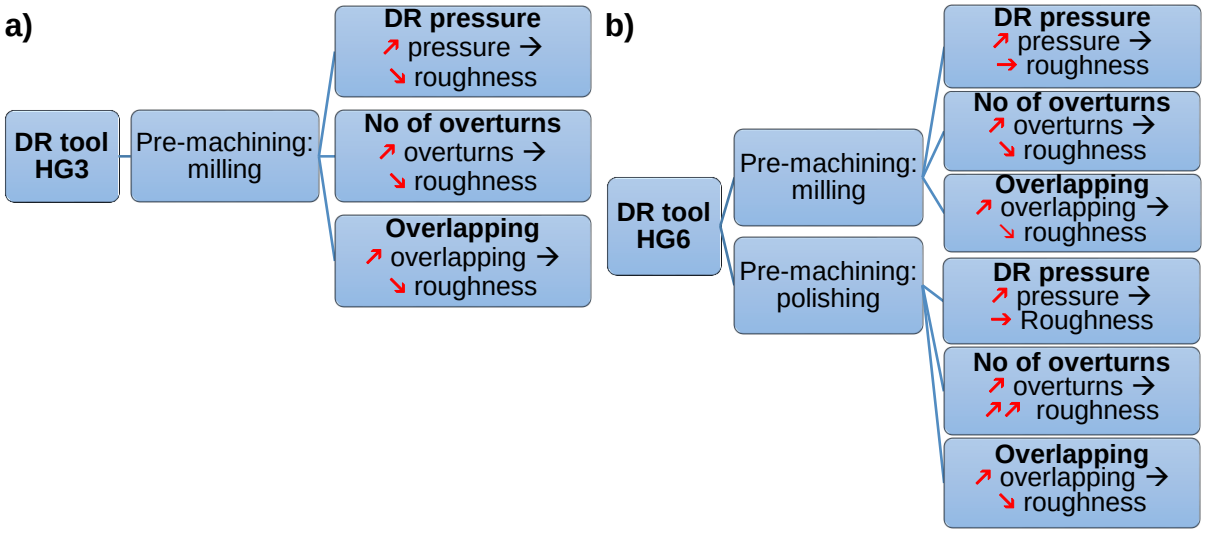

Figure 8-5: Overview of the influence of the pre-machining state and the DR parameters on the resulted surface roughness by variable DR tool: a) DR tool HG3 and b) DR tool HG 6

8.1.2 Influence of the DR process parameters on the resulting surface topography – mechanical stylus method

In this sub-chapter is investigated the resulted after DR trace(s) geometry in terms of trace's width and depth. The pre-machining condition was milled, and the specimens were treated with DR varying the following parameters: DR tool (HG3 or HG6), number of overturns or overlapping percentage. The trace topography was also investigated for the pre-machining state milled + polished + DR, but there were no significant differences between the two pre-machining states. Therefore, in this chapter, only the topography of the milled + DR specimens is shown. For every measurement value, the mean value of the three measurement paths was calculated.
Figure 8-6 depicts the trace(s) geometry of specimens treated with DR tool HG3.

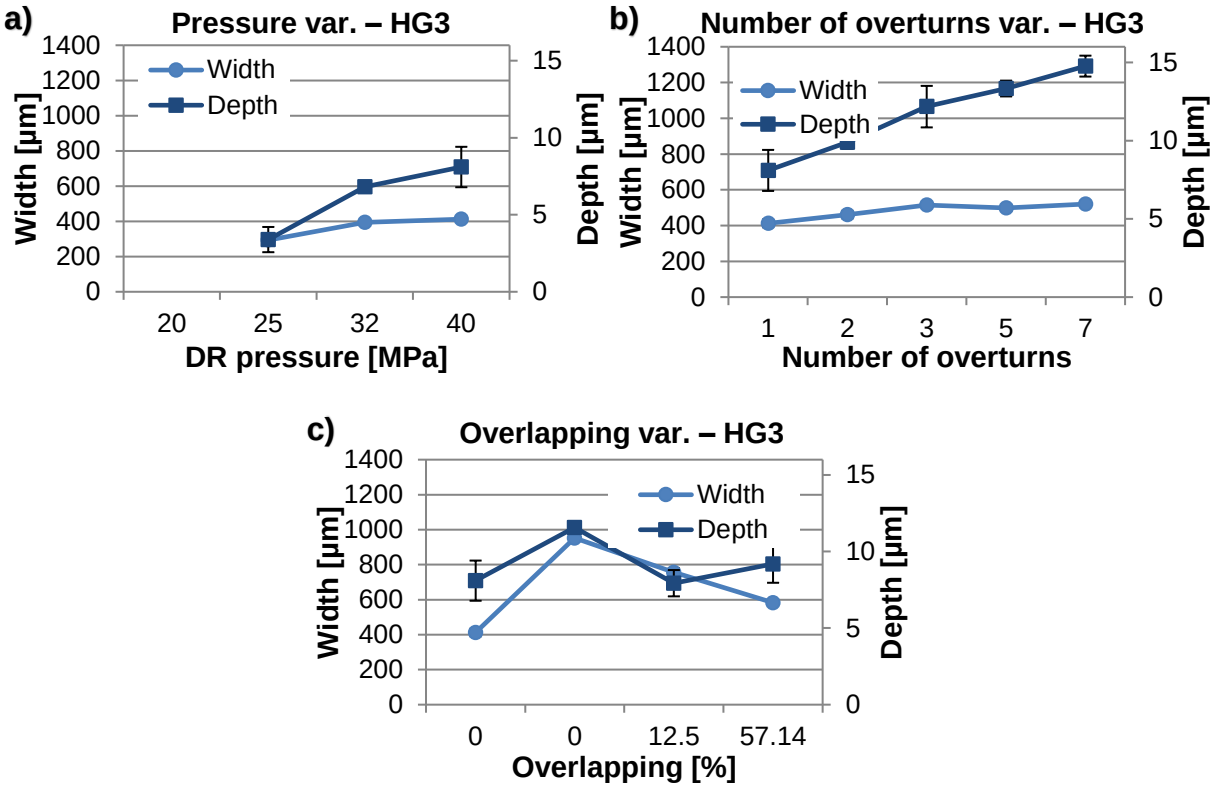

Figure 8-6: DR trace topography (experimentally derived) of milled + DR specimens by treatment with HG3 tool and variation of: a) DR pressure, b) number of overturns and c) percentual overlapping

Figure 8-6 a) shows the width (left ordinate axis, circle marks) and the depth (right ordinate axis, square marks) of the DR trace by variable DR pressure. No visible trace could be observed at a pressure of 20 MPa; from 25 to 40 MPa the DR trace expands to reach a width of 413 µm and a depth of 8 µm at DR pressure of 40 MPa. The overturn variation is plotted in Figure 8-6 b), where almost no change in the trace's width is visible in contrary to the trace's depth, which increases with near-linear progression. The depth of ca. 15 µm by 7 overturns is about 90 % higher than the one by single overturn. In Figure 8-6 c) is presented the overlapping variation, where the actual overlapping was calculated based on the single trace width, and the corresponding percentual values were plotted on the abscissa axis. A large discrepancy of up to 37 % points

between the target and the actual overlapping values is visible (defined were 20, 50 and 75 % overlapping). A possible reason for this discrepancy can be the mechanical set-up of the DR tooltip, which is hydrostatically supported and has several milimeter axial clearance. The existing axial clearance can be a source of radial instability of the tooltip, leading to difficult to define overlapping. The trace(s) width increase in case of overlapping with up to 100 % and this effect was expected considering the treatment without overlapping has only a single trace. With increasing the overlapping percentage, the traces' width decrease, which was also expected due to the geometrical definition of the overlapping parameter. The trace's depth remains constant at app. 8 – 9 µm except for the value for the second 0 % overlapping, which is an app. 12 µm. This deviation cannot be explained reasonably except for a possible faulty DR treatment.
Figure 8-7 represents the trace(s) width, and depth by DR treatment with tool HG6 and the same process parameter variations as in Figure 8-6. The pre-machining state of all specimens was milled.

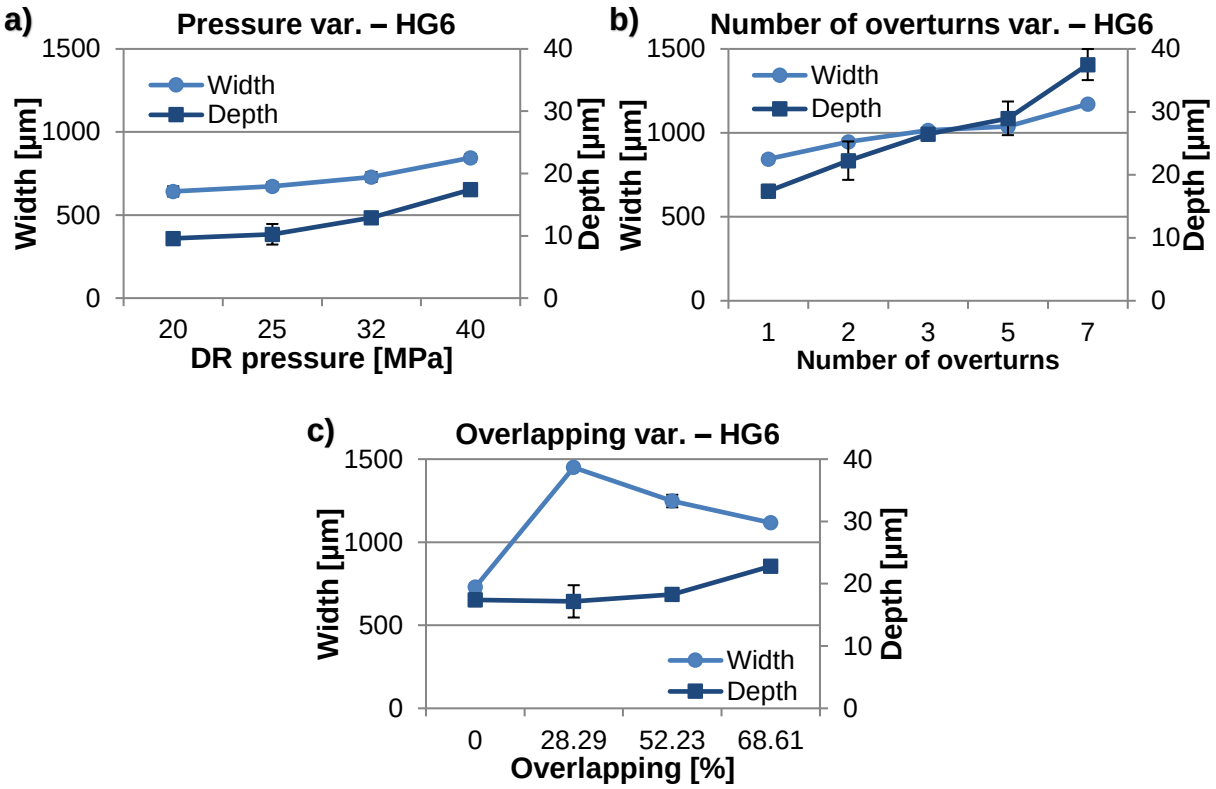

Figure 8-7: DR trace topography (experimentally derived) by treatment with HG6 tool and variation of: a) DR pressure, b) number of overturns and c) percentual overlapping

The pressure variation is shown in Figure 8-7 a), where both trace's width and depth increase near hyperbolic with increasing the DR pressure to reach at 40 MPa pressure a width of 845 µm (app. 30 % higher than at 20 MPa) and a depth of 17 µm (app. 85 % higher than at 20 MPa).
Figure 8-7 b) depicts the variation of the number of overturns by fixed DR pressure (40 MPa) and without overlapping. The trace's width increase almost linear from 845 µm for a single overturn to 1170 µm for 7 overturns (app. 38 % wider trace). Similar

trend but with a steeper slope can be observed for the trace's depth increasing from 17 µm (1 overturn) to 38 µm (7 overturns), meaning over 200 % deeper trace. The last parameter variation, namely the overlapping percentage (by fixed DR pressure of 40 MPa and 1 overturn) is plotted in Figure 8-7 c). Here, similar to Figure 8-6 c), the actual overlapping percentage was calculated based on the single trace width and the corresponding values were plotted on the abscissa axis. A discrepancy (maximum 6 % points) between defined overlapping (25, 50 and 75 %) and calculated overlapping can be observed, but it is not very strong, compared with the values of Figure 8-6 c). The traces' width, in case of overlapping, decreases linearly with increasing the overlapping percentage and the trace depth remains constant up to overlapping of 68 %, where it increases with an app. 35 %.

The results from this chapter showed that the topography changes after treatment with DR should not be neglected. The treatment with smaller DR tool (HG3) compared with the treatment with bigger DR tool (HG6) created smaller DR trace for all parameter variations. For both tools, the calculated overlapping based on the resulted DR traces differed from the defined one. In some cases, the discrepancy was in the amount of up to 37 % points. An overview of the influence of DR parameters on the resulted DR trace width and depth by variable DR tool can be seen in Figure 8-8.

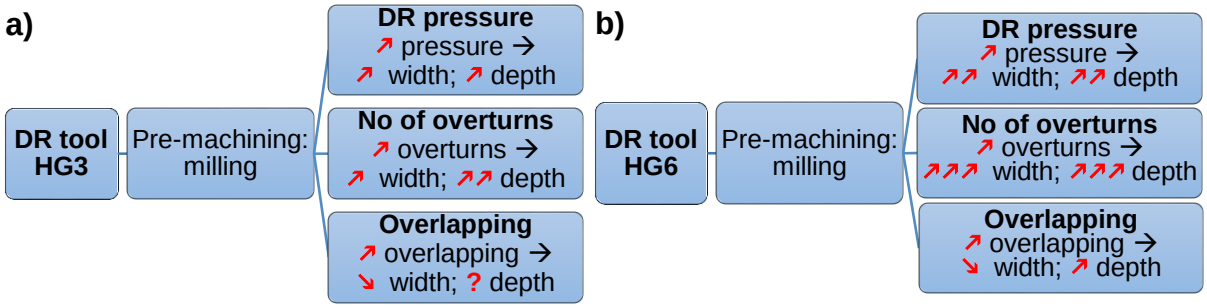

Figure 8-8: Overview of the influence of DR parameters on the resulted DR trace width and depth by variable DR tool: a) DR tool HG3 and b) DR tool HG 6

8.1.3 FE analysis of the surface topography after DR with variable process parameters

Similarly to the results from sub-chapter 8.1.2, the current sub-chapter describes the surface topography of the DR trace after DR with variable process parameters, using DR tool HG6. In this subchapter, the capability of the designed FE model to predict the macroscopic surface changes after DR was analysed. For this study, the DR trace shape was investigated, as the following DR parameters were varied: DR pressure (20, 25, 32 and 40 MPa) and overlapping percentage (0, 25, 50, 75 and 90 %). The actual overlapping was adapted to fit the percentual values from sub-chapter 8.1.2 but simplified was designated as mentioned above. The diagrams below are designed as follows: the surface of the DR trace is plotted on the abscissa axis, where the 0-coordinate describes the center of the DR tooltip. In case of DR with overlapping, the 0-coordinate describes the first DR trace. On the ordinate axis is plotted the z (vertical) - displacement of the surface elements distorted by the DR process. With different curves are plotted the trace(s) profiles by variable DR parameters. Figure 8-9 a) shows

the DR trace profiles by variation of the DR pressure. The trace width increase from 588 µm for a pressure of 20 MPa to 860 µm for 40 MPa. Compared to the experimentally derived values from Figure 8-7 a), the FEM derived values are in a good agreement, with a difference of app. 3 – 50 µm (maximum 10 %). The trace depth also increases with applying higher DR pressure, beginning from 10 µm (DR pressure 20 MPa) and raising to 19 µm (DR pressure 40 MPa). Here, compared with the experimental values, there is a good agreement at low and at high DR pressure (deviation up to 1.6 µm) and a satisfactory agreement for the values for 25 and 32 MPa (difference up to 4.3 µm). The possible explanation is as follows: in Figure 8-9 a) it is visible that the trace profiles have a very distinct peel-outs (the regions with the highest z-displacements), which grow with higher DR pressure, reaching up to 6 µm height (measured from the 0-level of the z-displacement). This trend is not clearly presented in the experimentally derived topography profiles of the DR trace due to the relatively high roughness in the transition zone between treated- and untreated material, where the peel-outs appear. The FEM derived trace depth was calculated as the difference between the highest and the lowest z-displacement. In contrary, the experimentally derived trace depth was visually determined, as often, there was no definite transition between treated- and untreated material and no visible peel-out. The 0-level in vertical (z) direction was also difficult to define, due to the available roughness.

Figure 8-9 b) and c) present the overlapping variation, by fixed DR pressure (p = 40 MPa). For better visibility, the variation was split into two diagrams, and the variation from 25 % to 75 % is plotted in Figure 8-9 b). The trace profile(s) looks quite different for the low or the high overlapping percentage, where for 25 % overlapping two narrow traces are visible and for up to 75 % overlapping no plateau surface was generated. The peel outs of the second traces (the right-hand side ones) reach for all overlapping values almost 10 µm height, indicating a high amount of plastically deformed material pushed out from the place of treatment. The trace width reduces with increasing the overlapping percentage, which was expected, due to the geometrically defined overlapping parameter. Compared to the experimentally derived values, the FEM values show a negligible difference of maximum 2 % (up to ca. 24 µm). The trace depth increase up to 50 % overlapping and stays on the same level for 75 % overlapping. The comparison between experimental and FEM values shows a good agreement only for 75 % overlapping (app. 3 % deviation) and a satisfactory agreement for 25 and 50 % overlapping (app. 18 – 25 % deviation).

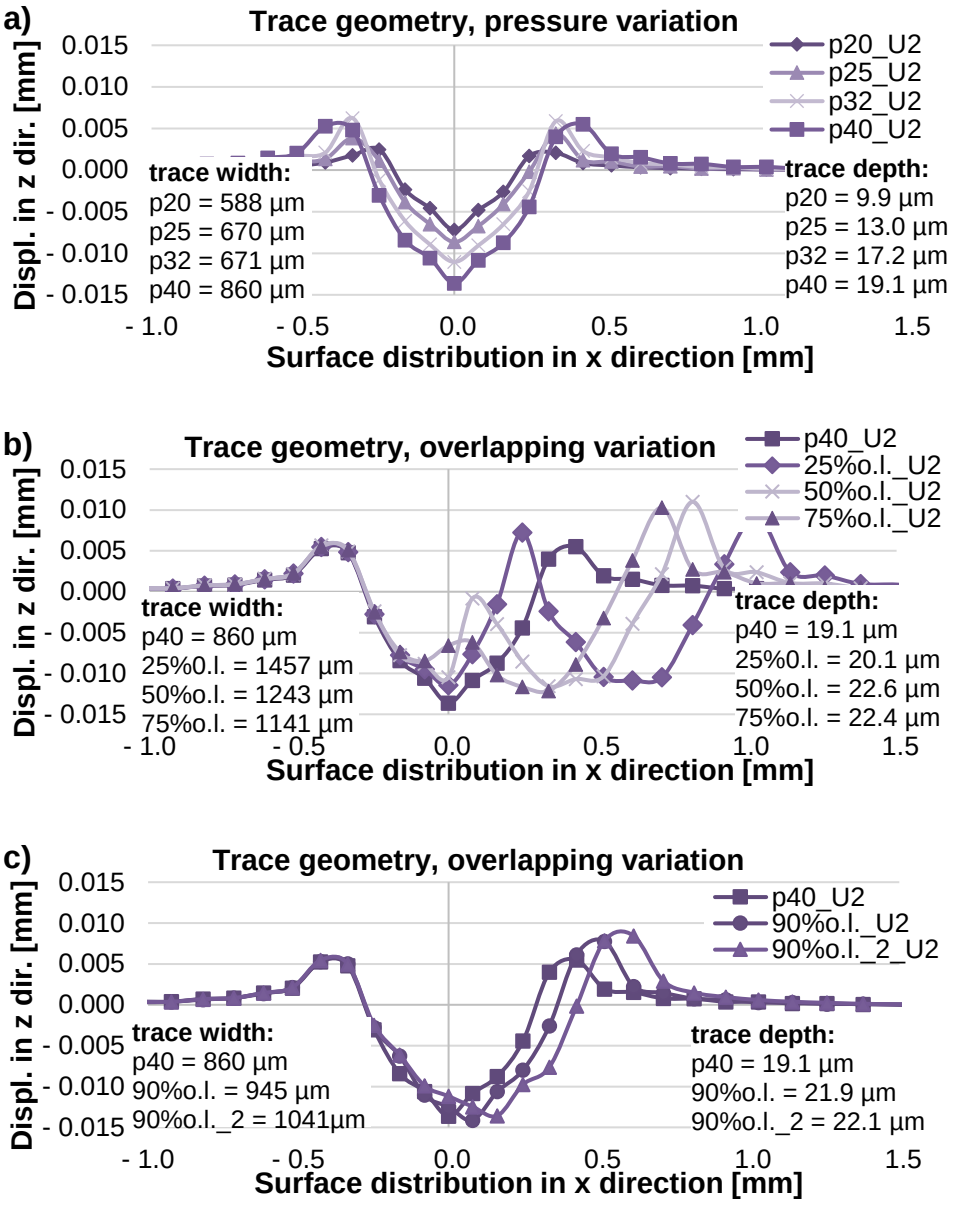

Figure 8-9: FEM trace geometry of DR specimens with tool HG 6, by variable: a) DR pressure, b) percentual overlapping (25 % - 75 %) and c) percentual overlapping 90 % realised with 2 (90%o.l.) or 3 (90%o.l._2) DR traces

Figure 8-9 c) depicts the surface topography after DR treatment with 90 % overlapping, where 90%o.l. means two DR traces were modelled and 90%0.l._2 means three traces. The goal by the treatment 90%0.l._2 was to achieve praxis-near surface, as under real conditions DR is mostly applied to treat a whole surface and not just a single- or two traces. Additionally, the 90 % overlapping was chosen as a praxis-near overlapping percentage. The trace width of specimens 90%o.l. and 90%0.l._2 increases almost linear compared to p40 (without overlapping). The treatment with three traces, overlapped with 90 % (90%0.l._2) generates a plateau-near surface on the bottom of the traces' profile, and this proves the treatment with 90 % overlapping (if applied to treat a whole surface) can create a smooth surface.

When comparing the DR trace depth of the single-treated specimen with those treated with 90 % overlapping, it is visible that the depth from the plane surface remains the

same. Although, when considering the higher peel outs, the total depth increase with an app. 3 µm to reach app. 22 µm. The traces' depth of specimens 90%o.l. and 90%0.l._2 remains almost the same.

8.2 Cold working changes due to pre-machining and DR

Chapter 8.2 presents an experimental and an FE modelling investigation of the cold working changes generated by the deep rolling process by variable pre-machining states. In subchapter 8.2.1 were examined the depth distributions of the Vickers micro-hardness and the indentation modulus of milled + DR specimens by variable process parameters. Subchapter 8.2.2 analyses the surface- and the depth distributions of the x-ray diffraction peaks widths (FWHM) after DR by variable pre-machining state and DR process parameters. FE modelling was employed in chapter 8.2.3 to investigate the evolution of the plastic strain during and after DR by variable process parameters. In Table 8-2 is plotted the experimental/modelling design with the corresponding process variations.

Table 8-2: Experimental and modelling design of the cold working investigation of pre-machined and DR specimens

Specimen No	Pre-machining state	DR pressure	Number of overturns	Overlapping percentage
M12	milling	20	1	0
M15	milling	40	1	0
M19	milling	40	7	0
M22	milling	40	1	75 %
P11	milling + polishing	20	1	0
P8	milling + polishing	40	1	0
P4	milling + polishing	40	7	0
P2	milling + polishing	40	1	75 %

8.2.1 Experimental investigation of the depth distribution of micro-hardness and indentation modulus of DR specimens

The current chapter analyses the depth distribution of the Vickers micro-hardness and the indentation modulus of milled + DR specimens with variable process parameters. The diagrams were designed as follows: for every specimen, a single diagram was dedicated, where on the abscissa axis, the depth distribution in z direction was plotted and on the ordinate axis, the corresponding investigated factor (micro-hardness or indentation modulus). Additionally, it is plotted an average of three measurement paths taken in the middle of the DR trace and an average of two measurements paths out of the DR trace. The two measurements paths out of the DR trace were positioned on the places, where the highest compressive residual stresses on the surface were measured (see chapter 7.5.3), aiming to investigate the possible micro-hardness changes due to the high compressive residual stresses presented in this area. As the position of this compressive residual stress maximum varied for the specimens treated with different DR process parameters, the position of these two measurement paths was

defined individually for each specimen. The measurement values on the very surface are missing, due to specifics of the experimental setup (see chapter 4.5).
Figure 8-10 represents the micro-hardness depth distribution of DR specimens with variable DR pressure (Figure 8-10 a) – p = 20 MPa and Figure 8-10 b) – p = 40 MPa) or with multiple overturns (Figure 8-10 c) – 7 overturns), or with overlapping (Figure 8-10 d) – 75 % overlapping). For all variations, it is notable that the measurement values deeper than 1.0 mm, where the DR treatment should not have an impact, fluctuate between 400 HV and 420 HV (except the measurement point 1.2 mm from Figure 8-10 d)). This fluctuation results due to the relatively small indentation imprint (the projected imprint has a rectangular shape with diagonal of below 20 µm), which in case of measurement between grains or in a single grain can lead to different values.

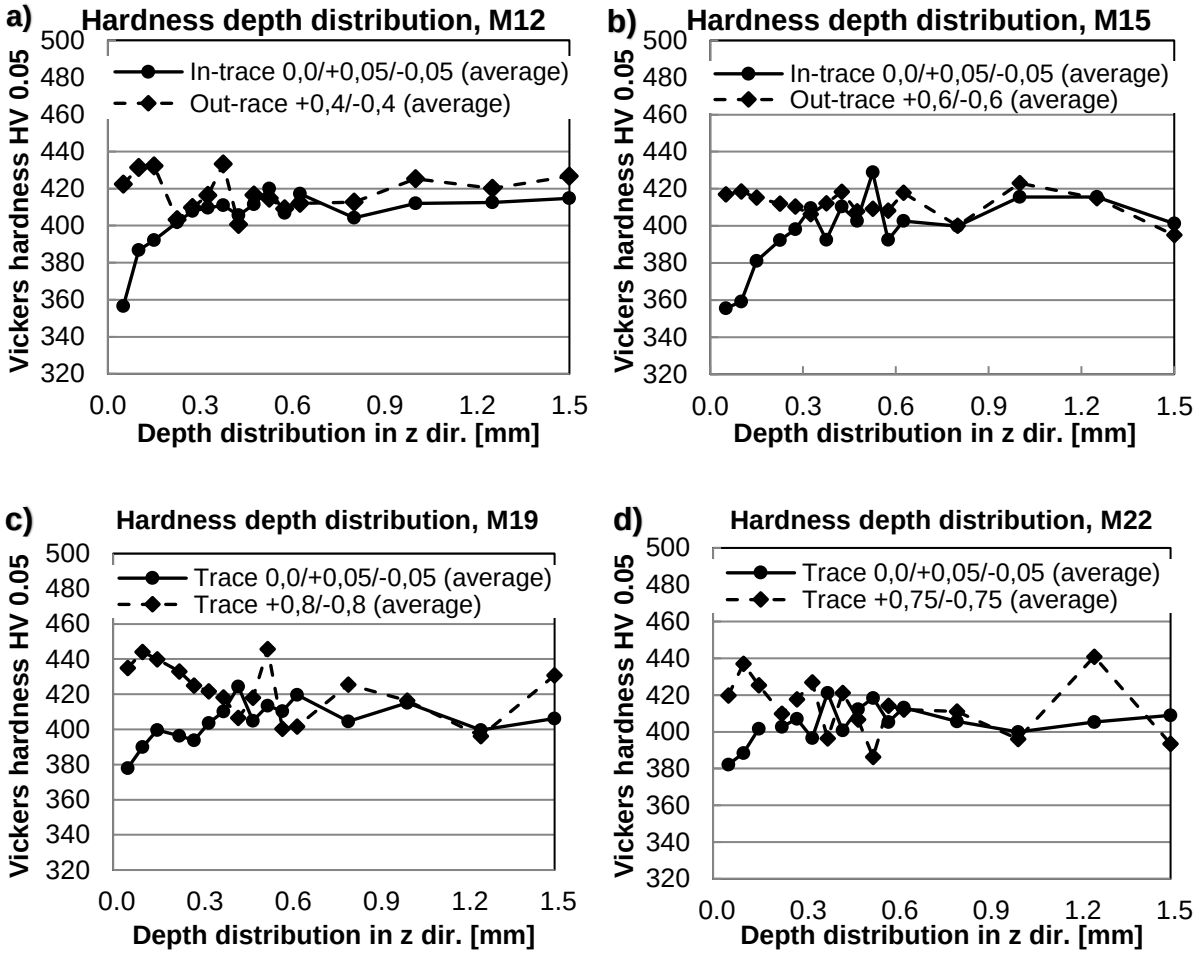

Figure 8-10: Depth distribution of micro-hardness (experimentally derived) in- and out of the DR trace of milled + DR specimens by variable DR parameters: a) M12 - DR pressure 20 MPa, b) M15 - DR pressure 40 MPa, c) M19 - DR pressure 40 MPa, 7 overturns and d) M22 - DR pressure 40 MPa and 75 % overlapping

Figure 8-10 a) and b) show the micro-hardness depth distributions of specimens M12 (p = 20 MPa) and M15 (p = 40 MPa). For both specimens, a very similar hardness gradient from the surface can be observed for the measurement path in the middle of the DR trace (Trace 0,0/+0,05/-0,05). Surprisingly, the near-surface values are with app. 50 HV lower than those of the base material, which can be an indication of work-

softening induced by the DR process. The measurement paths out of the trace (Trace +0,4/-0,4 and Trace +0,6/-0,6) show a greater scattering of the measured values without a clear tendency. Figure 8-10 c) and d) represents the micro-hardness depth distributions of specimens M19 (p = 40 MPa, 7 overturns) and M22 (p = 40 MPa, 75 % overlapping). Here, the near-surface hardness gradient of the in-trace paths is not as steep as for the specimens M12 and M15, and the near-surface hardness values are with app. 30 HV lower than those of the base material. The out of trace paths (Trace +0,8/-0,8 and Trace +0,75/-0,75) differ for both specimens, where the path of the M19 shows slightly increased micro-hardness values (app. 440 HV) near the surface, where the path of M22 shows similar but not that clear tendency due to the scattered values.

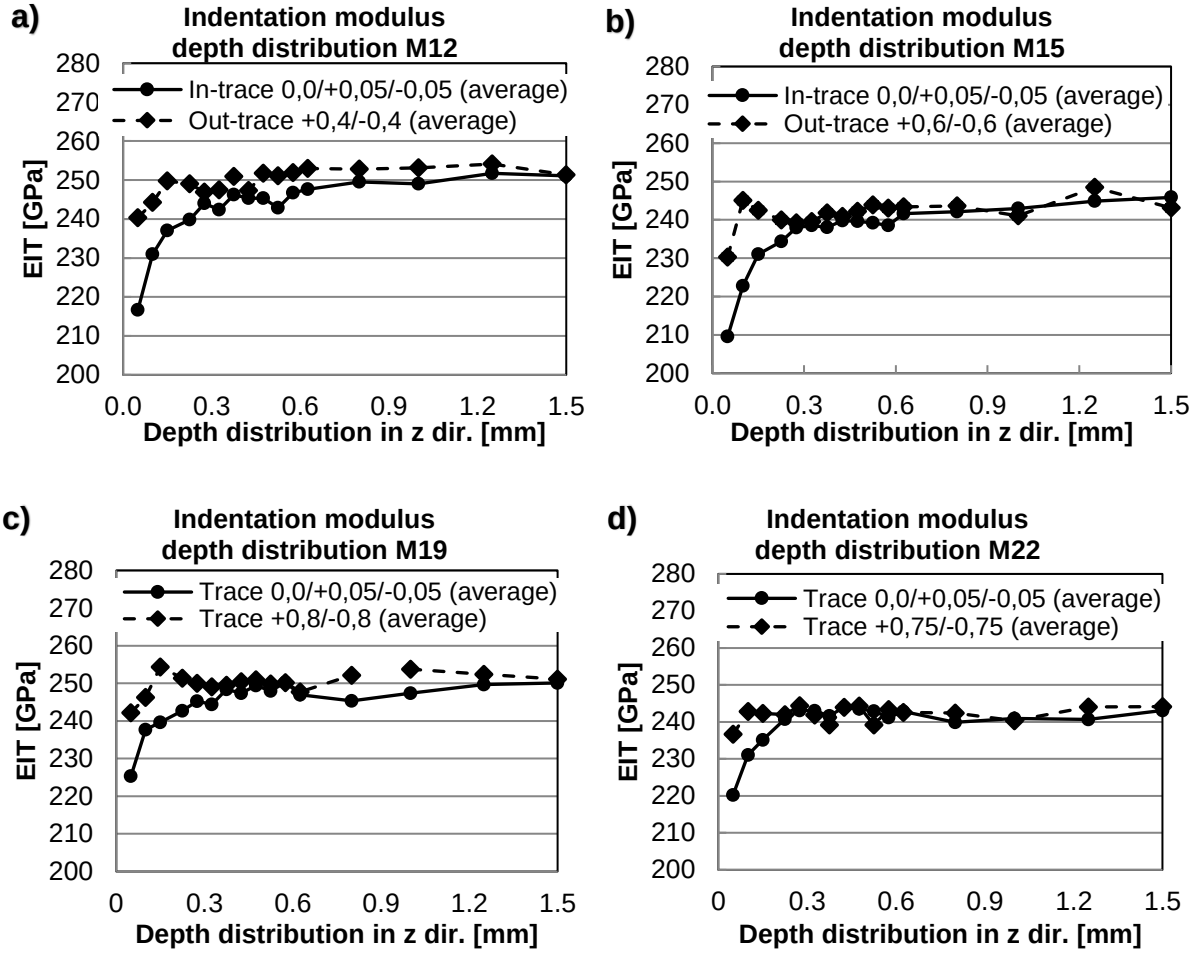

Figure 8-11: Depth distribution of indentation modulus (experimentally derived) in- and out of the DR trace by variable DR parameters: a) DR pressure 20 MPa, b) DR pressure 40 MPa, c) DR pressure 40 MPa, 7 overturns and d) DR pressure 40 MPa and 75 % overlapping

In Figure 8-11 are plotted the depth distributions of the indentation modulus (EIT) in- and out of the DR trace by the same process parameters variations as those showed in Figure 8-10. The EIT for homogeneous materials can be directly related to Young's modulus. It is a measure of the material's stiffness, where lower EIT indicates lower stiffness. Here, for all four specimens, the EIT of the base material is similar, namely 240 GPa – 250 GPa. Additionally, all in-trace paths exhibit a near-surface gradient,

where the values at 0.025 mm are lower than those of the base material. Anyhow, no distinct tendency of the gradients can be seen as the typical standard deviation of all values is an app. ± 5 GPa. The out of trace paths (designated with dashed lines and rhomb) show similar values for the base material, confirming good statistical reliability. Nevertheless, the near-surface stress gradients are not as steep as those of the in-trace paths but are similar for all four specimens.

8.2.2 X-ray diffraction peak widths investigation of DR by variable pre-machining state and DR process parameters

Subchapter 8.2.2 depicts the surface- and the depth distributions of the x-ray diffraction peaks widths, derived from the x-ray diffraction residual stress measurements shown in chapter 7.5. Considering the definition of the residual stresses types I – III, it is known, that when measuring stresses with x-ray diffraction, the stresses type I (macro stresses) lead to shifting of the position of the diffraction peak when tilting the specimens in different ψ (χ) angles. Stresses of type II (micro stresses) lead only to diffraction peak broadening. It is important to note that the peak broadening can be related not only to the material's properties, but it is also a function of the instrument's imperfections (instrumental broadening). Even the shape of the peak profile results from the convolution of all effects mentioned above when deducting the instrumental broadening, the width of the diffraction peak can be non-directly related to the micro-strain. The full-width at half maximum (FWHM) of the diffraction peak may be employed as a non-direct measure of the induced cold working and the related hardness change in the material, where higher value means increased hardness and vice versa.

X-ray diffraction peak widths (FWHM) - surface distribution

In Figure 8-12 are depicted the surface distributions of the FWHM for milled or milled + polished specimens treated with DR pressure of 20 MPa (M12 and P11) and 40 MPa (M15 and P8). As mentioned above, the width of the diffraction peak can be related to existing micro-strains. As the strain is direction-dependent, here similarly to the residual stress measurements, the FWHM was determined in both longitudinal and transverse to the DR trace directions. The measurement path was identical with this for the residual stress measurements, namely perpendicular to the DR trace, where the zero x-coordinate describes the middle of the DR trace. The different pre-machining states are designated with different colours: red – milled state and black – milled + polished state.

Figure 8-12 a) and Figure 8-12 b) depict the FWHM of specimens M12 (milled + DR) and P11 (milled + polished + DR), both treated with DR pressure of 20 MPa. In both longitudinal and transverse directions, an increase of the FWHM in the middle of the DR trace is visible, indicating an increased hardness. Due to missing data out of the DR trace for specimen M12, no comparison of the base material state between both pre-machining states can be made. The surface distribution of the FWHM in both measurement directions is very similar.

The FWHM surface distribution of specimens M15 (milled + DR) and P8 (milled + polished + DR), both treated with DR pressure of 40 MPa, is plotted in Figure 8-12 c) and

Figure 8-12 d). The base material state (values from 1.00 mm toward out of the trace) for the different pre-machining states and in both measurement directions differs significantly, i.e. the FWHM values of the milled state are much higher than those of the milled + polished state. Additionally, in the middle of the trace (for both measurement directions), the FWHM values of the milled state are slightly higher than those of the milled + polished state.

The shape of the surface profiles in longitudinal and transverse directions, in contrary to those of the specimens treated with DR pressure of 20 MPa (Figure 8-12 a) and b)) show a significant discrepancy. In the middle of the trace, the specimen P8 has slightly lower FWHM values in the transverse direction than in the longitudinal direction. However, the higher values in the trace in both directions are still recognisable. For specimen M15, the profiles have a different shape; namely, in the longitudinal direction, the FWHM values are slightly higher in the trace, and in the transverse direction, a plateau-shaped profile is visible.

The comparison from Figure 8-12 show in all cases that the milled + DR specimens have higher hardness than the milled + polished + DR specimens. In the DR trace, the treatment with higher DR pressure reduces the hardness in case of milled + DR state and in case of milled + polished + DR state does not lead to significant changes.

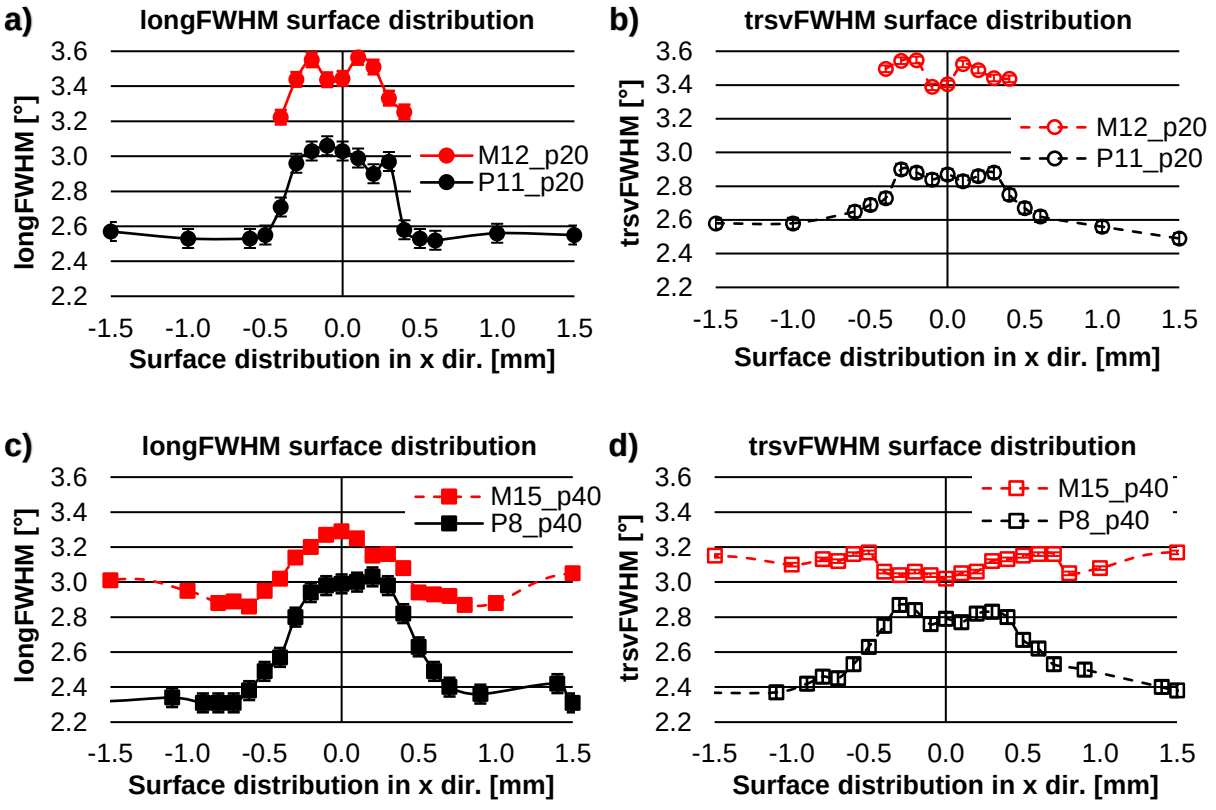

Figure 8-12: XRD FWHM surface distribution of DR with variable pressure: a) longitudinal direction DR 20 MPa, b) transverse direction DR 20 MPa, c) longitudinal direction DR 40 MPa and d) transverse direction DR 40 MPa

Figure 8-13 depicts the FWHM surface distribution of DR specimens with 7 overturns or with 75 % overlapping, by fixed DR pressure of 40 MPa. For both measurement

directions and both parameter variations, the milled + DR specimens have higher FWHM values than the milled + polished + DR specimens.
The treatment with 7 overturns (Figure 8-13 a) and b)) results in concave-shaped FWHM surface profiles. In some cases, the values in the middle of the trace even approach the base-material values. Compared to the in-trace values of single-trace DR with the same pressure (M15 and P8), this is an indication of resulted strain softening, i.e. reduced hardness. It can be concluded that for this material, the treatment with 7 overturns, in terms of strain hardening, is not very favourable. Additionally, the surface area influenced by the DR treatment in both directions is larger than this of the single-trace treatment with the same DR pressure.
The treatment with 75 % overlapping is depicted in Figure 8-13 c) and d). Here, the milled + DR specimen (M22) exhibits near plateau-shaped FWHM profiles in both longitudinal and transverse directions. The milled + polished + DR specimen (P2) has a convex-shaped profile in the longitudinal direction and concave-shaped one in the transverse direction. In both directions, the surface area influenced by the DR treatment is larger than this of the single-trace treatment with the same DR pressure.

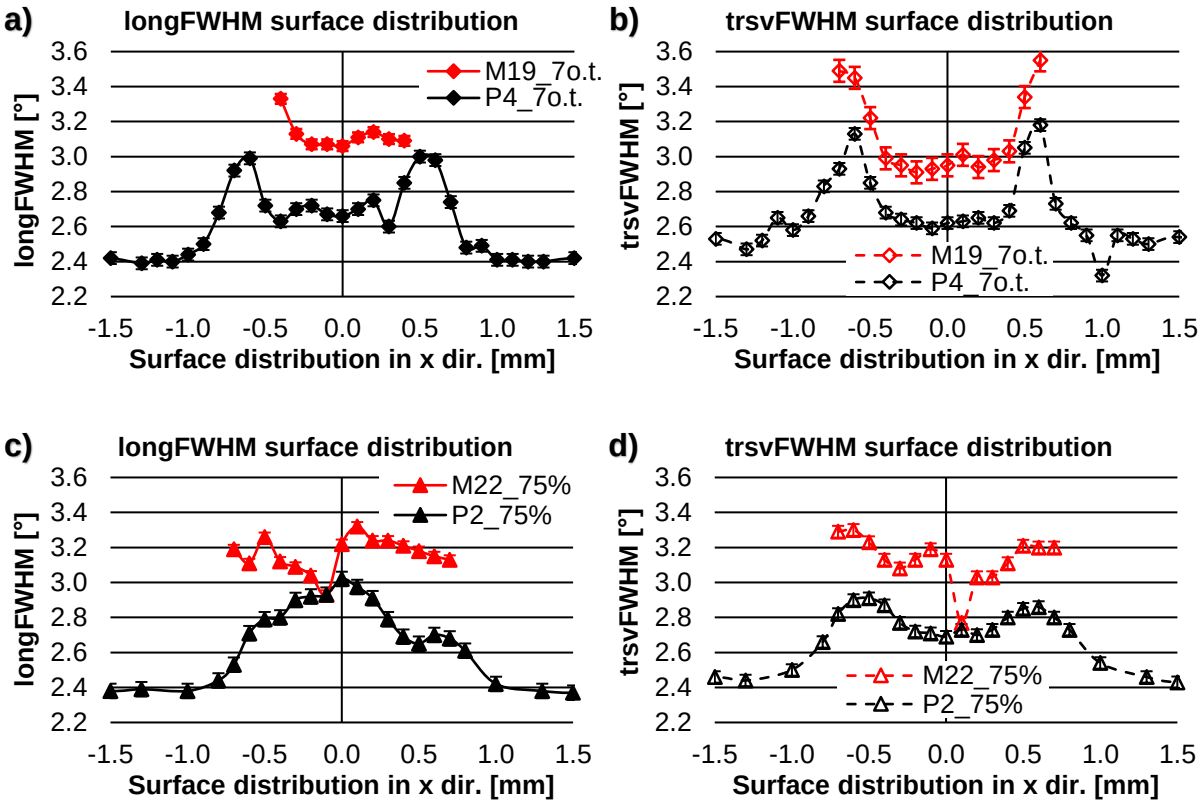

Figure 8-13: XRD FWHM surface distribution of DR with variable overturns or overlapping: a) longitudinal direction 7 overturns, b) transverse direction 7 overturns, c) longitudinal direction 75 % overlapping and d) transverse direction 75 % overlapping

X-ray diffraction peak width (FWHM) - depth distribution

In continuation to the results of the previous sub-chapter, the FWHM values of the same specimens (M12, M15, M19, M22, P11, P8, P4 and P2) were derived from the in-depth x-ray diffraction residual stress measurements.
In Figure 8-14 are plotted the FWHM depth distributions of DR with variable pressure. Here, contrary to the surface distributions, the difference between both pre-machining states is negligible. The values of the base material state (from 0.8 mm depth) are almost identical. In both longitudinal and transverse directions, the depth profiles follow a similar trend, exhibiting the highest values on the surface, followed by plateau-shaped section and dropping down to the base-material state values' level. Although, a clear trend can be observed by varying the DR pressure: the plateau-shaped section of the specimens treated with DR pressure of 20 MPa (Figure 8-14 a) and b)) reach only 0.225 mm depth and is followed by the abrupt decrease of the FWHM values to reach the base-material state level at 0.528 mm depth. In contrary, the plateau of the specimens treated with DR pressure of 40 MPa (Figure 8-14 c) and d)) extends to 0.475 mm depth and the values drop down to the base material state at 0.706 mm depth. In conclusion, it can be assumed that for this material state, increasing the DR pressure has a favourable effect on the resulted near-surface hardness distribution.

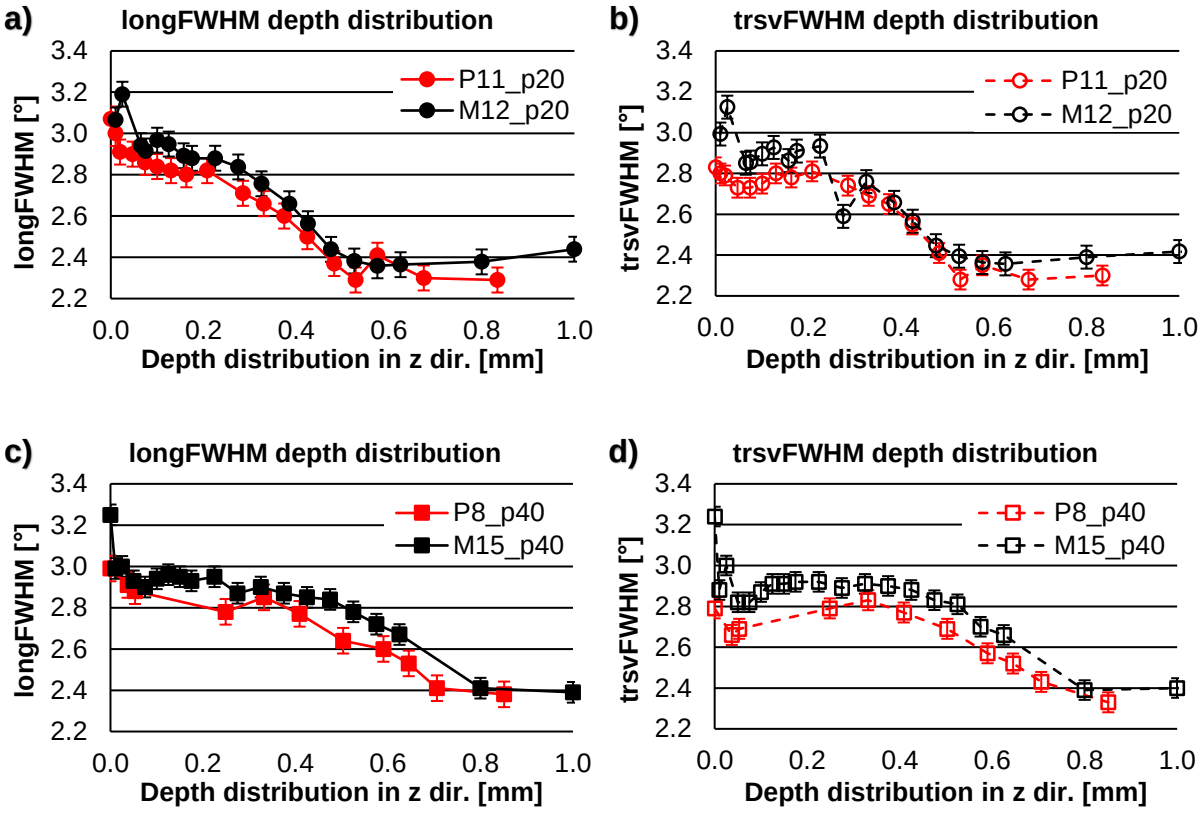

Figure 8-14: XRD FWHM depth distribution of DR with variable pressure: a) longitudinal direction DR 20 MPa, b) transverse direction DR 20 MPa, c) longitudinal direction DR 40 MPa and d) transverse direction DR 40 MPa

Figure 8-15 illustrates the depth distribution of the FWHM values for specimens treated with 7 overturns or with 75 % overlapping by fixed DR pressure of 40 MPa, both process parameters variations realised in milled or milled + polished pre-machining state. Here, similar to the results in Figure 8-14, there is a negligible difference between the values delivered by both pre-machining states. Figure 8-15 a) and b) characterise the depth distributions of FWHM of specimens treated with 7 overturns. The results are similar in both measurement directions. In comparison with the single-trace treatment with same DR pressure (Figure 8-14 c) and d) - specimens M15/P8), the treatment with 7 overturns leads to similar profile shape, but the plateau-shaped area has slightly lower values (app. 2.6 – 2.8 °) compared to the single-trace treatment (app. 2.8 – 2.3 °). This proves the observation from the surface FWHM distribution (see Figure 8-13 a) and b)) that the multiple overturn treatment lead to slight strain softening, compared to single overturn treatment.
The FWHM depth distribution of the specimens treated with 75 % overlapping are depicted in Figure 8-15 c) and d). Here, again, there is a minor discrepancy between the values of the different pre-machining states and both longitudinal and transverse measurement directions. Compared with the single-trace treatment (see Figure 8-14 c) and d)), the depth profiles do not differ significantly.

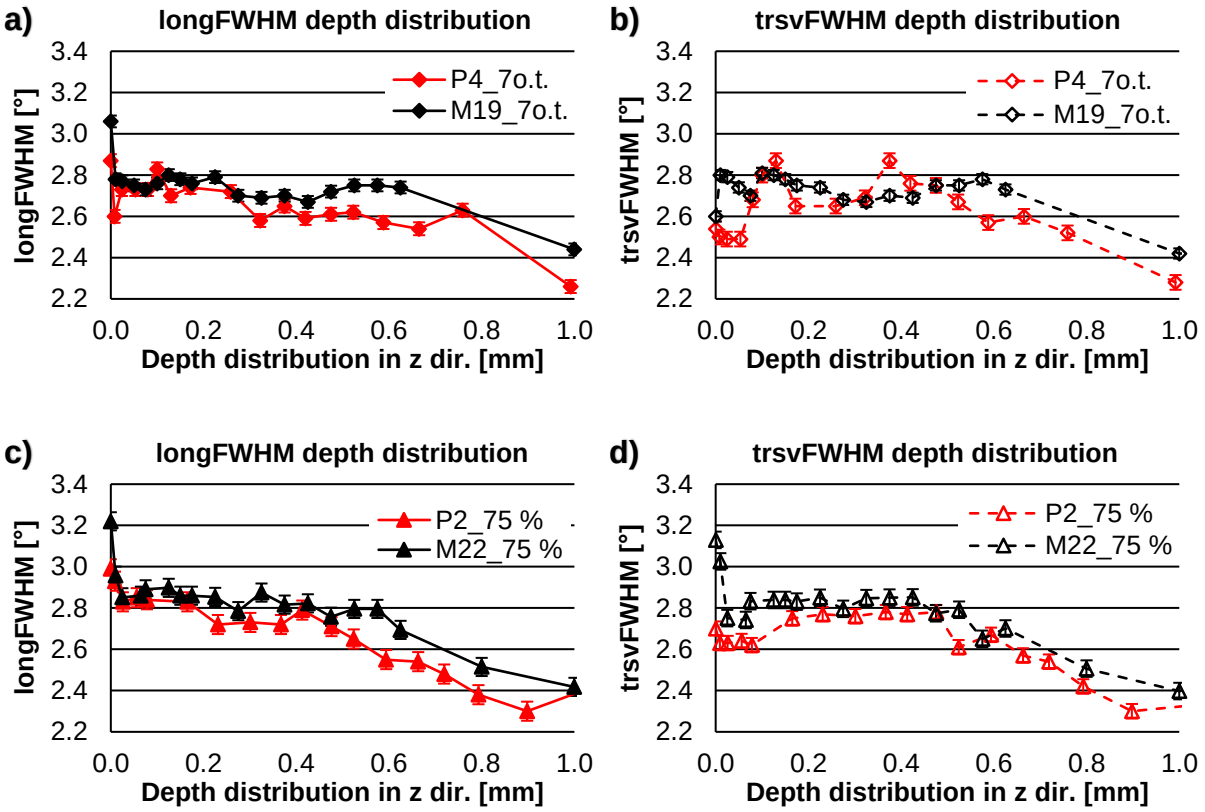

Figure 8-15: XRD FWHM depth distribution of DR with variable overturns or overlapping: a) longitudinal direction 7 overturns, b) transverse direction 7 overturns, c) longitudinal direction 75 % overlapping and d) transverse direction 75 % overlapping

As conclusions of the investigations presented in this subchapter, the following can be assumed:

- Surface FWHM distributions:
  - The variation of the pre-machining state led to a relatively clear tendency of higher FWHM values (higher hardness) of the milled state compared with the milled + polished state, where the highest difference exhibited specimens treated with low DR pressure. This is an indication of predominating pre-machining influence on the surface hardness distribution.
  - The treatment with 7 overturns led to slight strain softening in the middle of the DR trace, compared with single-overturn treatment.
  - Both treatments with 7 overturns or with 75 % overlapping led to larger area influenced by the DR process.
  - No clear trends were observed when comparing the longitudinal and transverse direction values.
- Depth FWHM distributions:
  - The differences of the measured values in depth by the variable pre-machining states were negligible, in contrary to the values of the surface profiles. The pre-machining effect diminished in depth of just 10 µm.
  - The FWHM depth profiles in longitudinal and transverse direction were very similar.
  - The variation of the DR pressure showed a clear trend, where the higher DR pressure increased the impact depth to over 700 µm.
  - The treatment with 7 overturns compared with single overturn led to slightly lower FWHM values, indicating a minor strain softening.
  - The treatment with 75 % overlapping compared with no overlapping delivered very similar FWHM depth profiles.

8.2.3 FEM investigation of the plastic strain after DR with variable process parameters

Additionally to the investigations of the previous subchapter, in this subchapter, the FEM was employed to analyse the surface and the depth distributions of the plastic deformation through plastic strain (as a tensor variable) after DR with variable pressure or overlapping percentage. It is important to notice that a direct comparison between the peak broadening investigations from subchapter 8.2.1 and the FEM plastic strain study from this subchapter is not very appropriate due to several reasons. Even though the peak broadening can be a non-direct measure for the resulted from the DR process plastic deformation, the study from subchapter 8.2.1 showed that the pre-machining has a crucial influence on the FWHM values. Additionally, the material state itself (in this case, quenched and tempered) without any pre- or post-treatment affects the FWHM values. These influences were not considered in the FEM modelling, as the work piece possessed only mechanical macro-properties and no microstructure or surface topography. The statistical reliability was also different for both x-ray and FEM investigations. While single FHWM value was calculated as a mean value of every diffraction peak for several tilting angles, the FEM value of the plastic strain was the determined plastic strain for the corresponding finite element node. The measurement

area for a single value of both techniques differed as well. I.e., the measurement spot of the x-ray diffraction had an amount of minimum 50 µm (the spot transforms in an ellipse, when tilting the specimen). At the same time, the FEM determined values were taken only from a single mathematically defined node.
Therefore, the FEM study can be considered as supplementary to the diffraction peak broadening one, as the FEM offers fast output data analysis with high variability of the investigated points/areas of interests.
As mentioned above, the FEM investigation was performed by variable DR pressure or number of overturns. In Figure 8-16 is depicted the trajectory of the DR tool during processing with overlapping. In case of DR without overlapping, a single trace was modelled. When an overlapping was defined, this was realised through a second trace, overlapping the first with a certain percentage. In the case of 90 % overlapping, two different cases were modelled: DR with two traces, where the second trace overlapped the first with 90 %. The second case included one additional trace (marked in red in Figure 8-16) to simulate quasi-surface praxis-near treatment. The surface distributions of the plastic strain, investigated below, was realised as defining a measurement path perpendicular to the DR trace(s), where the zero x-coordinate described the middle of the 1st DR trace. The plastic strain depth distributions were examined as a measurement path was defined in the middle of the 1st trace from the top surface of the work piece in z direction. Additionally, by DR with 90 % overlapping (the variation with 3 traces in total), a second measurement path was defined in the middle of the 2nd trace in order to investigate the possible changes in the plastic strain due to the multiple overlapping.
In the case of single-trace DR treatment, the surface measurement path was identical to those with overlapping, and the depth measurement path was defined in the middle of the DR trace in z direction. Similarly to the results from the previous subchapter, FEM derived plastic strain was also plotted in longitudinal and transverse to the DR trace directions.

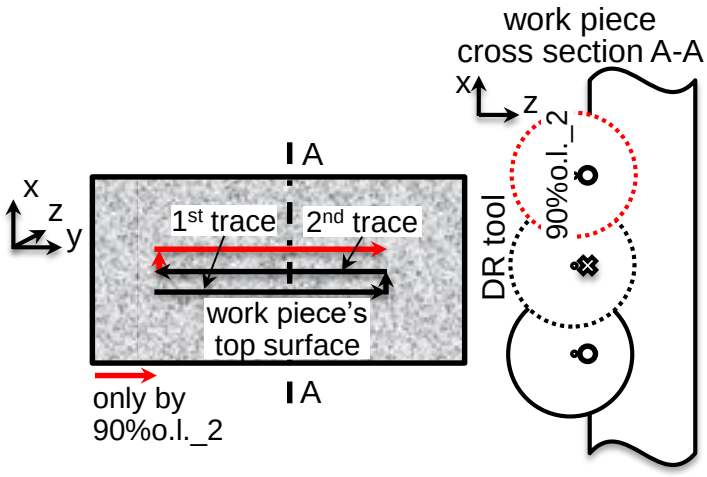

Figure 8-16: Description of the DR tool trajectory by overlapping

Figure 8-17 illustrates the FEM surface distribution of plastic strain by variable DR pressure. Here, a clear tendency can be observed, namely the anisotropy of the values

in longitudinal (Figure 8-17 a)) and transverse (Figure 8-17 b)) directions. The plastic strain in the longitudinal direction is in an amount of up to 0.003 %, in the transverse direction, it reaches over 0.03 %, which is factor 10 higher. This observation gives a hint about the sliding effect/friction of the DR tool with the work piece during processing. Low plastic deformation means low material's stretching caused by the relatively low friction coefficient between tool and work piece defined as a boundary condition. It means that the DR tool rolled over the work piece almost without any slide effect. The significant discrepancy of the values in longitudinal and transverse directions means that during processing the material withstood plastic stretching mainly in the transverse direction.

In the longitudinal direction, there is a scattering of the strain values, which is not high due to the very small diagram scale chosen. In the transverse direction, the plastic deformation increases progressively with raising the DR pressure, where in the center of the DR trace, the plastic deformation is positive (the material is stretched) and out of the trace is negative (the material is compressed). This was expected, as the DR tool pressure stretched material from the middle of the contact zone (middle of the DR trace) toward out of the DR trace. As a consequence, the stretched material was compressed in the direction out of the trace.

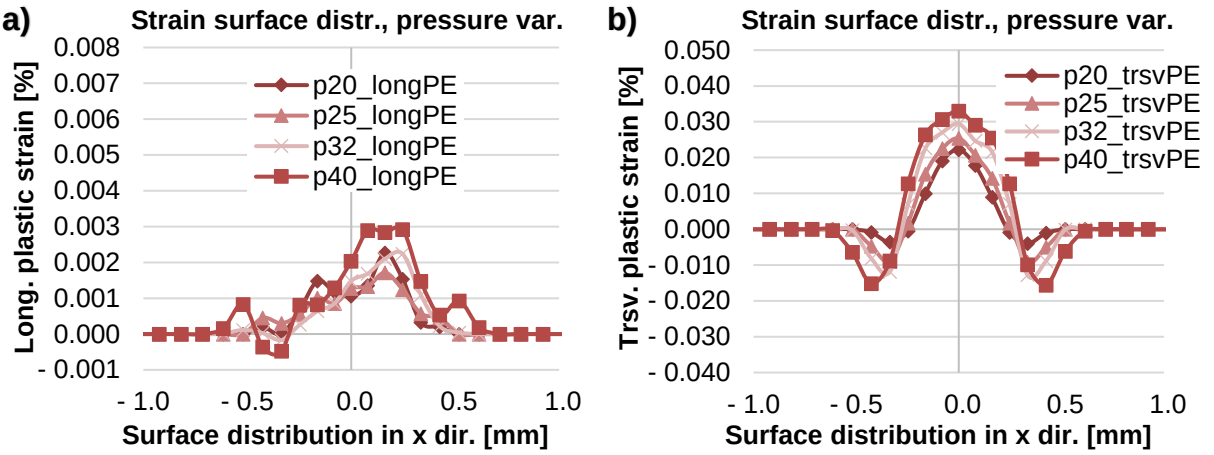

Figure 8-17: FEM surface distribution of plastic strain by variable DR pressure: a) longitudinal direction and b) transverse direction

In Figure 8-18 are plotted the surface plastic strain distributions by variable overlapping percentage. For clearer representation, the variation from 25 % to 75 % overlapping, compared to single-trace treatment is shown in Figure 8-18 a), longitudinal direction, and Figure 8-18 b), transverse direction; the variation from 75 % to 90 % overlapping, compared to single-trace treatment can be seen in Figure 8-18 c), longitudinal direction, and Figure 8-18 d), transverse direction. For all four diagrams, the zero x-coordinate describes the middle of the first trace (see Figure 8-16).

This comparison shows a clear trend, where increasing the overlapping percentage leads to higher plastic strain in both longitudinal and transverse directions. Also in both directions, an overlapping up to 75 % (see Figure 8-18 a) and b)) lead to double plastic strain peak, meaning up to this value (for the particular material, tool diameter and DR pressure) no homogeneous plastically deformed surface zone can be generated. In

general, this is disadvantageous for the fatigue strength of the treated part. The 90 % overlapping with two or three traces (Figure 8-18 c) and d)) leads to a single peak plastic strain meaning a homogeneous plastically deformed zone can be induced, in case of multiple overlapping traces.

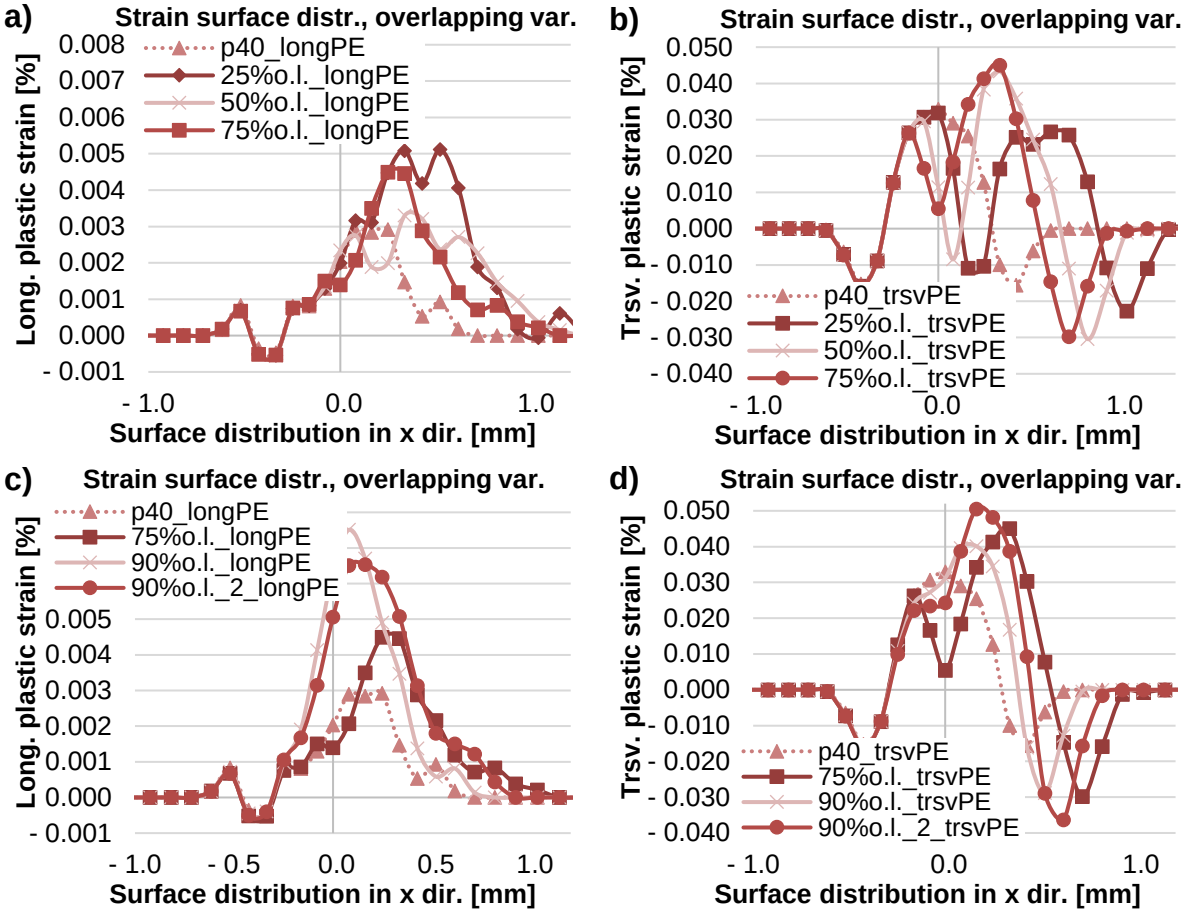

Figure 8-18: FEM surface distribution of plastic strain by variable overlapping percentage: a) longitudinal direction overlapping 25 % - 75 %, b) transverse direction overlapping 25 % - 75 %, c) longitudinal direction overlapping 75 % - 90 % and d) transverse direction overlapping 75 % - 90 %

The next study includes the plastic strain depth distribution after DR with variable pressure or overlapping percentage. The variation of the DR pressure is plotted in Figure 8-19. Here, similarly to the surface distribution, there is a significant discrepancy of the plastic strain values in longitudinal (Figure 8-19 a)) and transverse (Figure 8-19 b)) directions. This can be explained again with the predominant rolling friction, rather than sliding friction between DR tool and work piece. In both directions, higher DR pressure leads to deeper distributed and higher magnitude plastic strain. For all variations, the impact depth reaches 0.7 mm.

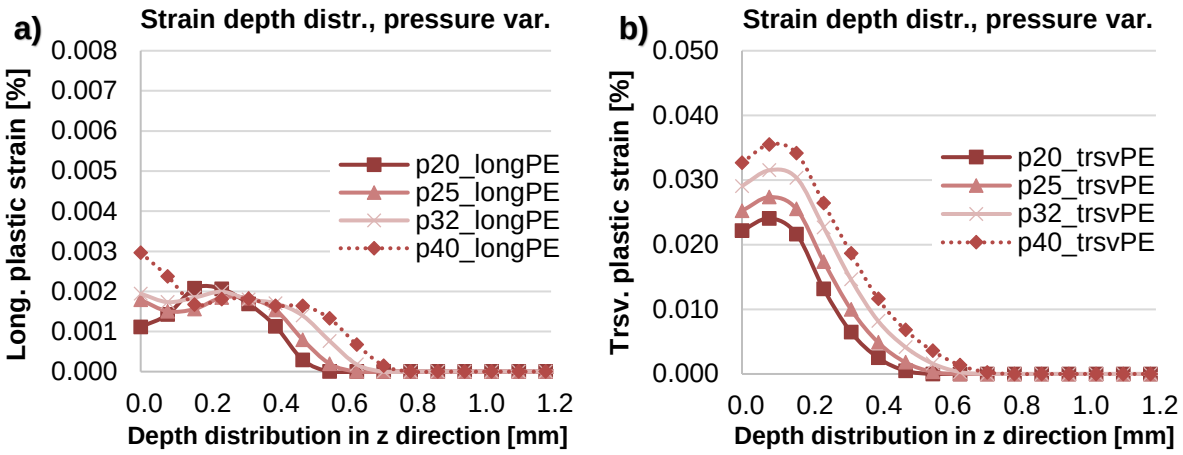

Figure 8-19: FEM depth distribution of plastic strain by variable DR pressure: a) longitudinal direction and b) transverse direction

Figure 8-20 represents the depth distribution of the plastic strain by variable overlapping percentage compared with single-trace treatment. Here, all overlapping variations were plotted in one diagram (each direction) but the measurement paths were taken in the middle of the first trace (see Figure 8-20 a) – longitudinal direction and Figure 8-20 b) – transverse direction) or in the middle of the second trace (see Figure 8-20 c) – longitudinal direction and Figure 8-20 d) – transverse direction). The goal was to observe if the plastic strain distribution in depth is homogeneous. The results from the first trace show the following trend: in the longitudinal direction, up to 75 % overlapping deliver almost identical depth profiles compared to single-trace treatment and only the treatment with 90 % overlapping increase the near-surface values. In the transverse direction, up to 75 % overlapping (compared to w/o overlapping), the near-surface values decrease with increasing overlapping percentage. At 90 % overlapping, the depth distribution looks very similar to the one without overlapping.

The depth distributions obtained in the middle of the second trace are depicted in Figure 8-20 c) and d). Here, the higher overlapping percentage raise the near-surface values in the longitudinal direction. Still, in the transverse direction, this trend is not observed, and the depth profiles do not show any tendency. All of them are more similar to each other, compared to the depth profiles determined at the first trace.

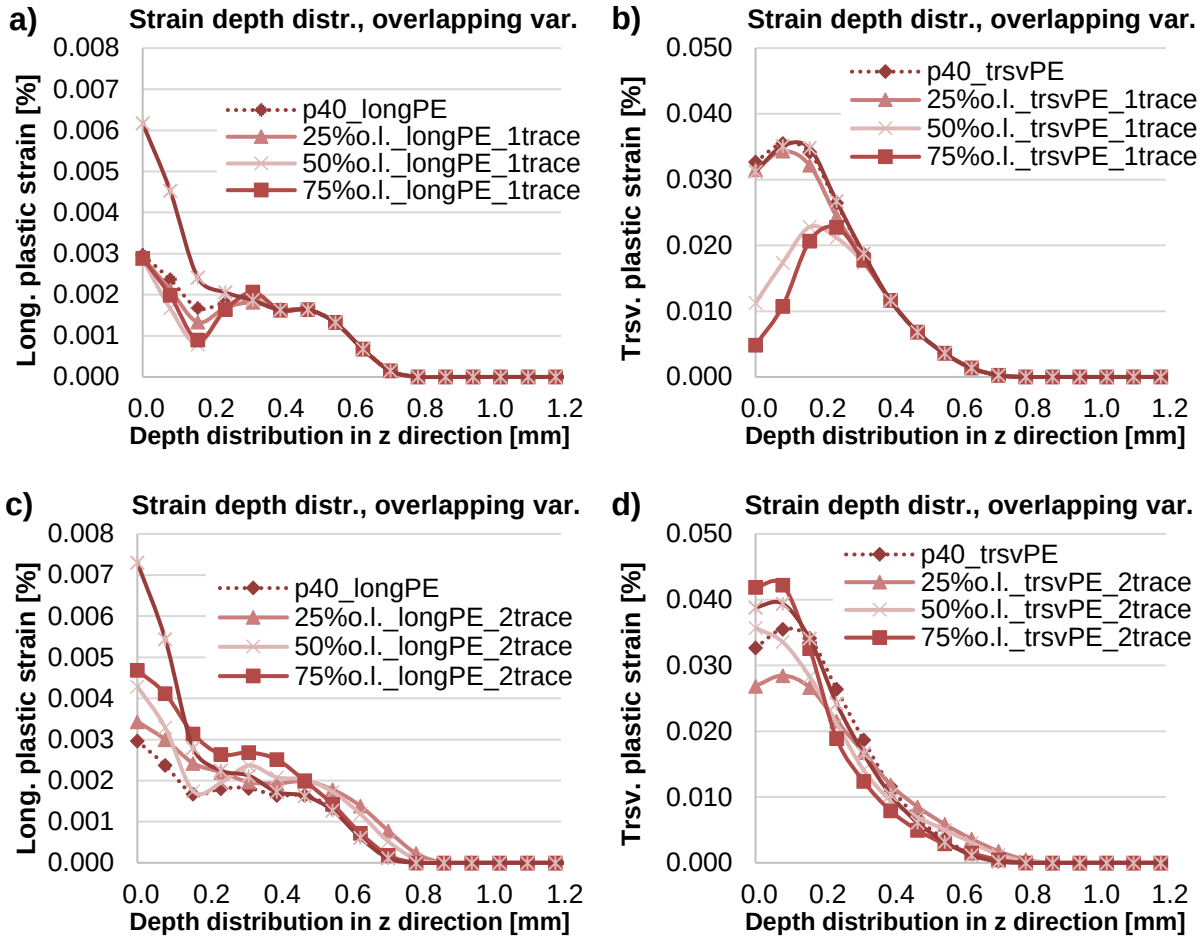

Figure 8-20: FEM depth distribution of plastic strain by variable overlapping percentage: a) longitudinal direction measured at the first trace, b) transverse direction measured at the first trace, c) longitudinal direction measured at the second trace and d) longitudinal direction measured at the second trace

For a better representation of the surface- and depth distributions of the plastic strain in all three directions: longitudinal, transverse and depth, graphics from the ABAQUS output database were extracted and plotted in Figure 8-21. Here, the DR pressure was fixed to 40 MPa, and no overlapping was defined. When considering the different scales of the three images, the observations regarding the anisotropy of the determined plastic strain values in longitudinal and transverse directions are even clearer.

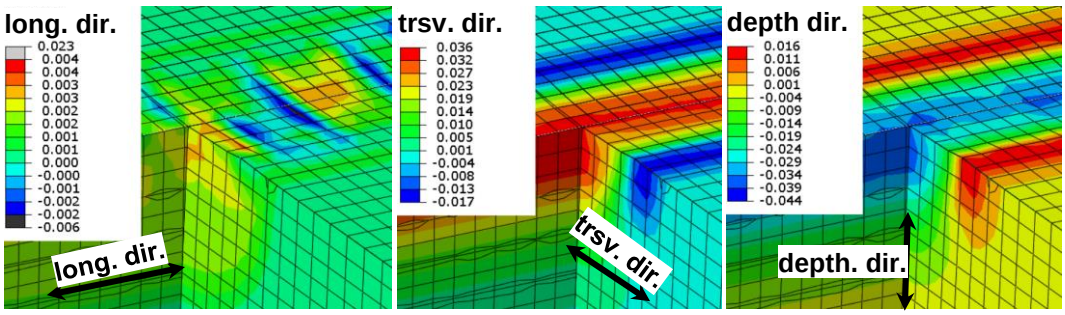

Figure 8-21: FEM graphic representation of the plastic strain surface- and depth distributions after single-trace DR with pressure of 40 MPa

In conclusion, the following can be stated for the FE determined plastic strain after DR:

- Plastic strain surface distribution:
  - It was observed a significant difference (app. factor 10) between the determined values in longitudinal and transverse directions. The significantly lower values in the longitudinal direction are an indication of predominant rolling rather than sliding friction between DR tool and work piece.
  - DR pressure variation – higher DR pressure resulted in higher plastic strain.
  - Overlapping variation – up to 75 % overlapping no homogeneous plastic strain zone was generated. 90 % overlapping with 2 or 3 traces can induce homogeneous plastic strain zone. Higher overlapping percentage resulted in higher plastic strain.
- Plastic strain depth distribution:
  - In depth, similar to the surface, the strong anisotropy of the plastic strain in longitudinal and transverse directions was observed (up to factor 6), where in the longitudinal direction significantly lower plastic strain was calculated than in the transverse direction.
  - Higher DR pressure led to higher plastic strain, and the plastic strain maximum laid below the surface (in the longitudinal direction at app. 160 µm and in the transverse direction at app. 10 µm).
  - The treatment with overlapping increased the plastic strain, especially at higher overlapping percentages (over 75 %).
  - The stress impact depth reached app. 700 µm for all parameter variations.

9 Results discussion

In this chapter, the most significant results shown in chapters 6, 7 and 8 will be compared and discussed.

Chapter 6 was devoted to the establishment of an FE model to simulate the DR process on flat geometry by variation of several process parameters. Some influencing factors were considered like mesh density and type, friction between tool and work piece, treatment velocity, etc. Special attention was drawn to the investigation of the material's elastoplastic definition, and its influence on the FE calculated residual stresses after DR. The last tend to be the most crucial disturbing factor for the prediction of the near-surface residual stresses, and the stress impact depth. The calibration of several material model types showed that the linearity of the material model, as well as its definition, plays an essential role for the calculation of the residual stresses after DR, especially at higher DR force, which causes high strains in the material. The near-surface stress deviation of up to 800 MPa caused only by the variation of the material model confirm the importance of this factor. The stress depth profiles delivered by variable material models (with kinematic- or isotropic hardening) showed the following tendency: in the longitudinal direction, the bi-linear models with isotropic or kinematic hardening differed by the position of the compressive residual stress maxima. I.e. the kinematic hardening model calculated stress maxima on the surface and the isotropic hardening – in depth (app. 50 µm). Stress impact depth was similar for both models. The non-linear model with isotropic hardening delivered similar results at lower DR force but at higher one led to significantly lower stress impact depth (app. 100 µm) compared to the bi-linear model with isotropic hardening.

In the transverse direction, at lower DR force, all profiles were similar with the highest deviation of the maximal compressive stress of less than 150 MPa. Stress impact depth was almost identical. At higher DR force, the bi-linear models with isotropic or kinematic hardening led to stress profiles with a difference in the surface stress of app. 200MPa, differing (with an app. 50 µm) position of the compressive stress maxima and identical stress impact depth. The non-linear model with isotropic hardening compared to the bi-linear one deliver similar surface stress, nearer to the surface (with an app. 50 µm) compressive stress maxima and significantly lower (with an app. 100 µm) stress impact depth.

Lastly, based on the qualitative comparison between FE- and experimentally derived stress profiles, the non-linear material model with isotropic hardening was chosen and employed later in the results from chapter 7.

Chapter 7 focused on the residual stress analysis of deep rolling by finite element modelling and x-ray diffraction. In subchapter 7.1, it was performed a comprehensive FE modelling investigation of the surface- and in depth residual stress distributions after DR with two parameter variations: the applied DR pressure (single-trace DR) and the percentual overlapping between two or three DR traces. In general, the information for the residual stress depth distribution is crucial for the prediction of fatigue behaviour, and it cannot be substituted only by the determination of the surface residual stresses. The stress impact depth, or how deep into the material the treatment influenced the residual stress state, is a crucial characterisation parameter. The presence

of deeper compressive residual stresses, not only high in amount, can retard crack propagations and can prevent new cracks formation even by the presence of tensile residual stresses on the surface. The definition “crack arrest/closure” describes this phenomenon (Gardin, et al., 2005).

The surface residual stress state after DR, investigated in the subchapter 7.1, was strongly anisotropic in both longitudinal and transverse directions, which anisotropy is typical for DR. In case of single-trace treatment, the rolling of the DR tool causes uneven material plastic flow with pronounced “peel outs” out of the DR trace. There, the compressed material transverse to the trace generates transverse compressive residual stress peak, which at high DR pressure approached the yield strength of the material. The longitudinal residual stresses were more moderate, and their distribution was smoother, as throughout the whole DR trace width, low to moderate compressive residual stresses were calculated. The application of high DR pressure enhanced the effects mentioned above.

The treatment with overlapping led in the longitudinal direction to moderate surface compressive stresses by up to 75 % overlapping. At 90 % overlapping of two or three DR traces, a high compressive stress peak appeared in the longitudinal direction (near the yield strength of the material). It could be assumed that further treatment with 90 % overlapping or higher, would transform the single compressive stress peak to a complete high compressive surface stress field. In the transverse direction, the overlapping up to 75 % delivered wavy like stress field, which fluctuated from near-zero stresses to an app. -1000 MPa. The 90 %overlapping created at one side of the trace a relatively smooth high compressive stress field and the further treatment could expand it.

The residual stress depth profiles by single-trace DR were anisotropic in both longitudinal and transverse directions. In the longitudinal direction, the compressive stress maximum was located at app. 180 µm below the surface which is a sign of rather Hertzian pressure influence domination than plastic stretching one (see subchapter 2.2.2, Figure 2-17). The higher DR pressure enhanced the stress impact depth but did not influence the surface stresses and the compressive stress maxima. In the transverse direction, the compressive stress maximum was also located below the surface, and it was balanced with moderate tensile stresses at higher depth. The higher DR pressure shifted the compressive stress maxima, and the stress impact depth deeper into the material.

The overlapping led to complex three dimensional (3D) stress distribution, which was displayed using 3D plots by the post-processing of the FE calculations. Such 3D representations could be performed using several experimental techniques as well but on a very high time cost. Besides, most of the suitable experimental techniques (excluding the neutron diffraction one) can be employed for these stress representations only as semi-destructive. Here, the removing of material to reach the depths of interest is another disturbing factor, which is absent by the FE modelling.

Additionally to the 3D plots, stress depth profiles were derived at different positions, like in the middle of the overlapped- or of the overlapping trace and comparisons between several overlapping percentages was performed. In both determination directions, especially near the surface, the stresses widely spread from near-zero to very

high compressive. Although, at greater depths, the differences diminished. This investigation emphasised the importance of the stress determination position, which in the case of FE modelling can be defined by default as precisely as the mesh density allows. In the case of experimental stress determination, the precision of the stress determination position can be aggravated by the precision of the specimen's positioning caused by faulty machine adjustment.

Subchapter 7.2 focused on the further exploitation of the DR process utilizing mechanical pre-stress of the work piece (see subchapter 2.2.1, Figure 2-14). This was performed using FE modelling. Here, the DR process was done on a flat work piece, as the last was elastically pre-stressed prior to DR using four-point bending setup. The pre-stressing was defined as a percentage of the material's yield strength. It was found that the pre-stress direction- and magnitude, as well as the DR direction, played a significant role by the generation of the residual stresses. For the investigated setup, applying longitudinal DR on the tensile pre-stressed side of the work piece, shifted the compressive residual stress maxima to higher depth and enhanced stress impact depth. The pre-stressing increased the anisotropy of the transverse stress depth profiles compared to those in the longitudinal direction. This setup delivered the most favourable residual stress state compared to the other possibilities like compressive pre-stress or transverse DR, or a combination of each of them. This study showed that mechanical pre-stressing could have a positive effect on the residual stress depth distribution, although the enhanced stress anisotropy has to be considered.

In the central subchapter 7.3 was undertaken a comprehensive experimental study of the residual stress state after DR by several variable process parameters. Additionally and in contrary to the FE analysis, here the pre-machining of the consecutively DR specimens was considered. Different pre-machining processing was defined to achieve rough (milled) or smooth (polished) surface and the influence of the pre-machining on the residual stress state after DR was investigated. It is essential to note that the differences in the stress state after DR resulted from the superposition of the residual stresses due to the pre-machining and the DR as well as by the surface topography resulted from the pre-machining. The surface topography is in general measurement-influencing factor (see subchapter 2.4.1). Special attention was drawn to the x-ray measurement technique itself, as several measurement-disturbing factors were considered. E.g., the measurement device, the diffraction peak determination, the device adjustment, the homogeneity of the residual stresses along the DR trace and the influence of the material removal used for the determination of the stress depth profiles. Two different diffractometers (with similar setup) situated in two independent laboratories were employed, and comparable surface residual stress measurements of DR specimens were performed.

Some of the investigated factors, e.g. the peak position determination, the 2θ range or the correction of the material removal, did not significantly influence the determined stress values. Nevertheless, the week sensitivity of the material removal correction needs to be carefully considered as the employed correction technique rely on some assumptions, which do not describe precisely enough the considered case (see subchapter 4.3.1).

Other factors like the homogeneity of the stresses along the DR trace or the employment of different measurement device led to some discrepancies in the determined stress values. The surface measurements along the DR trace led to relatively homogeneous values (± 50 MPa), except for some values which deviated with maximum ± 100 MPa. The comparison measurements using different diffractometers confirmed a good agreement between the stress values measured by both devices with a maximal deviation of ± 75 MPa.
The investigation of the surface residual stress state after DR (subchapter 7.3.3) was undertaken by variable process parameters (DR pressure, number of overturns or overlapping percentage) and different pre-machining states (milled or milled + polished).
In the milled + DR state, the surface stress profiles had a similar shape as the one delivered by the FE models. The tendency by the pressure variation was also similar to the one of the FEA. The seven overturns treatment, compared to single treatment led to higher compressive stress maximum (longitudinal and transverse directions) and lower tensile stresses in the middle of the trace (transverse direction). One of the surface stress profiles, see specimen M19 Figure 7-20 a), exhibited a lateral displacement (app. 200 µm) visible as asymmetry to the zero coordinate. For a comparison purpose, this displacement could be manually corrected. Although, by the determination of the stress depth profiles, and considering the lateral stress gradient, such lateral displacement can lead to misleading results.
In the Milled + polished + DR state, the surface stress profiles showed a similar tendency as in the milled + DR state with two exceptions. First, the specimen P11 (DR pressure 20 MPa) exhibited moderate compressive stresses in the longitudinal direction (higher compressive than those of the specimen treated with 40 MPa, M15) even out of the DR trace and slight compressive instead of minor tensile stresses in the transverse direction (see Figure 7-25 a)). This was a sign of residual stress state inherited from the previous manufacturing step, probably from the pre-machining. When considering that all specimens were treated with identical pre-machining parameters, and only one differed significantly, it becomes clear that the pre-machining under real conditions is a significant stress-disturbing factor. Second, in the transverse direction see Figure 7-25 b)), the specimen P4 treated with 7 overturns exhibited two symmetrical stress relaxation peaks, which could be the first sign of fatigue due to the multiple DR on the same place.
Subchapter 7.3.4 focused on the analysis of the residual stress depth profiles of milled + DR state or milled + polished + DR state by varied DR pressure, 7 overturns or 75 % overlapping. Additionally, at two randomly chosen specimens, the stress depth profiles were determined only in the milled state. Both specimens exhibited very similar stress state, with near-surface anisotropy, which for perpendicular face milling is not typical. Still, as the XRD measurement direction deviated from the cutting one, no further assumption could be made regarding this anisotropy. Anyhow, the stresses of all depth profiles tend to zero at a depth of app. 25 µm, therefore no significant influence of the milling on the residual stress depth profiles after DR was expected.
In the milled + DR state, similar to the observations made by the FE analysis, a strong stress anisotropy in longitudinal and transverse direction due to the DR process itself

was observed here as well. High DR pressure and multiple overturns were favourable (compared to low DR pressure and single overturn) as it delivered higher stress impact depth (up to 1 mm) in both directions. By treatment with 7 overturns, slight decreasing of the compressive stress maximum was observed, which could be considered as reached saturation point, where no significant further improvement was expected. The treatment with 75 % overlapping delivered similar stress depth profiles to the single treatment.

In the milled + polished + DR state, the stress depth profiles were similar to those of the milled + DR state with some exceptions. I.e., the higher DR pressure enhanced the compressive residual stress maximum (only in the longitudinal direction), and the seven overturns treatment increase it as well (only in the transverse direction). The stress impact depth, similarly to the milled + DR state, was positively influenced in both directions by higher DR pressure or treatment with 7 overturns. The stress state induced by the treatment with 75 % overlapping was similar to the one of the single trace.

The comparison of both pre-machining states, see 7.3.5, showed some discrepancies in the residual stress surface distribution. Usually, the differences were in the range of ±50 MPa and in rare cases up to ±150 MPa (by measurement standard deviation of an app. ±25 MPa to ±75 MPa). No systematic trend was found in these deviations. In depth, the residual stresses delivered by both pre-machining states and consecutive DR agreed well to each other with a maximal difference of ±100 MPa (by measurement standard deviation of the app. ±25 MPa to ±50 MPa).

The subchapter 7.4 was from significant importance for the presented thesis, as it was focused on the verification of the FE model used for the calculation of the stresses presented in chapter 6 and subchapter 7.1. Here, the FE derived surface- and depth stress profiles were compared to the XRD determined ones. DR pressure variation or treatment with 75 % overlapping as well as both pre-machining states (only by XRD) were considered.

On the surface, the following observations were drawn: at low DR pressure, where the XRD profiles of both pre-machining states exhibited deviations of up to ±150 MPa, the FE calculated stress profiles laid in between. In contrary to the XRD determined moderate compressive stresses out of the trace (assumed as inherited from the pre-machining), the FE calculated stresses tend to zero. At high DR pressure, the FE predictions slightly underestimated the compressive stresses in the trace, in the longitudinal direction (deviation under ±100 MPa) and instead of slight tensile-, near-zero stresses were calculated in the transverse direction (deviation under ±150 MPa). The FE surface stress profiles calculated for the DR treatment with 75 % overlapping were also in a reasonable agreement with the XRD determined ones, and the deviations were in the range of those of the different pre-machining states.

The relatively small discrepancies between FE modelled and XRD determined can be explained by surface issues due to the pre-machining (experimental) which is not presented in the FE models. Some FE friction simplification issues could not be neglected as well. For both FE and XRD, some deviations in the surface stresses along the DR trace were observed, and this can also be considered as a source of uncertainties.

To verify the stress depth profiles, the same DR process parameters were employed as for the surface stress profiles. In the longitudinal direction, the FE modelling of the

treatment with variable pressure delivered similar to the XRD derived stress depth profiles (deviation under ±100 MPa). The only difference was the FE calculated single compressive stress maximum compared to the XRD derived plateau-like maximum compressive stress area. The reason for this discrepancy could be the complex physical interdependency of the DR basic mechanisms affecting the residual stresses. E.g., the predominance of the Hertzian pressure, the plastic stretching or the slipping friction effects, which could not be adequately represented by the FE model. The FE model with 75 % overlapping delivered in longitudinal direction reasonable stress depth profile. Here, the stress was calculated in the first (overlapped) and second (overlapping) DR traces and compared to the XRD derived one (at the second trace). The FE determination of the two stress depth profiles mentioned above showed the advantages of this technique again, as employing an experimental technique for such stress determination will be time-consuming and difficult due to the proximity of both stress depth profiles. The difference between both FE calculated stress profiles was in the calculated compressive stress maximum and did not exceed ±150 MPa. To reach more homogeneous stress state in depth, a higher overlapping percentage is required. Compared to the XRD stress depth profile, the FE calculated agreed well, with maximal discrepancy of ±150 MPa and slight underestimation of the stress impact depth.
In the transverse direction, the FE predicted stress profile shape fitted to the XRD derived but quantitatively there were some notable discrepancies in the maximal compressive stress and the sub-surface stresses. Here, the FE overestimated the maximal compressive stress with up to ± 140 MPa (w/o overlapping) and up to ± 200 MPa (with overlapping). With overlapping, the FE predicted stress depth profiles determined at the first or the second trace differed profoundly from each other, as shape, as near-surface stress and as maximal compressive stress. It remained unclear if this deviation is realistic, as the XRD depth profile was determined only in the second trace. Notable were the FE calculated sub-surface tensile stresses of up to +430 MPa, which were not observed by the XRD stress profiles.
For the observed discrepancies in the depth stress profiles, several sources can be considered. On behalf of XRD, at higher depths, the lower measurement resolution (compared the FE) can lead to misleading results, as the stress profiles were represented based on the available measurement points. Some local stress peaks could be therefore missed. Additional issues can be created by the layer removal and the corresponding stress relaxation and redistribution. Although the applied stress correction did not have a significant influence on the stress depth profiles, such cannot be neglected due to the defined assumptions by the layer removal correction that do not correspond to the realistic layer removal conditions. E.g., the electro-polishing was applied to a small material section of an app. 1x1 mm, and this can lead to unpredictable stress redistribution due to the notch effect created. In contrary, the layer removal correction assumes complete material layer removed.
On behalf of FE modelling, the representation of the complex elastoplastic material behaviour could be a source of high fluctuations of the predicted residual stress state, as shown in subchapter 6.2. The material used for the FE modelling, as shown in subchapter 4.1.2, exhibits relatively moderate Bauschinger effect (reduced yield strength by consecutive reverse loading). Still, the observed reduction of the yield strength of

up to an app. 35 % at reversal strain near the necking point cannot be considered as negligible. As the Bauschinger effect is connected to the reversal strain, if the material exhibits such effect during DR process, the material model using isotropic hardening should represent the material behaviour correctly only at low strains (low DR pressure). At high strains (high DR pressure), the kinematic hardening rule should describe more precisely the material behaviour. Nevertheless, the comparison between several material models, see subchapter 4.1.2, showed that the FE predicted subsurface moderate tensile stresses (only in the transverse direction) in all considered cases (high and low DR pressure). Therefore, the observed discrepancy between the FE predicted and XRD determined transverse stress depth profiles could not be attributed to the hardening rule of the material model. The employing of strain rate dependent material model could be considered, as the current one represented the material behaviour only under quasi-static loading. Still, this should have a minor influence on the residual stress state, as the DR process does not cause material high deformation rates, in contrary to shot peening, where the deformation rates are very high, up to 10^5-10^6 (Meguid, et al., 2002).

Chapter 8 focused on the analysis of the surface topography and the cold working after two pre-machining states (milling or milling + polishing) and/or consecutive DR. The subchapter 8.1 was devoted to the investigation of the surface topography, and the subchapter 8.2 considered the cold working changes due to pre-machining and following DR. The analyses were performed using experimental- as well as FE investigations.

In subchapter 8.1.1, an experimental investigation of the surface roughness with profile method of pre-machined (milled or milled + polished) and/or DR specimens with variable process parameters (diameter of the DR tool, applied pressure, number of overturns or overlapping percentage) was performed. In the milled + DR state, the DR contributed to significantly reduced roughness (in most cases under 2 µm Rz, compared to the initial of 7 µm -12 µm) for all parameter variations but especially by high DR pressure or multiple overturns. In the milled + polished + DR state, due to the very low initial roughness (app. 0.05 µm Rz), the consecutive DR did not deliver further improvement, and the roughness even increased. The high DR pressure led to slightly higher roughness (up to 0.1 µm Rz), but the treatment with 7 overturns delivered significant deterioration (0.6 µm Rz). The observations made in subchapter 8.1.1 that the influence of the DR process cannot be distinguished from the pre-machining state. In case of high initial roughness, the DR process can be used as a smoothing operation, as it smashes the roughness peaks. In contrary, by very low initial roughness, the plastic deformation created by the DR induced artificial roughness, thus deteriorating the surface quality.

Subchapter 8.1.2 concerned the surface topography after milling + DR utilizing mechanical stylus method. The DR trace's width and depth were analysed by variable DR diameter tool, applied pressure, number of overturns or overlapping percentage. For both DR tool diameters, higher DR pressure and multiple overturns expanded the width and the depth of the DR trace. For tool diameter of 3 mm, the trace's width reached app. 500 µm and the depth did not exceed 15 µm. For the DR tool of 6 mm, as expected, larger deformations were observed – the maximal trace's width was app.

1200 µm and the depth app. 38 µm. The treatment with overlapping led to wider DR trace and emphasised the precision of applying defined overlapping, as the calculated from the trace's width overlapping differed from the defined one with up to 37 % points. This was considered in the FE analyses, and the calculated overlapping based on the experimentally measured DR trace's width was implemented in the FE model.
Similarly to the previous subchapter, the next one - 8.1.3 also considered the surface topography after DR with variable process parameters. Still, here the FE technique was employed, and the calculated results were compared to the experimentally derived of subchapter 8.1.2. By variable DR pressure, the FE reasonably predicted the trace's width with deviations of less than 10 %. The trace's depth was predicted also well, with deviations between 1.6 µm and 4.3 µm, which can be considered as minor, considering the experimental measurement uncertainties like roughness, waviness, etc. (delivering measurement standard deviation of several micrometers). The variation of the overlapping percentage showed that up to 75 % overlapping, no smooth surface could be generated (for the treated material). The treatment with 90 %, where two or three traces were overlapped, led to a plateau-near surface on the bottom of the traces' profile, which will expand in case of treatment a complete surface, thus creating a smooth surface. The depth of the trace for all overlapping variations was in the range of 20 µm to 22 µm.
The knowledge gained in subchapter 8.1.1 and 8.1.2 about the surface roughness and the topography after pre-machining and/or DR is important for the practical application of DR, as a single process or as part of a process chain. The analysis of the surface roughness showed the potential of DR as a finishing process. Nevertheless, the topography of the DR surface is strongly dependent on the chosen process parameters. The results from subchapter 8.1.2 showed the deformations due to DR, which in case of treatment of precise parts with low dimension tolerances cannot be considered as negligible.
Subchapter 8.2. was devoted to the analysis of the cold working changes due to DR with variable pressure, 7 overturns or 75 % overlapping.
In subchapter 8.2.1 an experimental investigation of the depth distribution of micro-hardness and indentation modulus of DR specimens was performed. The depth profiles were obtained in the middle of the DR trace or out of the trace, where the highest surface compressive residual stress in the transverse direction was determined. In the trace, surprisingly, the measured micro-hardness near the surface was lower than the one of the base material (app. 400 HV 0.05) for all parameter variations. This could be an indication of material work softening due to DR. Out of the trace, there was a vague trend of slightly increased micro-hardness near the surface. The indentation modulus, a measure for material's elasticity (comparable to the E-modulus), showed a tendency with lower values near the surface compared to the base material (app. 240 GPa to 250 GPa) for both measurement areas (in- or out of the trace). The investigations of this subchapter should be considered with caution as the determined micro-hardness and indentation modulus, due to the specifics of the measurement technique, are influenced by the residual stress state. The measurements are based on the application of a defined force to a Vickers indenter, which penetrates the material creating a specific imprint. Based on the applied force and the dimensions of the resulted imprint, the

micro-hardness and the indentation modulus can be calculated. In the case of high residual stresses, the indenter can penetrate easier or can be hindered. Tensile stresses will ease the indenter penetration, thus contributing to larger imprint and faulty calculated lower micro-hardness. In contrary, compressive stresses will hinder the indenter's penetration, leading to smaller imprint and calculated higher micro-hardness. As the determined residual stresses after DR were as some places very high compressive, this can lead to overestimation of the micro-hardness in those places.
In subchapter 8.2.2 were considered the x-ray diffraction peak widths (FWHM) on the surface and in depth after DR by variable pre-machining state and DR process parameters. This parameter is an indirect measure for the cold working in the material, and it is comparable to the indentation hardness (higher FWHM is an indication of increased hardness). On the surface, mostly the pre-machining influenced the peak width values. The milled + DR state compared to the milled + polished + DR state delivered for all DR parameter variations even out of the trace wider peak widths (means higher FWHM values). The single trace DR treatment led to FWHM maximum in the middle of the trace. The higher DR pressure led to lower FWHM in the milled + DR state but did not influence the values in the milled + polished + DR state. The treatment with 7 overturns led to maximal FWHM out of the trace, and the treatment with 75 % overlapping showed no recognisable trend. No significant difference between the FWHM values determined in longitudinal or transverse directions was observed. In depth, the differences between the profiles by different pre-machining states diminished at app. 10 µm below the surface. For all parameter variations, the FWHM was higher near the surface and decreased in depth. No significant differences were observed in longitudinal and transverse directions. The higher DR pressure led to a deeper layer with higher FWHM than those of the base material. The treatment with 7 overturns compared with single overturn lead to slightly lower FWHM values (compared to single treatment), indicating a minor strain softening. The treatment with 75 % overlapping (compared with no overlapping) delivered very similar FWHM values. The results from this subchapter confirmed again the importance of considering the pre-machining as an integral part of the final material state after DR, as especially near the surface, the pre-machining had the most dominant impact on the investigated FWHM.
The last subchapter 8.2.3 was focused on the plastic strain surface- and depth distributions by variable DR pressure or overlapping percentage, obtained through FE analysis. On the surface, a strong anisotropy (app. factor 10) of the plastic strain in longitudinal and transverse directions was observed. The significantly lower values in the longitudinal direction could be an indication of predominant rolling rather than sliding friction between DR tool and work piece. In addition, under realistic conditions, a plastic strain is induced due to the smashing of the existing work piece's surface roughness peaks. In the FE model in contrary, due to the absence of surface roughness, such an effect cannot be observed. In case this effect is pronounced, under real conditions, the near-surface plastic strain anisotropy due to the DR itself could be difficult to distinguish. Still, in depth, such a surface-roughness effect should not be significant.
For all parameter variations, the maximal surface plastic strain was calculated approximately in the trace's middle (by treatment with overlapping, in the middle of the overlapping trace). Only by overlapping of 90 %, a plateau-similar strain distribution in the

trace's middle was observed, noting that for this material and process conditions, overlapping over 90 % reasonable.
In depth, the strain anisotropy in both directions remained relatively high (up to factor 6). The higher DR pressure led to increasing plastic strain amount and impact depth (from 0.5 mm to 0.7 mm) in both directions. The treatment with overlapping, compared to the single treatment, led to a slightly increased plastic strain in the longitudinal direction and partially in the transverse direction (only for overlapping over 75 %). The determined values in both overlapped- and overlapping traces (by overlapping up to 75 %) showed that the plastic strain in depth is not completely homogeneous, as some modest differences were observed at depths up to an app. 0.2 mm. The treatment with 90 % overlapping delivered similar stress depth profiles determined in both overlapped- and overlapping traces, confirming that the 90 % overlapping is more reasonable than the lower overlapping percentage.
The considered in subchapters 8.2.1, 8.2.2 and 8.2.3 cold working changes due to pre-machining and consecutive DR should be in general comparable to each other. Despite that all three of them (indentation micro-hardness, x-ray diffraction peak width and FE plastic strain) can be connected to the material's hardness, the direct comparison is not completely appropriate due to several reasons. The indentation micro-hardness is connected to the elastoplastic response of the material to penetration of indenter. The penetration depth is influenced by the material hardness and the residual stresses presented in the material, and both material's features cannot be clearly distinguished from each other. The width of the diffraction peak, when neglecting instrumental peak broadening, is often connected to the hardness and cold working but in fact, is a measure of the amount of dislocation density and crystallite size. Both experimentally investigated parameters were obtained on material passed through a particular manufacturing chain before the pre-machining and the consecutive DR. At any stage of the manufacturing chain, changes of those parameters are possible.

10 Summary, conclusions and outlook

This thesis presented a comprehensive characterisation of the surface integrity by deep rolling (DR) on a flat surface employing finite element analysis and experimental techniques. The DR process is an established mechanical surface treatment used to improve the fatigue strength of the treated parts by reducing the surface roughness, inducing a cold worked layer and generating compressive residual stresses. The considered state of the art in chapter 2 of the thesis, showed that even well known, the DR leads to widely variable surface and sub-surface changes of the material's properties due to the great variability of the available process parameters. The improper choice of process parameters can lead to surface and sub-surface tensile residual stresses. It can deteriorate the surface roughness and can reduce the material's hardness, thus negatively affecting the fatigue strength. The DR process finds its place as a typical finishing treatment, mostly at the end of the product's manufacturing chain. The usually unknown material's state, inherited by all previous stages of the manufacturing chain, makes the prediction of the surface integrity after DR even more challenging. Next to the experimental approach, the finite element analysis (FEA) expands the possibilities to characterise the DR, but it is supported by numerous challenges during the definition of praxis-near process boundary conditions. In this thesis, an FE model of DR was presented, which in contrary to the most available models, employs a flat work piece instead of rotational symmetric one. The goal of using a flat work piece is, after establishing a plausible and stable model, to replace for future investigations the work piece with a complex three-dimensional shaped one. The FE model presented in the thesis was employed to characterise the surface and in-depth residual stress state, the surface topography and the plastic deformations after DR. These material's properties were mentioned above as significantly crucial for the fatigue strength. Supplementary to the FE analysis, experimental investigations of those material's features were performed, where the influence of the measurement device, and the different measurement techniques was considered. The results delivered by both experimental- and FE approach were discussed and compared.

Chapter 6 was devoted to the establishment of an FE model of the DR process, and it considered different boundary conditions influences on the calculated residual stresses. It was observed that the material representation was the most crucial influencing factor. The calibration of the material data showed that using different hardening rules (e.g. kinematic or isotropic) leads to fitting the experimental data to the material model only under certain conditions. The material models fitted well either only at low strains or only at high strains. Therefore, the employed different material models deliver widely variable residual stress depth profiles, as the near-surface stress values varied from zero to high compressive and the stress impact depth varied with up to 75 %. The maximal compressive stress was in contrary not very sensitive to the material model, and for all variations, values near the yield strength of the material were calculated. The findings in this chapter led to the considerations that for future investigations of DR implementing FE analysis, special attention should be drawn on the material modelling. A material representation combining both isotropic- and kinematic hardening rules, or such implementing multiple back stresses should be considered.

Chapter 7 was focused on the comprehensive characterisation of the residual stress surface and depth distributions after DR, and it was divided into three main parts: subchapters 7.1 and 7.2 - FE analysis, subchapter 7.3 - experimental work and subchapter 7.4 – comparison between FE analysis and experiments. The FE analysis was done by variable DR pressure or overlapping percentage. The surface- and depth residual stress distributions for all process variations were strongly anisotropic in the direction along the DR treatment compared to the transverse one. This stress anisotropy is typical for DR process, and it is a result of an anisotropic elastoplastic material deformation during treatment. In general, this anisotropy can be a drawback for the fatigue strength of the treated part as the loading direction during operation does not always agree to the processing direction. Nevertheless, the observed high compressive residual stresses (near the material yield strength) could contribute to significantly longer fatigue life. The FE modelling, as technique, showed its considerable advantage by representing numerous different measurement positions realised as 1D and 2D stress plots, which experimental realisation will be significantly more time-consuming. The additionally presented FE modelling of pre-stressed DR using static elastic pre-stress of the work piece, acknowledged again the asset of employing FE as technique, as the experimental realisation of such setup is accompanied with several challenges.
The subchapter 7.3 focused on the experimental characterisation of the residual stress surface and depth distributions after DR by variable pre-machining state and process parameters. For these studies, the x-ray diffraction technique was employed. On behalf of the measurement precision, several disturbing factors were examined like the influence of the measurement device, the measurement and the evaluation parameters as well as the measurement position. The comparison measurements using two different diffractometers confirmed in this particular case that the measuring device does not significantly affect the measured values. The measurement position, in contrary, led to some moderate fluctuations of the stress values. In general, good measurement precision and reproducibility were achieved. Still, when measuring stress state with high gradients, the positioning precision should not be neglected.
On behalf of the examined process chains (milling and consecutive DR or milling, polishing and consecutive DR), the examined residual stresses on the surface varied widely even by fixed DR parameters. Some asymmetries of the determined surface profiles were an indication of possible positioning issues or device's misalignment. Nevertheless, at depth, the discrepancies caused by variable pre-machining diminished to a negligible level. These observations emphasise the importance of considering the residual stress state not only on the surface, even this, compared to the determination of the stress depth profiles, considerably reduces the total measurement time. Even more importantly, the residual stress depth distribution has a more significant impact on the fatigue strength, as is serves to prevent sub-surface crack initiations and retards crack propagations. In this manner, the employment of FE technique is very advantageous, as, by the post-processing, the determination of the stress surface profiles and the depth ones costs the same time.
In this subchapter, the stress anisotropy observed by the FE analysis was confirmed. The variation of the process parameters showed that higher DR pressures and several overturns generate in most cases deeper distributed residual stresses, compared to

lower pressure and single overturn. Still, no significant enhancement of the maximal compressive stress could be reached; probably due to achieved saturation level (the maximal values were very high for all process variations).
The subchapter 7.4 was devoted to the comparison of the FE modelled to the experimentally determined stress profiles. On the surface, both techniques delivered very similar profiles with reasonably low differences. In depth, good agreement was achieved only in the direction longitudinal to the DR treatment, where some minor to moderate deviations were observed. In the transverse direction, all FE delivered depth profiles predicted at depth moderate tensile stresses, which were not present in the XRD determined profiles. The maximal compressive residual stresses were moderately overestimated by the FE analysis as well. In was difficult to state the exact source of these discrepancies, as it could be a combination of reduced sensitivity at high depths by the XRD technique and deviations due to the material representation or the friction conditions by the FE analysis.
Chapter 8 drew particular attention to the investigation of the surface topography and the hardness after DR, realised with experimental work and FE analysis. The experimental examinations of the surface roughness showed that the pre-machining has a more crucial influence than the DR process itself, i.e. in case of the milled state, the consecutive DR contributed to a significant reduction of the surface roughness. In contrast, no further improvement could be achieved in the milled + polished state, and in some cases, the surface quality even deteriorated. The shape of the DR trace was investigated using both experiments and FE modelling. Both techniques delivered very similar results, showing some macroscopic deformations, which in cases of narrow production tolerances, cannot be neglected.
The micro-hardness depth distributions after DR was investigated by means of Vickers indentation method. Here, for all process variations, no significant change of the hardness was observed in the DR trace. Out of the trace, the hardness on the surface even decreased. Additionally, x-ray diffraction peak widths (FWHM) were obtained and investigated, as they usually are considered as a non-direct measure of the hardness. In contrary to the Vickers micro-hardness depth profiles, the FWHM values were increased near the surface for all process parameters. On the surface, the FWHM values differed greatly by the different pre-machining states, as in general, the milled + DR state delivered significantly higher FWHM than the milled + polished + DR state.
Both the Vickers hardness and FWHM did not show any significant anisotropy of the values along- or transverse to the DR treatment.
Lastly, the plastic strain (also could be related to the hardness) was investigated using the FE analysis. Here, for all process variations was observed a significant anisotropy of the values along and transverse to the DR trace. In the longitudinal direction, the calculated values were with up to factor 10 lower than those in the transverse direction. A possible reason could be the defined friction boundary conditions.
The three considered methods for determination of the hardness were very difficult to compare, as in general, they are influenced by different factors. E.g., the residual stress state influences the Vickers indentation hardness, whyle the dislocation density and instrumental specifics have a significant impact on the FWHM. Both techniques, in the

considered cases, characterised the final material's hardness, not only the state generated by DR but also inherited by previous processing. In contrary, the FE analysis did not consider any pre-treatment and calculated plastic strain based only on the deformations caused by DR. The findings in chapter 8 emphasised the importance of considering the measurement/determination technique as such, as it can lead to difficult to interpret results or even to faulty conclusions.

As a conclusion, it could be stated that the presented thesis did contribute to the more comprehensive understanding of the investigated deep rolling process. The work drew attention to the influences of several process parameters, and process chains on the surface integrity described by the residual stress state, the surface topography and the cold working. The designed FE models delivered in most cases reasonable and experimentally comparable results. Despite some deviations, the models are capable of future uses, also with defined more complex part shapes.

LIST OF REFERENCES

Abrao, A. M. , et al. 2014. Surface and subsurface alterations induced by deep rolling of hardened AISI 1060 steel. [ed.] Springer. *Production Engineering Research and Development.* 2014, Vol. 8, pp. 551-558.

Achmus, C. 1999. *Messung und Berechnung des Randschichtzustands komplexer Bauteile nach dem Festwalzen.* [ed.] Papierflieger. Clausthal : s.n., 1999.

Altenberger, I. 2002. Alternative Mechanical Surface Treatments: Microstructures, Residual Stresses and Fatigue Behavior. *Conference Proceedings ICSP-8.* 2002, pp. 421-434.

Andablo-Reyes, E., Hidalgo-Alvarez, R. and de Vicente, J. 2011. Controlling friction using magnetic nanofluids. *Soft Matter.* 2011, Vol. 7, pp. 880-883.

Arunachalam, R. M. , Mannan, M. A. and Spowage, A. C. . 2004. Residual stress and surface roughness when facing age hardened Inconel 718 with CBN and ceramic cutting tools. *International Journal of Machine Tools Manufacture.* 2004, Vol. 44, pp. 879–887.

Askar'yan, G. A. and Moroz, E. M. 1963. Pressure on Evaporation of Matter in a Radiation Beam. *Soviet Journal of Experimental and Theoretical Physics.* 1963, Vol. 16, p. 1638.

Astakov, V. 2010. Surface Integrity–Definition and Importance in Functional Performance. [book auth.] J. P. Davim. *Surface Integrity in Machining.* London : Springer, 2010, pp. 1-35.

Balland, P., et al. 2013. An investigation of the mechanics of roller burnishing through finite element simulation and experiments. *International Journal o fMachine Tools & Manufacture.* 2013, Vol. 65, pp. 29-36.

Barrett, C. F. and Todd, R. 1984. Investigation of the effects of elastic pres-stressing technique on magnitude of compressive residual stress induced by shot peen forming of thick aluminum plates. *Proceedings of the 2nd International Conference on Shot Peening.* 1984, pp. 15-21.

Beghini, M., et al. 2014. Experimental parameter sensitivity analysis of residual stresses induced by deep rolling on 7075-T6 aluminium alloy. *Surface & Coatings Technology.* 2014, Vol. 254, pp. 175-186.

Berstein, B. and Fuchsbauer, B. 1982. Festwalzen und Schwingfestigkeit. *Materialwissenschaft und Werkstofftechnik.* 1982, Vol. 3, pp. 103-109.

Berstein, G. 1979. Oberflachenfeinwalzen und Festwaken - Grundlagen und Anwendung. Eßlingen : s.n., 1979.

Boardman, B. 1990. Fatigue Resistance of Steels. [book auth.] ASM Handbook Committee. *ASM Handbook, Volume 1: Properties and Selection: Irons, Steels, and High-Performance Alloys.* 1990, pp. 673-688.

Bouzid, W., Tsoumarev, O. and Sai, K. 2004. An investigation of surface roughness of burnished AISI, 1042 steel. [ed.] Springer-Verlag. *The International Journal of Advanced Manufacturing Technology.* 2004, Vol. 24, pp. 120–125.

Broggiato, G. B., Campana, F. and Cortese, L. 2008. The Chaboche nonlinear kinematic hardening model: calibration methodology and validation. *Meccanica.* 2008, Vol. 43, pp. 115–124.

Broszeit, E. 1984. Grundlagen der Schwingfestigkeitssteigerung durch Fest- und Glattwalzen. *Zeitschrift für Werkstofftechnik.* 1984, Vol. 15, pp. 416-420.

Brünnet, H. 2013. *Konzept zur eigenspannungsgerechten Produkt- und Prozessket-tengestaltung autofrettierter Bauteile unter Anwendung der Finite-Elemente-Methode.* [ed.] Schriftenreihe Fertigung und Konstruktion. Saarbrücken : s.n., 2013. p. 128. Vol. 50.

Brünnet, H., et al. 2014 a). Effect of different manufacturing process steps on the final residual stress depth profile along the process chain of autofrettaged thick-walled-cylinders. *Advanced Materials Research.* 2014 a), Vol. 996, pp. 676-681.

Brünnet, H., et al. 2014 b). Verification and Application of a new 3D Finite Element Approach to Model the Residual Stress Depth Profile After Autofrettage and Consecutive Reaming. *Procedia CIRP 13, 2nd CIRP Conference on Surface Integrity.* 2014 b), Vol. 13, pp. 72 – 77.

CAE Associates. 2013. Using Stress-Strain Data in a Finite Element Simulation. *Engineering Advantage.* 2013.

Calles, W. 1985. *Einfluss der Randschichtverformung durch Kaltrollen und Kugelstrahlen auf die Schwingfestigkeit der Titanlegierung TiAl6V4.* Aachen : Technische Hochschule Aachen, 1985. p. 55.

Dalaei, K., Karlsson, B. and Svensson, L. E. 2010. Stability of residual stresses created by shot peening of pearlitic steel and their influence on fatigue behaviour. *Procedia Engineering.* 2010, Vol. 2, pp. 613-622.

Dassault Systèmes. 2011. 2.4.1 Rigid body definition. *Abaqus Analysis User's Manual 6.11.* 2011.

—. 2014. Abaqus Analysis User's Manual 6.14. *Friction models in Abaqus/Explicit.* 2014.

Denkena, B., Reichstein, M. and Garcia, L. de Leon. 2007. Milling Induced Residual Stresses in Structural Parts out of Forged Aluminum Alloys. 2007.

DIN 14577. 2015. BS EN ISO 14577-1. *Metallic materials. Instrumented indentation test for hardness and materials parameters. Test method.* s.l. : Deutsches Institut für Normung, 2015.

DIN 8200. 1982. DIN 8200 - 1982-10 - Blasting; terms, classification of blasting techniques. s.l. : Deutsches Institut fur Normung E.V. (DIN), 1982.

DIN-EN 8580. 2003. DIN 8580:2003-09; Manufacturing processes - Terms and definitions, division. s.l. : Deutsches Institut fur Normung E.V. (DIN), 2003.

DIN-EN ISO 4287. 2010. DIN EN ISO 4287:2010-07 - Geometrical Product Specifications (GPS) - Surface texture: Profile method - Terms, definitions and surface texture parameters. s.l. : Deutsches Institut fur Normung E.V. (DIN), 2010.

Döbelin, N. 2013. Lesson 3 - Sample Preparation & Problems. *Lecture Handouts.* Upsala, Sweden : Profex - Open source XRD and Rietveld refinement, 2013.

Ecoroll GmbH. 2010. Operating Instruction No. 080592E/8, HGx-9 / HGx-19 / HGx-2. Celle : s.n., 2010.

Engel, B. 2005. Rückfederung Rückfederung – Phänomen und Phänomen und. *DGM – Fortbildungsseminar Tiefziehen.* 2005.

Fabbro, R., Peyre, P. and Berth, L. 1998. Physics and applications of laser shock processing of materials. [ed.] Laser institute of America. *Journal for laser applications.* 1998, Vol. 10, pp. 155-164.

Föppl, O. 1929. Das Drücken der Oberflächen von Bauteilen aus Stahl. *Stahl Eisen.* 1929, Vol. 49, pp. 575–577.

Gardin, C., et al. 2005. Crack propagation in compressive residual stress fields of crankshafts: experimental study and numerical simulation. *WIT Transactions on Engineering Sciences.* 2005, Vol. 49, pp. 231-240.

Gregg, D. W. and Thomas, S. J. 1966. Momentum Transfer Produced by Focused Laser Giant Pulses. *Journal of Applied Physics.* 1966, Vol. 37, pp. 2787–2789.

Hanson, K. 2015. Shot peening offers cost-effective way to make stronger metal products. *Cutting Tool Engineering.* 2015.

Hassan, A. D. 2018. A new prediction of the fatigue limit based on Brinell hardness and ultimate strength for high strength steels. [ed.] International Energy & Environment Foundation. *International journal of energy and environment.* 2018, Vol. 9, pp. 77-84.

Herbert, E. G. 1927. The work-hardening by abrasion, with an appendix on the "cloudburst" test and super hardening. *Journal of Iron and Steel.* 1927, pp. 65-82.

Hertz, H. 1882. Über die Berührung fester elastischer Körper. *Journal für die reine und angewandte Mathematik.* 1882, Vol. 92, pp. 156-171.

Hoffmann, J. E. 1984. *Der Einfluß fertigungsbedingter Eigenspannungen auf das Biegewechselverhalten von glatten und gekerbten Proben aus Ck 45 in verschiedenen Werkstoffzuständen.* [ed.] Deutscher Verband für Materialprüfung. Karlsruhe : s.n., 1984.

—. 2011. Residual stresses. *Script Structural durability, Part 1 - Mechanics of materials.* Kaiserslautern : Hochschule Kaiserslautern, 2011.

Holzapfel, H., et al. 1998. Einfluß der Kugelstrahlparameter auf die Randschichteigenschaften von 42CrMo4. *HTM - Härterei-Technische Mitteilungen.* 1998, Vol. 53, pp. 155-163.

Horger, O. J. E. 1936. Effect of the surface rolling on the fatigue strength of steel. *J. Appl. Mech.* 1936, Vol. 58, pp. 91–98.

Huang, X.P. 2005. A General Autofrettage Model of a Thick-Walled Cylinder Based on Tensile-Compressive Stress-Strain Curve of a Material. *The Journal of Strain Analysis for Engineering Design.* 2005, Vol. 40, pp. 599-607.

Jacob, L. 1920. Résistance et Construction des Bouches à Feu - Autofrettage. Tome 1. *Encyclopédie Scientifique, Bibliothèque de Méchanique Appliquée et Génie.* 1920.

Jawahir, S., et al. 2011. Surface integrity in material removal processes: Recent advances. *CIRP Annals - Manufacturing Technology.* 2011, Vol. 60, pp. 603-626.

Johnson, G. R. and Cook, W. H. 1983. A constitutive model and data for metals subjected to large strains, high strain rates and high temperatures. *Proceedings of the 7th International Symposium on Ballistics.* 1983, pp. 541–547.

Jung, U. 1996. *FEM-Simulation und experimentelle Optimierung des Festwalzens bauteilähnlicher Proben unterschiedlicher Größe.* Aachen : Shaker, 1996.

Kandil, F. A., Lord, D. and Fry, A. T. 2001. A review of residual stress measurement methods A guide to technique selection. *NPL Report.* 2001, Vol. MATC(A)O4.

Kelly, P. 2015. Lectures Solid Mechanics Part II: Engineering Solid Mechanics – small strain; Introduction to Plasticity. *http://homepages.engineering.auckland.ac.nz.* [Online] 2015. [Cited: 20 08 2019.] http://homepages.engineering.auckland.ac.nz.

Kim, J. C., Cheong, S. K. and Noguchi, H. 2013. Residual stress relaxation and low- and high-cycle fatigue behavior of shot-peened medium-carbon steel. *International Journal of Fatigue.* 2013, Vol. 56, pp. 114-122.

Klocke, F., et al. 2016. Deep rolling of fine blanking punch edges. *Int J Mater Form.* 2016, Vol. 9, pp. 489–498.

Klumpp, A., et al. 2016. Residual Stress States After Piezo Peening Treatment at Cryogenic and Elevated Temperatures Predicted by FEM Using Suitable Material Models. *Residual Stresses 2016; Materials Research Proceedings.* 2016, pp. 175-189.

Koenecke, W., Burrell, N. K. and Mehelich, C. 1982. Shot peening springs. *Springs.* 1982.

Kostryzhev, A. G. 2009. *Bauschinger effect in Nb and V microalloyed line pipe steels.* Birmingham : School of Metallurgy and Materials, College of Engineering and Physical Sciences, The University of Birmingham, 2009. p. 34.

Li, W., et al. 2012. Analytical prediction and experimental verification of surface roughness during the burnishing process. *International Journal of Machine Tools and Manufacture.* 2012, Vol. 62, pp. 67-75.

Liebisch, A. 1991. Bestimmung der Festwalzeigenspannungen in einsatzgehärteten Zahnrädern mit der Finite-Elemente-Methode. *Verein Deutscher Ingenieure Zeitschrift.* 1991, Vol. 133, pp. 73-79.

Lim, A., Castagne, S. and Wong, C. C. 2016. Quasi-static Process Modelling of Deep Cold Rolling on Ti-6Al-4V. *International Conference on Residual Stress.* 2016, Vol. 10, pp. 7-12.

Löhe, D., Lang, K. H. and Vöhringer, O. 2002. Residual Stresses and Fatigue Behavior. [book auth.] G. Totten, M. Howes and T. Inoue. [ed.] ASM International. *Handbook of residual stress and deformation of steel.* Materials Park, OH : s.n., 2002, pp. 27-53.

Lyubenova, N. and Baehre, D. 2015 c). Finite Element Modelling and Investigation of the Process Parameters in Deep Rolling of AISI 4140 Steel. *Journal of Materials Science and Engineering B.* 2015 c), Vol. 5, pp. 277-287.

Lyubenova, N. and Bähre, D. 2015 a). Finite Element modeling and investigation of the process parameters in Deep Rolling of a plane geometry. *12th International Conference on the Mechanical Behavior of Materials.* Karlsruhe : s.n., 2015 a).

—. 2017 a). Investigation of the Surface Residual Stresses in Single and Multiple Trace Deep Rolling on Flat AISI 4140 Specimens. *Conference Proceedings of the 13th International Conference on Shot Peening.* 2017 a), pp. 428-433.

—. 2017 b). The Impact of the Material Modeling on the Calculated Residual Stresses Induced by Deep Rolling. *International materials research meeting in the greater region - Current Trends in the Characterisation of Materials and Surface Modification.* Saarbrücken : s.n., 2017 b).

Lyubenova, N., et al. 2019. Impact of the Process Parameters, the Measurement Conditions and the Pre-Machining on the Residual Stress State of Deep Rolled Specimens. *Journal of Manufacturing and Materials Processing.* 2019, Vol. 3.

Lyubenova, N., Jacquemin, M. and Bähre, D. 2016. Influence of the Pre-Stressing on the Residual Stresses Induced by Deep Rolling. *Materials Research Proceedings.* 2016, Vol. 2, pp. 253-258.

Lyubenova, N., Thuillier, L. and Baehre, D. 2015 b). Modelling of the input parameters and investigations of the surface residual stresses and –deformations in Deep Rolling. *29th International Conference of Surface Modification Technology (SMT 29).* Copenhagen : VALARDOCS, 2015 b). pp. 86-93.

Macherauch, E. and Zoch, H. W. 2011. Röntgenographische Eigenspannungsbestimmung. [book auth.] Macherauch. *Praktikum in Werkstoffkunde.* s.l. : Vieweg+Teubner, 2011, p. 466.

Magalhaes, F. C., et al. 2016. Analytical Modeling of Surface Roughness, Hardness and Residual Stress Induced by Deep Rolling. [ed.] ASM International. *Journal of Materials Engineering and Performance.* 2016, Vol. 26.

Majzoobi, G. H., Jouneghani, F. Z. and Khademi, E. 2016. Experimental and numerical studies on the effect of deep rolling on bending fretting fatigue resistance of Al7075. *Int J Adv Manuf Technol.* 2016, pp. 2137–2148.

Manouchehrifar, A. and Alasvand, K. 2012. Simulation and Research on Deep Rolling Process Parameters. *Int J Advanced Design and Manufacturing Technology.* 2012, Vol. 5, pp. 31-37.

MAXIMATOR GmbH. 2015. Maximator - Maximum Pressure. *Valves, fittings, tubings: Maximator launches 15,000-bar series.* [Online] 16 06 2015. [Cited: 07 09 2019.] https://www.maximator.de/flycms/en/web/10/-XzsjZSLvJy2GAEtNEjdod9Uhthtd/Latest+News.html.

Meguid, S. A., Shagal, G. and Stranart, J. C. 2002. 3D FE analysis of peening of strain-rate sensitive materials using multiple impingement model. *International Journal of Impact Engineering.* 2002, Vol. 27, pp. 119-134.

Menig, R., Schulze, V. and Vöhringer, O. 2003. Comparison of surface characteristics and thermal residual stress relaxation of laser peened and shot peened AISI 4140. *Shot Peening ICSP 8.* 2003, pp. 498-504.

Meyer, D., Brinksmeier, E. and Hoffmann, F. 2011. Surface hardening by cryogenic deep rolling. *Procedia Engineering.* 2011, Vol. 19, pp. 258-263.

Meyer, H. und Epp, J. 2018. In Situ X-ray Diffraction Analysis of Stresses during Deep Rolling of Steel. *Quantum Beam Science.* 2018, Bd. 2, S. 1-11.

Moore, M. G. and Evans, W. P. 1958. Mathematical Correction for Stress in Removed Layers in X-Ray Diffraction Residual Stress Analysis. *SAE Technical Papers.* 1958, Vol. 66, pp. 340-345.

Mori, K. I., Osakada, K. and Matsuoka, N. 1995. Rigid-plastic finite element simulation of peening process with plastically deforming shot. *Transactions of the Japan Society of Mechanical Engineers, Part A.* 1995, Vol. 586, pp. 1337-1343.

Müller, E. 2005. Evolution of the residual stresses by stress rolling. *Proceedings of the 9th International Conference on Shot Peening.* 2005, pp. 436-441.

Neuman, F. 1964. Momentum transfer and cratering effects produced by giant laser pulses. *Applied Physics Letters.* 1964, Vol. 4, pp. 167–169.

O'Hara, P. 1999. Superfinishing and shot peening of surfaces to optimise roughness and stress. *Transactions on Engineering Sciences.* 1999, Vol. 25, pp. 321-330.

Panalytical. 2013. Introduction to sample preparation. *Basic XRD course.* 2013.

Pedersenal, T. F. and Hansson, I. L. 1989. Finite element calculations for correction of residual stress profiles of coated and uncoated materials measured by X-ray diffraction. *NDT International.* 1989, Vol. 22, pp. 347-352.

Perenda, J., et al. 2014. Modeling and experimental validation of the surface residual stresses induced by deep rolling and presetting of a torsion bar. *Int J Mater Form.* 2014, Vol. 9, pp. 435–448.

Perenda, J., et al. 2015. Residual stresses after deep rolling of a torsion bar made from high strength steel. *Journal of Materials Processing Technology.* 2015, Vol. 218, pp. 89-98.

Prevey, P. S. 2000. The Effect of Cold Work on the Thermal Stability of Residual Compression in Surface Enhanced IN718. *Proceedings: 20th ASM Materials Solutions Conference & Exposition.* 2000, pp. 1-9.

Prevéy, P., Hombach, D. and Mason, P. 1997. Thermal residual stress relaxation and distortion in surface enhanced gas turbine engine components. [ed.] ASM International. *Milam DL (ed) Proceedings of the 17th heat treating society conference.* 1997, pp. 3-12.

Rodríguez, A., et al. 2012. Surface improvement of shafts by the deep ball-burnishing technique. *Surface and Coatings Technology.* s.l. : Elsevier B.V., 2012. pp. 2817–2824.

Röttger, K. and Fricke, S. 2014. Deep rolling of bore holes with a diameter of 3 mm with a hydrostatic tool. *Conference Proceedings 2014: ICSP-12.* 2014, pp. 381-385.

Röttger, K. 2003. *Walzen hartgedrehter Oberflächen.* [ed.] Shaker. Aachen : s.n., 2003. p. 60.

Sadrossadat, S. M. and Johansson, S. 2009. The effect of casting parameters on residual stresses and microstructure variations of an Al-Si cast alloy. *Advances in X-ray Analysis.* 2009, Vol. 52.

Schaal, R. 2002. *Berechnung der Dauerfestigkeit festgewalzter Bauteile durch FEM-Festwalzsimulation und Methoden der linear-elastischen Bruchmechanik.* Aachen : Shaker Verlag, 2002.

Schajer, G. S. 2015. *Practical Residual Stress Measurement Methods.* s.l. : Wiley, 2015. Vol. 7.

Scholtes, B. and Macherauch, E. 1986. Auswirkungen mechanischer Randschichtverformungen auf das Festigkeitsverhalten metallischer Werkstoffe. [ed.] Hanser. *Zeitschrift für Metallkunde.* 1986, Vol. 77, pp. 322-327.

Scholtes, B. 1990. *Eigenspannungen in mechanisch randschichtverformten Werkstoffzuständen: : Ursachen, Ermittlung und Bewertung.* Oberursel : DGM-Informationsgesellschaft, 1990.

—. 1987. Residual stresses introduced by machining. [book auth.] A. Niku Lari. *Advances in Surface Treatments.* Oxford : Pergamon Press, 1987, p. 65.

Schuh, A., et al. 2007. Deep rolling of titanium rods for application in modular total hip arthroplasty. *Journal of biomedical materials research. Part B, Applied biomaterials.* 2007, Vol. 81, pp. 330–335.

Schulze, V. 2005 a). Introduction to Modern Mechanical Surface Treatment. *Modern Mechanical Surface Treatment: States, Stability, Effects.* Weinheim : Wiley-VCH, 2005 a), p. 4.

—. 2005 b). Procedures of mechanical surface treatments. [ed.] Wiley-VCH Verlag GmbH & Co. KGaA. *Modern Mechanical Surface Treatment.* 2005 b), p. 18.

—. 2015 c). Script DGM Symposium Surface Engineering. *Mechanische Oberflächenbehandlungen.* Dresden : s.n., 2015 c).

Schümann, K., et al. 2017. Investigation of Bauschinger effect in thermoplastic polymers for biodegradable stents. [ed.] De Gruyter. *Current Directions in Biomedical Engineering.* 2017, Vol. 3, pp. 623–625.

Schwarzer, J., Schulze, V. and Vöhringer, O. 2006. Finite Element Simulation of Shot Peening – A Method to Evaluate the Influence of Peening Parameters on Surface Characteristics. [book auth.] L. Wagner. *Shot Peening.* s.l. : Wiley-VCH Verlag GmbH & Co. KGa, 2006, Vols. 524-525, pp. 349–354.

Scuracchio, B. G., et al. 2013. Statistical analysis of coil springs durability with different shot peening conditions. *SAE Technical Papers.* 2013, pp. 1-6.

Sonntag, R., et al. 2015. Fatigue Performance of Medical Ti6Al4V Alloy after Mechanical Surface Treatments. *PloS one.* 2015, Vol. 10.

Straub, C. and May, D. 1949. Stress Peening. *The Iron Age.* 1949, pp. 66-70.

Sue, J. A. and Schajer, G. S. 1994. Stress Determination in Coatings. *Surface Engineering.* 1994, Vol. 5, pp. 647-653.

Surtee, I. and Nobre, J. P. 2017. Residual Stress Redistribution due to Removal of Material Layers by Electrolytic Polishing. *Residual Stresses 2016; Materials Research Proceedings.* 2017, Vol. 2, pp. 593-598.

Thum, A. and Bautz, W. 1935. Ursachen der Steigerung der Dauerhaltbarkeit gedrückter Stäbe. *Forschung auf dem Gebiet des Ingenieurwesens A.* 1935, Vol. 6, pp. 121–128.

Totten, G., Howes, M. and Inoue, T. . 2002. *Handbook of Residual Stress.* Ohio : ASM International, 2002.

Ulutan, D. , Alaca, B. E. and Lazoglu, I. 2007. Analytical modelling of residual stresses in machining. *Journal of Materials Processing Technology.* 2007, Vol. 183, pp. 77–87.

Vohringer, O. 1987. Changes In The State Of The Material By Shot Peening. [book auth.] H. Wohlfahrt, R. Kopp and o. Vöhringer. *Shot peening - conference proceedings ICSP-3.* s.l. : DGM Informationsgesellschaft, 1987, pp. 185-204.

Wang, Z. and Gong, B. 2002. Residual Stress in the Forming of Materials. [book auth.] G. Totten, M. Howes and T. Inoue. *Handbook of Residual Stress and Deformation of Steel.* Ohio : ASM International, 2002, pp. 141-149.

Wasniewski, E., et al. 2014. Material Removal, Correction and Laboratory X-Ray Diffraction. *Advanced Materials Research.* 2014, Bd. 996, S. 181-186.

Withers, P. J. and Bhadeshia, H. K. D. H. 2001. Residual stress part 1: Measurement techniques. *Materials Science and Technology.* 2001, Vol. 17, p. 355.

Xu, J., Zhang, D. and Shen, B. 1981. The Fatigue Strength And Fracture Morphology Of Leaf Spring Steel After Prestressed Shot Peening. *Proceedings of the 1st International Conference on Shot Peening.* 1981, pp. 367-374.

Yan, J. 1999. *Study of Bauschinger Effect in Various Spring Steels.* Toronto : Department of Metallurgy and Materials Science, University of Toronto, 1999.

Yao, C. F., et al. 2016. Surface integrity and fatigue analysis of shot-peening for 7055 aluminum alloy under different high-speed milling conditions. *Advances in Mechanical Engineering.* 2016, Vol. 8, pp. 1-10.

Zinn, W. and Scholtes, B. 2002. Residual Stress Formation Processes during Welding and Joining. [book auth.] G. Totten, M. Howes and T. Inoue. *Handbook of Residual Stress and Deformation of Steel.* Ohio : ASM International, 2002, pp. 391-396.

Zoch, H.-W. 1995. Randschichtverfestigung – Verfahren und Bauteileigenschaften. *HTM Härterei-Techn. Mitt. 50.* 1995, Vol. 5, pp. 287-294.